UC San Diego

UC San Diego Electronic Theses and Dissertations

Title

Fluid Dynamics of Active Suspensions: The Effects of Interparticle Interactions, External Fields and Confinement

Permalink

https://escholarship.org/uc/item/7vg9t600

Author

Ezhilan, Barath

Publication Date

2016

Peer reviewed|Thesis/dissertation

eScholarship.org Powered by the California Digital Library
University of California

UNIVERSITY OF CALIFORNIA, SAN DIEGO

Fluid Dynamics of Active Suspensions: The Effects of Interparticle Interactions, External Fields and Confinement

A Dissertation submitted in partial satisfaction of the
requirements for the degree
Doctor of Philosophy

in

Engineering Sciences (Mechanical Engineering)

by

Barath Ezhilan

Committee in charge:

Professor David Saintillan, Chair
Professor Juan Carlos del Alamo
Professor Alex Groisman
Professor Sutanu Sarkar
Professor Joseph Wang

2016

Copyright
Barath Ezhilan, 2016
All rights reserved.

The Dissertation of Barath Ezhilan is approved, and it is acceptable in quality and form for publication on microfilm and electronically:

_____

_____

_____

_____

_____

Chair

University of California, San Diego

2016

DEDICATION

To the memory of my grandfather, Balaraman.

EPIGRAPH

It really is a nice theory. The only defect I think it has is probably common to all philosophical theories. It's wrong.

—Saul Kripke

TABLE OF CONTENTS

LIST OF FIGURES

ACKNOWLEDGEMENTS

I am sincerely grateful to all the awesome people who have provided me academic and moral support during the last five years of my graduate study at UIUC and UCSD. I thank my advisor, David Saintillan for his incredible guidance throughout my graduate research career. With his penchant for solving hard and challenging problems, emphasis on rigorous treatment of the subject matter and consistent and clear communication of research, David has been a remarkable role model. I would also to like to thank my thesis committee members Juan Carlos del Alamo, Sutanu Sarkar, Alexander Groisman and Joseph Wang for their valuable advice and feedback on my research. I also thank my graduate co-ordinators at UIUC and UCSD, Kathyrn Smith and Lydia Ramirez, for their incredible help and timely support. Funding from National Science Foundation (NSF) Grants DMS-0930931, CBET-1151590 and DMS-1463965 and computational resources from Teragrid Grant TG-CTS100007 are gratefully acknowledged.

My graduate research has tremendously benefited from collaborations and discussions with several people. I thank Michael Shelley for his collaboration on concentrated active suspensions and his encouragements. A special thanks to Dr. Joseph Wang and his group members, especially Beatriz, Jinxing, Isaac, Wei, Renfeng and Allen for a fruitful and fun research collaboration. I also thank Alexandre Solon, Sho Takatori, Andrew Hazel, Bhargav Rallabandi, John Brady, Roman Stocker, Roberto Rusconi, Jeff Guasto, Amin Doostmohammadi, Patrick Underhill, Igor Aranson, Raymond Goldstein, Anke Lindner, Eric Clement, Saverio Spagnolie, Enkeleida Lushi and Tong Gao for insightful discussions and valuable feedback.

Over the last five years, I have also greatly benefited from the help and advice

of the members of the Saintillan research group. I am grateful to Amir for providing me with his codes that helped me get started with my graduate research. I greatly appreciate the advice and support from Jae Sung and Karthik during the early years of my PhD. I had an awesome time collaborating with Roberto, Amir, Maxime T and Maxime B on various exciting research problems. I also thank other members of the Saintillan Research Group, Adrien, Ku Da, Hari, Tom, Debasish, Ram, Shrenik, Brato and Danny for being a part of this research journey.

I greatly benefited from the courses offered by Brian Jewett, David Saintillan, Jonathan Higdon, Matthew West, Sascha Hilgenfeldt, Jonathan Freund, Anil Hirani, Ken Stolarsky and Carlos Pantano at Illinois, I thank these instructors for their dedication to teaching.

I attribute my passion for problem solving to my high school mathematics teachers, Balasubramanian and T R Subramanian, and I thank them for giving me their passion for mathematics and for laying a strong analytical foundation. I also thank my undergraduate mentor, Mahesh Ganesan, for encouraging me to pursue fluid mechanics research.

I couldn't have survived the intense five years of graduate school without the emotional support and blessings from my friends and well-wishers. Special thanks to Kevin, Joey, Sree, Ajay, Prana, RK, Elise, JD, Bharat, Bhargav, Bryan, Pronoy, Chris, Ranjani, Jomo, Prasanth, Velu, Sundar, Guru, Madhana, Aravind, Suresh, Tim and many others for giving me a sense of community at a place far away from home!

I am grateful to my parents, Ezhilan and Latha, as well as my brother Prem, sister-in-law Shobana and my nephew Rishi for their unconditional love and support. They are a tremendous inspiration to me and I owe them all my success.

Finally, thanks to the program directors of Insight Data Science, John, Zach, Wafa and Thushy, for helping me engineer an exciting career transition.

Chapter 1, in small part, is a reprint of the material that appears in my master's thesis 2012."Three-dimensional kinetic simulations of active suspensions: effect of chemotaxis and steric interaction" by Ezhilan, Barath, University of Illinois, 2012. I was the primary investigator and author of this manuscript.

Chapter 2, in full, is a reprint of the material as it appears in Physics of Fluids 2013. "Instabilities and nonlinear dynamics of concentrated active suspensions" by Ezhilan, Barath; Shelley, Michael J; Saintillan, David, the American Institute of Physics, 2013. I was the primary investigator and author of this paper.

Chapter 3, in full, is a reprint of the material as it appears in Physics of Fluids 2012. "Chaotic dynamics and oxygen transport in thin films of aerotactic bacteria" by Ezhilan, Barath; Alizadeh Pahlavan, Amir; Saintillan, David, the American Institute of Physics, 2012. I was the primary investigator and author of this paper.

Chapter 4, in part, is a reprint of the material as it appears in Journal of Fluid Mechanics 2015. "Transport of a dilute active suspension in pressure-driven channel flow" by Ezhilan, Barath; Saintillan, David, Cambridge University Press, 2015. I was the primary investigator and author of this paper.

Chapter 5, in part, is a reprint of the material as it appears in Journal of Fluid Mechanics: Rapids 2015. "On the distribution and swim pressure of run-and-tumble particles in confinement" by Ezhilan, Barath; Alonso, Roberto; Saintillan, David, Cambridge University Press, 2015. I was the primary investigator and author of this paper.

Also, as part of my PhD experience, I authored other papers not appearing in

this dissertation. They are the article published in Nanoscale 2015 entitled "Motion-based threat detection using microrods: Experiments and numerical simulations" by Ezhilan, Barath; Gao, Wei; Pei, Allen; Rozen, Isaac; Dong, Renfeng; Sanchez, Beatriz Jurado; Wang, Joseph; Saintillan, David, Royal Society of Chemistry, 2015, and the article published in Scientific Reports 2015 entitled "Vapor-driven propulsion of catalytic micromotors" by Dong, Renfeng; Li, Jinxing; Rozen, Isaac; Ezhilan, Barath; Xu, Tailin; Christianson, Caleb; Gao, Wei; Saintillan, David; Ren, Biye; Wang, Joseph.

VITA

2010	B. Tech. in Mechanical Engineering, National Institute of Technology, Tiruchirappalli
2011	M. S. in Mechanical Engineering, University of Illinois, Urbana Champaign
2016	Ph. D. in Engineering Sciences (Mechanical Engineering), University of California, San Diego

PUBLICATIONS

B. Ezhilan, A. Alizadeh Pahlavan, D. Saintillan, "Chaotic dynamics and oxygen transport in thin films of aerotactic bacteria", *Physics of Fluids*, **24** 091701 (2012).

B. Ezhilan, M. J. Shelley, D. Saintillan, "Instabilities and nonlinear dynamics of concentrated active suspensions", *Physics of Fluids*, **25** 070607 (2013).

B. Ezhilan, W. Gao, A. Pei, I Rozen, R. Dong, B. Jurado-Sanchez, J. Wang, D. Saintillan, "Motion-based threat detection using microrods: Experiments and numerical simulations", *Nanoscale*, **7** 7833-7840 (2015).

B. Ezhilan, D. Saintillan, "Transport of a dilute active suspension in pressure-driven channel flow", *Journal of Fluid Mechanics*, **777** 482-522 (2015).

R. Dong, J. Li, I. Rozen, B. Ezhilan, T. Xu, C. Christianson, W. Gao, D. Saintillan, B. Ren, J. Wang, "Vapor-driven propulsion of catalytic micromotors", *Scientific Reports*, **5** 13226 (2015).

B. Ezhilan, R. Alonso-Matilla, D. Saintillan, "On the distribution and swim pressure of run-and-tumble particles in confinement", *Journal of Fluid Mechanics: Rapids*, **781** R4 (2015).

ABSTRACT OF THE DISSERTATION

Fluid Dynamics of Active Suspensions: The Effects of Interparticle Interactions, External Fields and Confinement

by

Barath Ezhilan

Doctor of Philosophy in Engineering Sciences (Mechanical Engineering)

University of California, San Diego, 2016

Professor David Saintillan, Chair

This thesis is devoted to understanding the effect of inter-particle interactions, external fields and confinement in active suspensions. Active suspensions, such as a bath of swimming micro-organisms, have microstructural elements which are motile and exert active stresses on the suspending fluid. The internally generated stresses in active suspensions lead to an intrinsic coupling between the swimmer configurations and the immersing fluid.

The first theme of the thesis focuses on hydrodynamically driven self-organization in active suspensions. We first study the dynamics of concentrated active suspensions

in a 3D periodic domain using a coupled Smoluchowski-Stokes kinetic model and discover novel instabilities for both rear-actuated (pusher) and front-actuated (puller) swimmers, characterized by giant number density fluctuations, due to the coupled effects of hydrodynamic and steric interactions. Next, we incorporate chemotactic run-and-tumble effects in the kinetic model to study the dynamics in thin films of aerotactic bacteria. A transition to chaotic dynamics beyond a critical film thickness is reported, in agreement with experiments, and shown to be a consequence of the coupling between aerotactic response of bacteria and hydrodynamic disturbance flows.

The second theme focuses on the sole interplay between motility and confinement in dilute suspensions, ignoring the effect of inter-particle interactions. First, we investigate the dynamics of a confined suspension of Brownian swimmers using a simple kinetic model by prescribing a no-flux condition on the probability distribution function of particle configurations and explain several peculiar dynamics reported in experiments, viz., wall accumulation, as well as upstream swimming, centerline depletion and shear-trapping when a pressure-driven flow is imposed. Next, we calculate the swim pressure of non-Brownian run-and-tumble spherical swimmers using a kinetic model based on coupled bulk/surface probability density functions.

The third theme focuses on the effect of confinement on active self-organization. We discover a symmetry-breaking phase-transition to a spontaneous flowing state with net fluid pumping beyond a critical concentration in a strongly confined channel. The framework for studying confined active suspensions is also extended to explore geometric control of active self-organization in circular and other complex domains.

Chapter 1

Introduction

Biological systems are composed of autonomous agents that are motile and can self-propel by converting energy from the environment into directed or persistent motion. Motility and activity in such self-propelled particle (SPP) systems engender spectacular collective behavior characterized by remarkable spatio-temporal self-organization, in spite of the absence of any centralized co-ordination. Fish schools swirling like a stirred fluid to escape from a nearby predator, Aerial display of birds, locust marching in a field, rotating colony of fire ants, collectively swarming bacteria are a few examples of this phenomenon [2]. Over the last couple of decades, such non-equilibrium systems, composed of self-propelled units called 'active' particles have been termed 'active matter' and have excited research in areas as diverse as biophysics, colloidal science, statistical mechanics, fluid dynamics and applied mathematics.

The universal properties of such collective self-organization has been studied using minimal agent-based model introduced by Vicsek *et al.* [3], where the SPP are modeled as point particles, which move with a constant speed, obeying a noisy local rule, that requires the particle to align its direction with its neighbors. This

model demonstrates a disorder-to-order transition characterized by a sudden onset of collective motion above a critical concentration (or below a critical level of noise). While elucidating the basic ingredients necessary for spontaneous self-organization, these minimal models treat the medium in which the particles move as an inert substrate and do not account for the microscopic details of the interactions between the active particles and their suspending medium.

The focus of this thesis are wet active matter, or 'active suspensions', in which active particles are suspended in a viscous fluid. A paradigmatic example of active suspensions are suspensions of micro-organisms. These active suspensions are peculiar complex fluids, which display fascinating dynamics characterized by complex pattern formation and density fluctuations [4, 5], enhanced swimming speeds [6], spatio-temporal coherence [7] on length scales that exceed single particle length, 3D turbulent-like behavior [6, 5], nematic structures [8], enhanced passive tracer diffusivities [9, 10] and spontaneous chaotic motion which takes the form of whirls, jets and vortices [11, 12]. In these suspensions, the active particles interact via long range hydrodynamic interactions and the coupling between the active particles and the suspending medium is crucial to the understanding of the dynamics.

The collective motion in active suspensions can be understood by constructing the coupled kinetic equations for the swimmer configurations and a Stokes equation for the fluid velocity of the suspending medium. An introductory first principles derivation of such a model is presented in section 1.3 after reviewing a few basics of low Reynolds number locomotion in section 1.1 and polymer suspension theory in section 1.2. The motivation of the thesis is then presented in section 1.4 followed by an overview of the research results in section 1.5.

1.1 Single micro-swimmer dynamics

To understand the collective dynamics in active suspensions, it is first necessary to understand the motion of a single active particle, the preliminaries of which, we review in this section. For a detailed account, please see the review by Lauga [13].

1.1.1 Low Reynolds number regime

Micro-organisms such as Bacteria have a typically length of 4 μm and travel with a velocity of 20 $\mu m s^{-1}$. The Reynolds number, measuring the relative importance of inertial to viscous forces, given by $Re = \frac{UL}{\nu}$ (with U and L the characteristic velocity and length scales, and ν the kinetic viscosity of the fluid), associated with the swimming of these micro-organisms, is very small. This points to a crucial difference in mechanical swimming strategies of micro-organisms as compared to macroscopic organisms. While locomotion of macroscopic organisms in fluids generally utilize inertia to achieve propulsion by imparting momentum into the fluid, micro-organisms inhabit a highly viscous low-Reynolds number ($Re \ll 1$) world, where inertial propulsion mechanisms do not help.

1.1.2 Stokes flow

The fluid flows associated with the limit of zero Reynolds number ($Re = 0$) are called Stokes flow. In this limit, the inertial terms dropout of the incompressible Navier-Stokes equation, and momentum and continuum equation read,

$$\nabla q - \eta \nabla^2 \mathbf{u} = \mathbf{f}, \quad \nabla \cdot \mathbf{u} = 0. \tag{1.1}$$

where η is the shear viscosity of the fluid, q is the pressure in the fluid, $\mathbf{f}$ is the force acting on the fluid and $\mathbf{u}$ is the fluid velocity.

Two important properties of the Stokes equation are

- **Time independence**: The Stokes equation are independent of time. Any time dependence in the fluid velocity has to either come from the forcing term $\mathbf{f}$ or the boundary condition. Time-independence implies two crucial subproperties, instantaneity and time-reversibility.

- **Linearity**: Linearity of the Stokes equation allows for superposition of fundamental solutions to solve complex problems.

As a consequence of these two properties, a swimmer must deform in a way that is not invariant under time-reversal, to propel itself and this result is famously called the 'Scallop theorem' [14].

1.1.3 Minimal model for microswimmers: Pushers *vs* Pullers

Micro-organisms have evolved different propulsion strategies to survive the harsh world of zero Reynolds number, which is inherently unfavorable for mechanical swimming. Examples include ciliary or flagellar locomotion. In flagellar propulsion, a mechanism employed by model microswimmers such as motile bacteria and microalgae, the cyclic nonreciprocal deformation of the flagella imparts a net-propulsive force $\mathbf{F}_p$ in a direction opposite to that of the net-propulsion of the swimmer. In the limit of zero Reynolds number, the nuetrally buoyant swimmer is force-free, which implies that, the propulsive force $\mathbf{F}_p$ will be exactly balanced by the viscous drag force ($\mathbf{F}_d$ = -$\mathbf{F}_p$), which is exerted on the fluid by the cell body. To leading order, the active particle

has a net effect of exerting a force dipole on the fluid medium, which in the Stokes flow regime, drives a long-ranged flow (called a 'stresslet' flow) which decays with the inverse square of the distance from the particle center ($1/r^2$) in three dimensions.

Recent experiments [15, 16] have indeed confirmed the notion that, irrespective of the specifics of the swimming mechanisms employed by the microswimmers, the long-range fluid flows that they create have universal properties in the far-field, characterized by such stresslet flows. This allows us to classify microswimmers into two broad categories.

- **Pushers or rear-actuated swimmers**: Pusher particles exert their propulsive thrust through their tail and thus induces a negative force dipole. Common examples include motile bacteria such as *B. Subtilis* and *E. Coli*.

- **Pullers or front-actuated swimmers**: Puller particles exert their propulsive thrust through their head and thus induces a positive force dipole. Common examples include microalgae such as *C. reinhardtii*.

Note that, 'head' and 'tail' are defined with respect to the net direction of propulsion of the swimmer, henceforth, symbolized using $\mathbf{p}$.

1.1.4 Run-and-tumble motion of bacteria

To complete the discussion of the single (isolated) micro-swimmer dynamics, we finally discuss the run-and-tumble motion of swimming bacteria. A bacterium propels itself by rotating its flagella. When the flagella rotate in the counter clockwise direction, this leads to the bundling of the flagella resulting in a straight-line propulsion, called as the 'run' phase. This 'run' phase is interspersed by 'tumbling'

events, which occurs when the flagellar rotation abruptly changes to clockwise, leading to unbundling of the flagella and reorientation of the cell body. The tumbling event, is again followed by a run phase but now in a new, random direction. For bacteria, the tumbling event occurs at a rate $1s^{-1}$ lasting for a duration of $0.1s$ [17]. In an uniform environment, the bacterial motion resembles a classical random walk.

In the presence of the stimulant gradient (chemoattractants such as oxygen or nutrients, or chemorepellents such as fatty acids), bacteria can modulate their tumbling frequency based on the temporal sensing of the chemical gradients and perform a biased random walk to achieve chemotaxis (directed migration along a chemical gradient).

1.2 Concentration regimes in polymer suspensions

The continuum kinetic theory for active suspensions that will be presented in section 1.3 are direct extensions of classical models for their passive counterparts viz., suspensions of slender rod-like polymers proposed by Doi and Edwards [18]. While analyzing the interactions between slender rod-like polymers, with diameter b and length L, at finite concentration, they divided the polymer solutions into 4 concentration regimes. We briefly review them here.

- **Dilute solution**: A solution whose concentration is low enough that the average distance between the polymers $n^{-\frac{1}{3}}$ is much larger than the length of the polymer L or

$$n \lesssim n_1 \approx \frac{1}{L^3}, \tag{1.2}$$

where n is the number of particles per unit volume. In this regime, each polymer rotates freely without being influenced by other polymers (hydrodynamic and steric interactions are neglible).

- **Semi-dilute solution**: At concentrations corresponding to $n \gg n_1$, the rotation of the polymer is restricted due to the effect of other polymers, but the static properties are not affected seriously until the concentration reaches another characteristic concentration n_2. This concentration regime, Semi-dilute, occurs for a concentration n that satisfies the equation below.

$$n_1 \lesssim n \ll n_2 \approx \frac{1}{bL^2}. \tag{1.3}$$

In this regime the excluded volume effects are negligible but the hydrodynamic interactions are significant and have to be taken into account.

- **Concentrated isotropic solution**: When the concentration n becomes greater than n_2, the excluded volume effects become important and the polymer align nematically with their neighbours because of steric interactions. But the solution remains isotropic till the concentration increases beyond another critical value n^* which is of the order of $\frac{1}{bL^2}$. This concentration regime occurs when

$$n_2 \lesssim n \lesssim n^*. \tag{1.4}$$

Even though the solution is macroscopically isotropic, steric interactions influences static and dynamical properties and have to be taken into account.

- **Liquid crystalline solution**: When concentration n becomes greater than n^*,

the polymers align on a macroscopic scale in equilibrium (without any external field) and the solution becomes anisotropic. This occurs when

$$nbL^2 \geqslant 1. \tag{1.5}$$

1.3 Suspension level kinetic theory for active suspensions: *Doi-Saintillan-Shelley model*

The work presented in this thesis is centered on the continuum kinetic model proposed by Saintillan and Shelley [19, 20], which we review in this section.

Saintillan & Shelley [19, 20] developed a kinetic model for semi-dilute active suspensions that are self-consistently derived from a first-principles mean-field description where the interactions between the active particles and the suspending fluid are calculated using a coarse-graining approach. In this approach, a conservation equation for the configuration of the active particles is coupled with the Stokes equation for the local disturbance velocity (created by the force dipoles exerted by the active particles).

1.3.1 Smoluchowski equation

The configuration of the active particles is captured by the probability distribution function $\Psi(\mathbf{x}, \mathbf{p}, t)$ of finding an active particle at position $\mathbf{x} = (x, y, z)$ with orientation $\mathbf{p} = (\sin\theta\cos\phi,\, \sin\theta\sin\phi, \cos\theta)$ at time t, where $\mathbf{p}$ also defines the direction of swimming. The probability distribution function satisfies the Smoluchowski equation.

$$\frac{\partial \Psi}{\partial t} + \nabla_x \cdot (\dot{\mathbf{x}}\,\Psi) + \nabla_p \cdot (\dot{\mathbf{p}}\,\Psi) = 0, \tag{1.6}$$

where the translational flux velocity $\dot{\mathbf{x}}$ captures self-propulsion with constant velocity V_s in the direction of $\mathbf{p}$, advection by the background disturbance flow (which is perhaps created by other swimmers), and center-of-mass diffusion with isotropic and constant diffusivity d_t:

$$\dot{\mathbf{x}} = V_s\,\mathbf{p} + \mathbf{u}(\mathbf{x}) - d_t \nabla_x \ln \Psi. \tag{1.7}$$

Particle rotations are captured by the angular flux velocity $\dot{\mathbf{p}}$, which includes contributions from the rotation of the particles by the fluid (via Jeffery's equation), and from rotational diffusion with diffusivity d_r:

$$\dot{\mathbf{p}} = (\mathbf{I} - \mathbf{pp}) \cdot \nabla_x \mathbf{u}(\mathbf{x}) \cdot \mathbf{p} - d_r \nabla_p \ln \Psi, \tag{1.8}$$

following the notation $\nabla_x \mathbf{u} = \frac{\partial u_i}{\partial x_j}$.

1.3.2 Mean-field active stress and fluid velocity

The background flow $\mathbf{u}(\mathbf{x})$ is driven by the active stresses exerted by the particles as they propel themselves through the fluid. The microscale active particles creates a force dipole (to leading order) as they propel themselves, which in the Stokes regime, can be characterized by the symmetric first moment of the surface stress of a body called the 'stresslet'. The particle extra stress ($\mathbf{\Sigma}^a$) in a suspension containing a large number of interacting active particles can be calculated as a local distributional average of the individual stresslet contributions.

$$\mathbf{\Sigma}^a = \sigma_0 \mathbf{D}\left(\mathbf{x}, t\right), \tag{1.9}$$

where the tensor $\mathbf{D}(\mathbf{x},t) = \int_\Omega \Psi(\mathbf{x},\mathbf{p},t)(\mathbf{pp} - \mathsf{I}/3)\, d\mathbf{p}$ is the second orientational moment of the active particle probability distribution function, and can also be interpreted as a tensor order parameter characterizing the local nematic alignment of the particles. The sign of the stresslet strength σ_0 depends on the type of swimmer. $\sigma_0 > 0$ for pullers, $\sigma_0 < 0$ for pushers.

With the knowledge of the active particle extra stress, the fluid velocity $\mathbf{u}(\mathbf{x},t)$ can be obtained as a solution of the following momentum and continuity equations:

$$-\eta\nabla_x^2\mathbf{u} + \nabla_x p = \nabla_x \cdot \mathbf{\Sigma}^p, \quad \nabla_x \cdot \mathbf{u} = 0, \tag{1.10}$$

where η is the dynamic viscosity of the suspending Newtonian fluid and q is the pressure.

1.3.3 Stability of an uniform isotropic state

Saintillan & Shelley [19, 20] performed a stability analysis of the kinetic equations linearized around a uniform isotropic base state in an unconfined domain and showed the existence of a long-wave instability for the nematic alignment (or equivalently, for the active stress) of the particles in pusher suspensions. No such instability exists for puller suspensions. Non-linear simulations of the kinetic equations were also performed which reveal the growth of density fluctuations, which led to the formation of dense concentrated bands of active particles, correlated on the scale of the simulation domain, which form and breakup quasi-periodically.

To summarize, the mean-field kinetic theory approach demonstrates that self-organization in pusher suspensions are a result of hydrodynamic instabilities driven

by the active stresses and hence serves as a promising theoretical and computational tool to probe active suspensions.

1.4 Motivation and research questions

The analysis of Saintillan and Shelley [19, 20] considered the sole effect of hydrodynamic interactions in unconfined suspensions. However, in reality, the motion of the swimming particles are influenced by several other effects such as confinement, contact interactions, interaction with external fields like imposed flow or nutrient gradients. Incorporating these effects within the kinetic theory framework will help us provide a realistic description of the dynamics of active suspensions. The key questions tackled in this thesis and the motivation behind the desire to address them are enlisted below.

- **Steric *vs* hydrodynamic interactions**: Experiments on bacterial suspensions which report collective behavior are often performed in the concentrated regime, where excluded volume interactions between swimmers become important. The interesting question of the respective roles of steric *vs* hydrodynamic interactions in these dense systems has to be addressed to fully understand the dynamics of collective flocking reported in experiments.

- **Role of chemotactic interactions**: External chemical fields can also affect the self-organization in active suspensions. The dynamics is such chemotactic active suspensions is a result of a three-way coupling between the active particle transport, background fluid velocity and chemoattractant transport. While recent experiments [6] have hinted that this three-way coupling can lead to transition

to collective behavior beyond a critical thickness of bacterial films exposed to oxygen, such effects have not been considered in theory or simulations before. A detailed study of the role of chemotactic interactions in active suspensions could impact their suitability for future technological applications such as bacteria powered micro-mixers and also have broader implications for the understanding and treatment for pathogenic infections.

- **Capturing confinement effects within the mean-field framework**: Many swimming micro-organisms are often found in highly confined environments, for example, sperm in the reproductive tract, bacterial biofilms, etc. The interaction of the active particles with confining surfaces is highly non-trivial. Even in dilute systems, where particle-particle hydrodynamic and steric interactions can be neglected, microfluidic experiments on bacterial suspensions have reported several peculiar dynamics such as wall accumulation, as well as upstream swimming, centerline depletion and shear-trapping when a pressure-driven flow is imposed. There are controversial and competing mechanisms in the literature for the origin of these effects. A unified continuum treatment of confinement effects in active suspensions is still lacking and is critically important.

- **Calculation of the swim pressure**: An understanding of the distribution of active particles in confinement is especially critical for determining the mechanical force per unit area exerted by the suspension on the boundaries, or so-called 'swim pressure'. This novel concept, which has received much scrutiny recently, describes the force that must be applied on containing osmotic walls to keep self-propelled particles confined. While recent studies have proposed a simple ideal gas-like equation for swim pressure, examining the validity of the proposed

swim pressure equation via a first principles derivation within our continuum kinetic theory perspective is important and could form the basis of an analytical framework to investigate phoretic transport of passive payloads in active solutes.

- **Effect of confinement on collective self-organization**: Geometric confinement opens up the possibility of constructive control of the interaction-driven collective self-organization in active suspensions. Stability analysis of unconfined active suspensions show the zero wavenumber mode to be most unstable, the corresponding non-linear simulations show the concentration and director fields to be correlated over length scales comparable to the size of the simulation box. Confinement introduces another length scale into the picture and can potentially screen the correlation length of active self-organization. The existence of polarized and spatially inhomogeneous equilibrium distributions in confined active suspensions also has interesting implications for their stability when coupled to hydrodynamic interactions. The crucial interplay between confinement and interactions in active suspensions is thus, of vital importance and could inspire new technologies such as bacteria powered micropumps.

In this thesis, we address these questions by incorporating hydrodynamic, steric, chemotactic and confinement effects within the mean-field kinetic theory approach.

1.5 Overview of thesis research

This thesis is focused on the modeling of the effects of inter-particle interactions, external flows and confinement in active suspensions within the continuum kinetic theory framework. We consider a few model problems with the aim of elucidating the

physical mechanisms leading to peculiar dynamics in active suspensions that have been reported in experiments and also possibly discover novel properties that could have broader implications for potential technological applications involving active fluids.

The problem solving approach typically involves linear stability analysis, analytical manipulations using asymptotic, spectral / spherical harmonic expansions and large scale finite-volume / spectral simulations of the Smoluchowski-Stokes equations, performed on supercomputers.

The chapters are grouped under three themes, hydrodynamically driven self-organization (chapters 2 and 3), dilute confined active suspensions (chapter 4 and 5) and effect of confinement on active self-organization (chapter 6).

The first theme focuses on hydrodynamically driven self-organization in active suspensions. Specifically, we look at active suspensions in the semi-dilute and concentrated regimes and explore the interplay between motility and inter-particle effects such as hydrodynamic and steric interactions, as well as chemotactic interactions due to an externally imposed chemical gradient field.

- Chapter 2 presents a detailed investigation of the respective roles of steric *vs* hydrodynamic interactions in an unconfined concentrated active suspension using continuum kinetic theory and numerical simulations [21]. Steric interactions are captured by extending classic models for concentrated suspensions of rod-like polymers, in which contacts between nearby particles cause them to align locally. A theoretical base state analysis reveals that, in the absence of hydrodynamic interactions, local alignment due to steric interactions results in a transition from an isotropic state to a nematic state when volume fraction is increased.

The hydrodynamic stability of both states is investigated using a linear stability analysis and also confirmed using fully non-linear numerical simulations. The analysis reveals instabilities characterized by the emergence of chaotic unsteady flows and giant number density fluctations in both pusher and puller suspensions. While the self-organization in pusher suspensions occurs at volume fractions below the nematic transition threshold, for puller suspensions, it occurs at a higher concentration, above the nematic transition threshold. It is argued that the novel puller instability at higher concentrations is a consequence of a coupled effect of hydrodynamic and steric interactions.

- Chapter 3 presents a kinetic model and three-dimensional numerical simulations of suspensions of run-and-tumble aerotactic bacteria confined in free-standing liquid films surrounded by air [22]. The continuum kinetic model is extended to account for chemotactic run-and-tumble effects and is coupled to an advection-diffusion-reaction equation for oxygen transport. In thin films, oxygen and bacterial concentration profiles are shown to approach steady states. In thicker films, a transition to chaotic dynamics is shown to occur and is characterized by unsteady correlated motions, the formation of bacterial plumes, and enhanced oxygen transport and consumption. This transition, also observed in previous experiments, is shown to be a result of the coupling between the aerotactic response of the bacteria and the flow fields they generate via hydrodynamic interactions.

The second theme focuses on confined dilute active suspensions. Specifically, we look at the active suspensions in the dilute limit, where particle-particle interactions and particle-wall hydrodynamic interactions are neglected, to focus on the unique

interplay between motility, confinement and external pressure-driven flows.

- Chapter 4 presents an investigation of the effects of confinement and non-uniform shear on the dynamics of a dilute suspension of Brownian active swimmers by incorporating a detailed treatment of boundary conditions within the kinetic modeling framework [23]. Based on this model, the effects of confinement in the absence of flow is first investigated, in which case the dynamics is governed by a swimming Péclet number, or ratio of the persistence length of particle trajectories over the channel width, and a second swimmer-specific parameter whose inverse measures the strength of propulsion. In the limit of weak and strong propulsion, asymptotic expressions for the full distribution function are derived. For finite propulsion, analytical expressions for the concentration and polarization profiles are also obtained using a truncated moment expansion of the distribution function. In agreement with experimental observations, the existence of a concentration/polarization boundary layer in wide channels is reported and characterized, suggesting that wall accumulation in active suspensions is primarily a kinematic effect which does not require hydrodynamic interactions. The effects of a external pressure-driven Poiseuille flow is also considered and shown to lead to a net upstream swimming of the particles relative to the flow, and an analytical expression for the mean upstream velocity is derived in the weak flow limit. In stronger imposed flows, the formation of a depletion layer near the channel centerline is also predicted, due to cross-streamline migration of the swimming particles towards high-shear regions where they become trapped, and an asymptotic analysis in the strong flow limit is used to obtain a scale for the depletion layer thickness and to rationalize the non-monotonic dependence of

the intensity of depletion upon flow rate. We also analyze the effective rheology of a dilute active suspension under confinement and contrast it to the case of an unconfined suspension in uniform shear. Our theoretical predictions are all shown to be in excellent agreement with finite-volume numerical simulations of the kinetic model, and are also supported by recent experiments on bacterial suspensions in microfluidic devices.

- Chapter 5 explores the limit of zero translational diffusion (or zero temperature) in confined active suspensions [24], which is intractable within the continuum framework presented in chapter 4. The simple case of a dilute active suspension of non-Brownian athermal run-and-tumble spherical swimmers confined between two planar hard walls and interacting via purely steric forces with the wall is selected as a model system to analyze this limit. The spatial and orientational distribution in this system is calculated theoretically using a kinetic model based on coupled bulk/surface probability density functions, that incorporated a realistic treatment of surface interactions and exchange processes between surfaces and the bulk. The existence of a concentration wall boundary layer with thickness scaling with the run length, the absence of polarization throughout the bulk of the channel, and the presence of sharp discontinuities in the bulk orientation distribution in the neighborhood of orientations parallel to the wall in the near-wall region are demonstrated analytically. Our model is also applied to calculate the swim pressure in the system, which is shown to asymptotically approach the previously proposed ideal-gas behavior in wide channels but is found to decrease in narrow channels as a result of confinement. Monte-Carlo simulations are also performed for validation and excellent quantitative agreement

with our theoretical predictions is reported.

The effects of self-generated or externally induced inter-particle interactions and confinement were individually explored in the first and second themes respectively. The third theme completes the story by bringing together the analysis from the first two themes and exploring the effect of confinement on the hydrodynamically driven self-organization in active suspensions.

- Chapter 6 explores the dynamics in a suspension of hydrodynamically interacting active pusher particles confined between two parallel plates. As will be shown in chapter 4, this confined suspension will develop a base state that is spatially inhomogeneous and polarized in the wall-normal direction. Linear stability analysis of an one dimensional perturbation in the wall-normal direction to the base state reveals a symmetry-breaking phase-transition to a spontaneous flowing state above a critical level of activity or concentration. The fastest growing eigenmode leads to a symmetric velocity profile with net fluid pumping in the channel. The stability of the quiescent no-flow base state to a two dimensional perturbation is analyzed by performing non-linear simulations of the conservation equations. Above a critical concentration or activity, the quiescent no-flow base state is destabilized, confirming the predictions of the linear stability analysis. In weak confinement, there is a transition to spontaneous directional flows characterized by persistent unsteadiness. In stronger confinement, spontaneous flows are stabilized leading to steady fluid pumping in the channel. The possibility of constructive control of active self-organization using different confining geometries is also discussed.

Overall, the investigation presented in this thesis have established kinetic

theories based on the coupled Smoluchowski-Stokes equations to be powerful tool for modeling the complex dynamics in active suspensions.

Final note*: Each chapter of this thesis manuscript was written as stand-alone. Relevant background and technical introduction is provided within each chapter and they can thus be read independently.*

Acknowledgement: Chapter 1, in small part, is a reprint of the material that appears in my master's thesis 2012. "Three-dimensional kinetic simulations of active suspensions: effect of chemotaxis and steric interaction" by Ezhilan, Barath, University of Illinois, 2012. The dissertation author was the primary investigator and author of this manuscript.

Chapter 2

Instabilities and nonlinear dynamics of concentrated active suspensions

2.1 Introduction

Suspensions of motile microorganisms can show fascinating and complex large-scale dynamics that have been aptly termed *bacterial turbulence*. The dynamics of such active suspensions are characterized by persistent unsteadiness [11], the creation and destruction of coherent flow structures [4], enhanced fluid mixing [6, 25], temporal and spatial fluctuations in swimmer concentration [4], and dynamical transitions in the character of the system as system size [6] and swimmer concentration [12, 5, 8] are varied; see Ishikawa [26], Ramaswamy [27], Koch and Subramanian [28] and Saintillan and Shelley [29] for recent reviews of some of these phenomena.

Theoretical investigations have used a variety of approaches to predict, un-

derstand, and interpret these experiments. The active nematic theory of Simha and Ramaswamy [30] was an important early contribution. They posed a phenomenological continuum theory for the collective behavior of swimmers based upon previous classic models for nematic liquid crystals that included a destabilizing "active stress" generated by particle locomotion. This theory predicted, among other things, that in the Stokesian regime of negligible fluid inertia suspensions of swimmers with long-range orientational order would be unstable to hydrodynamic flows. There have since been other related theories. Examples include Aranson *et al.* [31], who developed a kinetic theory for the dynamics of a motile suspension in a thin fluid film where active fluid stresses as well as the alignment effects of pairwise swimmer collisions are modeled. Wolgemuth [32] developed a two-phase (fluid and swimmer) model of a bacterial suspension driven by active stresses that incorporates nematic elasticity.

Another approach has been to model and directly simulate the hydrodynamic interactions of many swimmers, as well as trying to capture within these simulations the effect of steric interactions [33, 34, 35, 36, 37, 38]. These simulations have reproduced qualitative aspects of experiments, such as the appearance of large-scale flows, and have shown that hydrodynamic interactions alone can be sufficient for producing collective dynamics and coherent structures. Recent work by Saintillan and Shelley [38] that simulated large-scale suspensions of hydrodynamically interacting slender swimming rods demonstrated this latter point, as well as highlighted the importance of the swimming mechanism to the appearance of large-scale flows. These simulations showed that transitions can occur as a function of swimmer concentration and system size, and that unstable suspensions can exhibit local flocking and concentration fluctuations not predicted by linear theories [38].

In seeking to understand experiments and their simulations of motile suspensions, Saintillan and Shelley [19, 20] developed a simple kinetic model based on first principles that couples a Smoluchowski equation for the distribution of particle configurations (positions and orientations) to the Stokes equations forced by the active stresses generated by the locomotion of the swimmers through the surrounding fluid (a similar model was also developed independently by Subramanian and Koch [39]). This Smoluchowski/Stokes system of partial differential equations is very similar to that developed by Doi and Edwards [18] to describe passive Brownian rod suspensions, as the active stress tensor resulting from locomotion shares the same tensorial form as the Brownian stress resulting from thermal fluctuations in passive suspensions. (See Hatwalne et al. [40] for a discussion of the fundamental differences in origin and interpretation of active and passive nematogenic stresses, which are particularly relevant for ordered phases). One very important difference is that the stresslet coefficient of the active stress is oppositely signed (negative) when the motile particles are *pushers* (rear-actuated swimmers). Both passive and active systems have an energy-like quantity, the relative conformational entropy, and for passive rods and (front-actuated) *pullers* this quantity decays to zero, implying global stability of the state of uniform isotropy. This is not so in the case of pushers, allowing the possibility of a continuous production of fluctuations from the swimmer motions and fluid coupling.

Two steady-state swimmer distributions play an important role for the kinetic theory of slender active particles. The first is the globally aligned "nematic" state, which requires neglect of rotational diffusion in the dilute limit when steric interactions are neglected. A linear analysis by Saintillan and Shelley [20] showed its instability to

hydrodynamic flow, in agreement with the earlier prediction of Simha and Ramaswamy [30]. The second state is uniform isotropy, and a linear analysis around it showed stability for suspensions of pullers, and an orientational instability for pushers if the system size or swimmer concentration are sufficiently high. For pullers, stability is global due to the monotonic decay of the system's conformational relative entropy [20]. These predictions, which are in qualitative agreement with experiments of bacterial suspensions within suspended films [41], were also confirmed using continuum simulations [19, 20, 42], which for pushers showed the emergence, from near uniform isotropy, of large-scale roiling flows that are characterized by concentration fluctuations and coherent structures. Puller suspensions showed relaxation to the uniform state. These dynamics are also consistent, at least qualitatively, with results from direct particle simulations [34, 38].

It is widely accepted that at high concentrations, steric interactions between swimmers become important with the expectation that sterically-induced nematic ordering will emerge. Certainly such ordering has been observed in the dynamics of dense bacterial suspensions [8], as well as in swarming flocks of motile bacteria [43, 44, 45], in which long-ranged fluid-mediated interactions may not always be significant. Simulations of self-propelled hard rods interacting solely via contact interactions in fact also show the emergence of coherent structures and correlated motions [46], raising the question of the relative roles of steric vs hydrodynamic interactions in dense active suspensions. In this chapter, we attempt some understanding of the joint effects of both types of interactions by studying a simple and classical extension of our previous kinetic theory for dilute suspensions that accounts for local alignment as a result of steric interactions. In particular, we follow Doi and Edwards [18] in their

modeling of steric interactions in dense rod suspensions, and use the local tensor order parameter of the particle orientation distribution to generate an alignment torque in the single particle fluxes. This torque is proportional to local rod concentration and stabilizes the locally aligned state against rotational diffusion. As this torque devolves from a force potential, it also generates a contribution to the extra stress which must be accounted for in the overall momentum balance [18]. Baskaran and Marchetti [47] developed and studied the linear stability properties of a kinetic theory, after a moment closure approximation, rather similar to the one studied here. Forest *et al.* [48] also recently developed a related, yet more elaborate theory that includes liquid crystalline contributions, and which they have used to investigate pattern formation in two dimensions.

We first investigate the linear stability of the full extended kinetic model to plane-wave perturbations for both the isotropic and nematically ordered base states. We find that modes of instability are restricted generically to the zeroeth, first, and second azimuthal modes on the sphere of orientations, and can be determined analytically in the long-wave limit for the isotropic base state. For pusher suspensions, we find that both isotropic and nematic states are expected to become unstable beyond a critical strength of steric coupling. For puller suspensions, hydrodynamic interactions are stabilizing in the dilute regime. However, increasing the strength of steric interactions destabilizes the isotropic base state, while the nematic state can likewise become unstable to hydrodynamic coupling. To investigate the fully nonlinear regimes, we then perform spectral/finite-difference simulations of the full kinetic equations in three dimensions. These simulations find some surprising behaviors, such as unexpected two-dimensional dynamics at low volume concentrations for pushers,

and very different coherent structures in unstable pusher and puller suspensions. We investigate the degree of ordering that emerges in these simulations and generally find that the suspensions show large regions of nematic order that are nonetheless transitory and unsteady. This seems roughly consistent with experimental observations on flocks of motile bacteria [8, 43, 44, 45]. As in our previous dilute model, we find that the power input by swimming is considerably larger for pushers than for pullers, even in the unstable regimes, but find that, unlike our previous work, sterically-mediated unstable puller suspensions can now also increase the power input to the system.

2.2 Kinetic model

2.2.1 Conservation equation

We consider a suspension of N active particles of length ℓ and thickness b (aspect ratio $r = \ell/b \gg 1$) in a volume V assumed to be a cube of linear dimension $L = V^{1/3}$. The mean number density is defined as $n = N/V$, and we also introduce an effective volume fraction $\nu = nb\ell^2$, which is the appropriate parameter to capture the isotropic-to-nematic transition in the case of passive rod-like particles [18]. The model we use to study the dynamics is an extension of our previous kinetic theory for dilute suspensions of self-propelled particles [19, 20] to account for local alignment as a result of steric interactions. We describe the configuration of the suspension by means of a continuum distribution function $\Psi(\mathbf{x}, \mathbf{p}, t)$ of center of mass $\mathbf{x}$ and director $\mathbf{p}$ (where $\mathbf{p}$ is a unit vector defining the orientation and swimming direction of the particles) at time t. By conservation of particles, $\Psi(\mathbf{x}, \mathbf{p}, t)$ satisfies a Smoluchowski

equation [18]

$$\partial_t \Psi + \nabla_x \cdot (\dot{\mathbf{x}}\Psi) + \nabla_p \cdot (\dot{\mathbf{p}}\Psi) = 0, \tag{2.1}$$

where ∇_p denotes the gradient operator on the unit sphere of orientations Ω and is defined as

$$\nabla_p = (\mathbf{I} - \mathbf{pp}) \cdot \frac{\partial}{\partial \mathbf{p}}, \tag{2.2}$$

and the distribution function is normalized as

$$\frac{1}{V} \int_V \int_\Omega \Psi(\mathbf{x}, \mathbf{p}, t)\, d\mathbf{p}\, d\mathbf{x} = n. \tag{2.3}$$

With this normalization, the constant distribution function $\Psi = n/4\pi$ corresponds to the uniform and isotropic state.

The flux velocities $\dot{\mathbf{x}}$ and $\dot{\mathbf{p}}$ in Eq. (2.1) describe the motion of the particles in the suspension and are modeled as

$$\dot{\mathbf{x}} = V_0 \mathbf{p} + \mathbf{u}(\mathbf{x}) - D\nabla_x \ln \Psi, \tag{2.4}$$

$$\dot{\mathbf{p}} = (\mathbf{I} - \mathbf{pp}) \cdot \nabla_x \mathbf{u} \cdot \mathbf{p} - \nabla_p U(\mathbf{x}, \mathbf{p}) - d\nabla_p \ln \Psi. \tag{2.5}$$

In Eq. (2.4), the center-of-mass velocity is expressed as the sum of three contributions: the particle swimming velocity $V_0\mathbf{p}$ (along the director $\mathbf{p}$), the local mean-field fluid velocity $\mathbf{u}(\mathbf{x})$, whose calculation is explained in Sec. 2.2.4, and translational diffusion with diffusivity D, assumed to be isotropic. Similarly, Eq. (2.5) models the angular flux velocity as the sum of three terms. The first term on the right-hand side uses Jeffery's equation [49, 50] to describe the rotation of a slender rod-like particle in the mean-field flow with velocity gradient $\nabla_x \mathbf{u}$. The second term, which will be discussed

in Sec. 2.2.2, models steric interactions due to concentration effects by means of a local alignment torque deriving from a potential $U(\mathbf{x}, \mathbf{p}, t)$ that depends on the local particle orientations. Finally, Eq. (2.5) also captures rotational diffusion with angular diffusivity d.

From the distribution function, we also define the concentration field $c(\mathbf{x}, t)$, director field (or polar order parameter) $\mathbf{n}(\mathbf{x}, t)$, and nematic order parameter $\mathbf{Q}(\mathbf{x}, t)$, as the zeroeth, first, and second moments of $\Psi(\mathbf{x}, \mathbf{p}, t)$ with respect to $\mathbf{p}$, respectively:

$$c(\mathbf{x}, t) = \int_{\Omega} \Psi(\mathbf{x}, \mathbf{p}, t)\, d\mathbf{p}, \tag{2.6}$$

$$\mathbf{n}(\mathbf{x}, t) = \frac{1}{c(\mathbf{x}, t)} \int_{\Omega} \Psi(\mathbf{x}, \mathbf{p}, t)\mathbf{p}\, d\mathbf{p}, \tag{2.7}$$

$$\mathbf{Q}(\mathbf{x}, t) = \frac{1}{c(\mathbf{x}, t)} \int_{\Omega} \Psi(\mathbf{x}, \mathbf{p}, t)(\mathbf{pp} - \mathbf{I}/3)\, d\mathbf{p}. \tag{2.8}$$

We also introduce the following quantities, which will become useful in the subsequent analysis:

$$\mathbf{D}(\mathbf{x}, t) = \int_{\Omega} \Psi(\mathbf{x}, \mathbf{p}, t)(\mathbf{pp} - \mathbf{I}/3)\, d\mathbf{p} = c(\mathbf{x}, t)\mathbf{Q}(\mathbf{x}, t), \tag{2.9}$$

$$\mathbf{S}(\mathbf{x}, t) = \int_{\Omega} \Psi(\mathbf{x}, \mathbf{p}, t)(\mathbf{pppp} - \mathbf{Ipp}/3)\, d\mathbf{p}. \tag{2.10}$$

2.2.2 Steric interactions

The emergence of collective motion in experiments on bacterial suspensions[12, 5, 8] typically occurs at such high volume fractions that steric interactions resulting from direct mechanical contacts between particles have a significant impact on particle dynamics. This was clearly noted recently by Cisneros *et al.* [8], who observed a transition to local directional order in concentrated suspensions of swimming *Bacillus*

subtilis. The aligning effect of collisions was also reported by Sokolov *et al.* [12] who observed collisions between pairs of bacteria swimming in two-dimensional stabilized films and found that colliding cells subsequently align and swim as a pair; similar dynamics have also been reported in suspensions of swimming *Paramecia* [51]. The importance of steric interactions is also especially clear in swarming experiments with bacterial colonies growing on flat substrates [43, 44, 45], in which case direct contacts likely even dominate the dynamics as long-ranged hydrodynamic interactions are partially screened by boundaries. In such experiments, local alignment and directionally correlated motion has also been reported to emerge [45].

Nematic alignment is well known to arise in concentrated suspensions of Brownian rod-like particles at thermal equilibrium as a result of steric interactions: in these systems, increasing concentration results in a transition from an isotropic to a nematic state by an entropic effect, as the effective volume occupied by a particle in the isotropic phase is larger than in the nematic phase [18, 52, 53]. A simple scaling for the critical number density for the transition can be obtained as $n \sim 1/b\ell^2$. This effect is commonly modeled in liquid crystal theories by means of a phenomenological free energy constructed based on symmetry arguments, such as the Landau-de-Gennes free energy [54, 55] which depends quadratically on the nematic order parameter tensor $\mathbf{Q}(\mathbf{x}, t)$ defined in Eq. (2.8). This approach has also previously been adapted to the case of active liquid crystals [56, 57] and active suspensions [32], in spite of these systems being out of thermal equilibrium.

A few more sophisticated models for concentrated active suspensions have been posed that are based on a microscopic description of collisions between self-propelled particles. Aranson *et al.* [31] proposed a continuum model for two-dimensional

bacterial suspensions, in which they described steric effects based on a pairwise collision operator having the effect of aligning particles coming into contact. This description, however, relies on the pair probability distribution function in the suspension, which Aranson *et al.* [31] approximated as the product of two singlet distributions. More recently, Baskaran and Marchetti [58, 59] also addressed the effect of collisions in two-dimensional collections of self-propelled hard rods. Using non-equilibrium statistical mechanics, they derived a kinetic theory in which expressions for the translational and orientational fluxes resulting from pairwise collisions were obtained. In particular, they showed that collisions modify the orientational flux by addition of an effective torque captured by the Onsager potential [60] commonly used in passive liquid crystalline suspensions, but also result in two additional contributions due to the coupling between translational and rotational motions; these contributions have complex forms that depend on the pair distribution function in the suspension and are not easily included in a mean-field model.

In this work, we adopt the classic mean-field treatment of steric interactions motivated by the work of Doi and Edwards [52, 18] on passive suspensions of Brownian rod-like particles, and model the effects of concentration by means of the additional torque in Eq. (2.5), which is expressed in terms of an interaction potential

$$U(\mathbf{x}, \mathbf{p}, t) = \int_{\Omega} \Psi(\mathbf{x}, \mathbf{p}', t) K(\mathbf{p}, \mathbf{p}') \, d\mathbf{p}', \tag{2.11}$$

where the kernel $K(\mathbf{p}, \mathbf{p}')$ describes steric interactions between two slender particles with orientations $\mathbf{p}$ and $\mathbf{p}'$. In their kinetic theory, Baskaran and Marchetti [59]

showed that an appropriate form is given by the classic Onsager potential [60]:

$$K(\mathbf{p}, \mathbf{p}') = U_0 |\mathbf{p} \times \mathbf{p}'|, \tag{2.12}$$

which realizes its minimum when $\mathbf{p}$ and $\mathbf{p}'$ are either parallel or anti-parallel. Here, we use the common approximation known as the Maier-Saupe potential [61]:

$$K(\mathbf{p}, \mathbf{p}') = -U_0 (\mathbf{p} \cdot \mathbf{p}')^2, \tag{2.13}$$

which has the same qualitative effect as the Onsager potential. Note that for Brownian particles, the constant U_0 has a clear thermodynamic origin and can be formally derived based on equilibrium statistical mechanics. In the case of an active suspension where thermal fluctuations are negligible, the parameter U_0 no longer has a clear energetic interpretation but should rather be interpreted as a phenomenological coefficient characterizing the effective magnitude of steric interactions. Its precise value is not easily predicted theoretically but could potentially be obtained using direct particle simulations such as ours [34, 38], though these have not yet been applied to the concentrated case of interest here owing to their high computational cost. Such simulations would also serve to verify the expression posited in Eq. (2.11) for the effective interaction potential.

Substituting Eq. (2.13) into Eq. (2.11) immediately yields

$$U(\mathbf{x}, \mathbf{p}, t) = -U_0 \, \mathbf{pp} : \mathbf{D}(\mathbf{x}, t) - \frac{U_0}{3} c(\mathbf{x}, t), \tag{2.14}$$

where $\mathbf{D}(\mathbf{x}, t)$ was defined in Sec. 2.2.1. Clearly, we see that the interaction potential

$U(\mathbf{x}, \mathbf{p}, t)$ at a given location $\mathbf{x}$ reaches its minimum when $\mathbf{p}$ is aligned with the principal axis of $\mathbf{D}(\mathbf{x}, t)$, which is also the preferred direction of alignment for the swimmers. Using this expression for $U(\mathbf{x}, \mathbf{p}, t)$, Eq. (2.5) for the angular flux velocity takes on the simple form

$$\dot{\mathbf{p}} = (\mathbf{I} - \mathbf{pp}) \cdot [\nabla_x \mathbf{u} + 2U_0 \mathbf{D}(\mathbf{x}, t)] \cdot \mathbf{p} - d\nabla_p \ln \Psi. \tag{2.15}$$

2.2.3 Diffusion coefficients

As the analysis of Sec. 2.3 will uncover, the rotational and translational diffusions play a central role in the system's stability. Understanding their origins and their dependence on volume fraction and local microstructure is therefore important. Several distinct phenomena can lead to particle diffusion. First, thermal diffusion can be significant in suspensions of artificial microswimmers (such as self-propelled nanorods), though it is typically negligible for biological swimmers. Biological swimmers, however, are still subject to diffusion even in very dilute systems owing to shape imperfections or noise in the swimming actuation [62, 63]. In the absence of interactions, these two effects could be described in terms of constant diffusion coefficients d_0 and D_0. At high concentrations, these diffusivities are likely to be affected by steric effects and to depend on the local structure of the suspension. In the case of a passive suspension of rod-like polymers, Doi and Edwards [18] suggest that the rotational diffusion in the semi-dilute to concentrated regimes be modeled as

$$d = C d_0 (n\ell^3)^{-2} \left(1 - \frac{3}{2}\mathbf{Q} : \mathbf{Q}\right)^{-1}, \tag{2.16}$$

and so d depends on the mean volume fraction $n\ell^3$ and local nematic order parameter $\mathbf{Q}(\mathbf{x}, t)$; this particular dependence on volume fraction was recently verified in computer simulations of rigid rods [65]. Doi and Edwards also predict that the translational diffusivity will become anisotropic, with stronger diffusion in the local direction of alignment (eigenvector of $\mathbf{Q}$ with largest eigenvalue) than in perpendicular directions.

In addition to thermal noise (or noise due to the swimming actuation), semi-dilute and concentrated systems are also subject to hydrodynamic diffusion, which results from fluid-mediated interactions between the particles and can in many cases be the dominant diffusion mechanism. In fairly dilute systems ($n\ell^3 < 1$), a theoretical argument by Subramanian and Koch [39] suggests that $d \propto n\ell^3$, and these scalings were indeed verified in our previous particle simulations [34, 38] based on slender-body theory (and which have no imposed stochasticity). The same simulation data, however, also suggests that this dependence may break down at higher concentrations, with d reaching what appears to be a plateau when $n\ell^3 \approx 1$. We are unaware of any numerical simulations of slender swimmers that include hydrodynamic interactions in the concentrated regime, so it is unclear what the dependence on volume fraction becomes beyond this limit.

Because of this multitude of potential diffusion mechanisms, and of the ambiguity of the scaling of the coefficients with volume fraction, we make in this chapter the simplest assumption of constant dimensional diffusivities d and D. A more detailed dependence on volume fraction is straightforward to include in the theory, though we do not discuss it further.

2.2.4 Mean-field fluid velocity

To close Eqs. (2.4)-(2.5) for the flux velocities, the fluid velocity $\mathbf{u}(\mathbf{x})$ generated by the active particles is required. This velocity captures mean-field hydrodynamic interactions between particles, and is driven by the force dipoles that the motile particles exert on the fluid as they propel themselves. In the low-Reynolds-number regime characteristic of microscale swimmers, it can be obtained as a solution of the momentum balance and continuity equation:

$$-\eta\nabla_x^2\mathbf{u} + \nabla_x q = \nabla_x \cdot \boldsymbol{\Sigma}, \quad \nabla_x \cdot \mathbf{u} = 0, \tag{2.17}$$

where η is the dynamic viscosity of the suspending Newtonian fluid and q is the pressure. The second-order tensor $\boldsymbol{\Sigma}(\mathbf{x}, t)$ denotes the particle extra stress in the suspension. This particle stress is obtained as a configurational average of the force dipoles exerted by the particles on the fluid [66, 67]. In the case of motile particles [68], it can be decomposed as the sum of four contributions, arising from the permanent dipole due to swimming, Brownian rotations (in the case of colloidal particles), resistance to stretching and compression by the local flow field, and steric torques: $\boldsymbol{\Sigma} = \boldsymbol{\Sigma}^s + \boldsymbol{\Sigma}^b + \boldsymbol{\Sigma}^f + \boldsymbol{\Sigma}^t$.

The first contribution $\boldsymbol{\Sigma}^s$ due to swimming, corresponding to the active stress, can be modeled as $\boldsymbol{\Sigma}^s(\mathbf{x}, t) = \sigma_s\mathbf{D}(\mathbf{x}, t)$ [40]. The stress magnitude or dipole strength σ_s depends on the mechanism for swimming and can be of either sign: $\sigma_s > 0$ for head-actuated swimmers, or pullers (such as the microalga *Chlamydomonas reinhardtii* [15, 16]), whereas $\sigma_s < 0$ for rear-actuated swimmers, or pushers (such as the bacteria *Bacillus subtilis* and *Escherichia coli* [62]). From dimensional analysis or from a

basic force balance [69], it is straightforward to show that $\sigma_s \propto \eta V_0 \ell^2$, where ℓ is the characteristic size of the particles.

The second contribution $\boldsymbol{\Sigma}^b$ only arises for particles subject to Brownian rotations, and is expressed as : $\boldsymbol{\Sigma}^b(\mathbf{x},t) = 3kT\mathbf{D}(\mathbf{x},t)$, where kT is the thermal energy of the solvent [70]. Note that $\boldsymbol{\Sigma}^b$ has the same tensorial form as $\boldsymbol{\Sigma}^s$, and therefore Brownian rotations simply offset the swimming dipole strength σ_s by $3kT$. As most suspensions of motile particles are only weakly affected by Brownian motion, we neglect the Brownian stress in the following discussion, though it can easily be included by modifying the value of σ_s.

The third contribution $\boldsymbol{\Sigma}^f$ arises because of the assumed inextensibility of the particles, which resist stretching (or compression) by the local fluid flow. This stress tensor was previously calculated for passive particles [70, 71], and is expressed as: $\boldsymbol{\Sigma}^f(\mathbf{x},t) = \sigma_f \mathbf{S}(\mathbf{x},t) : \mathbf{E}(\mathbf{x})$, where $\mathbf{E}(\mathbf{x}) = [\nabla_x \mathbf{u} + \nabla_x \mathbf{u}^T]/2$ is the rate-of-strain tensor, and the constant σ_f depends on the shape of the particle. For a slender particle of aspect ratio r, it can be obtained from slender-body theory as: $\sigma_f = \pi\eta\ell^3/6\ln(2r)$.

Finally, torques due to local steric interactions also result in a fourth stress contribution, which can be evaluated for a rod-like particle using slender-body theory. We calculate this stress tensor in Appendix A [72], where we show that it can be written in the form: $\boldsymbol{\Sigma}^t(\mathbf{x},t) = -\sigma_t\left[\mathbf{D}(\mathbf{x},t)\cdot\mathbf{D}(\mathbf{x},t) + c(\mathbf{x},t)\mathbf{D}(\mathbf{x},t)/3 - \mathbf{S}(\mathbf{x},t) : \mathbf{D}(\mathbf{x},t)\right]$, where for a slender body the constant σ_t can be estimated as: $\sigma_t = \pi\eta\ell^3 U_0/3\ln(2r)$. As discussed by Doi and Edwards [18], a similar stress contribution arises in passive suspensions of rod-like particles at thermal equilibrium.

From the form of the various stress tensors, it is straightforward to see that, in dilute suspensions, both $\boldsymbol{\Sigma}^s$ and $\boldsymbol{\Sigma}^b$ scale linearly with number density n, whereas $\boldsymbol{\Sigma}^f$

and $\boldsymbol{\Sigma}^t$ scale with n^2 in general. This explains why flow-induced stresses and steric stresses have been neglected in previous work on dilute suspensions [20]. However, they cannot be ignored in more concentrated systems such as the ones of interest here. Still, it should be noted that the expressions for the various particle stress tensors used herein remain inherently based on a low-volume-fraction assumption, as they do not include contributions from near-field interactions. In concentrated systems, more complex rheological laws have been derived for the flow-induced stress that account for higher-order reflections in the interactions between particles [73], though these laws are fairly complex and we are unaware of any similar calculation for the steric stress tensor. We therefore focus in this study on the leading-order corrections captured by the expressions derived above, with the caveat that they may not quantitatively capture dependences on volume fraction in very dense systems.

Another assumption of our model, which should be kept in mind, is the one-fluid approximation made when writing the momentum and continuity equations (2.17). In this model, we assume that the fluid and particle advection velocities can be described in terms of a single velocity field $\mathbf{u}$. This assumption, which is equivalent, from the point of view of hydrodynamics, to neglecting the volume of the particles, is again adequate only if the volume fraction is not too high. At high volume fractions, two-fluid models, which have been successfully developed for passive suspensions [74, 75, 76], would be more appropriate; a first attempt at describing active suspensions in this manner is due to Wolgemuth [32], though more work remains to be done in this area.

2.2.5 Non-dimensionalization

We non-dimensionalize the governing equations using the following characteristic scales for velocities, lengths and times:

$$u_c = V_0, \quad l_c = (n\ell^2)^{-1} = b/\nu, \quad t_c = l_c/u_c. \tag{2.18}$$

We also scale the distribution function Ψ with the mean number density n. Upon non-dimensionalization, the conservation equation (2.1) remains unchanged, but the flux velocities become:

$$\dot{\mathbf{x}} = \mathbf{p} + \mathbf{u}(\mathbf{x}) - \nu D^* \nabla_x \ln \Psi, \tag{2.19}$$

$$\dot{\mathbf{p}} = (\mathbf{I} - \mathbf{pp}) \cdot [\nabla_x \mathbf{u} + 2U_0^* \mathbf{D}(\mathbf{x}, t)] \cdot \mathbf{p} - \frac{d^*}{\nu} \nabla_p \ln \Psi. \tag{2.20}$$

where the dimensionless parameters D^*, d^* and U_0^* are defined as

$$D^* = \frac{D}{bV_0}, \quad d^* = \frac{db}{V_0}, \quad U_0^* = \frac{U_0}{V_0 l^2} \tag{2.21}$$

The momentum equation for the fluid velocity simplifies to: $-\nabla_x^2 \mathbf{u} + \nabla_x p = \nabla_x \cdot \boldsymbol{\Sigma}$, and the dimensionless particle stress tensor is now expressed as

$$\boldsymbol{\Sigma}(\mathbf{x}, t) = \alpha \mathbf{D} + \beta\nu \mathbf{S} : \mathbf{E} - 2U_0^* \beta\nu \left(\mathbf{D} \cdot \mathbf{D} + \frac{c}{3} \mathbf{D} - \mathbf{S} : \mathbf{D} \right), \tag{2.22}$$

where the dimensionless coefficients α and β are given by

$$\alpha = \frac{\sigma_s}{\eta V_0 \ell^2}, \quad \beta = \frac{\pi r}{6 \ln(2r)}. \tag{2.23}$$

In the remainder of the chapter, we exclusively use dimensionless variables, and omit asterisks on dimensionless parameters.

2.3 Stability analysis

2.3.1 Isotropic and nematic base states

The set of equations described in Sec. 2.2 forms a closed system that can be solved for the evolution of the distribution function Ψ in the suspension. Before we study the stability of this system, we first seek steady spatially uniform solutions of the equations of the form $\Psi_0(\mathbf{p})$, which will serve as base states for the linear stability analysis. Such solutions are obtained by setting the angular flux velocity $\dot{\mathbf{p}}$ to zero:

$$\nabla_p \ln \Psi_0 = \xi(\mathbf{I} - \mathbf{pp}) \cdot \mathbf{D}_0 \cdot \mathbf{p}, \tag{2.24}$$

where we have defined $\xi = 2U_0\nu/d$. This equation expresses a balance between angular diffusion and alignment as a result of steric interactions.

An obvious solution of Eq. (2.24) is given by $\Psi_0 = 1/4\pi$, which corresponds to an isotropic suspension. However, depending on the values of the parameter ξ, we show that this solution may not be unique. We specifically seek orientation distributions that are axisymmetric around a unit vector $\hat{\mathbf{z}}$, which is indeterminate and sets the local preferred direction of alignment. We also define two additional unit vectors $\hat{\mathbf{x}}$ and $\hat{\mathbf{y}}$ to form an orthonormal basis. In spherical coordinates with polar axis along $\hat{\mathbf{z}}$, we have

$$\mathbf{p} = \cos\phi \sin\theta\, \hat{\mathbf{x}} + \sin\phi \sin\theta\, \hat{\mathbf{y}} + \cos\theta\, \hat{\mathbf{z}}, \tag{2.25}$$

with $\theta \in [0, \pi]$ and $\phi \in [0, 2\pi)$. We seek axisymmetric distribution functions of the form $\Psi_0(\mathbf{p}) = \Psi_0(\theta)$. For such functions, an easy calculation shows that

$$\mathbf{D}_0 = A[\Psi_0] \left(\hat{\mathbf{z}}\hat{\mathbf{z}} - \frac{\mathbf{I}}{3} \right), \tag{2.26}$$

where the operator $A[\Psi_0]$ is defined as

$$A[\Psi_0] = \pi \int_0^\pi \Psi_0(\theta)(3\cos^2\theta - 1)\sin\theta \, d\theta. \tag{2.27}$$

Using Eq. (2.26), the conservation equation (2.24) simplifies to

$$\frac{\partial}{\partial\theta} \ln \Psi_0 = -\frac{\xi}{2} \sin 2\theta \, A[\Psi_0]. \tag{2.28}$$

This integrates to

$$\Psi_0(\theta) = C \exp\left(\frac{\xi}{4} \cos 2\theta \, A[\Psi_0] \right), \tag{2.29}$$

where the integration constant C is determined to normalize Ψ_0 according to Eq. (2.3). Note that the value of $A[\Psi_0]$ is still unknown. It can be obtained by applying the operator A to Eq. (2.29), which yields an implicit nonlinear equation. After simplifications, and defining $\delta = A[\Psi_0]\xi/4$, the solution for the orientation distribution is expressed as

$$\Psi_0(\theta) = \frac{\exp(\delta \cos 2\theta)}{2\pi \int_0^\pi \exp(\delta \cos 2\theta') \sin\theta' \, d\theta'}, \tag{2.30}$$

where the parameter δ must be a zero of the following function $g(\delta)$:

$$g(\delta) = \delta - \frac{\xi}{8} \frac{\int_0^\pi \sin\theta (3\cos^2\theta - 1) \exp(\delta \cos 2\theta) \, d\theta}{\int_0^\pi \sin\theta \exp(\delta \cos 2\theta) \, d\theta}. \tag{2.31}$$

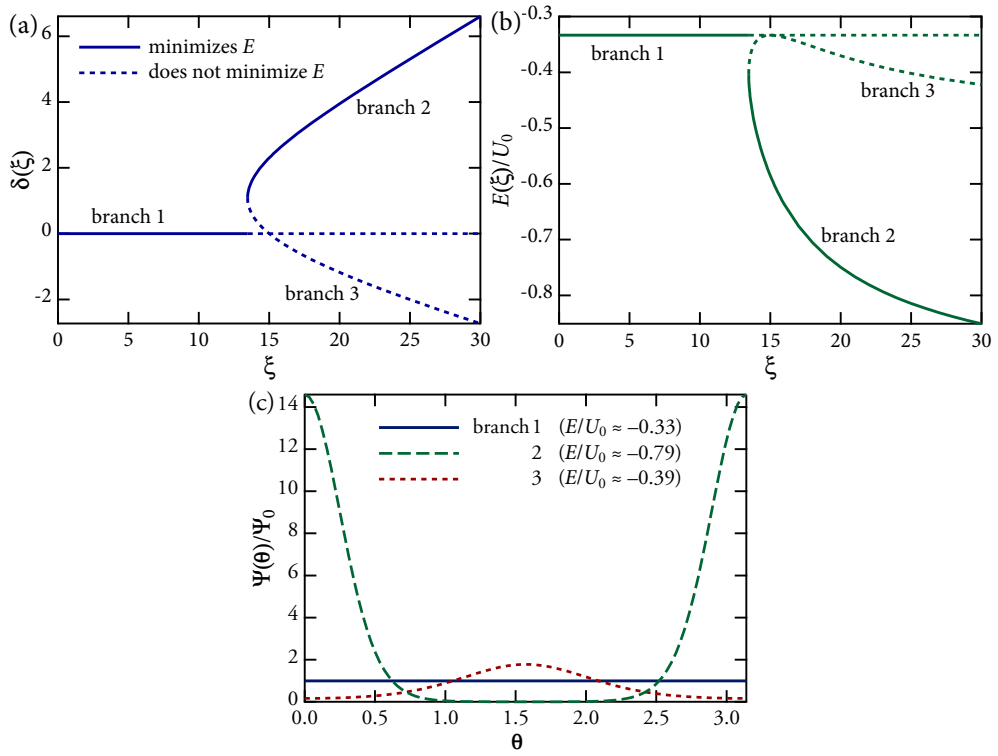

Figure 2.1: (Color online) (a) Solutions of the equation $g(\delta) = 0$, where g is defined in Eq. (2.31), as functions of $\xi = 2U_0\nu/d$. Full lines show the branches that, at a given value of ξ, minimize the steric interaction energy. (b) Steric interaction energy $E(\xi)$ along each of the three branches found in (a). (c) Orientation distributions for $\xi = 20$ corresponding to the three solution branches.

A zero of $g(\delta)$ is clearly obtained when $\delta = 0$ regardless of the value of ξ, and corresponds to the isotropic orientation distribution $\Psi_0 = 1/4\pi$. However, this solution is not unique, and all the zeroes of $g(\delta)$ are plotted in terms of ξ in Fig. 2.1(a). For low values of ξ (weak steric alignment torque), the isotropic solution is unique (branch 1). However, above the critical value of $\xi_1^c \approx 13.46$, a bifurcation occurs and two additional solutions arise (branches 2 and 3). Both of these correspond to nematic orientation distributions; δ increases with ξ along branch 2, whereas it decreases along branch 3. This third branch even becomes negative when $\xi \geq \xi_2^c = 15$, where it crosses branch 1. Beyond this value, branch 3 corresponds to an orientation distribution in which the

particles are laying preferentially in the x-y plane. The orientation distributions for all three branches at $\xi = 20$ are illustrated in Fig. 2.1(c).

In a physical system, the relevant solution is expected to minimize the total interaction energy, defined as

$$E = \int_{\Omega} \Psi_0(\mathbf{p}) U(\mathbf{p})\, d\mathbf{p} = -U_0 \int_{\Omega'} \int_{\Omega} \Psi_0(\mathbf{p}) \Psi_0(\mathbf{p}') (\mathbf{p} \cdot \mathbf{p}')^2\, d\mathbf{p}\, d\mathbf{p}', \tag{2.32}$$

or, for an axisymmetric orientation distribution:

$$E = -2\pi^2 U_0 \int_0^{\pi} \int_0^{\pi} \Psi_0(\theta) \Psi_0(\theta') \left[\sin^2\theta \sin^2\theta' + 2\cos^2\theta \cos^2\theta'\right] \sin\theta \sin\theta'\, d\theta\, d\theta'. \tag{2.33}$$

This energy was calculated along each branch and is plotted in Fig. 2.1(b). We find that when $\xi \geq \xi_1^c$ the energy minimum is always achieved on branch 2 with the largest value of δ, which corresponds to the nematic orientation distribution with the strongest alignment. In summary, the base-state orientation distribution is the isotropic one ($\Psi_0 = 1/4\pi$) when $\xi < \xi_1^c \approx 13.46$; above ξ_1^c, the base-state orientation distribution is expected to become nematic and to be given by Eq. (2.30) where the value for δ should be chosen on branch 2. Note that this discussion is based solely on energy minimization, but does not necessarily reflect the hydrodynamic stability of the various branches, as we describe in more detail below. This was previously noted by Doi and Edwards [18], who also predicted a range of ξ over which both isotropic and nematic phases can exist.

2.3.2 Linearized equations and eigenvalue problem

We now proceed to analyze the linear stability of the base states obtained in Sec. 2.3.1. We treat the case of an arbitrary base state Ψ_0, which can be either the isotropic state or a nematic state defined by Eq. (2.30). We denote by $\mathbf{D}_0$ and $\mathbf{S}_0$ the base-state values of the two tensors $\mathbf{D}(\mathbf{x},t)$ and $\mathbf{S}(\mathbf{x},t)$. Consider a small perturbation of the distribution function with respect to Ψ_0:

$$\Psi(\mathbf{x},\mathbf{p},t) = \Psi_0(\mathbf{p}) + \epsilon\tilde{\Psi}(\mathbf{x},\mathbf{p},t), \tag{2.34}$$

where $|\epsilon| \ll 1$ and $|\tilde{\Psi}| \sim O(1)$, and similar perturbations are also assumed for the other flow variables. After linearization of the governing equations, the following evolution equation can be obtained for the perturbation:

$$\begin{aligned} &\partial_t\tilde{\Psi} + \mathbf{p}\cdot\nabla_x\tilde{\Psi} - \nu D\nabla_x^2\tilde{\Psi} - \frac{d}{\nu}\nabla_p^2\tilde{\Psi} + \nabla_p\Psi_0\cdot(\mathbf{I}-\mathbf{pp})\cdot(\nabla_x\tilde{\mathbf{u}} + 2U_0\tilde{\mathbf{D}})\cdot\mathbf{p} \\ &-3\Psi_0\mathbf{pp} : (\tilde{\mathbf{E}} + 2U_0\tilde{\mathbf{D}}) + 2U_0\nabla_p\tilde{\Psi}\cdot(\mathbf{I}-\mathbf{pp})\cdot\mathbf{D}_0\cdot\mathbf{p} - 6U_0\tilde{\Psi}\mathbf{pp} : \mathbf{D}_0 = 0. \end{aligned} \tag{2.35}$$

The perturbation velocity $\tilde{\mathbf{u}}$ satisfies the same momentum equation as $\mathbf{u}$, but forced by the linearized stress tensor

$$\tilde{\boldsymbol{\Sigma}}(\mathbf{x},t) = \alpha\tilde{\mathbf{D}} + \beta\nu\mathbf{S}_0 : \tilde{\mathbf{E}} - 2\beta U_0\nu\left(\mathbf{D}_0\cdot\tilde{\mathbf{D}} + \tilde{\mathbf{D}}\cdot\mathbf{D}_0 + \frac{1}{3}\tilde{\mathbf{D}} + \frac{\tilde{c}}{3}\mathbf{D}_0 - \mathbf{S}_0 : \tilde{\mathbf{D}} - \tilde{\mathbf{S}} : \mathbf{D}_0\right). \tag{2.36}$$

To make analytical progress, we assume that the perturbation can be written as a plane wave with wave vector $\mathbf{k}$ of the form: $\tilde{\Psi}(\mathbf{x},\mathbf{p},t) = \hat{\Psi}(\mathbf{p})\exp(i\mathbf{k}\cdot\mathbf{x} + \sigma t)$, where

σ denotes the complex growth rate. In this case, Eq. (2.35) becomes:

$$\begin{aligned}\sigma\hat{\Psi} + i(\mathbf{p}\cdot\mathbf{k})\hat{\Psi} + \nu D k^2\hat{\Psi} - \frac{d}{\nu}\nabla_p^2\hat{\Psi} + \nabla_p\Psi_0\cdot(\mathbf{I}-\mathbf{pp})\cdot(\mathrm{i}\mathbf{k}\hat{\mathbf{u}} + 2U_0\hat{\mathbf{D}})\cdot\mathbf{p} \\ -3\Psi_0\mathbf{pp}:(\mathrm{i}\mathbf{k}\hat{\mathbf{u}} + 2U_0\hat{\mathbf{D}})\cdot\mathbf{p} + 2U_0\nabla_p\hat{\Psi}\cdot(\mathbf{I}-\mathbf{pp})\cdot\mathbf{D}_0\cdot\mathbf{p} - 6U_0\hat{\Psi}\mathbf{pp}:\mathbf{D}_0 = 0.\end{aligned} \tag{2.37}$$

Next, we solve for the Fourier component $\hat{\mathbf{u}}$ of the fluid velocity. Standard manipulations [77] on the continuity and momentum equations yield

$$\hat{\mathbf{u}} = \frac{i}{k}(\mathbf{I}-\hat{\mathbf{k}}\hat{\mathbf{k}})\cdot\hat{\boldsymbol{\Sigma}}\cdot\hat{\mathbf{k}}, \tag{2.38}$$

where $\hat{\mathbf{k}} = \mathbf{k}/k$ denotes the wave direction. One must keep in mind, however, that the particle stress tensor $\hat{\boldsymbol{\Sigma}}$ itself depends on $\hat{\mathbf{u}}$ through the flow-induced stress. Specifically, the linearized stress tensor can be written in Fourier space as

$$\hat{\boldsymbol{\Sigma}} = \beta\nu\,\mathbf{S}_0:(\mathrm{i}\mathbf{k}\hat{\mathbf{u}}) + \hat{\mathbf{C}}, \tag{2.39}$$

where the second-order tensor $\hat{\mathbf{C}}$ includes contributions from the active and steric stresses and is independent of $\hat{\mathbf{u}}$:

$$\hat{\mathbf{C}} = \alpha\,\hat{\mathbf{D}} - 2U_0\beta\nu\left(\mathbf{D}_0\cdot\hat{\mathbf{D}} + \hat{\mathbf{D}}\cdot\mathbf{D}_0 + \frac{1}{3}\hat{\mathbf{D}} + \frac{\hat{c}}{3}\mathbf{D}_0 - \mathbf{S}_0:\hat{\mathbf{D}} - \hat{\mathbf{S}}:\mathbf{D}_0\right). \tag{2.40}$$

In index notation, Eq. (2.38) can therefore be written

$$\hat{u}_i = \frac{i}{k}(\delta_{ij}-\hat{k}_i\hat{k}_j)(i\beta\nu S^0_{jklm}k_l\hat{u}_m + \hat{C}_{jk})\hat{k}_k, \tag{2.41}$$

from which

$$[\delta_{im} + \beta\nu(\delta_{ij} - \hat{k}_i\hat{k}_j)S^0_{jklm}\hat{k}_l\hat{k}_k]\hat{u}_m = \frac{i}{k}(\delta_{ij} - \hat{k}_i\hat{k}_j)\hat{C}_{jk}\hat{k}_k. \tag{2.42}$$

We define the second-order tensor $\mathbf{H}$ as

$$H_{im} = \delta_{im} + \beta\nu(\delta_{ij} - \hat{k}_i\hat{k}_j)S^0_{jklm}\hat{k}_k\hat{k}_l. \tag{2.43}$$

Inverting Eq. (2.42) for the velocity then yields the solution:

$$\hat{\mathbf{u}} = \frac{i}{k}\mathbf{H}^{-1}\cdot(\mathbf{I} - \hat{\mathbf{k}}\hat{\mathbf{k}})\cdot\hat{\mathbf{C}}\cdot\hat{\mathbf{k}} = \frac{i}{k}\mathbf{G}:\hat{\mathbf{C}}, \tag{2.44}$$

where we have introduced a third-order tensor $\mathbf{G} = \mathbf{H}^{-1}\cdot(\mathbf{I} - \hat{\mathbf{k}}\hat{\mathbf{k}})\hat{\mathbf{k}}$. Eq. (2.44) can be substituted into the linearized equation (2.37):

$$\begin{aligned}(\sigma + \nu Dk^2)\hat{\Psi} + (i\mathbf{p}\cdot\mathbf{k} - 6U_0\mathbf{pp}:\mathbf{D}_0)\hat{\Psi} - \frac{d}{\nu}\nabla_p^2\hat{\Psi} \\ - 3\Psi_0\mathbf{pp}:(-\hat{\mathbf{k}}\mathbf{G}:\hat{\mathbf{C}} + 2U_0\hat{\mathbf{D}}) + 2U_0\nabla_p\hat{\Psi}\cdot(\mathbf{I} - \mathbf{pp})\cdot\mathbf{D}_0\cdot\mathbf{p} \\ + \nabla_p\Psi_0\cdot(\mathbf{I} - \mathbf{pp})\cdot(-\hat{\mathbf{k}}\mathbf{G}:\hat{\mathbf{C}} + 2U_0\hat{\mathbf{D}})\cdot\mathbf{p} = 0.\end{aligned} \tag{2.45}$$

Noting that the only effect of the translational diffusivity D is simply to modify the growth rate by an amount of $-\nu Dk^2$, we define a reduced growth rate $\lambda = \sigma + \nu Dk^2$, which allows us to write Eq. (2.45) in the form of an eigenvalue problem with eigenvalue λ:

$$\mathscr{L}[\hat{\Psi}] = \lambda\hat{\Psi}, \tag{2.46}$$

where $\mathscr{L}$ is a linear integro-differential operator on the unit sphere of orientations

defined as

$$\begin{aligned}\mathscr{L}[\hat{\Psi}] = &-(i\mathbf{p}\cdot\mathbf{k} - 6U_0\mathbf{pp}:\mathbf{D}_0)\hat{\Psi} + \frac{d}{\nu}\nabla_p^2\hat{\Psi} \\ &+ 3\Psi_0\mathbf{pp}:(-\hat{\mathbf{k}}\mathbf{G}:\hat{\mathbf{C}} + 2U_0\hat{\mathbf{D}}) - 2U_0\nabla_p\hat{\Psi}\cdot(\mathbf{I}-\mathbf{pp})\cdot\mathbf{D}_0\cdot\mathbf{p} \\ &- \nabla_p\Psi_0\cdot(\mathbf{I}-\mathbf{pp})\cdot(-\hat{\mathbf{k}}\mathbf{G}:\hat{\mathbf{C}} + 2U_0\hat{\mathbf{D}})\cdot\mathbf{p}.\end{aligned} \tag{2.47}$$

Recalling that, for the base states derived in Sec. 2.3.1, we have

$$\mathbf{D}_0 = \frac{4\delta}{\xi}\left(\hat{\mathbf{z}}\hat{\mathbf{z}} - \frac{\mathbf{I}}{3}\right), \quad \nabla_p\Psi_0 = \frac{\partial\Psi_0}{\partial\theta}\hat{\mathbf{\Theta}} = -2\delta\sin 2\theta\Psi_0\hat{\mathbf{\Theta}}, \tag{2.48}$$

where $\hat{\mathbf{\Theta}} = \cos\theta\cos\phi\,\hat{\mathbf{x}} + \cos\theta\sin\phi\,\hat{\mathbf{y}} - \sin\theta\,\hat{\mathbf{z}}$ is a unit vector in the θ direction, the expression for $\mathscr{L}$ can be further simplified to:

$$\begin{aligned}\mathscr{L}[\hat{\Psi}] = &-\left[i\mathbf{p}\cdot\mathbf{k} - 12\delta\frac{d}{\nu}\left(\cos^2\theta - \frac{1}{3}\right)\right]\hat{\Psi} + \frac{d}{\nu}\nabla_p^2\hat{\Psi} \\ &+ \Psi_0(2\delta\sin 2\theta\hat{\mathbf{\Theta}} + 3\mathbf{p})\cdot(-\hat{\mathbf{k}}\mathbf{G}:\hat{\mathbf{C}} + 2U_0\hat{\mathbf{D}})\cdot\mathbf{p} + 2\delta\frac{d}{\nu}\sin 2\theta\frac{\partial\hat{\Psi}}{\partial\theta}.\end{aligned} \tag{2.49}$$

Based on the form of Eq. (2.49), we see that the stability is governed by several dimensionless parameters. In the absence of steric interactions ($U_0 \to 0$), the only parameters are the dimensionless rotational diffusivity d/ν (or, in terms of dimensional variables, $d/nV_0\ell^2$), and the dimensionless active stresslet $\alpha = \sigma_s/\eta V_0\ell^2$, which enters the tensor $\hat{\mathbf{C}}$. When steric interactions are included, additional dimensionless parameters are U_0 (or, in terms of dimensional variables, $U_0/V_0\ell^2$) and $\nu = nb\ell^2$, which together uniquely determine δ on any given branch of the base-state solution, and the shape parameter β multiplying the flow-induced and steric stresses.

2.3.3 Stability of the isotropic base state

Eigenvalue problem

We first study the stability of the uniform isotropic base state, for which the distribution function is given by $\Psi_0 = 1/4\pi$. This is the case that was considered in our previous study in the dilute limit [19, 20], where we uncovered a long-wavelength linear instability in suspensions of pushers that causes the particles to locally align as a result of hydrodynamic interactions. We expect the steric alignment torque to reinforce this effect, and possibly lead to a similar instability in suspensions of pullers. When $\Psi_0 = 1/4\pi$, the eigenvalue problem Eq. (2.46) simplifies greatly. We first note that $\mathbf{D}_0 = \mathbf{0}$ and that $\mathbf{S}_0$ is given in index notation by

$$S^0_{ijkl} = \frac{1}{15}\left[\delta_{ik}\delta_{jl} + \delta_{il}\delta_{jk} - \frac{2}{3}\delta_{ij}\delta_{kl}\right]. \tag{2.50}$$

The tensor $\hat{\mathbf{C}}$ defined in Eq. (2.40) can also be calculated as

$$\hat{C}_{ij} = \alpha\hat{D}_{ij} - 2U_0\beta\nu\left[\frac{1}{3}\hat{D}_{ij} - S^0_{ijkl}\hat{D}_{kl}\right] = \left(\alpha - \frac{2}{5}U_0\beta\nu\right)\hat{D}_{ij}, \tag{2.51}$$

where we have used the symmetry and tracelessness of $\hat{\mathbf{D}}$. The tensor $\mathbf{H}$ and its inverse can then be obtained as

$$\mathbf{H} = \left(1 + \frac{\beta\nu}{15}\right)\mathbf{I} - \frac{\beta\nu}{15}\hat{\mathbf{k}}\hat{\mathbf{k}}, \quad \mathbf{H}^{-1} = \left(1 + \frac{\beta\nu}{15}\right)^{-1}\left(\mathbf{I} + \frac{\beta\nu}{15}\hat{\mathbf{k}}\hat{\mathbf{k}}\right), \tag{2.52}$$

from which we easily find that

$$\mathbf{G} : \hat{\mathbf{C}} = \frac{\alpha - \frac{2}{5}U_0\beta\nu}{1 + \frac{\beta\nu}{15}}(\mathbf{I} - \hat{\mathbf{k}}\hat{\mathbf{k}}) \cdot \hat{\mathbf{D}} \cdot \hat{\mathbf{k}} \equiv \overline{\alpha}(\nu)(\mathbf{I} - \hat{\mathbf{k}}\hat{\mathbf{k}}) \cdot \hat{\mathbf{D}} \cdot \hat{\mathbf{k}}. \tag{2.53}$$

We have introduced the notation $\overline{\alpha}(\nu)$ for the prefactor:

$$\overline{\alpha}(\nu) = \frac{\alpha - \frac{2}{5}U_0\beta\nu}{1 + \frac{\beta\nu}{15}}, \tag{2.54}$$

which has an easy physical interpretation. In the dilute limit $\nu \to 0$, it is simply given by α, which is the dimensionless active dipole strength. Here, we find that interactions modify this dipole strength in two ways. First, the steric stress decreases the value of α by $-2U_0\beta\nu/5$, i.e. has a destabilizing effect since dilute suspensions are unstable for $\alpha < 0$ (pushers). Second, the denominator in Eq. (2.54) can be interpreted as the dimensionless viscosity in an isotropic suspension: $1 + \beta\nu/15 = 1 + \pi n\ell^3/6\ln(2r)$; flow-induced stresses are seen to result in a viscosity increase, which is linear in volume fraction and stabilizes the system (in the case of pushers) by effectively decreasing the magnitude of the active dipole strength.

Using Eq. (2.52), we simplify Eq. (2.47) for the operator $\mathscr{L}$ to

$$\mathscr{L}[\hat{\Psi}] = -i(\mathbf{p}\cdot\mathbf{k})\hat{\Psi} + \frac{d}{\nu}\nabla_p^2\hat{\Psi} - \frac{3\overline{\alpha}(\nu)}{4\pi}(\mathbf{p}\cdot\mathbf{k})[\mathbf{p}\cdot(\mathbf{I}-\hat{\mathbf{k}}\hat{\mathbf{k}})\cdot\hat{\mathbf{D}}\cdot\hat{\mathbf{k}}] + \frac{6}{4\pi}U_0\mathbf{pp}:\hat{\mathbf{D}}. \tag{2.55}$$

The four terms in $\mathscr{L}[\hat{\Psi}]$ originate from transport by the swimming velocity, rotational diffusion, alignment in the hydrodynamic flow driven by active and steric stresses, and alignment under the steric torque, respectively.

Spherical harmonic expansion

We solve the eigenvalue problem of Eq. (2.46) spectrally using an expansion of the eigenfunction $\hat{\Psi}(\mathbf{p})$ on the basis of spherical harmonics. We choose a spherical coordinate system in which $\mathbf{k}$ is aligned with the polar axis. Denoting by $\theta \in [0, \pi]$

and $\phi \in [0, 2\pi)$ the polar and azimuthal angles, respectively, we have:

$$\hat{\mathbf{k}} = [0, 0, 1], \quad \text{and} \quad \mathbf{p} = [\sin\theta\cos\phi, \sin\theta\sin\phi, \cos\phi]. \tag{2.56}$$

In this coordinate system, the spherical harmonic of degree ℓ and order $m = -\ell, ..., \ell$ is defined as

$$\mathscr{Y}_\ell^m(\theta, \phi) = \sqrt{\frac{2\ell+1}{4\pi}\frac{(\ell-m)!}{(\ell+m)!}} P_\ell^m(\cos\theta) \exp im\phi \tag{2.57}$$

in terms of the associated Legendre polynomial $P_\ell^m(\cos\theta)$. The spherical harmonics satisfy the orthogonality condition:

$$\langle \mathscr{Y}_\ell^m, \mathscr{Y}_{\ell'}^{m'} \rangle = \int_{\phi=0}^{2\pi} \int_{\theta=0}^{\pi} \mathscr{Y}_\ell^m(\theta, \phi) \mathscr{Y}_{\ell'}^{m'*}(\theta, \phi) \sin\theta \, d\theta d\phi = \delta_{\ell,\ell'}\delta_{m,m'}, \tag{2.58}$$

where * denotes the complex conjugate. These functions form a complete basis on the unit sphere Ω, on which we expand the mode shape $\hat{\Psi}$ as

$$\hat{\Psi}(\theta, \phi) = \sum_{\ell=0}^{\infty} \sum_{m=-\ell}^{\ell} \psi_\ell^m(\mathbf{k}) \mathscr{Y}_\ell^m(\theta, \phi). \tag{2.59}$$

After substituting Eq. (2.59) into Eq. (2.46) and applying orthogonality, the eigenvalue problem for the mode shape becomes an algebraic eigenvalue problem for the harmonic amplitudes:

$$\sum_{\ell'=0}^{\infty} \sum_{m'=-\ell'}^{\ell'} L_{\ell m}^{\ell' m'} \psi_{\ell'}^{m'} = \lambda \psi_\ell^m, \tag{2.60}$$

where the coefficients $L_{\ell m}^{\ell' m'}$ are defined as $L_{\ell m}^{\ell' m'} = \langle \mathscr{L}[\mathscr{Y}_\ell^m], \mathscr{Y}_{\ell'}^{m'} \rangle$. These can be obtained analytically as

$$\begin{aligned} L_{\ell m}^{\ell' m'} =& - ik[A_{\ell'}^{m'} \delta_{\ell,\ell'+1} + B_{\ell'}^{m'} \delta_{\ell,\ell'-1}]\delta_{m,m'} - \frac{d}{\nu}\,\ell(\ell+1)\delta_{\ell,\ell'}\delta_{m,m'} \\ &+ [4U_0/5 - \overline{\alpha}(\nu)/5](\delta_{\ell,2}\delta_{\ell,\ell'}\delta_{m,-1}\delta_{m,m'} + \delta_{\ell,2}\delta_{\ell,\ell'}\delta_{m,1}\delta_{m,m'}) \\ &+ [4U_0/5](\delta_{\ell,2}\delta_{\ell,\ell'}\delta_{m,0}\delta_{m,m'} + \delta_{\ell,2}\delta_{\ell,\ell'}\delta_{m,-2}\delta_{m,m'} + \delta_{\ell,2}\delta_{\ell,\ell'}\delta_{m,2}\delta_{m,m'}), \end{aligned} \tag{2.61}$$

where δ is the Kronecker delta and the constants A_ℓ^m and B_ℓ^m are given by:

$$A_\ell^m = \sqrt{\frac{(\ell - m + 1)(\ell + m + 1)}{(2\ell + 1)(2\ell + 3)}}, \quad B_\ell^m = \sqrt{\frac{(\ell - m)(\ell + m)}{(2\ell - 1)(2\ell + 1)}}. \tag{2.62}$$

In particular, inspection of Eq. (2.61) reveals that spherical harmonics diagonalize the operator $\mathscr{L}$, with the exception of the first term on the right-hand side of Eq. (2.55), which expresses transport by the swimming velocity. We also observe that sets of equations corresponding to different values of the order m are uncoupled and can therefore be solved separately. The only orders that can be subject to instabilities are $m = 0, 1, 2$ (as well as $m = -1, -2$, which are identical to $m = 1, 2$); other orders only undergo transport by the swimming velocity and damping by rotational diffusion.

In the long-wave limit of $k \to 0$, analytical solutions for the growth rates corresponding to modes of a given order m can be obtained. To each value of m is

associated a discrete infinite spectrum with countable eigenvalues:

$$m = 0: \quad \lambda_\ell^m = 4U_0/5\,\delta_{\ell,2} - \frac{d}{\nu}\,\ell(\ell+1), \tag{2.63}$$

$$m = 1: \quad \lambda_\ell^m = [4U_0/5 - \overline{\alpha}(\nu)/5]\,\delta_{\ell,2} - \frac{d}{\nu}\,\ell(\ell+1), \tag{2.64}$$

$$m = 2: \quad \lambda_\ell^m = 4U_0/5\,\delta_{\ell,2} - \frac{d}{\nu}\,\ell(\ell+1), \tag{2.65}$$

$$m \geq 3: \quad \lambda_\ell^m = -\frac{d}{\nu}\,\ell(\ell+1), \tag{2.66}$$

where the degree $\ell \geq m$ is a positive integer. In the limit of $k = 0$, the corresponding eigenfunctions (or mode shapes) are simply the spherical harmonics, and therefore form a complete set. Note that when k is strictly zero (spatially homogeneous suspension), the active term involving α in Eq. (2.64) should technically be discarded as there is no hydrodynamic flow in this limit. We find that modes $m = 0$ and 2 are unaffected by hydrodynamics, and become unstable for $\ell = 2$ provided that

$$\frac{4U_0}{5} - \frac{6d}{\nu} > 0, \quad \text{i.e.} \quad \xi = \frac{2U_0\nu}{d} > \xi_2^c = 15. \tag{2.67}$$

In Fig. 2.1(a), this corresponds to the intersection of branch 1 (isotropic base state), with branch 3, where we expect an exchange of stability to take place. Above this value of ξ, the isotropic base state is always unstable in the long-wave limit for both pushers and pullers, purely as a result of steric interactions.

The stability of mode $m = 1$ is more complex as it is also affected by hydrodynamics. We find that this mode becomes unstable for $\ell = 2$ if

$$\frac{\xi}{15}\left(1 + \frac{\beta\nu/10}{1 + \frac{1}{15}\beta\nu}\right) - \frac{\alpha\nu/30d}{1 + \frac{1}{15}\beta\nu} > 1. \tag{2.68}$$

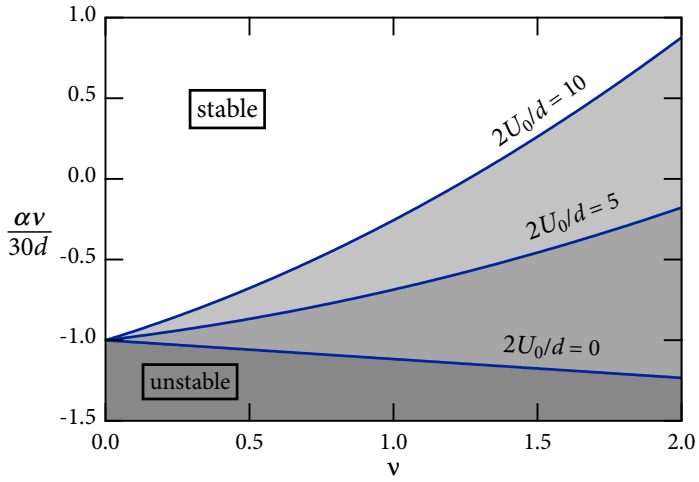

Figure 2.2: (Color online) Marginal stability curve in the long-wave limit ($k \to 0$) in terms of effective volume fraction ν and dimensionless dipole strength $\alpha\nu/30d$, for various values of $2U_0/d$ [see Eq. (2.68)]. In this plot, $\beta = 1.75$, corresponding to a particle aspect ratio of $r \approx 10$.

We see that steric interactions tend to destabilize this mode via the first term in Eq. (2.68), whereas active stresses are stabilizing in the case of pullers ($\alpha > 0$) and destabilizing in the case of pushers ($\alpha < 0$), in agreement with the dilute theory [19, 20]. Both effects are modulated by the effective volume fraction ν, through both steric and flow-induced (viscous) stresses. The marginal stability curve in the $(\nu, \alpha\nu/30d)$ plane (in the limit of $k \to 0$) is shown in Fig. 2.2 for various values of $2U_0/d$. In the dilute limit ($\nu \to 0$), all curves converge to $\alpha\nu/30d = -1$, which corresponds to the critical dipole strength below which dilute pusher suspensions are subject to instabilities as $k \to 0$ [41]. If steric interactions are neglected ($2U_0/d = 0$), increasing ν results in a decrease of this critical strength as a result of the increased effective viscosity of the suspension. However, when steric interactions are present ($2U_0/d > 0$), both the steric torque and steric stresses have a destabilizing effect and increase the critical value of $\alpha\nu/30d$, which even becomes positive at sufficiently large values of ν, i.e. both pusher and puller suspensions can be subject to instabilities.

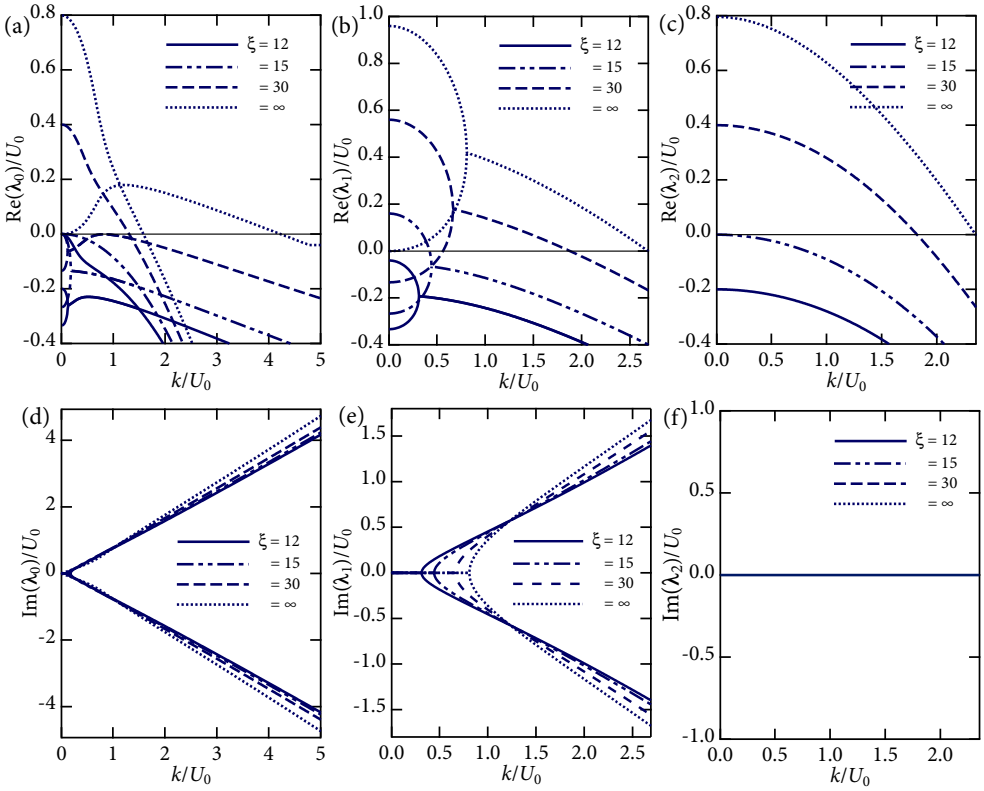

Figure 2.3: (Color online) Numerical solutions of the dispersion relations for the complex growth rates λ_0, λ_1, and λ_2 of azimuthal modes $m = 0, 1, 2$ as functions of the wavenumber k. (a), (b), and (c) show the real parts, while (d), (e), and (f) show the imaginary parts. In (b) and (e), we set $\beta = 0$ to isolate the leading-order effect of the steric torque, and $\alpha/4U_0 = -0.2$ (pushers).

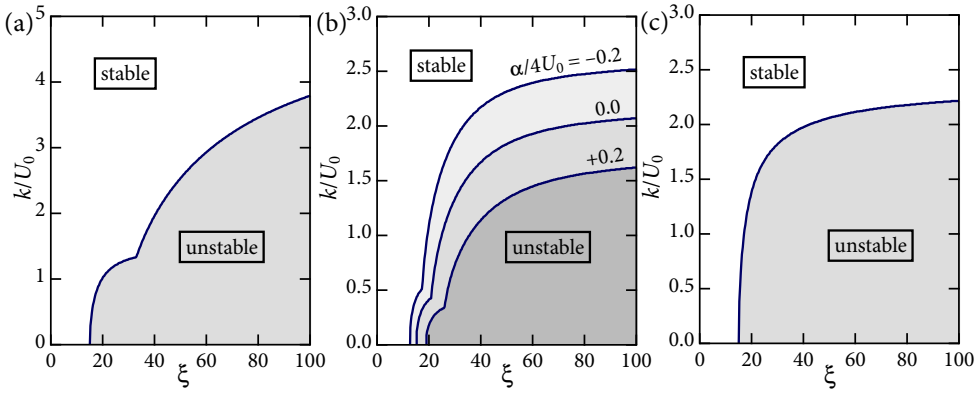

Figure 2.4: (Color online) Unstable range of wavenumbers as a function of $\xi = 2U_0\nu/d$ for azimuthal modes $m = 0$ (a), 1 (b), and 2 (c). For mode 1, we set $\beta = 0$ to isolate the leading-order effect of the steric torque.

At finite wavenumber (arbitrary value of $k > 0$), the growth rates can no longer be obtained analytically, but they can be calculated numerically by solving the algebraic eigenvalue problem Eq. (2.60) for each value of m, after truncation of the infinite sum at a finite degree ℓ chosen large enough to ensure convergence of the dominant eigenvalues. Numerical solutions for the real and imaginary parts of λ for modes $m = 0, 1, 2$ are shown in Fig. 2.3 for different values of $\xi = 2U_0\nu/d$, where only the first few eigenvalues with the largest real parts (or growth rates) are plotted. As ξ increases, some of these growth rates become positive as all three modes become unstable above a critical value ξ^c. The largest growth rates are always found to occur at $k = 0$ (infinite wavelength), and finite-wavelength interactions between the spherical harmonics lead to damping at high wavenumbers. In agreement with the long-wave analysis, modes $m = 0$ and 2 become unstable above $\xi^c = \xi_2^c = 15$; however, pullers ($\alpha > 0$) tend to stabilize mode $m = 1$ ($\xi^c > \xi_2^c$), whereas pushers ($\alpha < 0$) further destabilize it ($\xi^c < \xi_2^c$) as shown in Fig. 2.3(b). Fig. 2.4 also shows the range of unstable wavenumbers as a function of ξ for all three modes. In all three cases, the unstable range tends to a finite interval of the form $[0, k_c]$ as $\xi \to \infty$, where k_c is of order $O(1)$ [or, in dimensional units, $O(n\ell^2)$], and where the largest growth rate always occurs for $k = 0$.

2.3.4 Stability of the nematic base states

We now turn our attention to the stability of the nematic base state of Eq. (2.30), for which the coefficients $L_{\ell m}^{\ell' m'}$ in the algebraic eigenvalue problem of Eq. (2.60) can no longer be calculated analytically. Indeed, it can be seen that the operator $\mathscr{L}$ still only involves azimuthal modes $m = -2$, -1, 0, 1, and 2, but now has a complex

dependence on the polar angle θ through the anisotropic base state. The coefficients $L_{\ell m}^{\ell' m'}$ can, however, be calculated numerically, as can the corresponding eigenvalues. A significant number of polar modes have to be included for convergence, and this number is found to increase with ξ. For $\xi \lesssim 30$, we find that 20 polar modes are sufficient. Another notable difference with the isotropic case is the dependence of the eigenvalue problem, and therefore of the stability results, on the direction $\hat{\mathbf{k}}$ of the wave with respect to the base-state alignment direction, which can be characterized by a single angle $\Theta = \cos^{-1}(\hat{\mathbf{k}} \cdot \hat{\mathbf{z}})$.

In all the results described in this section, we set the rotational diffusivity d and the strength of steric interactions U_0 to the values: $d = 0.002$ and $U_0 = 0.1346$, and focus on the influence of varying the parameter $\xi = 2U_0\nu/d$, which is equivalent to varying the effective volume fraction ν. With this choice of parameters, $\nu = 0.1$ when $\xi = \xi_1^c = 13.46$. We also set the shape parameter β appearing in the particle stress Eq. (2.22) to $\beta = 1.75$, which corresponds to a particle aspect ratio of $r \approx 10$. These parameter values, which will also be used in the simulations of Sec. 2.4, were chosen so as to keep the factor $\beta\nu$, which sets the magnitude of the flow-induced and steric stresses, relatively small. This is motivated by the previous observation that the quadratic dependence of both stress tensors on effective volume fraction is based on a low-volume fraction assumption, see Sec. 2.2.4.

We first focus on the long-wave limit of $k \to 0$, in which case the convective term $-i(\mathbf{p} \cdot \mathbf{k})\hat{\Psi}$ in the definition of $\mathscr{L}$ in Eq. (2.49) vanishes. Figure 2.5 show the dependence of the maximum real part of the eigenvalue λ as a function of dimensionless active stress magnitude α on both nematic branches for $\xi = 20$. Results for two wave orientations Θ are shown. On branch 2 and for this value of ξ [Fig. 2.5(a)],

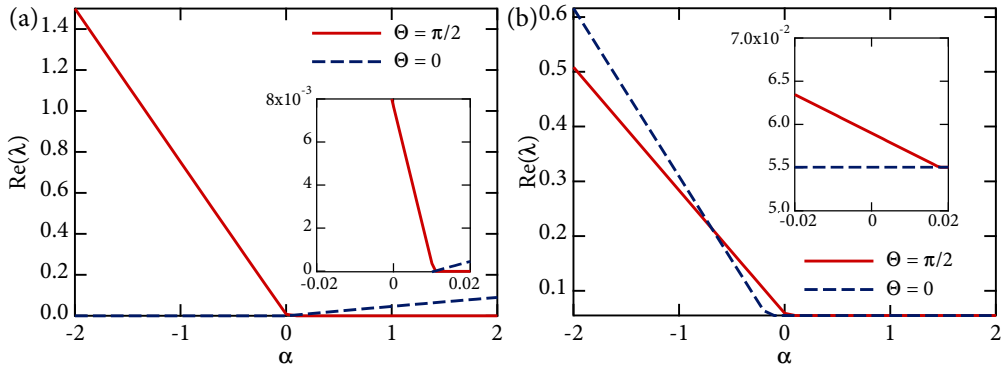

Figure 2.5: (Color online) Dependence of the maximum reduced growth rate $\mathrm{Re}(\lambda)$ governing the stability of the nematic base states on the dimensionless active stress magnitude α, for $\xi = 20$: (a) branch 2, (b), branch 3. Results for two different wave orientations Θ are shown. Insets show close-ups on the region near the origin.

both pushers and pullers are predicted to be unstable, though for different wave orientations. Branch 3, as shown in Fig. 2.5(b), is also unstable for all values of α, though it is further destabilized by activity in the case of pushers. We note an interesting dependence of the growth rate on the wave direction Θ: for a given value of α, waves of different orientations have distinct stability properties.

The precise dependence on the parameter ξ is shown in Fig. 2.6, where the stability of both nematic branches is illustrated for two different wave directions. Figs. 2.6(a) and (b) show the stability of branch 2, for $\Theta = 0$ and $\pi/2$, respectively. On this branch, which is the most energetically favorable base state according to the analysis of Sec. 2.3.1, we find that pushers ($\alpha = -1$) are always unstable for $\Theta = \pi/2$, though some wave orientations such as $\Theta = 0$ are observed to be stable at high values of ξ. In the case of pullers ($\alpha = +1$), activity has a stabilizing effect for low values of ξ (precisely when $\xi \lesssim 14.1$ for the present choice of parameters), but an instability occurs above this threshold for $\Theta = 0$. The case of movers, which do not exert any active stress, is characterized by a very low but positive growth rate, which

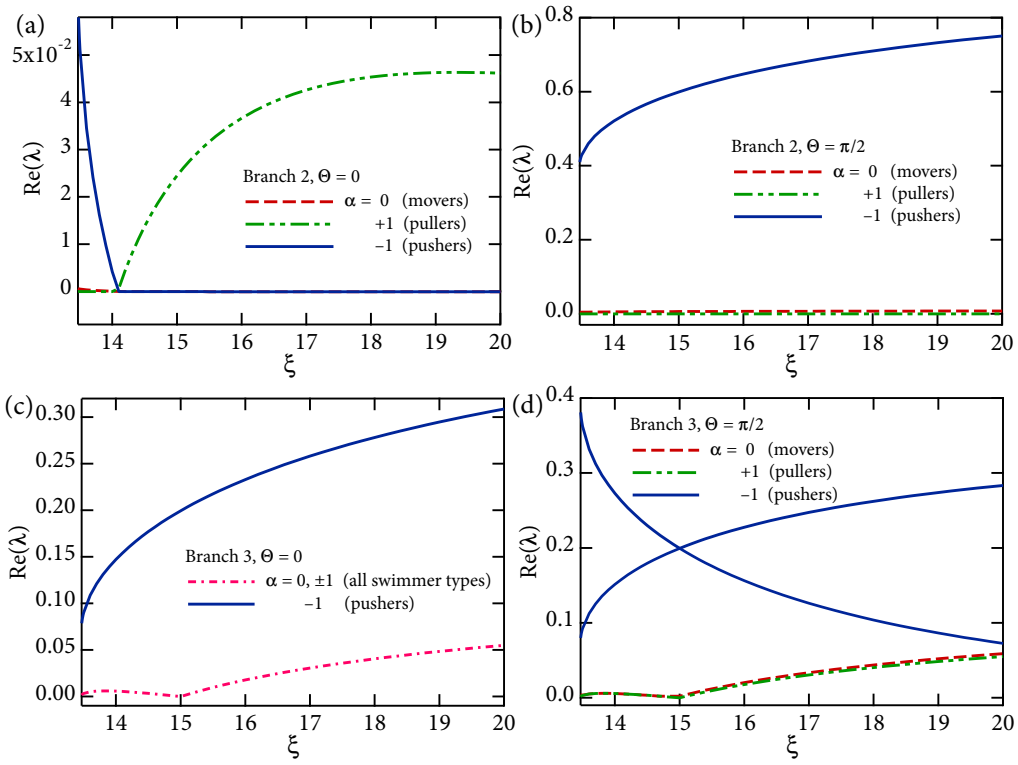

Figure 2.6: (Color online) Dependence of the maximum reduced growth rate $\mathrm{Re}(\lambda)$ on the parameter ξ, along both nematic branches, for two different wave directions Θ: (a) branch 2, $\Theta = 0$; (b) branch 2, $\Theta = \pi/2$; (c) branch 3, $\Theta = 0$; (d) branch 3, $\Theta = \pi/2$.

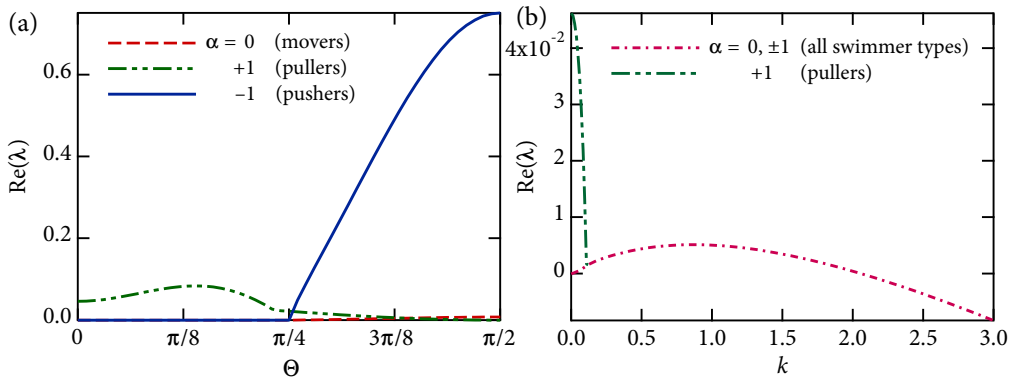

Figure 2.7: (Color online) Dependence of the maximum reduced growth rate $\mathrm{Re}(\lambda)$ on: (a) wave direction Θ (in the limit of $k \to 0$), and (b) wavenumber k (for a wave with orientation $\Theta = 0$). Both plots were obtained on branch 2, with $\xi = 20$.

is approximately two orders of magnitude smaller than the characteristic growth rate of either pushers or pullers; this weak instability can be shown to be a consequence of the steric stress rather than the active stress, and is observed to disappear when $\beta = 0$. The stability of the other nematic branch (branch 3), which is the least energetically favorable, is illustrated in Figs. 2.6(c) and (d); on this branch, we find that all types of particles exhibit instabilities.

As noted on Figs. 2.5 and 2.6, different wave orientations Θ can have different stability characteristics. This is described more precisely in Fig. 2.7(a), where we plot the maximum growth rate as a function of Θ on branch 2 when $\xi = 20$. In agreement with Fig. 2.6, we observe a positive growth rate in suspensions of pullers for low values of Θ (with $\Theta = 0$ corresponding to a wave in the direction of particle alignment), whereas pushers and movers are most unstable when $\Theta = \pi/2$ (corresponding to a wave in a direction perpendicular to that of the nematic base state). The precise range of unstable wave directions for a given swimmer type is also observed to depend on the value of ξ.

As in the case of the isotropic branch discussed in Sec. 2.3.3, the stability of the nematic branches has a non-trivial dependence on wavenumber k as a result of the convective term $-i(\mathbf{p}\cdot\mathbf{k})\hat{\Psi}$ (arising from the swimming velocity) in the operator $\mathscr{L}$. This dependence is illustrated in Fig. 2.7(b) in the case of a wave with direction $\Theta = 0$ at $\xi = 20$ on branch 2. While increasing k can initially destabilize certain eigenmodes, all growth rates are found to decay and eventually become negative at large enough values of k.

2.3.5 Summary of stability analysis and stability diagrams

The results of the stability analysis of the various isotropic and nematic base states are summarized in the form of stability diagrams in Fig. 2.8 for all three types of swimmers:

- *Movers*: the case of movers, which do not drive active stresses but result in flow-induced and steric stresses in addition to being subject to steric alignment torques, is shown in Fig. 2.8(a). The isotropic base state is found to be stable when $\xi < \xi_2^c = 15$, and unstable for higher values of ξ. The two nematic base states have distinct stability characteristics. Branch 3, which is the least favorable energetically as discussed in Sec. 2.3.1, is always unstable. Branch 2, in the long-wave limit, is subject to a weak instability with a very small growth rate. This instability is due solely to the steric stress and vanishes when $\beta = 0$; as will be discussed in Sec. 2.4, it is not observed in our simulations, where it is likely suppressed by the finite box size and translational diffusion. If the instability of branch 2 does not occur, we therefore find that there exists a finite range $\xi \in [\xi_1^c, \xi_2^c]$ over which both isotropic and nematic base states are

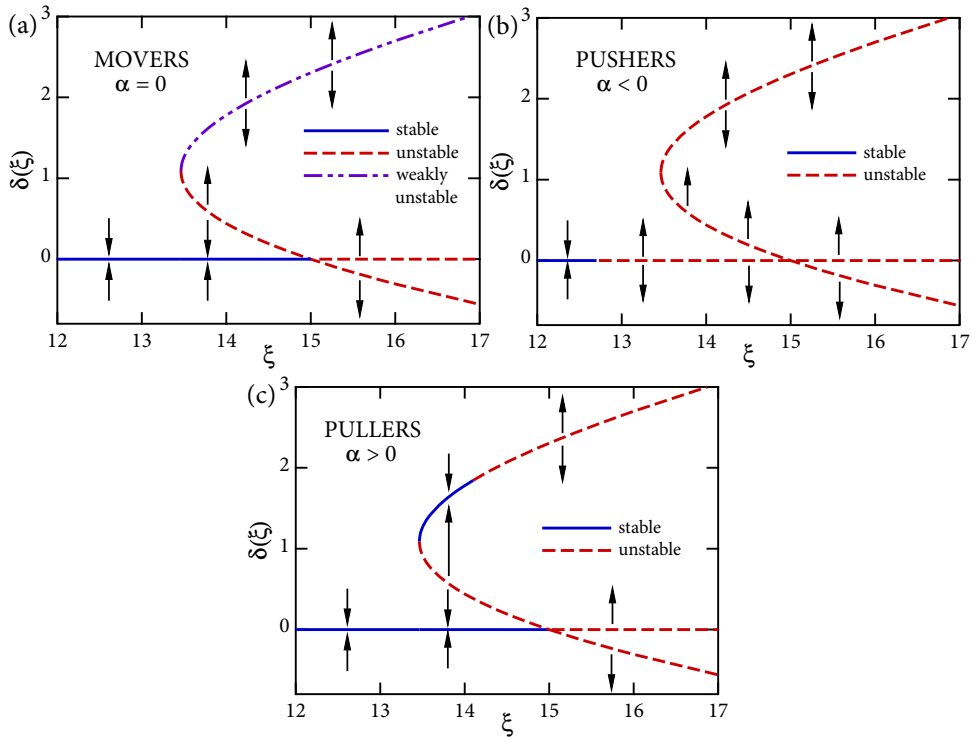

Figure 2.8: (Color online) Stability diagrams for: (a) movers ($\alpha = 0$), (b) pushers ($\alpha < 0$), and (c) pullers ($\alpha > 0$). A branch is labeled unstable if there exists a positive growth rate $\mathrm{Re}(\lambda) > 0$. In the case of movers, branch 2 is only weakly unstable, as the growth rates on that branch are very low (two orders of magnitude lower than on other unstable branches).

hydrodynamically stable (even though the nematic state of branch 2 realizes a lower minimum of the steric interaction energy). This was previously noted by Doi and Edwards [18], and suggests the existence of a hysteresis loop with possible phase separation near the isotropic-to-nematic transition.

- *Pushers*: the stability diagram for pushers, which also exert active stresses with $\alpha < 0$, is shown in Fig. 2.8(b). In this case, the isotropic case is found to become unstable above a critical value ξ^c that can be obtained from Eq. (2.64) as

$$\xi^c = 15 + \frac{\nu\overline{\alpha}(\nu)}{2d} = 15 + \frac{\nu}{2d}\left(\frac{\alpha - \frac{2}{5}U_0\beta\nu}{1 + \frac{\beta\nu}{15}}\right). \tag{2.69}$$

Because $\alpha < 0$, it is clear that $\xi^c < \xi_2^c = 15$, i.e. the isotropic base state becomes hydrodynamically unstable before the isotropic-to-nematic transition. In the case where $\beta\nu \ll 1$ and $U_0 = 0$ (dilute limit with no steric interactions), Eq. (2.69) reduces to the dilute marginal stability condition on α in the presence of rotational diffusion. The existence of an instability in the isotropic base state is not a surprising result in the light of our previous analysis of dilute suspensions, which were found to be always unstable in the case of pushers in the long-wave limit when diffusion was neglected [19, 20]. Rotational diffusion, however, can stabilize pusher suspensions at low values of ξ, which correspond to very low volume fractions or large values of d. This effect was previously noted by Subramanian and Koch [39] and Hohenegger and Shelley [41]. In the nematic regime, both branches 2 and 3 are found to be always unstable, at least over a certain range of the wave angle Θ. Pusher suspensions are therefore always expected to undergo unsteady chaotic dynamics when $\xi > \xi^c$; this is indeed

confirmed by our simulations in Sec. 2.4.

- *Pullers*: in the case of pullers, active stresses also arise (with $\alpha > 0$) but are known to have a stabilizing effect in dilute suspensions [19, 20]. As shown in Fig. 2.8(c), the isotropic case becomes unstable when ξ reaches $\xi_2^c = 15$, as in the case of movers; the instability that occurs above this value is solely due to steric effects, first through azimuthal modes $m = 0$, and 2, and finally through mode $m = 1$, which is stabilized by activity up to a higher value of ξ (Sec. 2.3.3). The nematic state of branch 3, as in the case of movers, is found to always be unstable. The effect of activity is seen most clearly on the nematic base state of branch 2, which is stable over a finite range of values of ξ just above $\xi_1^c \approx 13.46$, but becomes unstable at larger values of ξ. This differs fundamentally from the dilute case where isotropic puller suspensions are always predicted to be stable; As in the case of movers, there can exist a range of values of ξ near the isotropic-to-nematic transition where both isotropic and nematic base states are hydrodynamically stable, possibly leading to hysteresis and phase separation.

One should keep in mind that the stability results obtained above all pertain to the reduced growth rate $\lambda = \sigma + \nu D k^2$, and that translational diffusion D can therefore stabilize all branches, particularly at high wavenumbers. Also recall that all branches that are unstable as $k \to 0$ become stable at sufficiently large values of k even in the absence of translational diffusion, as a result of convection by the swimming velocity.

2.4 Numerical simulations

2.4.1 Simulation method and parameter selection

We complement the linear stability analysis of Sec. 2.3 by performing fully nonlinear simulations of the kinetic model of Sec. 2.2 in a periodic domain. The numerical method used is a direct extension of the work of Alizadeh Pahlavan and Saintillan [42], and is based on a finite-difference solution of the Smoluchowski equation (2.1) using second-order central finite differences in space and orientation and a second-order Adams-Bashforth time-integration scheme. A spectral solution of the Stokes equations is used, in which we use a three-point extrapolation scheme to evaluate the flow-induced stresses (which depend on the velocity gradient) at the current time step in terms of the two previous time steps. We use a total of 64^3 discretization points for the x, y and z spatial coordinates, and 16^2 points for the θ and ϕ angular coordinates, which parameterize the orientation vector $\mathbf{p}$ as in Eq. (2.56). Simulations were typically run using a 64-processor parallel computer.

All simulations shown were performed in a periodic cubic box with linear dimension $L/l_c = 50$. The particle translational and rotational diffusion coefficients are set to $D = 2.0$ and $d = 0.002$, and the dimensionless strength of steric interactions is set to $U_0 = 0.1346$, so that $\xi = \xi_1^c = 13.46$ is reached when $\nu = 0.1$; these values of d and U_0 are identical to those used in the stability analysis of the nematic base states in Sec. 2.3.4. Swimming particles are assumed to have an aspect ratio of $r = 10$, from which the parameter β appearing in the magnitude of the flow-induced and steric stress tensors is given by $\beta = 1.75$. Finally, we present results for two values of the dimensionless active stress: $\alpha = -1$ (pushers), and $\alpha = +1$ (pullers). Simulations

of movers ($\alpha = 0$) never evolved towards unsteady states and either converged to the isotropic or nematic base states depending on the value of ξ. In particular, we were never able to observe the weak instability of branch 2 predicted by the stability analysis; this discrepancy is likely consequence of the finite size of the domain in the simulations, and of translational diffusion. A few simulations of shakers, which are particles that do not swim ($V_0 = 0$) but exert an active stress ($\alpha = \pm 1$) are also discussed. Several values of the effective volume fraction ν are considered, so as to explore the various regimes highlighted in the stability diagrams of Fig. 2.8. In all simulations, the initial condition is uniform and isotropic with a weak random perturbation.

2.4.2 Results and discussion

Fig. 2.9 illustrate the dynamics in a number of simulations of pushers and pullers. Typical concentration fields observed in suspensions of pushers ($\alpha = -1$) are shown in Figs. 2.9(a)-(c) for the volume fractions $\nu = 0.05$, 0.07, and 0.2. In the first two cases, only the isotropic base state exists, as $\xi < \xi_1^c$. Based on the linear analysis of Sec. 2.3.3, the isotropic base state should be stable, in the long-wave limit, for $\xi < \xi^c \approx 0.039$ [obtained from Eq. (2.68)] and always unstable above this value. We indeed find that pusher suspensions are unstable for all three values of ν shown in Fig. 2.9, but stable when $\nu = 0.02$ (not shown). At the lowest unstable value of $\nu = 0.05$ [Fig. 2.9(a)], we find, however, that the instability is very weak and takes the form of two-dimensional concentration patterns; in the plane of the patterns, unsteady dynamics arise that are qualitatively very similar to our previous two-dimensional simulations of dilute suspensions [19, 20]. Further decreasing ν eventually stabilizes

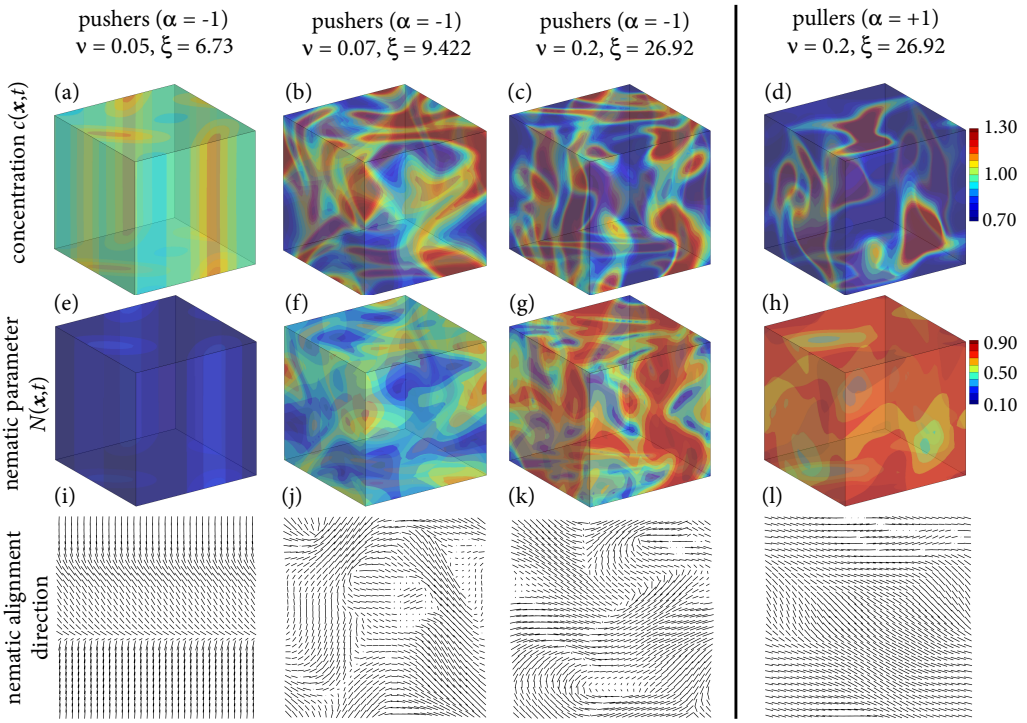

Figure 2.9: (Color online) Simulation results for pushers and pullers. Panels (a)-(d) show the concentration fields $c(\mathbf{x}, t)$ at an arbitrary time after the initial transient for the following cases: (a) pushers at $\nu = 0.05$, (b) pushers at $\nu = 0.07$, (c) pushers at $\nu = 0.2$, and (d) pullers at $\nu = 0.2$. Panels (e)-(h) show the corresponding nematic parameter fields $N(\mathbf{x}, t)$ defined in Eq. (2.70), for the same cases. Panels (i)-(l) show the nematic orientation fields in a two-dimensional slice, obtained by taking the eigenvector of $\mathbf{Q}(\mathbf{x}, t)$ with largest eigenvalue (enhanced online).

the system completely. The emergence of two-dimensional patterns close to the marginal stability condition is unexpected and not predicted by the linear analysis; it is reminiscent, however, of previous observations made on the dynamics of active pusher suspensions in shear flows [42], where stabilization by the flow was also shown to lead to a transition from three- to two-dimensional instabilities. At the higher volume fraction of $\nu = 0.07$, which is still below the isotropic-to-nematic transition, three-dimensional unsteady concentration patterns arise, which are qualitatively similar to those previously observed in dilute instabilities [42]. These patterns continually form and break up in time, leading to chaotic dynamics. At the higher concentration of $\nu = 0.2$, which is above the isotropic-to-nematic transition, the patterns still persist and do not look significantly different; other statistics, however, such as the degree of particle alignment, will exhibit distinct features.

In the case pullers ($\alpha = +1$), the linear stability results are also confirmed. We do find that the isotropic base state is always stable when $\xi < \xi_2^c$, and that the nematic branch is also stable for $\xi \gtrsim \xi_1^c$, see Fig. 2.8(c). At high values of ν or ξ, an instability is observed as shown in Fig. 2.9(d) for $\nu = 0.2$, and also takes the form of three-dimensional unsteady patterns. These patterns, however, have a different morphology from those obtained in the case of pushers, and tend to have globular shapes compared to the sheets that pushers tend to form. The existence of this instability is truly a consequence of the combination of steric interactions and activity, as dilute suspensions of pullers were found to be always stable in previous work [20, 42], and as concentrated suspensions of movers, for which $\alpha = 0$, are also observed to be stable in our simulations.

We characterize the local degree of nematic alignment of the particles by

defining the following nematic parameter $N(\mathbf{x},t)$:

$$N(\mathbf{x},t)=\frac{3}{2}\left[-\min_{\mathbf{p}\in\Omega}\left(\frac{U(\mathbf{x},\mathbf{p},t)}{U_0 c(\mathbf{x},t)}\right)-\frac{1}{3}\right]=\frac{3}{2}\max_{\mathbf{p}\in\Omega}\left[\mathbf{pp}:\mathbf{Q}(\mathbf{x},t)\right]=\frac{3}{2}e_Q, \qquad (2.70)$$

where e_Q is the largest eigenvalue of the nematic order parameter tensor $\mathbf{Q}(\mathbf{x},t)$. It is straightforward to see that $N(\mathbf{x},t)=0$ for an isotropic orientation distribution, and 1 for a perfectly aligned distribution. Also note that for the base-state distributions we have $N=A[\Psi_0]=4\delta/\xi$, with N tending to 1 as $\xi\to\infty$. The nematic parameter is illustrated in Figs. 2.9(e)-(h), for the same cases as for the concentration field. In the case of pushers, the value of N is very low near the marginal stability limit ($\nu=0.05$), which is a consequence of the dominant effect of rotational diffusion and explains the weak instability observed in this case. As ν increases, fluctuations in N become stronger, as does the overall level of alignment. This is especially clear when $\nu=0.2$, where many large domains of very strong nematic alignment are present in the suspensions [Fig. 2.9(g)]. In the case of unstable puller suspensions [Fig. 2.9(h)], alignment is yet stronger, with N reaching values above 0.6 almost everywhere in the flow. A careful observation of the initial transient in the case of pullers reveals that the suspension, which is nearly isotropic in the initial condition, first quickly evolves towards the nematic base state, which then itself becomes destabilized; this interesting fact, which is not observed in the case of pushers, will be further discussed below.

Figures 2.9(i)-(l) also show the nematic alignment field, obtained by calculating the eigenvector $\mathbf{s}(\mathbf{x},t)$ of the tensor $\mathbf{Q}(\mathbf{x},t)$ with eigenvalue e_Q. In pusher suspensions, orientations are spatially correlated over large length scales, although the strong fluctuations in the unstable regimes lead to finite domains of correlation separated by what appears to be defects. In unstable puller suspensions, we find that these defects

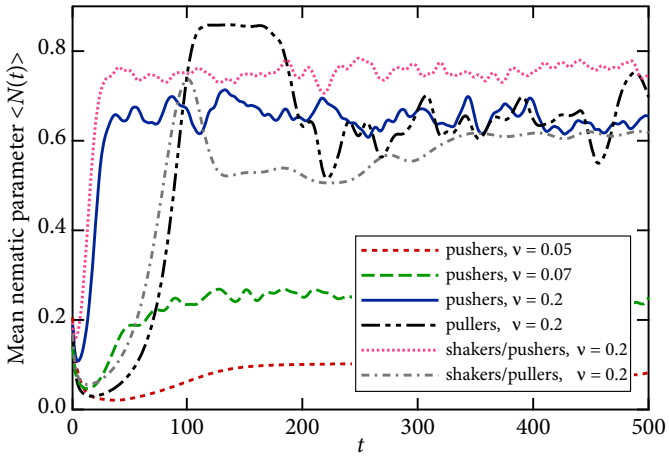

Figure 2.10: (Color online) Spatially averaged nematic parameter $\langle N(\mathbf{x}, t)\rangle$, defined in Eq. (2.70), as a function of time in suspensions of pushers ($\alpha = -1$), pullers ($\alpha = +1$), as well as shakers ($V_0 = 0$, $\alpha = \pm 1$) at various volume fractions.

become fewer, and the orientations are strongly correlated over the entire scale of the system.

The qualitative differences between unstable pusher and puller suspensions at high values of ξ can be interpreted based on the linear stability results. In the case of pushers, all steady base states are unstable when $\xi > \xi^c \approx 0.039$. We do not expect any significant qualitative changes in the dynamics when ν or ξ is further increased, as the nematic base state is never approached; the only clear feature occurring at very high concentrations is an enhancement of the local degree of alignment, as illustrated in Fig. 2.9(g). The case of pullers, however, is different: the isotropic state is stable up to the nematic transition, and a stable nematic state can also be observed close to the transition [Fig. 2.8(c)]; when increasing ξ further, this aligned configuration is also destabilized by activity, leading to fluctuations close to the nematic equilibrium. This is precisely what is observed in Figs. 2.9(d) and (h), where the isotropic initial condition first becomes unstable, briefly giving way to a nematically aligned state,

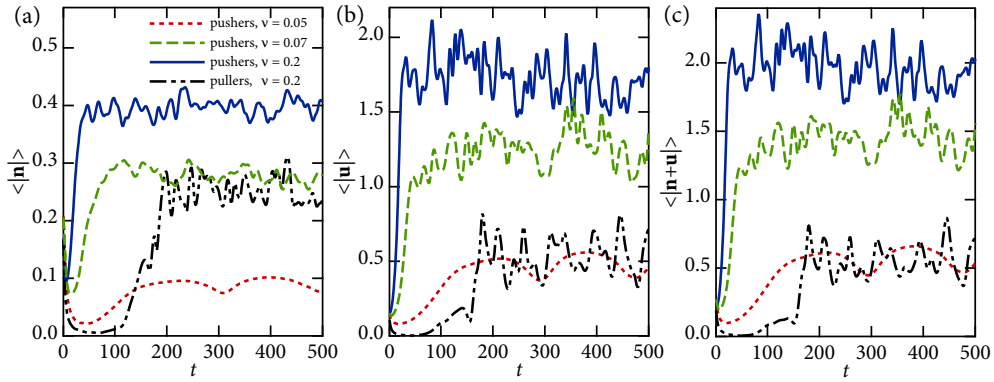

Figure 2.11: (Color online) Time evolution of the spatial averages of: (a) $|\mathbf{n}(\mathbf{x},t)|$, (b) $|\mathbf{u}(\mathbf{x},t)|$, and (c) $|\mathbf{n}(\mathbf{x},t)+\mathbf{u}(\mathbf{x},t)|$, in suspensions of pushers at $\nu = 0.05$, 0.07, and 0.2, and pullers at $\nu = 0.2$.

which subsequently also destabilizes and leads to fluctuations with a strong degree of alignment and long-ranged spatial orientation correlations. The dynamics described here are seen most clearly in Fig. 2.10, which shows the spatial average of the nematic parameter N as a function of time. Note that the initial non-zero value of $\langle N(t)\rangle$ in this figure is due to the initial perturbation introduced in the distribution function at $t = 0$, which is weakly anisotropic. In the case of pushers, we clearly see that unsteady dynamics emerge directly from the initial isotropic configuration, and that increasing ν really only modifies the mean degree of alignment at steady-state, with a stronger alignment occurring at the highest concentrations. In the case of pullers, we observe that the whole suspension first aligns nematically, with the mean degree of alignment quickly reaching a plateau at $N \approx 0.85$, which is very close to the theoretical value of $4\delta/\xi \approx 0.86$ for the nematic base state of branch 2 when $\xi = 26.92$. After a short period, this nematic state subsequently destabilizes and the value N decreases again to fluctuate around a mean of 0.6.

All the instabilities described in Sec. 2.3 lead to the growth of the local nematic alignment of the particles, irrespective of their polar orientation. Indeed, all terms

involving active stresses and steric effects in the kinetic model only involve the nematic order parameter tensor $\mathbf{Q}(\mathbf{x},t)$ (as well as the fourth moment $\mathbf{S}(\mathbf{x},t)$ through the steric and flow-induced stesses). However, our previous study of dilute suspensions [20] has shown that the polar order parameter $\mathbf{n}(\mathbf{x},t)$ also grows as a result of the instability, because an initially weak polarity exists in the initial condition. As argued in our previous work, this non-zero director field is precisely what leads to the growth of concentration fluctuations in the nonlinear regime, via the nonlinear source term appearing in the governing equation for the concentration field:

$$\partial_t c + \mathbf{u}\cdot\nabla_x c - D\nabla_x^2 c = -V_0\nabla_x\cdot(c\mathbf{n}). \tag{2.71}$$

The same effect is observed in the present work, and results on the polar order parameter and its relation to the hydrodynamic velocity are illustrated in Fig. 2.11. The spatially averaged norm $\langle|\mathbf{n}(\mathbf{x},t)|\rangle$ of the polar order parameter is shown as a function of time in Fig. 2.11(a) for the same simulations as in Fig. 2.9. In pusher suspensions, a clear net polarity is observed, which is weak close to the marginal stability limit ($\nu = 0.05$), but becomes quite strong at higher values of ν. Polarity also emerges in unstable puller suspensions, though it only grows once the nematic state is destabilized, and the steady-state value of $\langle|\mathbf{n}|\rangle$ is found to be significantly less than in pusher suspensions at the same volume fraction, even though both suspensions have nearly the same average value of the nematic parameter as seen in Fig. 2.10. Fig. 2.11(b) also shows the magnitude of the hydrodynamic velocity averaged over space as a function of time. The fluid velocity shows similar trends as the polar order parameter: it increases with ν for pushers, and is typically weaker in unstable puller suspensions than in pusher suspensions at the same value of ξ. What is perhaps

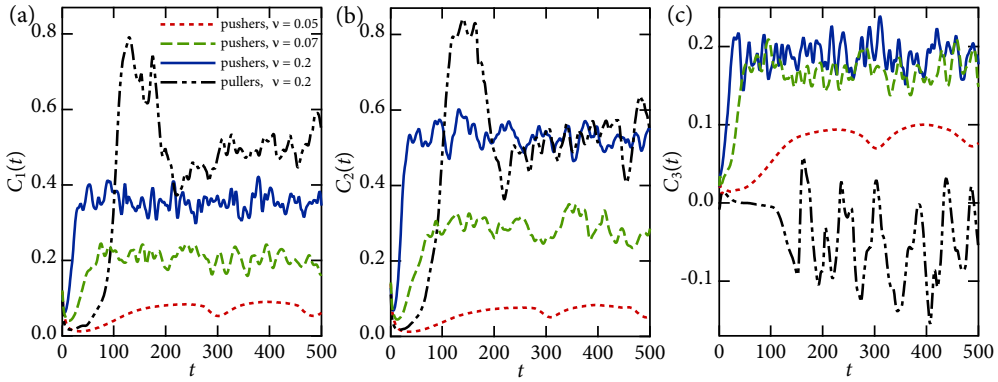

Figure 2.12: (Color online) Time evolution of the correlation defined in Eqs. (2.72)–(2.74): (a) $C_1(t)$, (b) $C_2(t)$, and (c) $C_3(t)$, in suspensions of pushers at $\nu = 0.05$, 0.07, and 0.2, and pullers at $\nu = 0.2$.

most unexpected is the different nature of the interaction between $\mathbf{u}$ and $\mathbf{n}$ in pusher and puller suspensions, as illustrated in Fig. 2.11(c) showing the spatial average of $\langle|\mathbf{n}+\mathbf{u}|\rangle$, which can be interpreted as an effective swimming velocity in the presence of hydrodynamic interactions. In the case of pushers, the effects of polar alignment and hydrodynamic flow are compounded, resulting in a net velocity that is of the order of $\langle|\mathbf{n}|\rangle + \langle|\mathbf{u}|\rangle$. Such is not the case for pullers, where the mean swimming motions due to the polarity impedes transport by the hydrodynamic flow.

These observations are easily explained by considering correlations between hydrodynamic velocity $\mathbf{u}(\mathbf{x},t)$, polar order parameter $\mathbf{n}(\mathbf{x},t)$, and nematic direction of alignment $\mathbf{s}(\mathbf{x},t)$. Precisely, we define the following quantities:

$$C_1(t) = \frac{1}{V}\int_V c(\mathbf{x},t)N(\mathbf{x},t)\frac{|\mathbf{u}(\mathbf{x},t)\cdot\mathbf{s}(\mathbf{x},t)|}{|\mathbf{u}(\mathbf{x},t)|}\,d\mathbf{x}, \tag{2.72}$$

$$C_2(t) = \frac{1}{V}\int_V c(\mathbf{x},t)N(\mathbf{x},t)\frac{|\mathbf{n}(\mathbf{x},t)\cdot\mathbf{s}(\mathbf{x},t)|}{|\mathbf{u}(\mathbf{x},t)|}\,d\mathbf{x}, \tag{2.73}$$

$$C_3(t) = \frac{1}{V}\int_V c(\mathbf{x},t)\frac{\mathbf{u}(\mathbf{x},t)\cdot\mathbf{n}(\mathbf{x},t)}{|\mathbf{u}(\mathbf{x},t)|}\,d\mathbf{x}, \tag{2.74}$$

which are plotted in Fig. 2.12 as functions of time. The function $C_1(t)$, which shows

the correlation between the orientations of the hydrodynamic velocity and the nematic alignment direction $\mathbf{s}(\mathbf{x}, t)$ is plotted in Fig. 2.12(a): a net correlation is observed in all simulations, regardless of swimmer type, and becomes stronger at higher concentrations. This is not surprising, as the effect of the flow on orientation is precisely to align particles with the flow via Jeffery's equation in Eq. (2.5). More precisely, Jeffery's equation causes nematic alignment along the principal axis of maximum extension of the velocity gradient. As shown in Fig. 2.12(b), the nematic alignment direction is also strongly correlated with the direction of the polar order parameter $\mathbf{n}(\mathbf{x}, t)$, which again could have been expected. The difference between pushers and pullers is most clear in Fig. 2.12(c), which shows the function $C_3(t)$ characterizing the correlation between polar order parameter and hydrodynamic velocity. In the case of pushers, a positive correlation is found, corresponding to particles swimming preferentially in the same direction as the flow velocity; this is in agreement with the results of Fig. 2.11(c), where we found that the effects of $\mathbf{u}$ and $\mathbf{n}$ on the mean total swimmer velocity are compounded for pushers. The situation is quite different for pullers, where $C_3(t)$ is typically negative, indicating that pullers swim preferentially against the flow, resulting in an effective decrease in their total velocity as observed in Fig. 2.11(c). While we do not yet have a complete explanation for this behavior, it is consistent with our previous particle simulations in the dilute and semi-dilute regimes, where we found that hydrodynamic interactions tend to enhance the mean swimming speed of pushers, but decrease that of pullers [34, 38].

The hydrodynamic flows arising in the simulations are driven by the active stress exerted by the particles, which effectively injects mechanical energy into the system. The amount of active power transferred by the swimmers to the mean-field

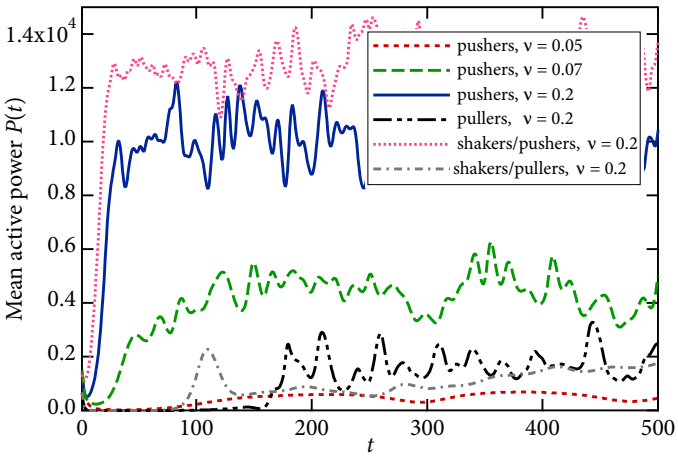

Figure 2.13: (Color online) Mean active power $P(t)$ defined in Eq. (2.75) as a function of time, in suspensions of pushers at $\nu = 0.05$, 0.07, and 0.2, and pullers at $\nu = 0.2$. The plot also shows results for shakers ($V_0 = 0$, $\alpha = \pm 1$) at $\nu = 0.2$.

flow can be estimated by a simple mechanical energy balance on the momentum equation as follows [20]

$$P(t) = -\alpha \int_V \int_\Omega [\mathbf{pp} : \mathbf{E}(\mathbf{x}, t)] \Psi(\mathbf{x}, \mathbf{p}, t)\, d\mathbf{p}\, d\mathbf{x} = -\alpha \int_V \mathbf{E}(\mathbf{x}, t) : \mathbf{D}(\mathbf{x}, t)\, d\mathbf{x}, \quad (2.75)$$

where we see that power is directly linked to the relation between the nematic order parameter in the suspension and the local rate-of-strain tensor. In semi-dilute systems [20], it was found that $P(t)$ increases in suspensions of pushers as a result of instabilities, but decreases to zero in suspensions of pullers, which were always stable. Results for the present simulations are shown in Fig. 2.13. In agreement with the semi-dilute case, pusher suspensions have a net positive power, which increases with increasing ν as the instabilities become stronger. In the case of unstable puller suspensions, a net positive power is also observed, though its value is significantly less than for pushers at the same concentration. Considering that the prefactor $-\alpha$ in Eq. (2.75) is of negative sign for pullers, this again hints at a fundamentally different type of interaction between

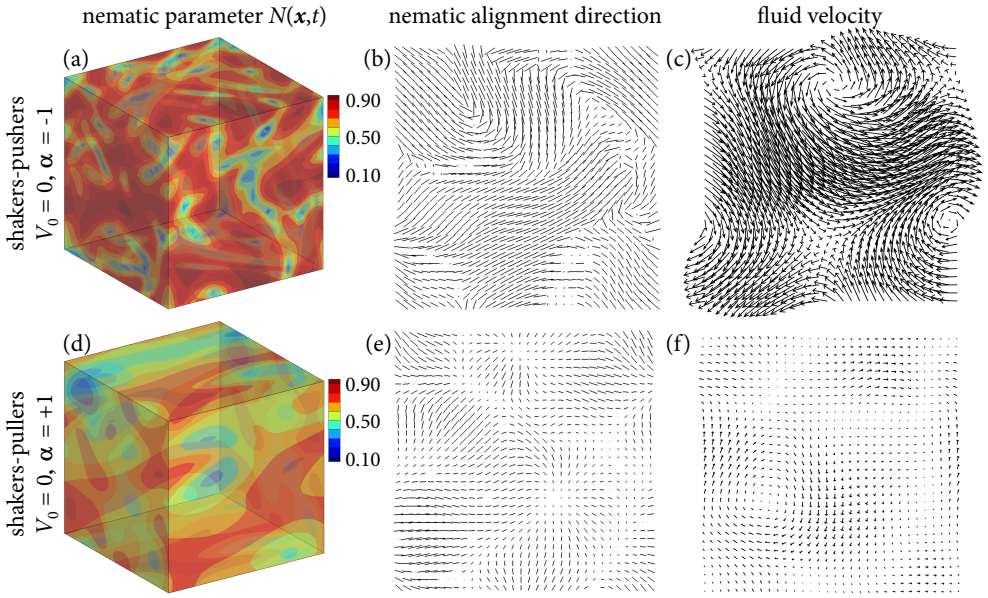

Figure 2.14: (Color online) Simulation results for shakers ($V_0 = 0$) at an effective volume fraction of $\nu = 0.2$ ($\xi = 26.92$). Panels (a)-(c) are for pushers ($\alpha = -1$) and (d)-(f) for pullers ($\alpha = +1$). (a) and (d) show the nematic parameter $N(\mathbf{x}, t)$ defined in Eq. (2.70); (b) and (c) show the nematic orientation fields in a two-dimensional slice, obtained by taking the eigenvector of $\mathbf{Q}(\mathbf{x}, t)$ with largest eigenvalue; (c) and (f) show the hydrodynamic velocity fields in a two-dimensional slice.

particle orientations and local self-induced flow in puller suspensions, through the net negative sign of the product $\mathbf{E}(\mathbf{x}, t) : \mathbf{D}(\mathbf{x}, t)$.

We finish the discussion of our simulations by presenting results on suspensions of shakers, which are particles that drive active stresses (with α of either sign) but do not swim: $V_0 = 0$. The linear stability of shaker suspensions is the same as that of pusher or puller suspensions in the long-wave limit, as we saw in Sec. 2.3 that letting $k \to 0$ is equivalent to eliminating the convective term due to swimming in the linearized eigenvalue problem. We verify indeed in our simulations that instabilities arise in shaker suspensions (either pushers or pullers) according the same diagrams as obtained in Fig. 2.8, and lead to the local alignment of the particles and to the emergence of complex flows. Typical results for both types of shakers are shown in

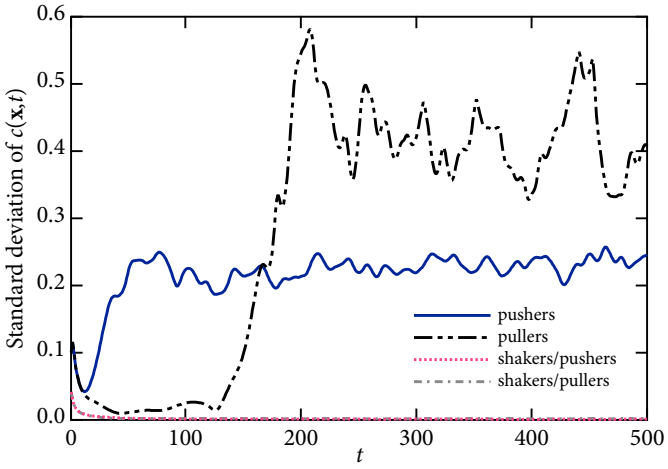

Figure 2.15: (Color online) Standard deviation $\sqrt{(\langle c\rangle - 1)^2}$ of the concentration field $c(\mathbf{x}, t)$ as a function of time, in suspensions of pushers ($\alpha = -1$), pullers ($\alpha = +1$), and shakers ($V_0 = 0$) of both types, at $\nu = 0.2$.

Fig. 2.14. We find that results for the nematic parameter, nematic alignment field, and hydrodynamic velocity field are very similar to what was obtained previously in the case of actual pushers and pullers. This is confirmed in Figs. 2.10 and 2.13, where shakers are seen to align as strongly and exert as much power as their swimming counterparts, if not more. One significant difference, however, is that shaker suspensions of either type are never subject to concentration instabilities, even in the nonlinear regime: the instability when $V_0 = 0$ only pertains to the particle orientations, and there is no mechanism for growth of concentration fluctuations. This is again easily understood by consideration of Eq. (2.71) for the concentration field, where the nonlinear source term $-V_0\nabla_x \cdot (c\mathbf{n})$ vanishes when $V_0 = 0$. The evolution of the variance of the concentration field for pushers, pullers, and both types of shakers at the same concentration of $\nu = 0.2$ is illustrated in Fig. 2.15 and confirms this result. It is found that the variance quickly decays to zero in suspensions of shakers, even though strong fluctuations of the nematic parameter and velocity field are taking place. In suspensions of regular pushers and pullers, the concentration variance increases as expected and in agreement

with the dynamics shown in Fig. 2.9.

2.5 Concluding remarks

We have presented a continuum model for the dynamics in concentrated suspensions of hydrodynamically interacting active particles, such as swimming microorganisms or artificial microswimmers. The model is an extension of our previous theory for dilute suspensions [20], and is based on a Smoluchowski equation for the distribution of particle positions and orientations, coupled to the Stokes equations for the fluid flow with an added stress arising from activity. In dense systems, this model is modified by addition of a steric interaction torque in the equation for the angular flux velocity, which causes neighboring particles to align. In addition, flow-induced stresses due to the inextensibility of the particles in the flow, and steric stresses resulting from direct contact interactions also have to be included in the concentrated regime. Based on this model, two types of uniform base-state solutions are possible: the isotropic state (branch 1), which exists for all concentrations; two nematic states (branches 2 and 3), which arise only above a critical value of $\xi = 2U_0\nu/d$. The nematic base state with the strongest alignment (branch 2) always realizes the minimum steric interaction energy for the system.

We first performed a linear stability analysis of these base states for pushers ($\alpha < 0$), movers ($\alpha = 0$), and pullers ($\alpha < 0$), as summarized in Fig. 2.8. Movers, which are particles that do not exert an active stress but still swim, are stable in the isotropic state up to $\xi = \xi_2^c = 15$; the nematic branch 2, which is subject to a weak instability as a result of the steric stress, is likely to be stable in a number of situations in finite systems (as it was found to be in our simulations). In the case of pushers,

activity has a destabilizing effect: the isotropic state becomes unstable at a low value of ξ, and the nematic branches are always unstable. Pullers, however, are more stable than pushers: the isotropic state has the same stability as movers, and the nematic branch 2 is first stable over a finite range of values of ξ, but then becomes unstable at high ξ.

Numerical simulations of the kinetic equations confirmed all the results of the stability analysis. In particular, unstable chaotic solutions were obtained in suspensions of pushers even before the isotropic-to-nematic transition, whereas higher values of ν were required to observe an instability in the case of pullers. While both types of swimmers are subject to instabilities at high concentrations, the characteristics of the flows that emerge in the nonlinear regime differ qualitatively. While the instability for pushers is only intensified by steric interactions which cause stronger particle alignment, the dynamics in the unstable regime are relatively unaffected as ν increases above the nematic transition; on the other hand, the instability in puller suspensions appears to occur from the nematic state, and leads to fluctuations with very strong alignment but weaker hydrodynamic fluctuations and active power than for pushers.

These results again highlight the fundamentally different nature of interactions between particles and self-generated flows in suspensions of pushers and pullers, which has been reported previously in many contexts. Jeffery's equation, which governs the orientational dynamics of the swimmers in the fluid flow, causes all types of particles to align with the principal axes of the rate-of-strain tensor; however, pushers tend to drive extensional flows whereas pullers drive compressional flows. This important difference is clear for instance when considering the product $\mathbf{E}(\mathbf{x},t) : \mathbf{D}(\mathbf{x},t)$ appearing in the definition of the active power in Eq. (2.75): in the case of pushers, $\mathbf{E} : \mathbf{D}$ tends

to be positive, whereas it tends be negative in unstable puller suspensions.

A few limitations of the present model should be kept in mind. First, the expressions derived in Sec. 2.2.4 are based on a dilute approximation, as they only consider the interaction of a single particle with a mean-field flow (in the case of the flow-induced stress) or with a mean-field orientation distribution (in the case of the steric stress). These expressions involve linear and quadratic corrections to the Newtonian stress in terms of volume fraction, but are unlikely to be quantitatively accurate in very dense systems, where more complex rheological laws would be needed. However, we do not expect the effects of these stresses to change qualitatively at high volume fractions. A perhaps greater limitation of the model is the one-fluid assumption in which particles have no volume, which allowed us to describe fluid and particle motions in terms of the same hydrodynamic velocity field. Nevertheless, we believe that the present model captures most salient features of interactions in concentrated active suspensions, and casts new light on the subtle interaction of hydrodynamic and steric effects in these systems.

Acknowledgement: Chapter 2, in full, is a reprint of the material as it appears in Physics of Fluids 2013. "Instabilities and nonlinear dynamics of concentrated active suspensions" by Ezhilan, Barath; Shelley, Michael J; Saintillan, David, the American Institute of Physics, 2013. The dissertation author was the primary investigator and author of this paper.

2.A Steric stress tensor calculation

In this Appendix, we derive an expression for the stress tensor resulting from steric interactions, in the case of a suspension of slender rod-like particles. As

discussed in Sec. 2.2.2, steric interactions result in an effective angular velocity given by Eq. (2.20):

$$\dot{\mathbf{p}} = 2U_0(\mathbf{I} - \mathbf{pp}) \cdot \mathbf{D} \cdot \mathbf{p}, \tag{2.76}$$

where the second-order tensor $\mathbf{D}$ is defined in Eq. (2.9). We model the particle dynamics using leading-order slender-body theory [78], which for a stationary particle in a quiescent liquid simplifies to

$$s\dot{\mathbf{p}} = \frac{\ln(2r)}{4\pi\eta}(\mathbf{I} + \mathbf{pp}) \cdot \mathbf{f}(s), \tag{2.77}$$

where $s \in [-\ell/2, \ell/2]$ is a linear coordinate along the axis of the particle, and $\mathbf{f}(s)$ denotes the linear force distribution along the rod. This expression can be inverted for the force distribution:

$$\mathbf{f}(s) = \frac{4\pi\eta}{\ln(2r)}\left(\mathbf{I} - \frac{1}{2}\mathbf{pp}\right) \cdot s\dot{\mathbf{p}} = \frac{8\pi\eta U_0 s}{\ln(2r)}(\mathbf{I} - \mathbf{pp}) \cdot \mathbf{D} \cdot \mathbf{p}. \tag{2.78}$$

Following Batchelor [66], the effective stress tensor in the suspension is then expressed as a configurational average of the stresslets, or first force moments, on the particles:

$$\boldsymbol{\Sigma}^t(\mathbf{x}, t) = -\left\langle \int_{-\ell/2}^{\ell/2} \mathbf{f}(s)\mathbf{p}s \, ds \right\rangle = -\frac{\pi\eta\ell^3 U_0}{3\ln(2r)}\langle(\mathbf{I} - \mathbf{pp}) \cdot \mathbf{D} \cdot \mathbf{pp}\rangle, \tag{2.79}$$

where $\langle\cdot\rangle$ denotes an orientational average:

$$\langle h\rangle = \int_\Omega h(\mathbf{p})\Psi(\mathbf{x}, \mathbf{p}, t) \, d\mathbf{p}. \tag{2.80}$$

In index notation, Eq. (2.79) becomes

$$\Sigma^t_{ij} = -\frac{\pi\eta\ell^3 U_0}{3\ln(2r)}\langle(\delta_{ik} - p_i p_k)D_{kl}p_l p_j\rangle = -\frac{\pi\eta\ell^3 U_0}{3\ln(2r)}[D_{il}\langle p_l p_j\rangle - \langle p_i p_j p_k p_l\rangle D_{kl}]. \quad (2.81)$$

Recalling that $\langle p_l p_j\rangle = D_{lj} + (c/3)\delta_{lj}$ where c is the concentration, we obtain:

$$\Sigma^t_{ij} = -\frac{\pi\eta\ell^3 U_0}{3\ln(2r)}\left[D_{il}(D_{lj} + \frac{c}{3}\delta_{lj}) - \langle p_i p_j p_k p_l\rangle D_{kl}\right]. \quad (2.82)$$

After subtracting an isotropic tensor, which does not affect the velocity of the flow and only modifies the pressure, we arrive at the final expression:

$$\boldsymbol{\Sigma}^t(\mathbf{x},t) = -\sigma_t\left[\mathbf{D}(\mathbf{x},t)\cdot\mathbf{D}(\mathbf{x},t) + \frac{c(\mathbf{x},t)}{3}\mathbf{D}(\mathbf{x},t) - \mathbf{S}(\mathbf{x},t):\mathbf{D}(\mathbf{x},t)\right], \quad (2.83)$$

where $\sigma_t = \pi\eta\ell^3 U_0/3\ln(2r)$ and the fourth-order tensor $\mathbf{S}$ is defined in Eq. (2.10).

Chapter 3

Chaotic dynamics and oxygen transport in thin films of aerotactic bacteria

3.1 Introduction

The ability of motile bacteria to modulate their motions in response to changes in concentration of chemical cues or nutrients plays a central role in the development and growth of microorganismal colonies, as well as in cell-cell communication processes such as quorum sensing [79]. The directed migration of motile bacteria such as *Escherichia coli* and *Bacillus subtilis* along a chemical gradient, or "chemotaxis", is a consequence of their run-and-tumble dynamics, by which periods of motion along straight lines ("runs") are interspersed by random reorientation events ("tumbles") resulting from the unbundling and rebundling of their flagella [17, 80]. By modulating the frequency of tumbling events based on experienced temporal changes in chemical

concentration, bacteria are able to undergo a biased random walk in the gradient direction. In large-scale suspensions, this mode of locomotion often results in complex spatial patterns, with accumulation near sources of oxygen and nutrients [81], or the formation of stable multicellular aggregates [82].

As they locomote through fluid environments, bacteria not only interact with chemical substances but can also interact with each other in sufficiently concentrated suspensions via fluid-mediated hydrodynamic interactions. A neutrally buoyant self-propelled particle swimming through a viscous medium exerts a net force dipole on the fluid [62], thereby driving a flow that can affect the motions of its neighbors. In a suspension of many swimmers, the resulting fluid flows can be quite strong and overcome the individual swimming motions. This results in complex correlated dynamics [11], accompanied by giant number fluctuations [8] and enhanced swimmer and tracer diffusion [10, 83, 9]. While these effects have been studied both theoretically [19, 20, 41, 39, 37, 84] and numerically [33, 34, 38], their impact on nutrient transport and bacterial chemotactic response has not yet been addressed.

In recent experiments, Sokolov *et al.* [6] studied suspensions of the bacterium *Bacillus subtilis* confined in free-standing liquid films. As a result of aerotaxis (or directed response to an oxygen stimulus), the bacteria were found to accumulate near the interfaces where the oxygen concentration was the highest. In thin films ($\lesssim 100\,\mu$m), a steady concentration profile was reached with a spatially homogeneous bacterial distribution in the plane of the film. As the thickness was increased ($100 - 500\,\mu$m), a transition to inhomogeneous three-dimensional chaotic motions took place, with unsteady plumes of bacteria penetrating the bulk of the film and enhanced oxygen transport. In yet thicker films ($\gtrsim 500\,\mu$m), a stagnant bacterial layer at the center

of the film was also reported. As argued by Sokolov *et al.*, these dynamics are likely a consequence of the coupling between the aerotactic response of the bacteria and the flow fields set up via hydrodynamic interactions. Recent attempts at elucidating this coupling have focused on linear stability analysis in uniform gradients [85, 1], and have shown that the convective motion driven by bacterial active stresses may be responsible for these observations. However, these models did not account for oxygen transport and were not able to capture the strongly nonlinear regimes of the experiments.

In this chapter, we address this problem by extending a previous kinetic model for active suspensions [19, 20, 41] to account for run-and-tumble aerotaxis in thin liquid films, and explicitly model the three-way coupling between bacterial dynamics, oxygen transport, and fluid flow. Using three-dimensional numerical simulations, we study the emergence of nonlinear dynamics and pattern formation in these films, and are able to quantitatively capture and explain the three regimes reported in experiments [6] and to correlate them with the prediction from the linear stability analysis of Kasyap and Koch [1].

3.2 Kinetic Model

The configuration of a suspension of motile bacteria is modeled by a distribution function $\Psi(\mathbf{x}, \mathbf{p}, t)$ of center-of-mass position $\mathbf{x}$ and orientation $\mathbf{p}$, normalized as $\frac{1}{V}\int_V d\mathbf{x} \int d\mathbf{p}\, \Psi(\mathbf{x}, \mathbf{p}, t) = n$ where n is the mean number density in the domain of volume V. The distribution function satisfies a conservation equation

$$\partial_t \Psi + \nabla_x \cdot (\dot{\mathbf{x}}\Psi) + \nabla_p \cdot (\dot{\mathbf{p}}\Psi) = -\lambda\Psi + \frac{1}{4\pi}\int d\mathbf{p}'\, \Psi'\lambda', \tag{3.1}$$

where the right-hand side models the run-and-tumble dynamics of the swimmers [86, 39, 87, 88]. Specifically, the first term $-\lambda\Psi$ describes bacteria that tumble away from orientation $\mathbf{p}$ (with tumbling rate λ), whereas the integral term accounts for tumbling from orientation $\mathbf{p}'$ to $\mathbf{p}$. The flux velocities $\dot{\mathbf{x}}$ and $\dot{\mathbf{p}}$ in Eq. (3.1) are modeled as [20]

$$\dot{\mathbf{x}} = U_0\mathbf{p} + \mathbf{u} - D\nabla_x \ln\Psi, \tag{3.2}$$

$$\dot{\mathbf{p}} = (\mathsf{I} - \mathbf{pp}) \cdot (\gamma\mathsf{E} + \mathsf{W}) \cdot \mathbf{p} - d\nabla_p \ln\Psi. \tag{3.3}$$

The center-of-mass velocity in Eq. (3.2) results from the constant self-propulsion velocity $U_0\mathbf{p}$ (in the direction of $\mathbf{p}$), the local fluid velocity $\mathbf{u}(\mathbf{x}, t)$, and translational diffusion with diffusivity D. Similarly, Eq. (3.3) accounts for the rotation of the particle in the local flow field via Jeffery's equation [50], where $\mathsf{E} = (\nabla_x\mathbf{u} + \nabla_x\mathbf{u}^{\mathsf{T}})/2$ and $\mathsf{W} = (\nabla_x\mathbf{u} - \nabla_x\mathbf{u}^{\mathsf{T}})/2$ are the rate-of-strain and vorticity tensors, respectively, and $\gamma \in [-1, 1]$ is a shape parameter. For a spheroidal particle, $\gamma = (r^2 - 1)/(r^2 + 1)$ where r is the aspect ratio, and $\gamma \approx 1$ for a slender particle such as most types of bacteria. We also account for rotary diffusion with diffusivity d.

The fluid velocity $\mathbf{u}$ appearing in Eqs. (3.2)–(3.3) is driven by the active stresses generated by the swimming bacteria, and satisfies the steady Stokes equations

$$\nabla_x q - \eta\nabla_x^2\mathbf{u} = \nabla_x \cdot \boldsymbol{\Sigma}^p, \quad \nabla_x \cdot \mathbf{u} = 0, \tag{3.4}$$

where q is the pressure and η is the viscosity of the medium. The active particle stress tensor $\boldsymbol{\Sigma}^p(\mathbf{x}, t)$ captures the effect of the force dipoles due to self-propulsion and can

be modeled as [40, 68]

$$\boldsymbol{\Sigma}^p(\mathbf{x},t) = \sigma_0 \int \Psi(\mathbf{x},\mathbf{p},t)(\mathbf{pp} - \mathbf{I}/3)\, d\mathbf{p}, \tag{3.5}$$

where the stress magnitude σ_0 is a negative constant for rear-actuated swimmers, also known as pushers, such as most motile bacteria.

We model oxygen transport using an advection-diffusion-reaction equation for the oxygen concentration field $s(\mathbf{x},t)$ (normalized by its constant value at the film boundaries, taken to be the oxygen saturation concentration):

$$\partial_t s + \mathbf{u}(\mathbf{x},t)\cdot\nabla_x s - D_0\nabla_x^2 s = -\kappa c(\mathbf{x},t) f[s(\mathbf{x},t)]. \tag{3.6}$$

In Eq. (3.6), oxygen is advected by the local flow and diffuses with diffusivity D_0. Consumption by the bacteria is modeled as a second-order reaction, where κ is the consumption rate in oxygen-rich environments, $c(\mathbf{x},t) = \int d\mathbf{p}\Psi(\mathbf{x},\mathbf{p},t)$ is the bacterial concentration, and the function $f(s) = \max\{0, [(s-0.1)/0.9]^{0.2}\}$ accounts for the experimental observation that oxygen consumption diminishes drastically when its concentration falls below $\approx 10\,\%$ of its saturation value [89].

Finally, the tumbling bias, which couples bacterial dynamics to oxygen concentration and leads to aerotaxis, is modeled in Eq. (3.1) by letting the tumbling rate depend on s as $\lambda = \lambda_0 \exp(-\xi\, \mathcal{D}_t s)$ [80, 86], where ξ is the aerotactic response strength, and $\mathcal{D}_t s$ is a Lagrangian derivative capturing the rate of change of s as experienced by a bacterium moving with velocity $U_0\mathbf{p} + \mathbf{u}$: $\mathcal{D}_t s = \partial_t s + (U_0\mathbf{p} + \mathbf{u})\cdot\nabla_x s$. Bacteria for which $\mathcal{D}_t s > 0$ therefore have a lower tumbling rate, causing them to migrate towards oxygen-rich regions. Within this framework, the tumbling rate only depends on the

instantaneous rate of change of s along bacterial trajectories rather than on the time history of the concentration field experienced by the swimmers. Eqs. (3.1)–(3.6) form a closed system for the coupled dynamics of bacteria, oxygen, and fluid flow, and are the basis of this study. A similar system was also recently proposed by Lushi *et al.* [90] to model suspensions of chemotactic bacteria where the chemoattractant is secreted by the swimmers.

3.3 Simulation results

We solve this system numerically in a doubly periodic geometry (periodic in the x-y plane, bounded in the z-direction) mimicking the liquid films of the experiments of Sokolov *et al.* [6] We denote by L the film thickness, with $z = 0, L$ corresponding to the free surfaces. The boundary condition on Ψ is expressed as $\hat{\mathbf{z}} \cdot \int \dot{\mathbf{x}} \Psi d\mathbf{p} = 0$ at $z = 0, L$, and ensures that the mean concentration of bacteria is conserved. For the fluid flow, a free-shear-stress boundary condition is used to model air-liquid interfaces: $u_z = 0$ and $\partial_z u_x = \partial_z u_y = 0$ at $z = 0, L$. Both boundary conditions are easily implemented using a reflection condition for the distribution function. The normalized oxygen concentration has a prescribed value of 1 at both interfaces. Spectral solutions of Eqs. (3.4) and (3.6) are used, coupled to a finite-difference solution (second-order in time, space, and orientation) of the conservation equation for the distribution function [91]. The initial condition for $\Psi(\mathbf{x}, \mathbf{p}, 0)$ is uniform isotropic ($\Psi_0 = n/4\pi$) with a weak random perturbation, while the oxygen concentration inside the film is initially zero.

Parameter values are chosen for direct comparison with the experiments of Sokolov *et al.* [6]. The bacteria are *Bacillus subtilis*, with length $\ell = 4\,\mu$m, $U_0 = 20\,\mu$m/s, $\sigma_0 = -2.7 \times 10^{-18}\,$kg.m^2/s [92], and a mean number density of $n = 2 \times$

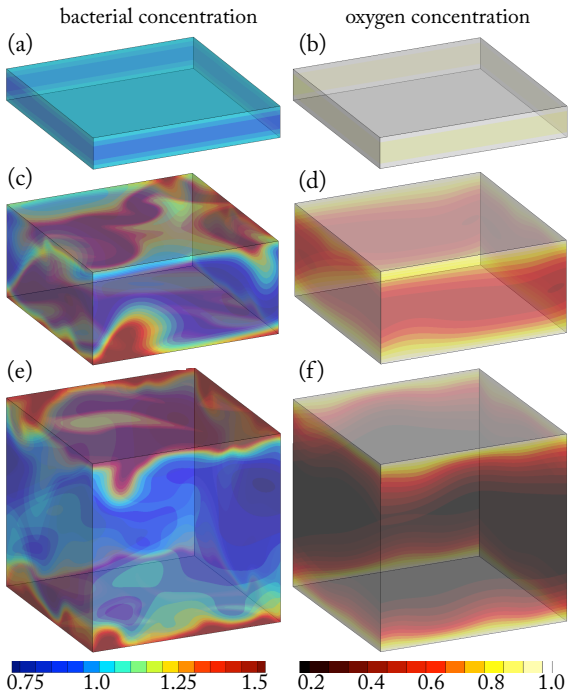

Figure 3.1: (Color online) Snapshots of bacterial (left) and oxygen (right) concentration fields at statistical steady state for different film thicknesses: (a)-(b) $L = 100\,\mu$m, (c)-(d) $L = 300\,\mu$m, and (e)-(f) $L = 600\,\mu$m (enhanced online).

$10^{16}\,\text{cell/m}^{-3}$ [6]. Based on the experiments, we estimate the translational diffusivity to be $D = 1.3 \times 10^{-10}$ m^2/s, and an estimate for the rotational diffusivity can then be obtained from the generalized Taylor dispersion [34] relation $d = U_0^2/6D \approx 0.5$ s^{-1}. The oxygen diffusivity and consumption rate are set to $D_0 = 2 \times 10^{-9}\,\text{m}^2/\text{s}$ and $\kappa = 6.7 \times 10^{-18}$ m^3/cell/s, respectively [6]. There is some uncertainty as to the actual values of the base tumbling rate and chemotactic strength in bacterial suspensions; we choose the values $\lambda_0 = 1.9$ s^{-1} and $\xi = 3.1$ s, which are close to previous estimates from experiments [17]. Finally, the film thickness is varied over the range $L = 50 - 600$ μm, which is also the range considered in the experiments of Sokolov *et al.* [6].

As the simulations start, oxygen rapidly diffuses into the film on a time scale $L^2/8D_0$ of the order of a few seconds, and consumption by the bacteria begins. Both

effects drive the formation of oxygen gradients inside the film, to which the bacteria respond by modifying their run-and-tumble dynamics so as to migrate preferentially towards the oxygen-rich regions near the boundaries. This aerotactic response leads to anisotropic orientation distributions, thereby inducing active stresses that, in some cases, can drive three-dimensional flows.

Simulations for various film thicknesses are illustrated in Fig. 3.1, showing typical bacterial and oxygen concentration fields at an arbitrary time past the initial transient. Based on the film thickness L, we distinguish three regimes with qualitatively different dynamics. In *regime I*, which is shown in Figs. 3.1(a)-(b) and corresponds to thin films ($L \lesssim 200\,\mu$m), bacterial and oxygen concentrations quickly reach steady-state profiles that are uniform in the x-y plane. At steady state, diffusion across the film leads to a nearly uniform oxygen profile, and by consequence to a weak bacterial migration. This weak aerotaxis, along with the strong confinement which constrains the growth of instabilities and limits flows in the z-direction, explain the lack of unsteady dynamics in this case. As L is increased to $\approx 200 - 400\,\mu$m, *regime II* is observed and is characterized by the emergence of unsteady dynamics on the scale of the system [Fig. 3.1(c)-(d)]. After an initial transient, a statistical steady state is reached when the effects of active input power, oxygen diffusion, and consumption by the bacteria are balanced. The bacteria are found to concentrate significantly near the boundaries, but their distribution constantly fluctuates in time with the formation of dense unsteady plumes penetrating the bulk of the film and thereby resulting in fluid mixing. The oxygen concentration away from the boundaries is diminished, which further enhances aerotaxis. Above $L \gtrsim 400\,\mu$m [Fig. 3.1(e)-(f)], *regime III* is also characterized by a strong bacterial migration towards the boundaries and unsteady

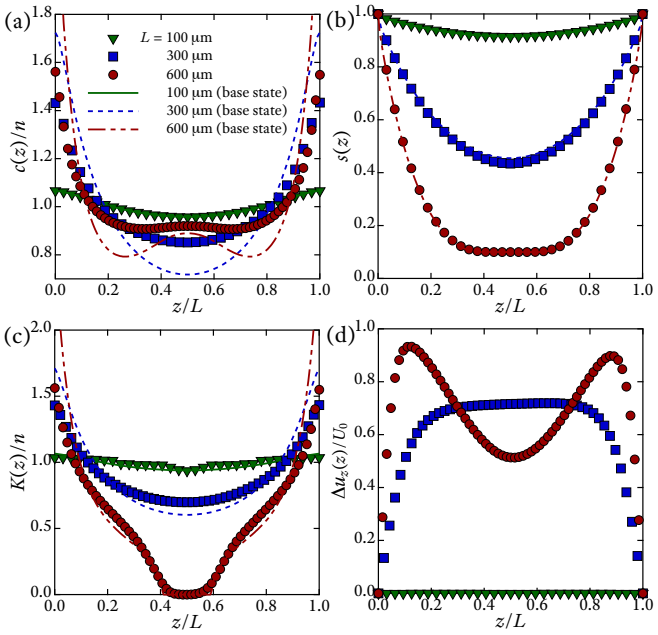

Figure 3.2: (Color online) Vertical profiles for different film thicknesses L: (a) bacterial concentration $c(z)/n$, (b) oxygen concentration $s(z)$, (c) oxygen consumption $K(z)/n$, and (d) rms of the vertical fluid velocity $\Delta u_z(z)$. Simulation results (symbols) are compared to the base state (lines).

flow dynamics, but also exhibits a strong oxygen depletion layer and an additional accumulation of bacteria near the center of the film (see Fig. 3.2). The bacterial plumes are found to intensify, and fluid velocities are reduced near the centerline. The existence and characteristics of all three regimes are consistent with the experimental observations of Sokolov *et al.* [6], as are the critical film thicknesses above which they arise.

Figure 3.2 shows vertical profiles of various fields averaged over time (after the initial transient) and in the plane of the film. We compare these profiles to a 'base state' equilibrium solution of the kinetic equations corresponding to a steady distribution function that only depends on z and $\theta = \cos^{-1} p_z$, with no fluid flow. Bacterial concentration profiles are plotted in Fig. 3.2(a), and exhibit strong peaks near the boundaries owing to aerotaxis. The profiles become sharper as L increases, yet

they are not as sharp as in the base state, a consequence of the large-scale flows that emerge in thick films and facilitate transport of bacteria into the bulk. Interestingly, we find that the oxygen profiles in Fig. 3.2(b) are only weakly affected by interactions and remain close to the base state for all values of L; an estimate of the Péclet number for oxygen transport, $\mathrm{Pe}_o = LU_0/D_0$, yields values of order $O(1)$, suggesting that this is likely a result of the strong oxygen diffusion. While $s(z)$ is nearly uniform in thin films (hence the weak aerotaxis in regime I), strong gradients form in thicker films. In regime III ($L = 600\,\mu$m), an oxygen depletion layer (defined as $s(z) \leq 0.1$) forms in the center of the film, where consumption nearly ceases. The appearance of this layer is accompanied by a slight accumulation of bacteria at the centerline [see Fig. 3.2(a)]. This accumulation should really be interpreted as a lack of depletion, as bacteria in this region no longer experience oxygen gradients and therefore become incapable of migrating away by aerotaxis. A similar dense immobile layer was reported in $530\,\mu$m films by Sokolov *et al.* [6].

The oxygen consumption $K(z) = \langle cf[s] \rangle$ (where $\langle \cdot \rangle$ denotes averaging over x, y, and t) is plotted in Fig. 3.2(c). Consumption occurs primarily near the boundaries as expected. For all film thicknesses, hydrodynamic interactions are found to increase consumption slightly near the center of the film with respect to the base state, as a result of the enhanced transport by the flow. In very thick films (regime III), however, consumption ceases completely near the centerline (where $s \leq 0.1$), leading to bacterial accumulation.

The emergence of large-scale flows with increasing L is illustrated in Fig. 3.2(d), showing the rms $\Delta u_z(z)$ of the vertical velocity across the film. There is no flow in regime I, which coincides with the base state. In regime II, significant velocities

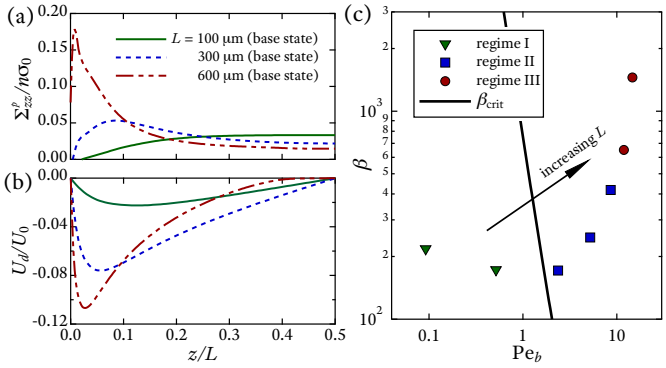

Figure 3.3: (Color online) Base-state profiles of (a) active stress component $\Sigma^p_{zz}/n\sigma_0$, and (b) aerotaxic drift U_d/U_0. (c) Base-state values of β and Pe_b and corresponding regimes in simulations, compared to the marginal stability curve β_{crit} of Kasyap and Koch [1]. The data points correspond to values of L in the range $50 - 600\,\mu$m.

[$\sim O(U_0)$] are seen across most of the film, with the effect of enhancing transport from the boundaries into the bulk (bacterial plumes). However, the profile shape changes in regime III as the depletion layer forms, with high velocities now localized near the boundaries and low velocities in the center. In both regimes II and III, horizontal velocities (not shown) are also significant and can reach values of up to $\approx 5U_0$.

The unsteady dynamics arising in thick films are directly linked to the coupling between the bacterial aerotactic response and hydrodynamic interactions, and cannot be explained solely based on either effect: in fact, setting either $\xi = 0$ (unbiased tumbling) or $\mathbf{u} = \mathbf{0}$ (no hydrodynamic interactions) in the simulations has the effect of stabilizing the suspensions for all values of L considered here. A mechanism for such taxis-driven instabilities was recently proposed by Kasyap and Koch [1] for bacteria swimming in a uniform gradient, where they argued that the anisotropic orientation distributions resulting from chemotaxis yield active stresses that drive flows tending to reinforce density fluctuations in directions normal to the chemical gradient. Based on a linear analysis, they showed that the onset of instability is governed by two dimen-

sionless groups: a bacterial Péclet number $\mathrm{Pe}_b = 3LU_d\lambda_0/U_0^2$, where $U_d = U_0 \int p_z \Psi \, d\mathbf{p}$ is the aerotactic drift velocity, and a parameter $\beta = -3\Sigma_{zz}^p L/2\eta U_d$ comparing the magnitudes of active and viscous stresses. They predicted that instabilities should occur when β exceeds a critical value β_{crit} obtained analytically as a function of Pe_b. To test this prediction, we consider base-state profiles of Σ_{zz}^p and U_d in Fig. 3.3(a)–(b), where both quantities are found to increase significantly with L near the boundaries. Estimates of Pe_b and β based on the extrema of Σ_{zz}^p and U_d are shown in Fig. 3.3(c) and compared to β_{crit}. The marginal stability curve is found to predict the onset of unsteady dynamics in the simulations remarkably well (transition from regime I to II). We find that this transition is primarily associated with an increase in Pe_b (or aerotactic drift), whereas the transition from II to III is accompanied by a sharp increase in β (or active stresses).

3.4 Conclusions

Using a kinetic model and numerical simulations, we have studied the transition to chaotic dynamics occurring in liquid films of aerotactic bacteria as film thickness is increased. Our results, which are consistent with experiments [6] and a linear stability theory [1], emphasize the importance of active stresses in these suspensions, which can drive unsteady flows and enhance both bacterial and oxygen transport across the film. A similar conclusion was also reached by Lushi *et al.* [90], who studied the effects of self-generated flows on chemotactic aggregation when the chemoattractant is secreted by the swimmers: they find that, in suspensions of pushers such as bacteria, self-generated flows have a strong impact on the aggregation patterns, which become unsteady as a result of strongly mixing flows advecting both swimmers and chemoattractant. These

observations all suggest that mixing and transport by hydrodynamic interactions likely play a significant role in facilitating the access of motile bacteria to oxygen and other nutrients in large-scale suspensions.

Acknowledgement: Chapter 3, in full, is a reprint of the material as it appears in Physics of Fluids 2012. "Chaotic dynamics and oxygen transport in thin films of aerotactic bacteria" by Ezhilan, Barath; Alizadeh Pahlavan, Amir; Saintillan, David, the American Institute of Physics, 2012. The dissertation author was the primary investigator and author of this paper.

Chapter 4

Transport of a dilute active suspension in pressure-driven channel flow

4.1 Introduction

The interaction of active self-propelled particles with rigid boundaries under confinement plays a central role in many biological processes. Spermatozoa are well known to accumulate at rigid boundaries [93, 94], with complex implications for their transport in the female tract during mammalian reproduction [95, 96, 97]. The aggregation of bacteria near surfaces and their interaction with external flows in confinement has a strong effect on their ability to adhere and form biofilms [98, 99, 100]. It also impacts their interactions with the gastrointestinal wall during digestion, with consequences for various pathologies [101, 102]. Confinement has also been shown to affect cell-cell interactions and collective motion in dense sperm and bacterial

suspensions and can also result in spontaneous unidirectional flows [103, 104, 105]. In engineering, the ability to concentrate or separate bacteria by controlling their motions in microfluidic devices with complex geometries has been demonstrated [106, 107, 108, 109, 110], as well as the ability to harness bacterial swimming power to actuate gears [111, 112] or transport cargo [113, 114]. Particle-wall interactions are also critical in systems involving synthetic microswimmers [115, 116, 117], as these inherently reside near surfaces due to sedimentation.

The prominent feature of confined active suspensions is the tendency of swimming particles to accumulate near boundaries. This was first brought to light by Rothschild [93], who measured the concentration of swimming bull spermatozoa in a glass chamber and reported a nonuniform distribution across the channel with a strong spike in concentration near the walls. Berke *et al.* [118] repeated the same experiment using suspensions of *Escherichia coli* in microchannels and also observed an accumulation of bacteria at the channel walls. They further reported the tendency of bacteria to align parallel to the boundaries, which led them to consider wall hydrodynamic interactions due to the force dipole exerted on the fluid by the self-propelled particles as a potential mechanism for migration. Hydrodynamic interactions are indeed known to have an impact on the trajectories of swimming particles near no-slip walls [119, 120], and have been shown to lead to attraction of sperm cells towards walls [121]. Li and co-workers [122, 123] also observed wall accumulation in suspensions of *Caulobactor crescentus* but presented an alternate mechanism based purely on kinematics that explains accumulation as a result of the collisions of the bacteria with the wall, leading to their reorientation parallel to the surface. The possibility of a non-hydrodynamic mechanism for wall accumulation is indeed supported by various

simulations that neglected wall hydrodynamic interactions [124, 125], suggesting that such interactions in fact only play a secondary role in this process.

Several other interesting effects have also been reported when an external flow is applied on the suspension. One such effect is the propensity of motile particles to swim upstream in a pressure-driven flow. This was noted for instance by Hill *et al.* [126], who tracked the trajectories of *Escherichia coli* in a shear flow near a rigid surface in a microfluidic channel, and proposed a complex mechanism for upstream swimming based on the chirality of the flagellar bundles and on hydrodynamic interactions. Such interactions were characterized more precisely by Kaya and Koser [127], who demonstrated that the *Escherichia coli* cells undergo modified Jeffery's orbits [49] near the walls and suggested that this detail is crucial in understanding the upstream migration. A clearer picture of this phenomenon emerged in yet more recent work by Kaya and Koser [128], who systematically analyzed *Escherichia coli* motility near a surface as a function of the local shear rate. At low shear rates, circular trajectories were observed due to the chirality of the cells, as previously explained by Lauga *et al.* [119]. At higher shear rates, positive rheotaxis was reported and accompanied by rapid and continuous upstream motility. This directional swimming was explained as a result of the combined effects of surface hydrodynamic interactions, which were thought to cause the swimming cells to dip towards the walls, and of reorientation by the shear flow, which aligns the cells against the flow. Upstream motility was also recently discussed by Kantsler *et al.* [97] in the case of mammalian spermatozoa, where the combination of shear alignment, wall steric interactions and cell chirality was shown to lead to steady spiraling trajectories in cylindrical capillaries.

While most experimental studies under confinement have focused on near-wall

aggregation and swimming dynamics, the behavior of self-propelled micro-organisms under flow in the bulk of the channels is also of interest. In recent work, Rusconi *et al.* [129] analyzed the effects of a Poiseuille flow on the trajectories and distributions of motile *Bacilus subtilis* cells, with focus on the central portion of the channel. In sufficiently strong flow, they reported the formation of a depletion layer in the central low-shear region of the channel, accompanied by cell trapping in the high-shear regions surrounding the depletion. This trapping was attributed to the strong alignment of the swimming cells with the flow under high shear, which hinders their ability to swim across streamlines. Quite curiously, they reported that maximum depletion is achieved at a critical imposed shear rate of approximately 10 s^{-1}, above which both trapping and depletion become weaker. A simple Langevin model capturing the effects of self-propulsion, shear rotation, and diffusion was also proposed to explain these observations, and was able to reproduce the salient features of the experiments.

Other interesting effects arise in pressure-driven flow due to the ability of active particles to modify the effective rheology of their suspensions. This problem was recently addressed by Gachelin *et al.* [130], who devised a microfluidic rheometer to measure the rheology of *Escherichia coli* suspensions as a function of shear rate in microchannels of width 100 μm. At low shear rates and in dilute suspensions, the effective viscosity was found to be lower than that of the suspending medium, in agreement with theoretical models for unconfined suspensions in simple shear flow [40, 131, 68] and to previous bulk measurements [6]. It was then found to increase at intermediate shear rates, and finally shear-thin at high shear rates as predicted by Saintillan [68]. Their study also cast light on the precise influence of flow on wall accumulation, and showed that increasing the flow rate causes a decrease in the

bacterial concentration at the walls.

Models and simulations explaining the mechanisms leading to these rich dynamics have been relatively scarce. Direct numerical simulations of hydrodynamically interacting swimming particles confined to a gap between two plates were first performed by Hernandez-Ortiz and coworkers [33, 132] using a simple dumbbell model, and indeed captured a strong particle accumulation at the boundaries in dilute systems. As the mean swimmer density was increased, collective motion and mixing due to particle-particle hydrodynamic interactions led to a decrease in the concentration near the walls. Accumulation was also observed in simulations of self-propelled spheres by Elgeti and Gompper [125], who entirely neglected hydrodynamic interactions. This study, as mentioned above, suggests that wall hydrodynamic interactions are not required to explain migration, and neither is shape anisotropy. Rather, the simple combination of cell swimming, steric exclusion by the walls, and diffusive processes is sufficient to capture accumulation, and Elgeti and Gompper [125] also proposed a simple Fokker-Planck description of the suspension that shares similarities with the present work and was able to explain their results. A similar continuum model was also proposed by Lee [133], who derived analytical expressions for the ratio of particles in the bulk vs near-wall region in the limits of weak and strong rotational diffusion. Very recently, Li and Ardekani [134] performed direct numerical simulations of confined suspensions of spherical squirmers that propel via an imposed slip velocity, and reported strong accumulation at the boundaries irrespective of the details of propulsion. They also noted the tendency of particles to align normal to the wall in the near-wall region.

The effects of an external flow have also been addressed using discrete particle

models and simulations. The dynamics of isolated deterministic microswimmers in Poiseuille flow were studied in detail by Zottl and coworkers [135, 136], who found that such swimmers perform either an upstream-oriented periodic swinging motion or a periodic tumbling motion depending on their location in the channel. Suspensions of interacting swimmers in pressure-driven flow have also been simulated, notably by Nash *et al.* [137] and Costanzo *et al.* [124], who both observed aggregation at the walls together with upstream swimming as a result of the rotation of the particles by the flow. More recently, Chilukuri *et al.* [138] extended the simulation method of Hernandez-Ortiz *et al.* [132] to account for a Poiseuille flow. Similar trends as reported earlier were observed, including wall accumulation and upstream swimming, as well as the reduction of accumulation with increasing flow rate. In addition, they also reported the formation of a depletion layer near the channel centerline in strong flows, in agreement with the microfluidic experiments of Rusconi *et al.* [129]. Simple scalings for the dependence of this depletion with shear rate, swimming speed and channel width were also proposed.

While these various numerical simulations have been able to reproduce the relevant features of previous experiments, a clear unified theoretical model capable of capturing and explaining all of the above effects based on conservation laws and microscopic swimmer dynamics is still lacking. In unconfined systems, much progress has been made over the last decade in the description of the behavior of active suspensions using continuum kinetic theories [29, 139, 39]. One such class of models, introduced by Saintillan and Shelley [140, 141] to explain the emergence of collective motion in semi-dilute suspensions, is based on a conservation equation for the distribution function $\Psi(\boldsymbol{x}, \boldsymbol{p}, t)$ of particle positions and orientations, in which fluxes

arise due to self-propulsion, advection and rotation by the background fluid flow, as well as diffusive processes. When coupled to a model for the fluid flow (whether externally imposed or driven by the swimmers themselves), this conservation equation can be linearized for the purpose of a stability analysis or integrated in time to investigate nonlinear dynamics. This approach, which also relates to other models developed in the context of active liquid crystals [47, 139, 48], has been very successful at elucidating the mechanisms leading to collective motion at a suspension level. However, attempts to apply such continuum kinetic theories to confined suspensions have been few and far between, in part due to the complexity of the boundary conditions that need to be enforced on the distribution function.

In this chapter, we present a simple continuum theory for the dynamics and transport of a dilute suspension of Brownian active swimmers in a pressure-driven channel flow between two parallel flat plates. To focus on the effects of steric confinement and its interaction with the flow, we neglect particle-particle and particle-wall hydrodynamic interactions entirely but incorporate a detailed treatment of the boundary conditions for the distribution function. As we show below, our theory is able to capture all the different regimes discussed above, including wall accumulation in the absence of flow, and upstream swimming, depletion at the centerline and trapping in high-shear regions when a flow is applied. We introduce the governing equations, boundary conditions and nondimensionalization in §4.2, where we also derive a simpler approximate model based on moment equations. The equilibrium distributions in the absence of flow are obtained in §4.3, where wall accumulation is seen to be accompanied by a net polarization of the particle distribution near the boundaries, and where a very simple expression is derived for the concentration profile across the channel in terms of

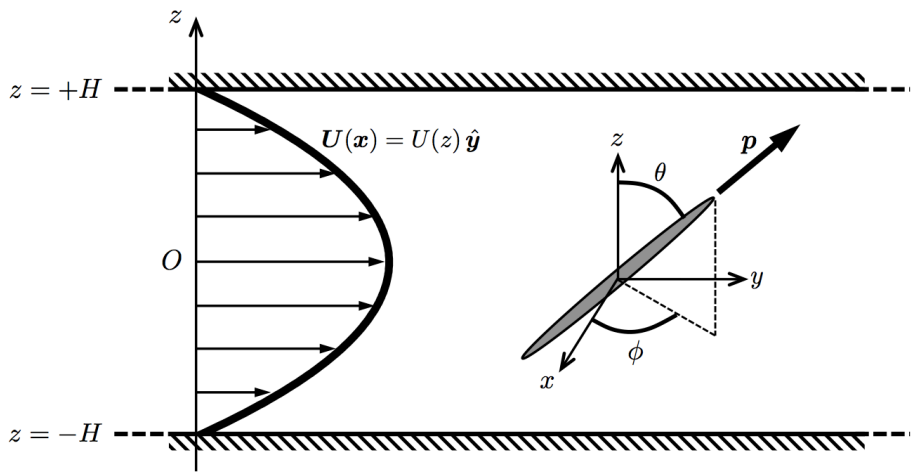

Figure 4.1: Problem definition: a dilute suspension of slender active particles with positions $\mathbf{x} = (x, y, z)$ and orientations $\mathbf{p}$ is confined between two parallel flat plates ($z = \pm H$) and subject to an imposed pressure-driven parabolic flow.

the parameters of the problem. The effects of an external Poiseuille flow are discussed in §4.4, where a numerical solution of the governing equations captures upstream swimming and shear trapping in the relevant parameter ranges, and where both effects are also explained theoretically using asymptotic analysis in the weak and strong flow regimes. We analyze the effective rheology of a dilute suspension in Poiseuille flow and its influence on the mean velocity profile at low particle concentrations in §4.5. Finally, we summarize our results in §4.6 and discuss them in the light of the recent literature in the field.

4.2 Governing equations

4.2.1 Problem definition and kinetic model

We analyze the dynamics in a dilute suspension of self-propelled slender particles confined between two parallel flat plates and placed in an externally imposed pressure-driven flow as illustrated in figure 4.1. The channel half-width is denoted by H, and is assumed to be much greater than the characteristic length L of the particles ($H/L \gg 1$), so that the finite size of the particles can be neglected. The external flow follows the parabolic Poiseuille profile

$$\mathbf{U}(\mathbf{x}) = U(z)\,\hat{\mathbf{y}} = U_m\left[1 - (z/H)^2\right]\hat{\mathbf{y}}, \tag{4.1}$$

with maximum velocity U_m at the centerline ($z = 0$). The shear rate varies linearly with position z across the channel:

$$S(z) = \frac{\mathrm{d}U}{\mathrm{d}z} = -\dot{\gamma}_w \frac{z}{H}, \tag{4.2}$$

where $\dot{\gamma}_w = 2U_m/H$ is the maximum absolute shear rate attained at the walls ($z = \pm H$).

Following previous models for active suspensions [140, 141], the configuration of the active particles is captured by the probability distribution function $\Psi(\mathbf{x}, \mathbf{p}, t)$ of finding a particle at position $\mathbf{x} = (x, y, z)$ with orientation $\mathbf{p} = (\sin\theta\cos\phi, \sin\theta\sin\phi, \cos\theta)$ at time t, where $\mathbf{p}$ also defines the direction of swimming. Conservation of particles is

expressed by the Smoluchowski equation [18]

$$\frac{\partial \Psi}{\partial t} + \nabla_x \cdot (\dot{\boldsymbol{x}}\, \Psi) + \nabla_p \cdot (\dot{\boldsymbol{p}}\, \Psi) = 0, \tag{4.3}$$

where the translational flux velocity $\dot{\mathbf{x}}$ captures self-propulsion with constant velocity V_s in the direction of $\mathbf{p}$, advection by the imposed flow, and center-of-mass diffusion with isotropic and constant diffusivity d_t:

$$\dot{\boldsymbol{x}} = V_s\, \boldsymbol{p} + \boldsymbol{U}(z) - d_t \nabla_x \ln \Psi. \tag{4.4}$$

Particle rotations are captured by the angular flux velocity $\dot{\mathbf{p}}$, which includes contributions from the imposed flow via Jeffery's equation [49, 50], and from rotational diffusion with diffusivity d_r:

$$\dot{\boldsymbol{p}} = S(z)(\hat{\mathbf{z}} \cdot \mathbf{p})(\mathbf{I} - \mathbf{pp}) \cdot \hat{\mathbf{y}} - d_r \nabla_p \ln \Psi. \tag{4.5}$$

We have assumed that the particles have a high aspect ratio, a good approximation for common motile bacteria as well as many self-propelled catalytic micro-rods. Particle-particle hydrodynamic interactions have also been neglected based on the assumption of infinite dilution; such interactions could otherwise be included via an additional disturbance velocity in the expressions for $\dot{\mathbf{x}}$ and $\dot{\mathbf{p}}$ [141]. As a result, we expect the distribution of particles to be uniform along the x and y directions, and at steady state the Smoluchowski equation (4.3) for $\Psi(\mathbf{x}, \mathbf{p}, t) = \Psi(z, \mathbf{p})$ then simplifies to

$$V_s \cos\theta \frac{\partial \Psi}{\partial z} - d_t \frac{\partial^2 \Psi}{\partial z^2} + S(z) \nabla_p \cdot \left[\cos\theta (\mathbf{I} - \mathbf{pp}) \cdot \hat{\mathbf{y}}\, \Psi \right] = d_r \nabla_p^2 \Psi. \tag{4.6}$$

This equation simply expresses the balance of self-propulsion, translational diffusion, particle alignment by the imposed flow, and rotational diffusion.

In this work, we treat the translational and rotational diffusivities d_t and d_r as independent constants, which could result from either Brownian motion or various athermal sources of noise [62, 63]. The athermal contribution to diffusion may arise due to tumbling or other fluctuations in the swimming actuation of motile micro-organisms, or from fluctuations in the chemical actuation mechanism of catalytic particles. In many active suspensions, such athermal fluctuations are in fact the dominant source of diffusion.

4.2.2 Boundary conditions

In the continuum limit, the impenetrability of the channel walls is captured by prescribing that the normal component of the translational flux be zero at both walls:

$$\hat{\mathbf{z}}\cdot\dot{\mathbf{x}} = 0 \quad \text{at} \quad z = \pm H. \tag{4.7}$$

Inserting equation (4.4) for the translational flux, this leads to a Robin boundary condition for the probability distribution function:

$$d_t \frac{\partial \Psi}{\partial z} = V_s \cos\theta \, \Psi \quad \text{at} \quad z = \pm H, \tag{4.8}$$

expressing the balance of translational diffusion and self-propulsion in the wall-normal direction. Equation (4.8) implies that particles pointing towards a wall ($\cos\theta > 0$ for the top wall at $z = +H$) incur a positive wall-normal gradient ($\partial\Psi/\partial z > 0$), whereas particles pointing away from the wall ($\cos\theta < 0$) incur a negative gradient.

This suggests that sorting of orientations should occur and lead to a net polarization towards the walls, accompanied by near-wall accumulation. These effects will indeed be confirmed in §4.3. It is important to note that the boundary condition (4.8) requires that the wall-normal swimming flux be balanced by a diffusive flux. In the complete absence of translational diffusion ($d_t = 0$), the swimming flux can no longer be balanced at the wall: this singular limit, which is ill-posed in our mean-field theory, will not be addressed here. Note also that the balance of the wall-normal fluxes hints at a length scale of $\ell_a = d_t/V_s$ for wall accumulation, as we demonstrate more quantitatively below.

Other types of boundary conditions have been considered in previous works. In particular, several studies have implemented the condition

$$\int_{\Omega} \hat{\mathbf{z}}\cdot\dot{\mathbf{x}}\,\Psi\,\mathrm{d}\mathbf{p} = 0 \quad \text{at} \quad z = \pm H, \tag{4.9}$$

where Ω denotes the unit sphere of orientation. Equation (4.9) captures the zeroth orientational moment of (4.8) and is easily implemented numerically using a reflection condition on the distribution function. It was first used by Bearon *et al.* [142] in a two-dimensional model of suspensions of gyrotactic swimmers constrained to a planar domain. Ezhilan *et al.* [22] also imposed equation (4.9) in the case of a chemotactic active suspension confined to a thin liquid film, where the primary mechanism for accumulation was chemotaxis as opposed to kinematics. In the absence of external fields, however, this boundary condition allows for a uniform isotropic solution throughout the channel and is therefore unable to capture near-wall accumulation or upstream swimming when a flow is imposed (see Appendix A for more details). Kasyap and Koch [143] also considered chemotactic active suspensions in thin films but used a

position/orientation decoupling approximation for the probability distribution function $\Psi(\mathbf{x}, \mathbf{p}, t)$, allowing them to derive a boundary condition for the number density field expressing the balance of the chemotactic and diffusive fluxes at the boundaries. To our knowledge, the only previously reported use of the boundary condition (4.8) for a confined active suspension was in the work of Elgeti and Gompper [125], whose analysis was restricted to equilibrium distributions in the absence of flow and in the limits of narrow channels or weak propulsion.

Finally, it should be kept in mind that the simple boundary condition (4.8) neglects the finite size of the particles and is therefore inaccurate very close to the walls, where steric exclusion prohibits certain particle configurations and should lead to a depletion layer as observed in experiments [117]. The implications of steric exclusion are discussed further in Appendix B, where a more detailed boundary condition is derived and enforced on the hypersurface separating allowed from forbidden configurations [144, 145, 146]. As we show there, the effects of steric exclusion are weak in wide channels ($H/L \gg 1$) such as the ones considered in this work.

4.2.3 Dimensional analysis and scaling

Dimensional analysis of the governing equations reveals three dimensionless groups:

$$Pe_s = \frac{V_s}{2d_r H}, \quad Pe_f = \frac{\dot{\gamma}_w}{d_r}, \quad \Lambda = \frac{d_t d_r}{V_s^2}. \tag{4.10}$$

The first parameter Pe_s, or swimming Péclet number, can be interpreted as the ratio of the characteristic timescale for a particle to lose memory of its orientation due to rotational diffusion over the time it takes it to swim across the channel width. Equivalently, it is also the ratio of the persistence length of particle trajectories

($\ell_p = V_s/d_r$) over the channel width ($2H$). The second parameter Pe_f, or flow Péclet number, compares the same diffusive timescale to the characteristic time for a particle to align under the imposed velocity gradient. The third parameter Λ relates the translational and rotational diffusivities to the swimming speed and is a fixed constant for a given particle type. It can be interpreted as an inverse measure of the strength of propulsion of a swimmer with respect to fluctuations, and the limits of $\Lambda \to 0$ and $\Lambda \to \infty$ describe the strong and weak propulsion cases, respectively. When Λ is held constant, Pe_s also reduces to an inverse measure of confinement, with $Pe_s \to 0$ and $Pe_s \to \infty$ describing the limits of weak and strong confinement, respectively.

In the following, we nondimensionalize the governing equations using the characteristic time, length and velocity scales

$$t_c = d_r^{-1}, \quad \ell_c = H, \quad v_c = H d_r, \tag{4.11}$$

and also normalize the distribution function Ψ by the mean number density n defined as

$$n = \frac{1}{2H} \int_{-H}^{H} \int_{\Omega} \Psi(z, \mathbf{p}) \, \mathrm{d}\mathbf{p} \, \mathrm{d}z. \tag{4.12}$$

After nondimensionalization, the conservation equation (4.6) becomes

$$Pe_s \cos\theta \frac{\partial \Psi}{\partial z} - 2\Lambda Pe_s^2 \frac{\partial^2 \Psi}{\partial z^2} + \frac{Pe_f}{2} S(z) \nabla_p \cdot [\cos\theta (\mathbf{I} - \mathbf{pp}) \cdot \hat{\mathbf{y}} \, \Psi] = \frac{1}{2} \nabla_p^2 \Psi, \tag{4.13}$$

where the dimensionless shear rate profile is simply $S(z) = -z$. The boundary

condition (4.8) also becomes

$$\frac{\partial \Psi}{\partial z} = \frac{1}{2\Lambda P e_s} \cos\theta \, \Psi \quad \text{at} \quad z = \pm 1. \tag{4.14}$$

Note that the choice of H for the characteristic length scale is convenient as it sets the positions of the boundaries to $z = \pm 1$ in the dimensionless system. However, we will see below that alternate length scales are more judiciously chosen in certain limits due to the presence of boundary layers.

4.2.4 Orientational moment equations

Equation (4.13), together with boundary condition (4.14), cannot be solved analytically in general. While a numerical solution is possible as we show below, analytical progress can still be made in terms of orientational moments of the distribution function [29]. More precisely, we introduce the zeroth, first, and second moments of $\Psi(z, \mathbf{p})$ as

$$c(z) = \langle 1 \rangle, \quad \mathbf{m}(z) = \langle \mathbf{p} \rangle, \quad \mathbf{D}(z) = \langle \mathbf{pp} - \mathbf{I}/3 \rangle, \tag{4.15}$$

where the brackets $\langle \cdot \rangle$ denote the orientational average

$$\langle h(\mathbf{p}) \rangle = \int_\Omega h(\mathbf{p}) \Psi(z, \mathbf{p}) \, \mathrm{d}\mathbf{p}. \tag{4.16}$$

The zeroth moment $c(z)$ corresponds to the local concentration of particles. The next two moments are directly related to the polarization vector $\mathbf{P}(z)$ and to the nematic order parameter tensor $\mathbf{Q}(z)$ commonly used in the description of liquid-crystalline

systems [139] as

$$\mathbf{m}(z) = c(z)\mathbf{P}(z), \quad \mathbf{D}(z) = c(z)\mathbf{Q}(z). \tag{4.17}$$

Knowledge of these as well as higher moments also allows one to recover the full distribution function as

$$\Psi(z, \mathbf{p}) = \frac{1}{4\pi}\, c(z) + \frac{3}{4\pi}\, \mathbf{p}\cdot\mathbf{m}(z) + \frac{15}{8\pi}\, \mathbf{pp} : \mathbf{D}(z) + ..., \tag{4.18}$$

which can also be interpreted as a spectral expansion of $\Psi(z, \mathbf{p})$ on the basis of spherical harmonics. Near isotropy this expansion converges rapidly, which justifies truncation after a few terms. If only the first three terms corresponding to c, $\mathbf{m}$ and $\mathbf{D}$ are retained, a closed system of equations can be derived for these variables by taking moments of the conservation equation (4.13) [47, 29].

In the problem of interest to us here, symmetries dictate that the only non-zero components of $\mathbf{m}$ and $\mathbf{D}$ are m_z and $D_{zz} = -2D_{xx} = -2D_{yy}$ in the absence of flow. When a flow is applied in the y direction, m_y and $D_{yz} = D_{zy}$ are also expected to become non-zero, and D_{yy} need no longer be equal to D_{xx}. The governing equations for these variables can be obtained as

$$Pe_s\frac{\mathrm{d}m_z}{\mathrm{d}z} - 2\Lambda Pe_s^2\frac{\mathrm{d}^2c}{\mathrm{d}z^2} = 0, \tag{4.19}$$

$$Pe_s\frac{\mathrm{d}D_{zz}}{\mathrm{d}z} - 2\Lambda Pe_s^2\frac{\mathrm{d}^2m_z}{\mathrm{d}z^2} + \left(\frac{1}{6\Lambda}+1\right)m_z = -\frac{1}{10}Pe_fS(z)m_y, \tag{4.20}$$

$$Pe_s\frac{\mathrm{d}D_{yz}}{\mathrm{d}z} - 2\Lambda Pe_s^2\frac{\mathrm{d}^2m_y}{\mathrm{d}z^2} + m_y = \frac{2}{5}Pe_fS(z)m_z, \tag{4.21}$$

$$\frac{4}{15}Pe_s\frac{\mathrm{d}m_z}{\mathrm{d}z} - 2\Lambda Pe_s^2\frac{\mathrm{d}^2D_{zz}}{\mathrm{d}z^2} + 3D_{zz} = \frac{4}{7}Pe_fS(z)D_{yz}, \tag{4.22}$$

$$-\frac{2}{15}Pe_s\frac{\mathrm{d}m_z}{\mathrm{d}z} - 2\Lambda Pe_s^2\frac{\mathrm{d}^2D_{yy}}{\mathrm{d}z^2} + 3D_{yy} = -\frac{3}{7}Pe_fS(z)D_{yz}, \tag{4.23}$$

$$\frac{1}{5}Pe_s\frac{\mathrm{d}m_y}{\mathrm{d}z} - 2\Lambda Pe_s^2\frac{\mathrm{d}^2D_{yz}}{\mathrm{d}z^2} + 3D_{yz} = Pe_fS(z)\left(\frac{1}{10}c + \frac{5}{14}D_{zz} - \frac{2}{7}D_{yy}\right). \tag{4.24}$$

No equation is needed for D_{xx}, which can simply be deduced from D_{yy} and D_{zz} using the tracelessness of $\mathbf{D}$. In each of these equations, the first term on the left-hand side arises due to self-propulsion, the second term captures translational diffusion, and the third term rotational diffusion. Terms on the right-hand side arise from the externally applied pressure-driven flow and vanish in the absence of flow ($Pe_f = 0$).

Boundary conditions for these variables are also readily obtained by taking moments of equation (4.14), yielding

$$\frac{\mathrm{d}c}{\mathrm{d}z} = \frac{1}{2\Lambda Pe_s}m_z, \tag{4.25}$$

$$\frac{\mathrm{d}m_z}{\mathrm{d}z} = \frac{1}{2\Lambda Pe_s}\left(D_{zz}+\frac{1}{3}c\right), \quad \frac{\mathrm{d}m_y}{\mathrm{d}z} = \frac{1}{2\Lambda Pe_s}D_{yz}, \tag{4.26}$$

$$\frac{\mathrm{d}D_{zz}}{\mathrm{d}z} = \frac{2}{15\Lambda Pe_s}m_z, \quad \frac{\mathrm{d}D_{yy}}{\mathrm{d}z} = -\frac{1}{15\Lambda Pe_s}m_z, \quad \frac{\mathrm{d}D_{yz}}{\mathrm{d}z} = \frac{1}{10\Lambda Pe_s}m_y, \tag{4.27}$$

all to be enforced at $z = \pm 1$. For symmetry reasons, we expect c, m_y, D_{yy}, D_{zz} to be even functions of z, whereas m_z and D_{yz} are expected to be odd functions. While we consider rotational diffusion as the only orientation decorrelation mechanism

in this work, all the derivations shown here can be easily modified to account for run-and-tumble dynamics instead by modifying numerical prefactors in the third terms on the left-hand sides of equations (4.22)–(4.24).

Integrating equation (4.19) and making use of the boundary condition (4.25) easily shows that (4.19) can be replaced by

$$m_z - 2\Lambda Pe_s \frac{\mathrm{d}c}{\mathrm{d}z} = 0 \tag{4.28}$$

at every point in the channel, underlining the direct relation between transverse polarization and concentration gradients. We also note that the normalization condition (4.12) on the distribution function translates into an integral condition on the concentration field expressing conservation of the total particle number:

$$\int_{-1}^{1} c(z)\,\mathrm{d}z = 2. \tag{4.29}$$

As we discuss next, solution of the system (4.19)–(4.24) subject to the boundary conditions (4.25)–(4.27) and to the integral constraint (4.29) is possible under certain assumptions, and provides results that are in excellent quantitative agreement with the full numerical solution of the Smoluchowski equation (4.13) over a wide range of values of the Péclet numbers.

4.3 Equilibrium distributions in the absence of flow

We first analyze the case of no external flow ($Pe_f = 0$), where we expect the boundary condition (4.14) to lead to near-wall accumulation and polarization as a

result of self-propulsion. In this case, the full governing equation (4.13) simplifies to

$$Pe_s \left(\cos\theta \frac{\partial \Psi}{\partial z} - 2\Lambda Pe_s \frac{\partial^2 \Psi}{\partial z^2} \right) = \frac{1}{2} \nabla_p^2 \Psi, \tag{4.30}$$

subject to condition (4.14) at the walls. We note some interesting mathematical properties of these equations. First, taking the cross-sectional average of equation (4.30) yields

$$\nabla_p^2 \left(\int_{-1}^{1} \Psi \, \mathrm{d}z \right) = 0, \tag{4.31}$$

which implies that the gap-averaged orientation distribution is isotropic in the absence of flow. Using the conservation constraint (4.29), we obtain

$$\int_{-1}^{1} \Psi \, \mathrm{d}z = \frac{1}{2\pi}, \tag{4.32}$$

which also implies that the first and higher-order moments all average to zero across the channel width when there is no flow.

It is also easily seen that the uniform and isotropic distribution $\Psi = 1/4\pi$ is an exact solution of equation (4.30) for all parameter values, though it violates the boundary condition (4.14) when $\Lambda \neq \infty$. Inspection of the equations shows that, in the limit of $\Lambda Pe_s = d_t/2V_s \to 0$, there is a loss of the higher derivative in both the governing equation and the boundary condition. This singular limit suggests the existence of an accumulation layer near the channel walls where the distribution departs from the uniform isotropic state. Inside this boundary layer, the effects of self-propulsion must be balanced by translational diffusion, notwithstanding the small value of ΛPe_s. Rescaling the governing equation inside the boundary layer, however, does not lead to analytical simplifications for finite Λ, so we turn to the simplified

moment equations for further characterization of particle distributions near the walls in §4.3.1, where a simple analytical solution is derived together with a scaling for the thickness of the accumulation layer. We then describe how the limits of strong and weak propulsion can be addressed using asymptotic expansions in §4.3.2 and §4.3.3.

4.3.1 Theory based on moment equations

In the absence of flow, the moment equations derived in §4.2.4 only involve c, m_z and D_{zz}, and simplify to:

$$m_z - 2\Lambda Pe_s \frac{\mathrm{d}c}{\mathrm{d}z} = 0, \tag{4.33}$$

$$Pe_s \frac{\mathrm{d}D_{zz}}{\mathrm{d}z} - 2\Lambda Pe_s^2 \frac{\mathrm{d}^2 m_z}{\mathrm{d}z^2} + \left(\frac{1}{6\Lambda} + 1\right) m_z = 0, \tag{4.34}$$

$$\frac{4}{15} Pe_s \frac{\mathrm{d}m_z}{\mathrm{d}z} - 2\Lambda Pe_s^2 \frac{\mathrm{d}^2 D_{zz}}{\mathrm{d}z^2} + 3D_{zz} = 0, \tag{4.35}$$

subject to the integral constraint (4.29) and to the boundary conditions

$$\frac{\mathrm{d}m_z}{\mathrm{d}z} = \frac{1}{2\Lambda Pe_s}\left(D_{zz} + \frac{1}{3}c\right), \quad \frac{\mathrm{d}D_{zz}}{\mathrm{d}z} = \frac{2}{15\Lambda Pe_s} m_z \quad \text{at } z = \pm 1. \tag{4.36}$$

Using this set of equations, we first proceed to derive a relation between the values of the concentration and wall-normal polarization at the boundaries. First, we integrate equation (4.35) across the channel width and use the second boundary condition in (4.36) to arrive at

$$\int_{-1}^{1} D_{zz}(z)\,\mathrm{d}z = 0. \tag{4.37}$$

Now, combining equations (4.33) and (4.34), integrating from z to 1 and making use

of the first boundary condition gives

$$D_{zz} - 2\Lambda Pe_s \frac{\mathrm{d}m_z}{\mathrm{d}z} + \frac{6\Lambda + 1}{3} c = 2\Lambda\, c(1). \tag{4.38}$$

This relation can be integrated once more across the channel width. Using condition (4.37) together with the parity properties of c and m_z, this simplifies to

$$c(\pm 1) = \left(1 + \frac{1}{6\Lambda}\right) \mp Pe_s m_z(\pm 1), \tag{4.39}$$

providing a simple relation between concentration and polarization at the walls. Inserting this relation into the first condition in (4.36) yields a new set of boundary conditions that does not involve the concentration:

$$\frac{\mathrm{d}m_z}{\mathrm{d}z} = \frac{1}{2\Lambda Pe_s}\left(D_{zz} + \frac{6\Lambda + 1}{18\Lambda}\right) \mp \frac{1}{6\Lambda} m_z, \quad \frac{\mathrm{d}D_{zz}}{\mathrm{d}z} = \frac{2}{15\Lambda Pe_s} m_z \quad \text{at } z = \pm 1. \tag{4.40}$$

Equations (4.34)–(4.35), together with these boundary conditions, form a coupled system of second-order linear ordinary differential equations for m_z and D_{zz} that can be solved analytically. Once these variables are known, the concentration profile is easily obtained from the polarization by integration of (4.33) along with condition (4.39).

Solving these equations yields complicated expressions for c, m_z and D_{zz} that are omitted here for brevity. The profiles, which are illustrated in figure 4.2 and will be discussed in more detail below, reveal one important finding: while a significant wall-normal polarization exists in the near-wall region, nematic alignment is relatively weak throughout the channel for $\Lambda \gtrsim 0.1$. This suggests seeking a yet simpler solution

that neglects nematic order altogether. If the moment expansion (4.18) is truncated after two terms, the equations for c and m_z simplify to

$$m_z - 2\Lambda Pe_s \frac{\mathrm{d}c}{\mathrm{d}z} = 0, \quad -2\Lambda Pe_s^2 \frac{\mathrm{d}^2 m_z}{\mathrm{d}z^2} + \left(\frac{1}{6\Lambda} + 1\right) m_z = 0, \tag{4.41}$$

subject to the conditions

$$\frac{\mathrm{d}m_z}{\mathrm{d}z} = \frac{c}{6\Lambda Pe_s} \quad \text{at} \quad z = \pm 1, \quad \text{and} \quad \int_{-1}^{1} c(z)\,\mathrm{d}z = 2. \tag{4.42}$$

Solving these equations is straightforward and provides elegant expressions for the concentration and polarization profiles:

$$c(z) = \frac{B\left[6\Lambda \cosh B + \cosh Bz\right]}{6\Lambda B \cosh B + \sinh B}, \tag{4.43}$$

$$m_z(z) = \frac{6\Lambda Pe_s B^2 \sinh Bz}{3\left(6\Lambda B \cosh B + \sinh B\right)}, \tag{4.44}$$

where

$$B^{-1} = \Lambda Pe_s \sqrt{\frac{12}{1 + 6\Lambda}} \tag{4.45}$$

defines the dimensionless decay length of the excess concentration at the walls. In dimensional terms, this decay length is given by $B^{-1}H = \ell_a\sqrt{3/(1+6\Lambda)}$ where $\ell_a = d_t/V_s$. In the limit of strong propulsion ($\Lambda \ll 1$), it simplifies to $\sqrt{3}\,\ell_a$. In the limit of weak propulsion ($\Lambda \gg 1$), it becomes $\ell_d/\sqrt{2}$ where $\ell_d = \sqrt{d_t/d_r}$ is a purely diffusive length scale. For Brownian particles, ℓ_d is typically of the order of the particle size L, though this may not be the case for active particles subject to athermal sources

of noise. Next, we focus more precisely on these two limits by rescaling the governing equations with the appropriate scales identified here.

4.3.2 Strong propulsion limit: $\Lambda \to 0$

In the limit of small Λ, the above discussion suggests rescaling the Smoluchowski equation using the accumulation length scale ℓ_a, yielding

$$\cos\theta \frac{\partial \Psi}{\partial z} - \frac{\partial^2 \Psi}{\partial z^2} = \Lambda \nabla_p^2 \Psi, \tag{4.46}$$

subject to the boundary condition

$$\frac{\partial \Psi}{\partial z} = \cos\theta \, \Psi \quad \text{at} \quad z = \pm H^*. \tag{4.47}$$

Here, $H^* = (2\Lambda Pe_s)^{-1}$ is the channel half-height rescaled by the accumulation length scale ℓ_a. The gap-averaged isotropy constraint is now expressed as

$$\int_{-H^*}^{H^*} \Psi \mathrm{d}z = \frac{H^*}{2\pi}. \tag{4.48}$$

The leading-order solution corresponding to $\Lambda = 0$, which was previously obtained by Elgeti and Gompper [125], is written

$$\Psi^{(0)}(z,\theta) = \frac{H^* \cos\theta}{4\pi \sinh\left(H^* \cos\theta\right)} \exp\left(z \cos\theta\right), \tag{4.49}$$

and it is easily seen that it satisfies zero wall-normal flux pointwise throughout the channel. In particular, it shows that wall accumulation is possible even in the absence of rotational diffusion and is simply a result of a coupling between self-propulsion,

translational diffusion and confinement. This solution can then be corrected to order $O(\Lambda)$ by solving the first-order inhomogeneous equation

$$\cos\theta\,\Psi^{(1)}(z,\theta) - \frac{\partial\Psi^{(1)}}{\partial z} = \nabla_p^2 \int_{-H^*}^{z} \Psi^{(0)}(z,\theta)\,\mathrm{d}z. \tag{4.50}$$

subject to boundary condition (4.47). An exact analytical solution to this equation can again be obtained but is cumbersome and omitted here for brevity.

4.3.3 Weak propulsion limit: $\Lambda \to \infty$

In the limit of large Λ, the Smoluchowski equation is rescaled using the diffusive length scale ℓ_d as

$$\frac{1}{\sqrt{\Lambda}}\cos\theta\frac{\partial\Psi}{\partial z} - \frac{\partial^2\Psi}{\partial z^2} = \nabla_p^2\Psi, \tag{4.51}$$

subject to

$$\frac{\partial\Psi}{\partial z} = \frac{1}{\sqrt{\Lambda}}\cos\theta\,\Psi \quad \text{at} \quad z = \pm H^{\dagger}. \tag{4.52}$$

where $H^{\dagger} = (2\sqrt{\Lambda}Pe_s)^{-1}$. The leading-order solution in the limit of $\Lambda \to \infty$ is uniform and isotropic and corresponds to the case of a passive particle: $\Psi^{(0)}(z,\theta) = 1/4\pi$. It can be corrected asymptotically using a regular perturbation expansion in powers of $\Lambda^{-1/2}$:

$$\Psi\left(z,\theta\right) = \Psi^{(0)}\left(z,\theta\right) + \Lambda^{-1/2}\,\Psi^{(1)}\left(z,\theta\right) + \Lambda^{-1}\,\Psi^{(2)}\left(z,\theta\right) + ... \tag{4.53}$$

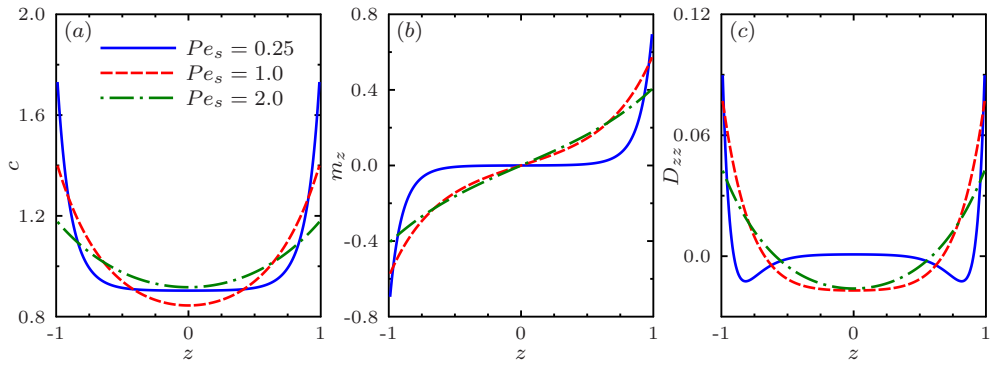

Figure 4.2: (Color online) Equilibrium distributions in the absence of flow and for various swimming Péclet numbers Pe_s (with $\Lambda = 1/6$), obtained by numerical solution of equation (4.13) using finite volumes: (a) concentration c, (b) wall-normal polarization m_z, and (c) wall-normal nematic order parameter D_{zz}.

Recursively solving for higher-order terms yields

$$\Psi^{(1)}(z,\theta) = \frac{3}{4\pi\sqrt{2}\cosh\left(\sqrt{2}H^{\dagger}\right)}\sinh(\sqrt{2}z)\cos\theta, \tag{4.54}$$

$$\Psi^{(2)}(z,\theta) = \left[-\frac{1}{15}\frac{\cosh\sqrt{2}z}{\cosh(\sqrt{2}H^{\dagger})} + \frac{\tanh(\sqrt{2}H^{\dagger})}{5\sqrt{3}}\frac{\cosh(\sqrt{6}z)}{\sinh(\sqrt{6}H^{\dagger})}\right]\left(\cos^2\theta - \frac{1}{3}\right), \tag{4.55}$$

which both satisfy the appropriate boundary conditions. Quite remarkably, it can be seen that successive terms in the expansion (4.53) correspond to successive orientational moments of the distribution function in equation (4.18), with $\Psi^{(1)}$ and $\Psi^{(2)}$ describing the polarization and nematic order, respectively.

4.3.4 Numerical results and discussion

Figure 4.2 shows the full numerical solution for the concentration c, wall-normal polarization m_z and nematic order parameter D_{zz} obtained by finite-volume solution of the Smoluchowski equation (4.13) as described in Appendix B. Here, we fix the value of Λ and focus on the effect of Pe_s, which an inverse measure of confinement.

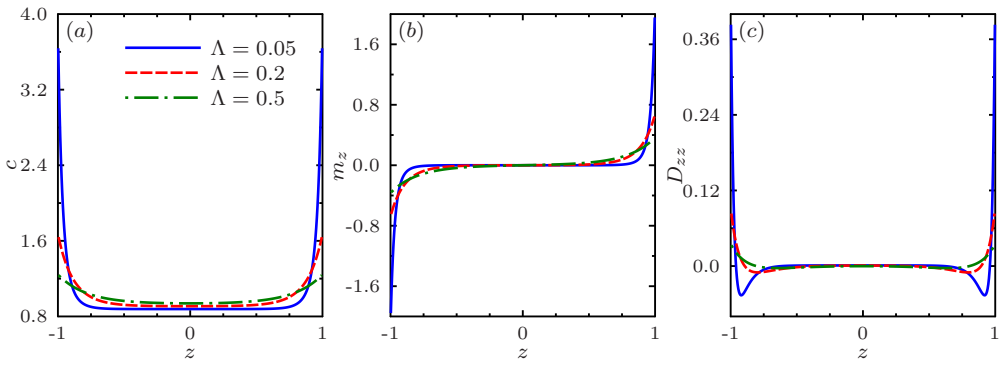

Figure 4.3: (Color online) Equilibrium distributions in the absence of flow and for various values of Λ (with $Pe_s = 0.25$), obtained by numerical solution of equation (4.13) using finite volumes: (a) concentration c, (b) wall-normal polarization m_z, and (c) wall-normal nematic order parameter D_{zz}. Solutions based on moment equations are nearly identical, as illustrated in figure 4.4.

The concentration profiles shown in figure 4.2(a) exhibit significant accumulation of particles near the boundaries, especially at low values of Pe_s. As anticipated, this accumulation is accompanied by polarization towards the boundaries as a direct consequence of the boundary condition (4.25), as well as by a weak nematic alignment. As Pe_s increases, the spatial heterogeneity and anisotropy near the walls progressively extend through the entire channel as the two boundary layers thicken and eventually merge. Further increase in the swimming Péclet number leads to a flattening of the profiles, which is especially significant when $Pe_s > 1$. This flattening is a direct consequence of the scaling of translational diffusion with Pe_s^2 in equation (4.13), causing it to overwhelm self-propulsion which scales with Pe_s. The influence of Λ is illustrated in figure 4.3, where it is seen to be similar to that of Pe_s: increasing Λ leads to a thickening of the boundary layers and flattening of the concentration profiles, again due to the scaling of translational diffusion with Λ in equation (4.13).

The finite-volume numerical solution of the full conservation equation (4.13) is in excellent quantitative agreement with the two- and three-moment approximations

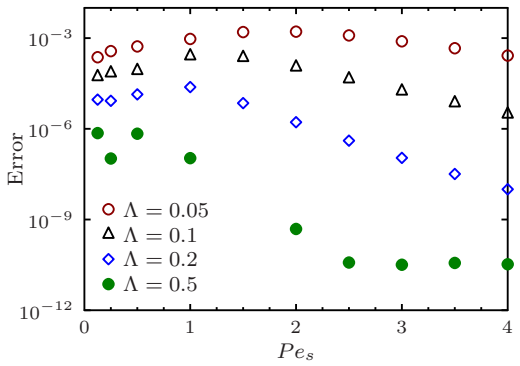

Figure 4.4: (Color online) The relative rms error for the concentration between the finite-volume solution and the two-moment analytical solution (4.43) for different values of Λ. Solutions based on moment equations are nearly identical to the finite-volume solution for sufficiently large values of Λ.

derived previously, which are not shown in figure 4.2 as they are nearly indistinguishable over the entire channel width as long as $\Lambda \gtrsim 0.1$. The rms error between the two-moment solution of equation (4.33) and the finite-volume solution is indeed plotted in figure 4.4, where it remains below 10^{-3} for all values of Pe_s considered here when $\Lambda \gtrsim 0.1$. This finding may seem quite surprising considering the strong approximation made when truncating expansion (4.18) after only two terms, and strongly validates the use of approximate moment equations such as (4.19)–(4.24) when modeling active suspensions, at least in the absence of flow. For very small values of Λ, however, nematic alignment at the walls becomes significant as seen in figure 4.3(c), so that the nematic tensor can no longer be neglected and the two-moment solution loses its accuracy; in this case, the alternate expressions derived in the small Λ limit in §4.3.2 can be used instead.

The influence of Pe_s on wall accumulation is analyzed more quantitatively in figure 4.5, showing the values of the wall concentration $c(\pm 1)$, the boundary layer thickness δ defined as the distance from the wall where $c(1-\delta) = 1$, and the fraction

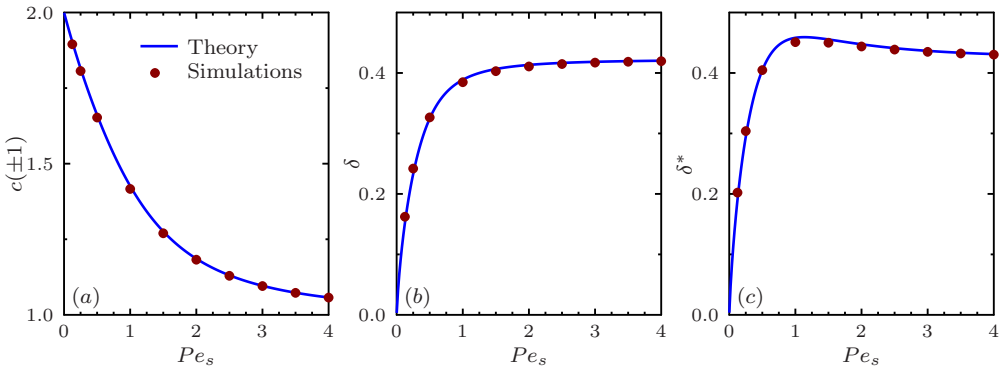

Figure 4.5: (Color online) Wall accumulation in the absence of flow as a function of Pe_s (at $\Lambda = 1/6$): (a) concentration $c(\pm 1)$ at the walls; (b) boundary layer thickness δ, defined as the distance from the wall where $c(1-\delta) = 1$; (c) fraction δ^* of particles inside the boundary layer, defined as the integral of $c(z)$ over the boundary layer thickness. The solid line shows the theoretical prediction based on the two-moment solution (4.43), and symbols show full numerical results using finite volumes.

δ^* of particles inside the boundary layer defined as

$$\delta^* = \int_{1-\delta}^{1} c(z)\,\mathrm{d}z. \tag{4.56}$$

Analytical expressions for these quantities can be derived from the two-moment solution (4.43). In particular, the boundary layer thickness is obtained as

$$\delta(Pe_s) = 1 - \frac{1}{B}\log\left\{\frac{\sinh B}{B} \pm \left[\left(\frac{\sinh B}{B}\right)^2 - 1\right]^{1/2}\right\}, \tag{4.57}$$

which has the two limits

$$\lim_{Pe_s\to 0}\delta(Pe_s) = 0 \quad \text{and} \quad \lim_{Pe_s\to\infty}\delta(Pe_s) = 1 - \frac{1}{\sqrt{3}}. \tag{4.58}$$

Similarly, the fraction of particles inside the boundary layer is given by

$$\delta^*(Pe_s) = 1 - \frac{6\Lambda B\,(1-\delta)\cosh B + \sinh\left[B\,(1-\delta)\right]}{6\Lambda B\cosh B + \sinh B}, \tag{4.59}$$

and has the same limits as $\delta(Pe_s)$ when $Pe_s \to 0$ and ∞.

As shown in figure 4.5(a), the wall concentration reaches its maximum in the limit of $Pe_s \to 0$, and steadily decreases towards 1 as Pe_s increases due to the smoothing effect of translational diffusion. This is accompanied by an increase in the boundary layer thickness δ, which asymptotes at high values of Pe_s. The fraction δ^* of particles near the walls shows a similar trend, but interestingly also exhibits a weak maximum for $Pe_s \approx 1.135$ when wall accumulation due to self-propulsion and translational diffusion are of similar magnitudes; at this value of Pe_s, $\delta^* \approx 0.46$ corresponding to nearly half the particles being trapped near the walls. As previously observed in figure 4.4, excellent agreement is obtained between the two-moment approximation and the numerical solution of the full governing equations.

4.4 Equilibrium distributions and transport in flow

4.4.1 Weak-flow limit: regular asymptotic expansion

We now proceed to analyze the effects of an external pressure-driven flow, first focusing on the case of a weak flow for which $Pe_f \ll 1$. Since the parameter Λ is fixed for a given type of swimmers, we keep it constant in the rest of the chapter and focus on the effects of Pe_s and Pe_f. The form of the governing equations suggests seeking an approximate solution as a regular expansion of the moments of the distribution

function in powers of Pe_f. The leading-order $O(Pe_f^0)$ solution corresponding to the absence of flow was previously calculated in §4.3. It is henceforth denoted by $c^{(0)}$, $\mathbf{m}^{(0)}$, $\mathbf{D}^{(0)}$, and we recall that $m_y^{(0)} = D_{yz}^{(0)} = 0$. Inspection of the moment equations (4.19)–(4.24) reveals that the interaction of the applied shear profile $S(z)$ with this leading-order solution perturbs m_y and D_{yz} at order $O(Pe_f)$. On the other hand, c, m_z, D_{zz} and D_{yy} are only perturbed by the flow at order $O(Pe_f^2)$ due to its interaction with m_y and D_{yz}. Based on these observations, we expand the solution as

$$c(z) = c^{(0)}(z) + Pe_f^2\, c^{(2)}(z) + O(Pe_f^3), \tag{4.60}$$

$$m_z(z) = m_z^{(0)}(z) + Pe_f^2 m_z^{(2)}(z) + O(Pe_f^3), \tag{4.61}$$

$$D_{zz}(z) = D_{zz}^{(0)}(z) + Pe_f^2 D_{zz}^{(2)}(z) + O(Pe_f^3), \tag{4.62}$$

$$D_{yy}(z) = D_{yy}^{(0)}(z) + Pe_f^2 D_{yy}^{(2)}(z) + O(Pe_f^3), \tag{4.63}$$

$$m_y(z) = Pe_f m_y^{(1)}(z) + O(Pe_f^3), \tag{4.64}$$

$$D_{yz}(z) = Pe_f D_{yz}^{(1)}(z) + O(Pe_f^3). \tag{4.65}$$

We focus here on determining the leading-order corrections to m_y and D_{yz}, which capture streamwise polarization and nematic alignment with the applied shear, respectively. The $O(Pe_f)$ moment equations are written

$$Pe_s \frac{\mathrm{d}D_{yz}^{(1)}}{\mathrm{d}z} - 2\Lambda Pe_s^2 \frac{\mathrm{d}^2 m_y^{(1)}}{\mathrm{d}z^2} + m_y^{(1)} = \frac{2}{5} S(z) m_z^{(0)}, \tag{4.66}$$

$$\frac{Pe_s}{5} \frac{\mathrm{d}m_y^{(1)}}{\mathrm{d}z} - 2\Lambda Pe_s^2 \frac{\mathrm{d}^2 D_{yz}^{(1)}}{\mathrm{d}z^2} + 3D_{yz}^{(1)} = S(z) \left(\frac{1}{10} c^{(0)} + \frac{1}{2} D_{zz}^{(0)} \right), \tag{4.67}$$

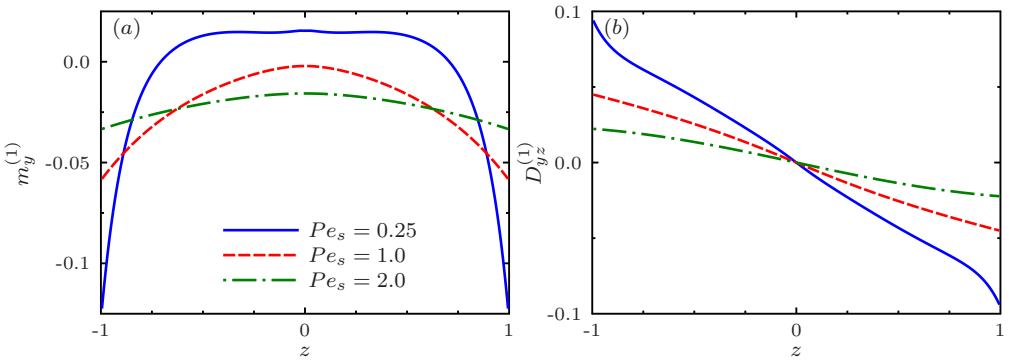

Figure 4.6: (Color online) Effect of a weak applied flow: leading-order $O(Pe_f)$ corrections of (a) streamwise polarization m_y and (b) shear nematic alignment D_{yz} for different values of the swimming Péclet number, obtained by numerical solution of equations (4.66)–(4.68).

subject to boundary conditions

$$\frac{\mathrm{d}m_y^{(1)}}{\mathrm{d}z} = \frac{1}{2\Lambda Pe_s} D_{yz}^{(1)}, \quad \frac{\mathrm{d}D_{yz}^{(1)}}{\mathrm{d}z} = \frac{1}{10\Lambda Pe_s} m_y^{(1)} \quad \text{at} \;\; z = \pm 1. \tag{4.68}$$

Note that the forcing terms on the right-hand sides of equations (4.66)–(4.67) are known and capture the interaction of the local shear rate $S(z)$ with the equilibrium distributions in the absence of flow.

A numerical solution of equations (4.66)–(4.68) is plotted in figure 4.6 for different values of Pe_s. At low values of the swimming Péclet number, figure 4.6(a) shows an upstream polarization ($m_y < 0$) near the boundaries, and a downstream polarization ($m_y > 0$) near the center of the channel. The upstream polarization, which has previously been observed in both experiments and simulations and is at the origin of the well-known phenomenon of upstream swimming, is a simple and direct consequence of the shear rotation of the particles near the wall, which tend to point towards the walls in the absence of flow as explained in §4.3. This interaction is encapsulated in the right-hand side in equation (4.66). The downstream polarization

near the centerline is a more subtle effect arising from self-propulsion through the first term on the left-hand side of (4.66). As Pe_s increases and the boundary layers thicken, upstream swimming becomes weaker near the boundaries due to the weaker wall-normal polarization there; however, m_y is also observed to become negative across the entire channel due to the thickening of the polarized boundary layers into the bulk of the channel as previously shown in figure 4.2(b).

The mean streamwise swimming velocity $\overline{V}_y$ of the active particles with respect to the imposed flow can be defined in terms of the polarization as

$$\overline{V}_y = \frac{1}{2}\int_{-1}^{1} Pe_s\, m_y(z)\,\mathrm{d}z = \frac{Pe_s Pe_f}{2}\int_{-1}^{1} m_y^{(1)}(z)\,\mathrm{d}z = Pe_s Pe_f\,\overline{m}_y^{(1)}. \tag{4.69}$$

An expression for $\overline{m}_y^{(1)}$ can be derived based on the moment equations. We first take the cross-sectional average of equation (4.66) and use the first boundary condition to obtain

$$\overline{m}_y^{(1)} = -\frac{1}{5}\int_{-1}^{1} z\, m_z^{(0)}(z)\,\mathrm{d}z. \tag{4.70}$$

Since $m_z^{(0)}$ is an odd function of z with $m_z^{(0)}(z) \geq 0$ for $z \geq 0$, the integrand on the right-hand side is always positive across the channel, and therefore the mean upstream polarization is negative: $\overline{m}_y^{(1)} < 0$. This also implies that $\overline{V}_y < 0$, i.e., there is a net upstream flux of particles against the mean flow for all values of Λ and Pe_s in the weak flow limit. Using equation (4.34) for $m_z^{(0)}(z)$, we can rewrite the right-hand side as

$$\overline{m}_y^{(1)} = -\frac{1}{5\left(\frac{1}{6\Lambda}+1\right)}\left[2\Lambda Pe_s^2\int_{-1}^{1} z\,\frac{\mathrm{d}^2 m_z^{(0)}}{\mathrm{d}z^2}\,\mathrm{d}z - Pe_s\int_{-1}^{1} z\,\frac{\mathrm{d}D_{zz}^{(0)}}{\mathrm{d}z}\,\mathrm{d}z\right]. \tag{4.71}$$

After integration by parts and application of the boundary condition on $m_z^{(0)}(z)$ together with equation (4.37), this simplifies to

$$\overline{m}_y^{(1)} = -\frac{2Pe_s}{15\left(\frac{1}{6\Lambda}+1\right)}\left[c^{(0)}(1) - 6\Lambda Pe_s\, m_z^{(0)}(1)\right]. \tag{4.72}$$

Recalling that $c^{(0)}(1)$ and $m_z^{(0)}(1)$ are related via equation (4.39), we obtain two expressions for the mean streamwise swimming velocity in terms of either the concentration or wall-normal polarization at the top wall in the absence of flow:

$$\overline{V}_y = -\frac{4\Lambda}{5}Pe_s^2 Pe_f\left[c^{(0)}(1) - 1\right] = -\frac{2}{15}Pe_s^2 Pe_f\left[1 - 6\Lambda Pe_s m_z^{(0)}(1)\right]. \tag{4.73}$$

Since the concentration at the wall in the absence of flow always exceeds the mean when $Pe_s > 0$, equation (4.73) again confirms that $\overline{V}_y < 0$.If we further make use of the simplified two-moment analytical solution (4.43) for the concentration profile, we arrive at a simple expression for the mean upstream velocity in terms of the swimming and flow Péclet numbers:

$$\overline{V}_y = -\frac{4\Lambda}{5}Pe_s^2 Pe_f\left[\frac{B\cosh B - \sinh B}{6\Lambda B\cosh B + \sinh B}\right]. \tag{4.74}$$

This simple analytical prediction for $\overline{V}_y$ will be tested against numerical simulations at arbitrary Pe_f in §4.4.2, where it will be shown to provide an excellent estimate for the swimming flux up to $Pe_f \approx 2$.

The effects of the external flow on nematic alignment are also illustrated in figure 4.6(d), where D_{yz} is found to vary almost linearly across the channel width and has the same sign as the external shear rate profile $S(z)$. The right-hand side in

equation (4.67) provides a simple explanation for these findings, where we see that shear nematic alignment results primarily from the interaction of the flow with the concentration profile and with the wall-normal nematic alignment. As Pe_s increases, shear nematic alignment decreases due to the decrease in c and D_{zz} inside the boundary layers as seen in figures 4.2(a) and (c), and to self-propulsion through the first term on the left-hand side of equation (4.67).

4.4.2 Strong-flow limit: scaling analysis

As we shall see in §4.4.3 and figure 4.7, the regime of high flow Péclet number is also quite interesting as it can result in a depletion near the channel centerline surrounded by regions where particles become trapped. The thickness of this depletion region will be found to decrease with increasing flow strength, suggesting the presence of another boundary layer near $z = 0$ in the limit of $Pe_f \gg 1$. Insight into this regime can be gained by analyzing the behavior of the governing equation (4.13) for $Pe_f \gg 1$ and $Pe_s \ll 1$. If the swimming Péclet number is low, the wall boundary layers are very thin and have negligible impact on the dynamics in the bulk of the channel. Inspection of equation (4.13) suggests that, in the outer region away from both the channel walls and the centerline, the dominant balance is between shear alignment and rotational diffusion:

$$\frac{Pe_f}{2}\, S(z)\nabla_p\cdot\left[\cos\theta(\mathbf{I}-\mathbf{pp})\cdot\hat{\mathbf{y}}\,\Psi\right] \approx \frac{1}{2}\nabla_p^2\Psi. \tag{4.75}$$

In this region, the concentration is expected to be nearly uniform, and the particle orientation distribution is primarily nematic as a result of the competition between the

local shear rate and rotational diffusion (as would occur in a passive rod suspension). This corresponds to the shear-trapping region where cross-streamline migration is very weak due to the strong alignment with the flow.

However, as we move closer and closer to the centerline, the local shear rate decreases, causing a concomitant decrease in shear alignment and increase in cross-streamline migration due to self-propulsion. This transition corresponds to the edge of the central boundary layer from which particles are depleted, and the position δ_D of this transition region (or half-thickness of the depletion layer) can be estimated by balancing the magnitudes of the terms describing self-propulsion and shear alignment in equation (4.13):

$$\frac{Pe_s}{\delta_D} \sim \frac{Pe_f}{2}\delta_D, \tag{4.76}$$

from which we find

$$\delta_D \approx C\sqrt{\chi}, \tag{4.77}$$

where the prefactor C is a numerical constant and where we have defined

$$\chi = \frac{Pe_s}{Pe_f} = \frac{V_s}{2\dot{\gamma}_w H}. \tag{4.78}$$

The dimensionless group χ can be interpreted as the ratio of the timescale $\dot{\gamma}_w^{-1}$ it takes a particle to align with the flow over the characteristic timescale $2H/V_s$ it takes it to swim across the channel width: if χ is small, particles align with the flow much faster than they can cross the channel, leading to significant shear-trapping; on the other hand, if χ is large, particles cross the channel much faster than they align with the flow and shear-trapping does not occur. As we show in Appendix C, this scaling for δ_D can indeed also be derived by considering the individual trajectories of deterministic

swimmers released from the centerline, which can be shown to become trapped at a distance of the order of δ_D. It will also be shown to agree quite well with numerical results in §4.4.3, where we will find that $\delta_D \approx 2.404\sqrt{\chi}$ provides an excellent estimate for the thickness of the depletion layer when $Pe_s \lesssim 0.25$ and $Pe_f \gtrsim 50$.

To gain further understanding of the effect of shear rate on the intensity of depletion, we rescale lengths by δ_D inside the central boundary layer to rewrite the governing equation (4.13) as

$$\frac{\Gamma}{C}\cos\theta\frac{\partial\Psi}{\partial z} - 2\Lambda\frac{\Gamma^2}{C^2}\frac{\partial^2\Psi}{\partial z^2} - \frac{C\Gamma}{2}z\,\nabla_p\cdot\left[\cos\theta(\mathbf{I}-\mathbf{pp})\cdot\hat{\mathbf{y}}\,\Psi\right] = \frac{1}{2}\nabla_p^2\Psi, \tag{4.79}$$

where the dimensionless group $\Gamma = \sqrt{Pe_s Pe_f}$ emerges as the most significant parameter governing the profile of the depletion layer. Unsurprisingly, we find that self-propulsion and shear rotation have the same magnitude upon rescaling. In this region, self-propulsion, which scales with Γ, has the effect of enhancing depletion by driving particles away from the centerline; this competes against translational diffusion, scaling with Γ^2, which has the effect of smoothing concentration gradients and thus hampers depletion. This suggests the following dependence of the concentration profile on Pe_f. As flow strength is increased from small values, the depletion layer forms and continually narrows according to equation (4.77) for δ_D. As long as $\Gamma < 1$, self-propulsion dominates translational diffusion and increasing Pe_f (and therefore Γ) enhances depletion. This trend reverses when $\Gamma \sim O(1)$, when translational diffusion starts to overcome self-propulsion, leading to a subsequent decrease in the strength of depletion for $\Gamma > 1$. This qualitative explanation for the non-monotonic dependence of the strength of depletion upon Γ (and hence upon the mean shear rate of the imposed Poiseuille flow) is consistent with the experimental observations of Rusconi

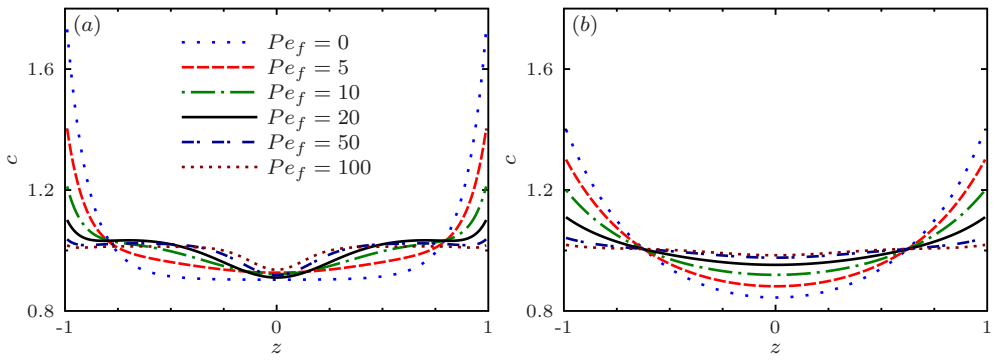

Figure 4.7: (Color online) Equilibrium concentration profiles (at $\Lambda = 1/6$) for (a) $Pe_s = 0.25$ (strong wall accumulation) and (b) $Pe_s = 1.0$ (weak accumulation) and for various values of the flow Péclet number Pe_f, obtained by finite-volume solution of the governing equation (4.13).

et al. [129], and is also borne out by numerical solutions of the governing equations as we describe next.

4.4.3 Arbitrary flow strengths: finite-volume calculations and discussion

We now test and extend the key predictions from the weak-flow asymptotics and strong-flow scaling analysis from the preceding sections by performing finite-volume numerical simulations of the governing equation (4.13) for arbitrary values of Pe_s and Pe_f using the algorithm of Appendix C. Typical concentration profiles are illustrated in figure 4.7 for various values of Pe_f, and for the two values of $Pe_s = 0.25$ and 1.0 corresponding to cases where wall accumulation in the absence of flow is strong and weak, respectively. In both cases, the leading effect of the external flow on c is to decrease wall accumulation. This trend is easily understood as a result of the alignment of the particles with the flow, which reduces wall-normal polarization and thereby hinders accumulation. This decrease in accumulation also results in a net

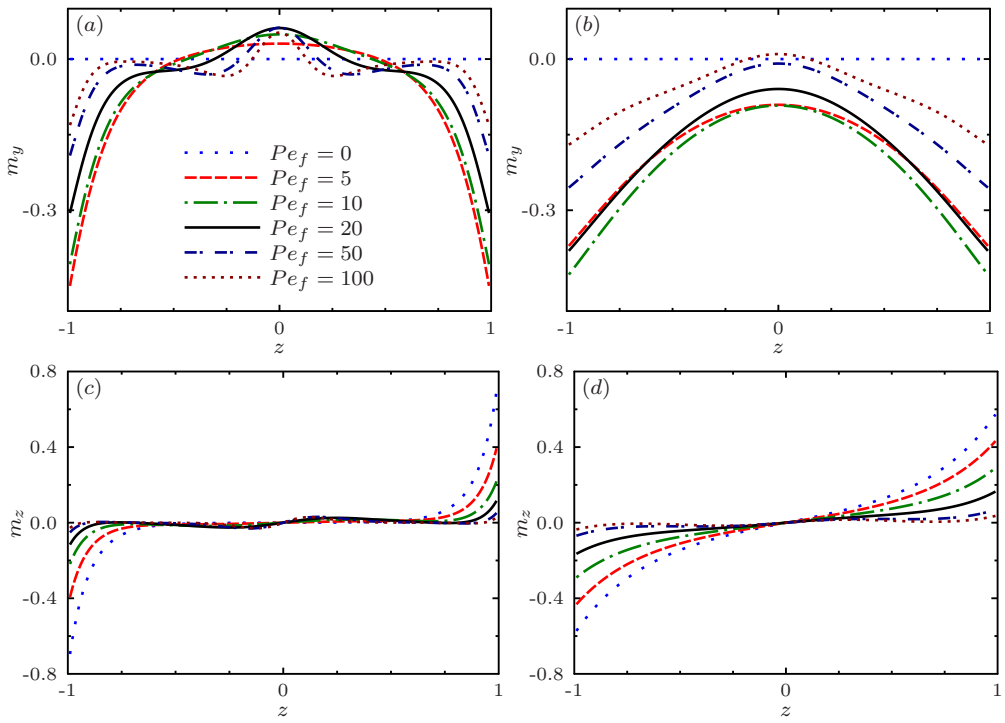

Figure 4.8: (Color online) Equilibrium streamwise and wall-normal polarization profiles (at $\Lambda = 1/6$) for (a)–(c) $Pe_s = 0.25$ and (b)–(d) $Pe_s = 1.0$ and for various values of the flow Péclet number Pe_f, obtained by finite-volume solution of the governing equation (4.13). The streamwise polarization m_y is shown on the top row (a)–(b), and the wall-normal polarization m_z on the bottom row (c)–(d).

increase in the concentration in the central parts of the channel and in the flattening of the profiles in the strong-flow limit. When Pe_s is small as in figure 4.7(a), a depletion layer is also observed to form near the channel centerline and to progressively narrow with increasing Pe_f, in agreement with the theoretical predictions of §4.4.2. At high values of Pe_f, the three distinct regions identified in §4.4.2 (wall accumulation, shear-trapping, and centerline depletion) in fact become clearly visible. However, if the swimming Péclet number is increased to $Pe_s = 1.0$ as in figure 4.7(b), the thickening of the wall boundary layers suppresses shear-trapping and depletion at the centerline, leading to a nearly uniform concentration profile in the strong flow limit.

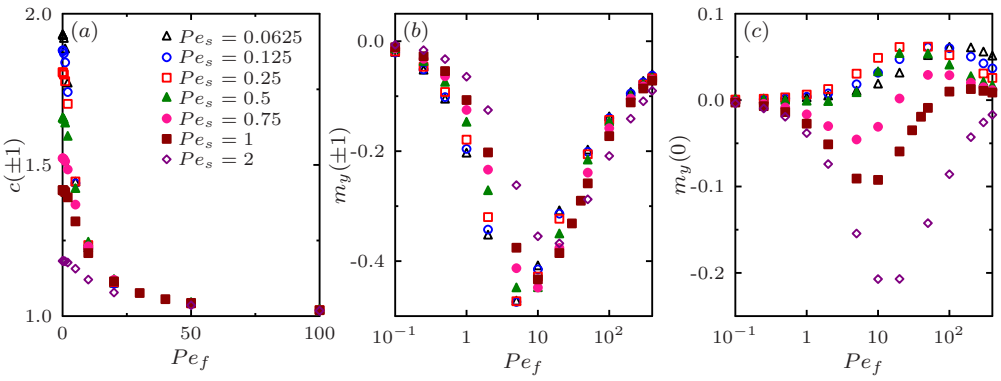

Figure 4.9: (Color online) Effect of swimming and flow Péclet numbers on: (a) wall concentration $c(\pm 1)$, (b) streamwise polarization $m_y(\pm 1)$ at the channel walls, and (c) streamwise polarization $m_y(0)$ at the channel centerline.

Corresponding profiles for the wall-normal and streamwise polarization are also shown in figure 4.8. As expected, rotation of the particles by the flow causes a decrease in the wall-normal polarization, and also results in a non-zero streamwise polarization m_y as previously discussed in §4.4.1. This streamwise polarization is especially strong in the near-wall region where m_y is negative, indicating upstream swimming. It is significantly weaker near the center of the channel, where it is found to be positive for $Pe_s = 0.25$ but remains negative across the entire channel when $Pe_s = 1.0$ due to the overlap of the two wall boundary layers.

These trends are made more quantitative in figure 4.9, showing the dependence of $c(\pm 1)$, $m_y(\pm 1)$ and $m_y(0)$ on the swimming and flow Péclet numbers. As previously discussed, the wall concentration is seen to decrease with increasing flow strength irrespective of the value of Pe_s, and asymptotically tends to 1 in the strong-flow limit as the concentration profiles flatten. Figure 4.9(b) shows that the streamwise polarization at the walls is always negative, which implies that the active particles always swim upstream near the boundaries. Interestingly, we find that there is maximum upstream swimming at $Pe_f \approx 10$, and the upstream motion is reduced at higher values of the

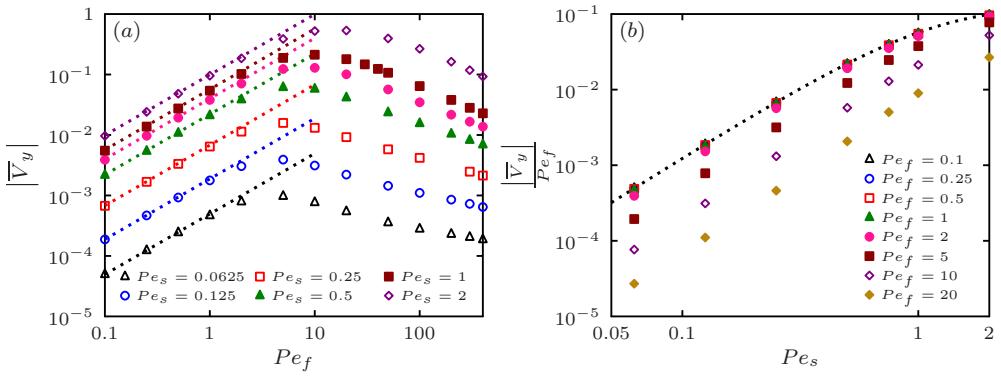

Figure 4.10: (Color online) (a) Magnitude of the average upstream swimming velocity $|\overline{V}_y|$ as a function of Pe_f for different values of Pe_s (at $\Lambda = 1/6$), and (b) dependence of $|\overline{V}_y|/Pe_f$ on Pe_s for different values of Pe_f. Symbols show finite-volume numerical simulations, and dotted lines show the theoretical prediction of equation (4.73).

flow Péclet number. The streamwise polarization at the channel centerline shows complex trends as shown in figure 4.9(c). As predicted by the weak-flow asymptotic analysis of §4.4.1, $m_y(0)$ is found to be positive for low values of Pe_s and negative for high values of Pe_s. Its absolute value increases with flow strength in both cases up to $Pe_f \approx 10$, beyond which further increasing flow strength reduces the polarization. The decrease in both $m_y(\pm 1)$ and $m_y(0)$ at high Pe_f is a likely consequence of the dominant effect of the shear alignment term in equation (4.13), which promotes nematic rather than polar order.

The dependence of the average streamwise swimming velocity $\overline{V}_y$ defined in equation (4.69) on both Péclet numbers is shown in figure 4.10, where numerical results are compared to the weak-flow theoretical prediction of equation (4.73). Consistent with figure 4.9(b) for the streamwise polarization at the walls, we find that $\overline{V}_y < 0$, and that $|\overline{V}_y|$ first increases nearly linearly with Pe_f in agreement with the predictions of §4.4.1. This increase persists up to $Pe_f \approx 10$, beyond which $|\overline{V}_y|$ starts decreasing again. Excellent quantitative agreement is found with equation (4.73) for $Pe_f \lesssim 2.0$.

This is confirmed in figure 4.10(b), showing the dependence of $|\overline{V}_y|/Pe_f$ on swimming Péclet number: the upstream velocity is found to increase with Pe_s, primarily as a result of the corresponding increase in swimming speed of individual particles, and a collapse of all the curves onto the theoretical prediction of equation (4.73) is observed when $Pe_f \lesssim 2.0$.

As seen in figure 4.7(a), shear-trapping and centerline depletion are observed in the central portion of the channel at high flow Péclet number if Pe_s is sufficiently low. This is illustrated more clearly in figure 4.11, where concentration and wall-normal polarization profiles are shown in the central portion of the channel for various values of the flow Péclet number and for $Pe_s = 0.125$. This value was chosen to match the experiments of Rusconi *et al.* [129], where the following parameters were reported: $V_s = 50\,\mu$m, $d_r = 1$ s^{-1}, and $2H = 400\,\mu$m. As seen in figure 4.11(a), increasing Pe_f from zero first results in a decrease in the concentration at the centerline, corresponding to the formation of the depletion layer. As the concentration decreases, the width of the depletion layer is also found to decrease. This trend continues up to $Pe_f \approx 20$, above which the concentration at the centerline starts increasing again, even though the depletion layer keeps narrowing. These trends are in very good agreement with the experiments of Rusconi *et al.* [129], who also reported a non-monotonic dependence of the strength of depletion on shear rate; in fact, the profiles shown in figure (4.11) are very similar to the experimental profiles at equivalent values of Pe_f. The trends on the concentration profile are easily understood based on figure 4.11(b) for the wall-normal polarization, which reflects the net swimming velocity across the channel and provides insight into cross-streamline migration. Indeed, the polarization profiles exhibit peaks on both sides of the depletion layer, corresponding to a strong migration away from

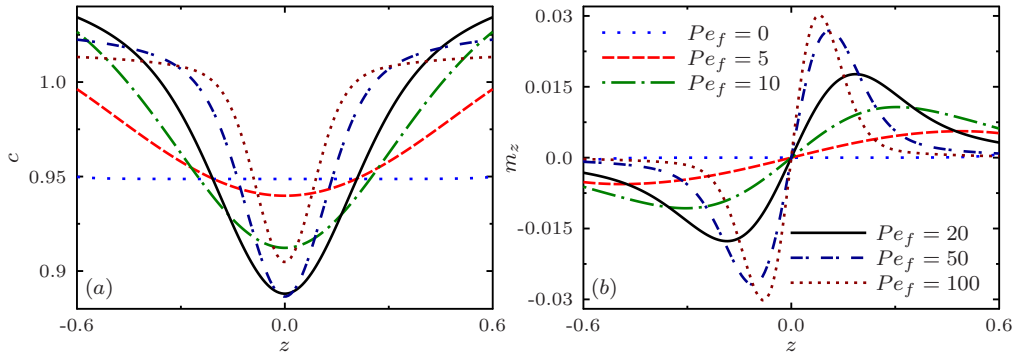

Figure 4.11: (Color online) (a) Concentration profiles in the central portion of the channel for $Pe_s = 0.125$ and various values of the flow Péclet number Pe_f, obtained by finite-volume solution of equation (4.13). (b) Corresponding profiles of the wall-normal polarization m_z.

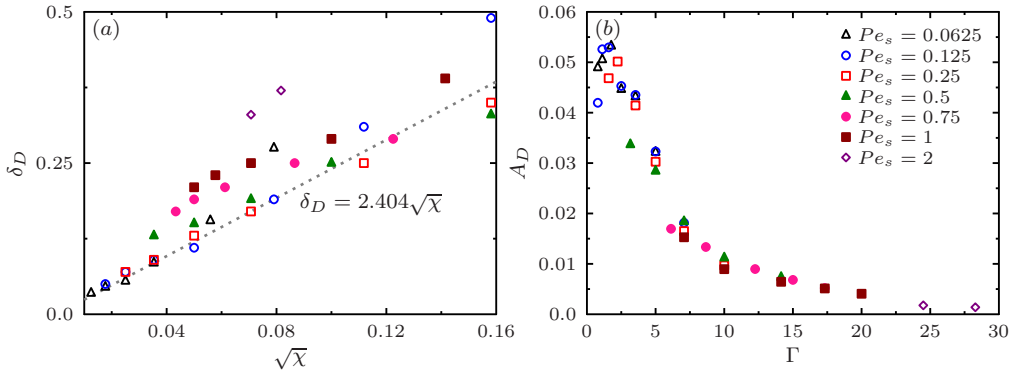

Figure 4.12: (Color online) (a) Depletion layer thickness δ_D, defined as the distance from the centerline where the wall-normal polarization reaches its maximum, as a function of $\sqrt{\chi} = \sqrt{Pe_s/Pe_f}$. (b) Depletion index A_D defined in equation (4.80) as a function of $\Gamma = \sqrt{Pe_s Pe_f}$.

the center. These peaks increase in magnitude and also shift towards the centerline as flow strength increases and the depletion layer narrows. Beyond those peaks, m_z quickly decays to zero where the concentration profiles plateau in accordance with equation (4.28) and shear-trapping of the particles takes place.

These trends are tested more quantitatively against the strong-flow scaling analysis of §4.4.2 in figure 4.12. We first define the thickness δ_D of the depletion layer as the distance from the centerline where m_z reaches its maximum, when such a

maximum exists. Based on the analysis of §4.4.2, we expect δ_D to scale linearly with $\sqrt{\chi} = \sqrt{Pe_s/Pe_f}$ in strong flows, and this is indeed confirmed in figure 4.12(a). We find that δ_D can only be defined when $\sqrt{\chi} \lesssim 0.16$ or $Pe_f \gtrsim 40 Pe_s$, which corresponds to the shear-trapping regime. Best agreement with the scaling prediction is obtained in the low Pe_s and high Pe_f limit, and a linear least-square fit to the data for $Pe_s \leq 0.25$ and $Pe_f \geq 50$ shows that $\delta_D \approx 2.404\sqrt{\chi}$. As Pe_s increases, the numerical results depart from this prediction, primarily due to the thickening of the wall boundary layers which causes them to interact with the parts of the channel where shear-trapping and depletion occur. We further quantify the shape of the depletion layer by introducing a depletion index A_D measuring the amount of particles depleted from the center due to trapping in high-shear regions:

$$A_D = \int_0^{\delta_D} c(z)\,\mathrm{d}z - \delta_D c(\delta_D). \tag{4.80}$$

As we argued in §4.4.2 based on equation (4.79), the shape of the depletion layer is expected to depend upon $\Gamma = \sqrt{Pe_s Pe_f}$, and indeed the numerical data for the depletion index for various values of Pe_s and Pe_f is found to collapse onto a master curve when plotted vs Γ in figure 4.12(b). In agreement with the trends observed in figure 4.11(a), the depletion index shows a non-monotonic dependence on Γ, with maximum depletion occurring for $\Gamma \approx 2$.

The dynamics in the limits of $Pe_s \ll 1$ and $Pe_f \gg 1$ are summarized schematically in figure 4.13, where the channel can be roughly divided into three distinct regions. Region (A), with thickness $\delta \sim \Lambda Pe_s$, abuts the channel wall and is characterized by wall accumulation and a net polarization towards the wall. These effects occur even in the absence of flow, and are in fact mitigated by the flow which tends to decrease the

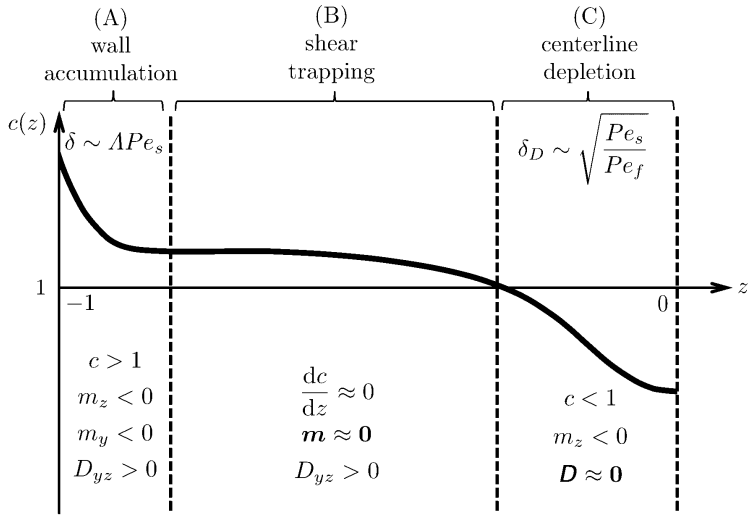

Figure 4.13: Schematic summary of the dynamics in the limits of $Pe_s \ll 1$ and $Pe_f \gg 1$. The channel can be roughly divided into three regions: (A) near the walls, particles accumulate in a boundary layer of thickness $\delta \sim \Lambda Pe_s$; (B) away from the walls and centerline, strong nematic alignment by the flow leads to shear-trapping and a nearly uniform concentration profile; (C) near the centerline, particle propulsion leads to a depletion layer of thickness $\delta_D \sim \Gamma$. The diagram only shows the left half of the channel $z \in [-1, 0]$; the corresponding diagram in the other half can be obtained by symmetry and by noting that m_z is an even function of z, whereas m_y and D_{yz} are both odd functions.

wall concentration and rotate particles to induce upstream polarization. Away from both the wall and the channel centerline is region (B), where the concentration profile is nearly uniform and shear trapping occurs: here, polarization is weak but there is a strong nematic alignment of the particles due to the applied shear. The local shear rate decreases in magnitude as we approach the centerline and enter region (C), which has a characteristic thickness of $\delta_D \sim \sqrt{Pe_s/Pe_f}$: in this region, particles are depleted due to a net polarization towards the walls, which drives migration away from the center but is counterbalanced by translational diffusion. Increasing Pe_s causes both regions (A) and (C) to widen, up to a point where they merge and the three regions can no longer be distinguished. Increasing Pe_f, on the other hand, tends to weaken wall accumulation but does not change the thickness of region (A), while it also causes the narrowing of region (C).

4.5 Effective rheology in pressure-driven flow

As they propel themselves, active particles exert stresses that modify the effective rheology of the suspension. While the rheology of dilute active suspensions has previously been studied in simple linear flows in unbounded domains [68, 147], the effects of confinement and of non-uniform shear in pressure-driven flow have yet to be analyzed. Microfluidic experiments by *et al.* [130] have shown trends similar to theoretical predictions in simple shear flow, yet we expect departures due to the non-uniform distribution and orientation of the particles across the channel. We first show in §4.5.1 how the perturbation to the imposed flow due to the particles can be obtained, and we use it to define an effective viscosity in §4.5.2.

4.5.1 Flow modification by the particles

The particle extra stress due to the presence of the active swimmers has been modeled in our previous work [68, 21] and is the sum of two contributions:

$$\boldsymbol{\Sigma}^p(\boldsymbol{x}) = \alpha \mathbf{D}(\mathbf{x}) + \beta \mathbf{S}(\mathbf{x}) : \mathbf{E}(\boldsymbol{x}). \tag{4.81}$$

Here, the tensors $\mathbf{D}$ and $\mathbf{S}$ are related to the second and fourth moments of the distribution function:

$$\mathbf{D}(\mathbf{x}) = \langle \mathbf{pp} \rangle - \frac{\mathbf{I}}{3}, \qquad \mathbf{S}(\mathbf{x}) = \langle \mathbf{pppp} \rangle - \frac{\mathbf{I}}{3} \langle \mathbf{pp} \rangle, \tag{4.82}$$

and $\mathbf{E}$ is the local rate-of-strain tensor of the imposed pressure-driven flow:

$$\mathbf{E}(\mathbf{x}) = \frac{1}{2}(\nabla \mathbf{U} + \nabla \mathbf{U}^T) = -\frac{Pe_f z}{2} \left(\hat{\mathbf{y}}\hat{\mathbf{z}} + \hat{\mathbf{z}}\hat{\mathbf{y}} \right). \tag{4.83}$$

The dimensionless coefficients α and β are defined as

$$\alpha = \frac{\sigma_0 n}{\mu d_r}, \qquad \beta = \frac{4\pi n \ell^3}{3 \log(2A)}, \tag{4.84}$$

where σ_0 is the intrinsic swimming dipole exerted by the particles as a result of self-propulsion, and A is the particle aspect ratio. The first term in equation (4.81) models the active stress due to propulsion, where $\alpha < 0$ for a pusher particle such as common bacteria and $\alpha > 0$ for a puller particle. The second term in the stress definition arises due to the inextensibility of the particles which resist stretching by the flow, and is the same as that in a suspension of passive rods [71].

To determine the modification of the flow by the particles, we solve the Stokes equations forced by the particle extra stress:

$$-\nabla_x^2 \mathbf{u} + \nabla_x q = \nabla_x \cdot \boldsymbol{\Sigma}^p, \qquad \nabla_x \cdot \mathbf{u} = 0, \tag{4.85}$$

where q denotes the pressure. We seek a solution for the velocity that is only a function of z. By continuity, we know that

$$\frac{\mathrm{d}u_z}{\mathrm{d}z} = 0, \tag{4.86}$$

which implies that $u_z(z) = 0$ using the no-penetration condition at the walls. In components, the momentum equation becomes:

$$-\frac{\mathrm{d}^2 u_x}{\mathrm{d}z^2} = \frac{\mathrm{d}\Sigma^p_{xz}}{\mathrm{d}z}, \qquad -\frac{\mathrm{d}^2 u_y}{\mathrm{d}z^2} = \frac{\mathrm{d}\Sigma^p_{yz}}{\mathrm{d}z}, \qquad \frac{\mathrm{d}q}{\mathrm{d}z} = \frac{\mathrm{d}\Sigma^p_{zz}}{\mathrm{d}z}. \tag{4.87}$$

Realizing that $\Sigma^p_{xz} = 0$, we can integrate the first relation in (4.87) to show that $u_x(z) = 0$. The third relation shows that a pressure gradient balances particle normal stresses in the z-direction. Finally, the y-component of the momentum equation is easily solved subject to the no-slip condition as

$$u_y(z) = \frac{z+1}{2} \int_{-1}^{1} \Sigma^p_{yz} \, \mathrm{d}z - \int_{-1}^{z} \Sigma^p_{yz} \, \mathrm{d}z, \tag{4.88}$$

where

$$\Sigma^p_{yz}(z) = \alpha D_{yz} - \beta Pe_f z \int_{\Omega} \Psi \, p_y^2 p_z^2 \, \mathrm{d}\mathbf{p}. \tag{4.89}$$

By symmetry, it can be seen that the first integral in equation (4.88) is zero, and

therefore

$$u_y(z) = -\int_{-1}^{z} \Sigma_{yz}^{p}\,\mathrm{d}z. \tag{4.90}$$

4.5.2 Effective viscosity

Knowledge of the velocity profile $u_y(z)$ allows us to define an effective viscosity. Two distinct definitions are considered here. We first define a dimensionless local particle viscosity η_p as

$$\eta_p(z) = \frac{\Sigma_{yz}^{p}(z)}{U'(z)} = -\frac{\Sigma_{yz}^{p}(z)}{Pe_f z} = -\frac{\alpha}{Pe_f z} D_{yz} + \beta\langle p_y^2 p_z^2\rangle. \tag{4.91}$$

This local viscosity varies across the channel width due to the change in shear rate, which also causes a change in the local orientation distribution. We see that it involves the fourth moment of the distribution function, which needs to be evaluated numerically. A simpler expression can however be derived based on the three-moment expansion and closure approximation introduced in §4.2.4:

$$\eta_p(z) = -\frac{\alpha}{Pe_f z} D_{yz} + \beta\left[\frac{c}{15} + \frac{1}{7}(D_{yy} + D_{zz})\right]. \tag{4.92}$$

In the asymptotic limit of $Pe_f \ll 1$ (weak flow), we can also use the regular expansion introduced in §4.4.1 to obtain an asymptotic expression for the viscosity:

$$\eta_p(z) = -\frac{\alpha}{z} D_{yz}^{(1)} + \beta\left[\frac{c^{(0)}}{15} + \frac{1}{7}\left(D_{yy}^{(0)} + D_{zz}^{(0)}\right)\right] + O(Pe_f). \tag{4.93}$$

While expressions such as (4.91)–(4.93) describe the local modification of the solvent viscosity by the particles, a global measure of the effective viscosity that does

not depend on z is of greater practical use, especially for comparison with experiments. To define such a quantity, we follow the approach of Gachelin *et al.* [130] and consider the modification of the net flow rate in the channel by the particles. The flow rate per unit width of the imposed external flow is easily obtained as

$$\dot{Q}_e = \int_{-1}^{1} Pe_f(1 - z^2)\,\mathrm{d}z = \frac{2Pe_f}{3}. \tag{4.94}$$

Similarly, the flow rate due to the flow perturbation calculated in §4.5.1 is

$$\dot{Q}_p = \int_{-1}^{1} u_y(z)\,\mathrm{d}z. \tag{4.95}$$

We then define the relative Newtonian viscosity η_r as

$$\eta_r = \frac{\dot{Q}_e}{\dot{Q}_e + \dot{Q}_p} = \left(1 + \frac{3}{2Pe_f}\int_{-1}^{1} u_y(z)\,\mathrm{d}z\right)^{-1}. \tag{4.96}$$

A relation between the relative velocity η_r and the local particle viscosity of equation (4.91) is easily derived:

$$\eta_r = \left(1 + \frac{3}{2}\int_{-1}^{1}\int_{-1}^{z} z\eta_p(z)\,\mathrm{d}z\right)^{-1}. \tag{4.97}$$

4.5.3 Numerical results

Numerical results were obtained for $u_y(z)$, $\eta_p(z)$ and η_r for both pullers and pushers using finite-volume simulations. The modification of the flow by the particles is illustrated in figure 4.14, showing profiles of $u_y(z)$ for different values of Pe_f. In the case of puller particles shown in figure 4.14(a), we find that $u_y(z)$ has a nearly

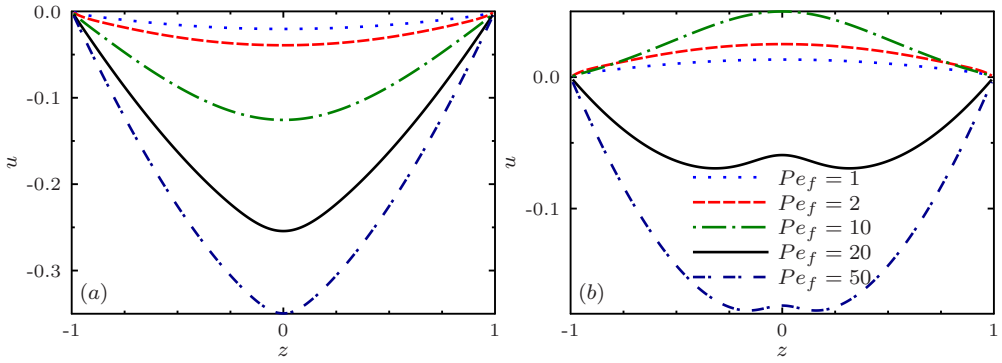

Figure 4.14: (Color online) Flow modification by the particles in suspensions of (a) pullers ($\alpha = +1$) and (b) pushers ($\alpha = -1$), for various values of the flow Péclet number. In both cases, $Pe_s = 0.125$ and $\beta = 0.1$.

parabolic profile and is negative across the entire channel, indicating a reduction in the total velocity of the suspension due to the particles, which becomes stronger with increasing flow strength. This corresponds to an effective increase in the viscosity of the suspension as will be confirmed below, and is consistent with previous predictions in linear shear where puller suspensions were always found to be more viscous than suspensions of passive rods as a result of activity [68]. The trends are significantly more complex in the case of pushers, as shown in figure 4.14(b). At low flow rates, u_y is found to be positive, indicating an enhancement of the flow by the particles. The situation reverses at high flow rates, where u_y becomes negative. This non-monotonic trend will be reflected in the viscosity data below. We also observe a weak maximum in the velocity profile near the centerline, which indicates a non-uniform viscosity across the channel.

Profiles of the local viscosity $\eta_p(z)$ for the same parameter values are plotted in figure 4.15. In suspensions of pullers, the particle viscosity is indeed found to be positive everywhere in the channel. In weak flows, it is maximum near the walls due to

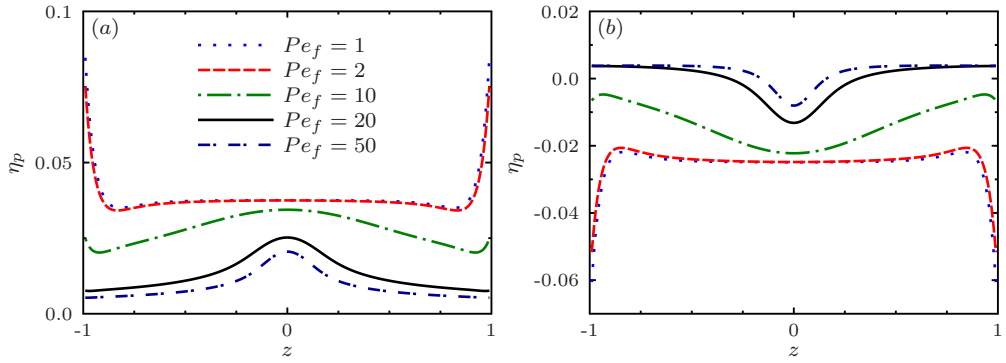

Figure 4.15: (Color online) Local particle viscosity $\eta_p(z)$ calculated using equation (4.91) in suspensions of (a) pullers ($\alpha = +1$) and (b) pushers ($\alpha = -1$), for various values of the flow Péclet number. In both cases, $Pe_s = 0.125$ and $\beta = 0.1$.

particle accumulation there. As the flow strength increases, shear-thinning is observed as in the classic case of passive rod-like particles [148], though it occurs primarily near the walls, leading to a weak maximum in the viscosity near the centerline at high values of Pe_f; this is consistent with the standard explanation of shear-thinning in rod suspensions due to the nematic alignment of the particles with the flow, which is strongest in the high-shear near-wall regions. The case of pushers is illustrated in figure 4.15(b). At low flow rates, the particle viscosity is negative throughout the channel due to activity, which explains the enhancement of the flow observed in figure 4.14(b). As Pe_f increases, the viscosity becomes positive near the channel walls due to the strong nematic alignment of the particles there, which causes the passive contribution to the stress to dominate the active contribution in equation (4.81), but it remains negative near the centerline where the shear rate is weak. This change in sign explains the non-monotonicity of the velocity profile in figure 4.14(b): for a given pressure gradient, the flow is hindered near the walls where $\eta_p > 0$, whereas it is enhanced near the centerline where $\eta_p < 0$.

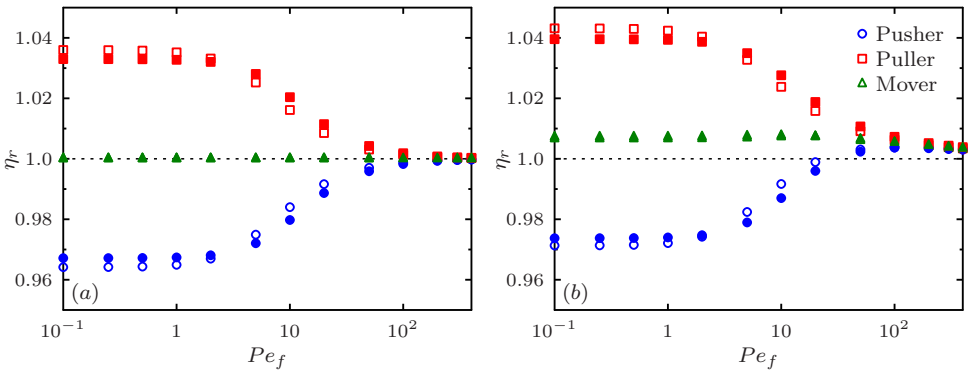

Figure 4.16: (Color online) Global relative viscosity η_r (open symbols) calculated using equation (4.96) in suspensions of pushers ($\alpha = -1$), pullers ($\alpha = +1$) and movers ($\alpha = 0$), for $Pe_s = 0.125$ and for various values of the flow Péclet number. Two values of the parameter β are shown: (a) $\beta = 0.001$, and (b) $\beta = 0.1$. The data is compared to the relative viscosity of an unconfined suspension in uniform simple shear flow with shear rate equal to the mean shear rate in the channel (full symbols).

The net effect of these results on the flow rate is summarized in figure 4.16, showing the relative viscosity η_r as a function of Pe_f for two different values of β for pushers and pullers, as well as for so-called movers, which are particles that swim ($V_s \neq 0$) but do not exert any active stress ($\alpha = 0$). When β is low in figure 4.16(a), the particle stress is dominated by the active contribution, which leads to an increase in viscosity in suspensions of pullers, and a decrease in suspensions of pushers. Both effects become weaker with increasing flow strength due to the alignment of the particles with the flow. When passive stresses are more significant in figure 4.16(b), a net increase in viscosity is observed. Both puller and mover suspensions exhibit shear-thinning. In the case of pushers, a non-monotonic dependence of the viscosity on Pe_f is observed: $\eta_r < 1$ at low flow rates when activity dominates, but it becomes greater than 1 at intermediate flow rates due to passive stresses, before exhibiting shear thinning at high values of Pe_f. These trends are indeed in agreement with the experimental

observations of Gachelin *et al.* [130], who reported a non-monotonic dependence of the relative viscosity with flow rate in microfluidic experiments using bacteria. Figure 4.16 also compares the relative viscosity to that of a uniform unconfined suspension under simple shear flow with shear rate $\dot{\gamma} = \dot{\gamma}_w/2$, where only mild discrepancies are observed; note, however, that these discrepancies are expected to amplify at higher values of the swimming Péclet number, due to the increased influence of confinement on the particle orientation distribution inside the channel.

4.6 Discussion

4.6.1 Summary of main results

We have used a combination of theory and numerical simulations to analyze the distributions and transport properties of an infinitely dilute suspension of self-propelled particles confined between two parallel flat plates, both in quiescent conditions and under an imposed pressure-driven flow. Our analysis focused on incorporating the effects of confinement within the kinetic theory framework previously developed by Saintillan and Shelley [140], which is based on a Smoluchowski equation for the distribution of the active particle positions and orientations. In particular, we demonstrated that prescribing a zero-normal-flux condition on the particle distribution function at the boundaries captures several key features reported in experiments on dilute active suspensions under confinement. We presented a finite-volume algorithm for the numerical solution of the Smoluchowski equation, which allows for an easy implementation of the boundary conditions, and also developed a simpler system of equations for the orientational moments of the distribution function, which enabled

us to perform analytical calculations in the absence of flow and under a weak imposed flow. An asymptotic scaling analysis was also performed on the full Smoluchowski equation under strong flow. The numerical simulation data was used to test and further understand the analytical calculations and predictions.

We first considered the dynamics in the absence of flow. In this case, the governing equations involve a swimming Péclet number Pe_s, which is the ratio of the persistence length of swimmer trajectories to the channel height, as well as a parameter Λ that is fixed for a given swimmer type and whose inverse measures the strength of propulsion. In the limit of wide channels, the channel can be divided into two regions: a near-wall accumulation region where the particles tend to concentrate and have a net polarization towards the wall, and a bulk region away from the walls where the distribution is nearly uniform and isotropic. Asymptotic expressions for the full distribution function were also derived as series in powers of Λ in the weak and strong propulsion limits. In particular, it was shown that the characteristic thickness of the accumulation layer scales with d_t/V_s in the strong propulsion limit ($\Lambda \ll 1$), and with $\sqrt{d_t/d_r}$ in the weak propulsion limit ($\Lambda \gg 1$). For finite values of Λ, analytical expressions for the concentration and polarization profiles were obtained by solving the moment equations and displayed excellent agreement with the finite-volume numerical simulation of the full distribution function for a wide range of values of the swimming Péclet number so long as $\Lambda \gtrsim 0.1$. Based on these results, we proposed and validated a simple mechanism for wall accumulation, where the presence of the wall breaks the polar symmetry of the active particles and leads to sorting of orientations. This mechanism differs from previous explanations based on hydrodynamic interactions or surface alignment due to collisions, and led us to conclude that both pusher

and puller particle suspensions will exhibit similar wall accumulation in the dilute limit. Hydrodynamic and surface alignment interactions are, however, expected to quantitatively affect the profiles in more concentrated systems and to lead to different distributions for pusher and puller particles.

Next, we analyzed the effects of an imposed pressure-driven flow. When a flow is applied on the suspension, the physics is now governed by three dimensionless groups: the swimming Péclet number Pe_s and parameter Λ introduced above, as well as a flow Péclet number Pe_f comparing the imposed shear rate to rotational diffusion. In the weak flow limit, we calculated the leading-order corrections of the streamwise polarization and shear nematic alignment due to the flow and showed that near-wall upstream swimming is a consequence of shear rotation of the particles inside the accumulation layer near the walls. We derived an analytical expression for the average upstream swimming velocity of the active particles relative to the imposed flow, which was compared against numerical simulations and provides an excellent estimate for $Pe_f \lesssim 2$. In the strong flow limit, we developed a scaling analysis to show that when $Pe_s \ll 1$ and $Pe_f \gg 1$ the channel can be roughly divided into three regions: the near-wall accumulation region with thickness $\delta \sim \Lambda Pe_s$, a depletion region near the centerline with thickness $\delta_D \sim \Gamma = \sqrt{Pe_s/Pe_f}$, and a shear-trapping region away from the wall and centerline where the concentration is nearly uniform and particle alignment is primarily nematic. The extent of the central depletion shows a non-monotonic variation with flow strength, with a maximum depletion occurring at a critical flow strength such that $\Gamma \sim O(1)$.

Finally, we also studied the effective dilute rheology of the suspension and showed that while the local effective viscosity of pullers is positive throughout the

channel, that of pushers can be either positive or negative in different parts of the channel depending on flow strength. We also defined a global relative viscosity based the modification of the net flow rate by the particles, and observed trends for pushers that are in agreement with the recent experimental measurements of Gachelin *et al.* [130].

4.6.2 Discussion and comparison to previous works

The phenomena analyzed in this study have received considerable attention in experiments as well as other models and simulations, so we compare and contrast them here to these prior works. As mentioned in the introduction, the wall accumulation predicted by our model in the absence of flow is well known in experiments on bacterial suspensions, where accumulation layers of $\approx$ 1 to 50 μm are typically reported [118, 122, 123, 149], with increases in concentration of up to 50 times the bulk density very close to the wall [123]. Such high concentrations at the walls are consistent with our numerical results of figure 4.3, which predict high values of $c(\pm 1)$ in the strong-propulsion limit of $\Lambda \ll 1$ relevant to bacteria. Indeed, a rough estimate for *E. coli* provides $\Lambda \approx 0.01$, though it is difficult to precisely measure d_t in experiments since long-time mean-square displacements are dominated by Taylor dispersion. This strong accumulation is also consistently observed in simulations [33, 137, 124, 125, 105, 134], which also exhibit the preferential alignment of the swimmers towards the wall that our model predicts. A similar alignment has also been reported in a few experiments [62, 105], though detailed observations of swimming micro-organisms near walls has also revealed complex complex scattering dynamics due to the interactions of the flagellar appendages with the boundaries [96, 150].

These observations seem to contradict mechanisms purely based on Stokes-dipole hydrodynamic interactions with the no-slip walls, as these predict reorientation of the cells parallel to the walls in the case of pushers [118]. Rather, they appear to support the prediction that accumulation layers derive predominantly from a polarity-sorting mechanism across the channel together with a balance of self-propulsion and diffusion at the walls. We note that this mechanism was also proposed in the work of Elgeti and Gompper [125], who performed simulations of self-propelled Brownian spheres between two flat plates. Their numerical results support the trends described in §4.3.4 on the effect of confinement as captured by Pe_s. Elgeti and Gompper [125] also wrote down a continuum model that shares similarities with ours, which they used to analyze the strong propulsion and narrow gap limits. Their conclusions are in agreement with the discussion of §4.3.2 and §4.3.3.

The distributions and dynamics predicted by our theory under imposed flow also agree with the bulk of prior studies, both experimental and numerical. The reorientation of near-wall swimmers against the flow leading to upstream swimming has been reported ubiquitously in many experiments [126, 127, 128, 97] and simulations [137, 124, 138], with several of these studies proposing similar mechanisms as that described herein, namely the shear rotation of the polarized cells near the walls. Quite remarkably, the peak in the upstream swimming flux at a critical flow strength visible in the simulation data of figure 4.10(a) was also reported in the experiments of Kantsler *et al.* [97].

The dynamics in strong flows in the central part of the channel has only received little attention in previous studies. Our interest in this problem was sparked by the recent microfluidic experiments of Rusconi *et al.* [129], which were the first to predict

centerline depletion and shear trapping. Our scaling analysis and numerical results of §4.4.2 and §4.4.3 are in excellent agreement with their observations. In particular, the shape of the concentration profiles near the channel centerline obtained in figure 4.11 are quite similar to those shown in figure 2(a) of their paper. Further, we observed in our study a non-monotonic dependence of the depletion index on Γ, with maximum depletion occurring for $\Gamma \approx 2$. In the experiments of Rusconi *et al.* [129], a similar non-monotonic trend was reported, with the strongest depletion occurring in the range of $\gamma \approx 2.5$ – 10 s^{-1}. From their data, we estimate $Pe_f \approx 5$ – 20 and $Pe_s \approx 0.125$, from which we find $\Gamma \approx 0.8$ – 1.6 in reasonable agreement with our numerical results. A simple analytical model based on a Fokker-Planck equation was also introduced in their paper, though only limited results were obtained in the low-Pe_f limit.

Since the experiments of Rusconi *et al.* [129], the existence of centerline depletion in strong flows was also confirmed in the numerical simulations of Chilukuri *et al.* [138], which provided additional insight into the shape of the depletion layer and its scaling with flow strength. By fitting the dip in concentration at the centerline with a parabola, they were able to extract the profile curvature from their simulation data, and showed that it collapses onto a master curve when plotted vs $\dot{\gamma}_w H/2V_s$, in agreement with our prediction that the shape of the depletion is controlled by $\chi = Pe_s/Pe_f = V_s/2\dot{\gamma}_w H$. Their also reported similar particle orientations as predicted in figures 4.6(a) and 4.8(a): namely, swimmers are preferentially aligned with the flow in the bulk of the channel, even though they tend to swim upstream near the walls. Finally, we recall that our theoretical scaling for the width of the depletion layer is also in agreement with the analytical model of Zottl and Stark [135], which is discussed in more detail in Appendix D and determines the distance away from the

centerline where a deterministic swimmer leaving $z = 0$ with a given orientation fully aligns with the flow, i.e., becomes trapped by shear alignment.

4.6.3 Concluding remarks

The favorable agreement of our predictions with both experiments and simulations validates our model and in particular our choice of boundary condition. We reiterate that particle-particle and particle-wall hydrodynamic interactions were entirely neglected in this work, suggesting that the salient features of confined active suspensions such as wall accumulation, upstream swimming, centerline depletion and shear-trapping can all be explained in the absence of such interactions. Yet even in dilute suspensions, particle-wall hydrodynamic interactions are known play a role [120] and are expected to slightly modify the results described here. Pusher and puller suspensions are no longer equivalent when hydrodynamic interactions are included and therefore may adopt slightly different distributions, whereas this distinction is irrelevant in the present model. As particle density increases, we also expect particle-particle hydrodynamic interactions to become significant, and to destabilize the equilibrium distributions obtained in §4.3 if the concentration is sufficiently high. A preliminary one-dimensional stability analysis accounting for flow modification by the particles suggests the existence of a symmetry-breaking bifurcation above a critical concentration in suspensions of pushers, leading to unidirectional flow with net fluid pumping; such an instability was also previously predicted using various phenemenological models for active liquid crystals [151, 152, 153, 154, 155]. Further increases in concentration may also lead to the onset of bacterial turbulence [156, 149]. These predictions have yet to be confirmed from a hydrodynamics first-principles

perspective and may also be investigated computationally using a generalization of the finite-volume algorithm presented in Appendix C, or by numerical solution of the approximate equations for the orientational moments of the distribution function, which were shown to be highly accurate in the absence of an external flow. Since the equilibrium states under confinement are non-uniform and polarized in the wall-normal direction, the instabilities in confined active suspensions could have multifold origins. These aspects will be the focus of chapter 6.

Our study has only focused on the limit of high-aspect-ratio particles. If the aspect ratio of the particles is not high, some of the conclusions of this work may change. The distributions in the absence of flow, including the formation and structure of the wall accumulation layers, are not expected to change even in the limit of spherical particles, as confirmed by previous simulations of Brownian active spheres [125]. However, small-aspect-ratio particles will be subject to a weaker alignment with the local shear in an imposed flow, which is expected to widen and eventually suppress the centerline depletion layer in strong flows. This concept may provide interesting avenues for the sorting of active particles by shape in microfluidic devices.

As a final comment, we recall that a crucial ingredient of our analysis is the presence of translational diffusion in the dynamics of the swimmers, which acts to balance the swimming flux at the boundaries and leads to diffuse accumulation layers. In the limit of strong propulsion or weak diffusion ($\Lambda \to 0$), we saw that accumulation is enhanced, and we expect the formation of concentration singularities at the walls in the strict limit of $d_t = 0$. This limit is not easily addressed in the context of our theory, though a very recent attempt at describing accumulation in this case was proposed by Elgeti and Gompper [157]. The development of a more detailed framework in the

absence of diffusion may prove particularly relevant for describing the accumulation of fast-swimming bacteria undergoing run-and-tumble dynamics, notably in applications involving the interaction of bacterial suspensions with suspended passive objects [111, 112, 113, 114] and is the focus of the next chapter.

Acknowledgement: Chapter 4, in part, is a reprint of the material as it appears in Journal of Fluid Mechanics 2015. "Transport of a dilute active suspension in pressure-driven channel flow" by Ezhilan, Barath; Saintillan, David, Cambridge University Press, 2015. The dissertation author was the primary investigator and author of this paper.

4.A Comparison between the no-flux and reflection boundary conditions

In this Appendix, we compare the no-flux boundary condition of equation (4.8), which is central to our model, to the reflection boundary condition used in previous works [22, 142]. The reflection boundary condition ensures that

$$\Psi\left(\pm 1, \theta, \phi\right) = \Psi\left(\pm 1, \pi - \theta, \phi\right), \tag{4.98}$$

at the channel walls, where θ and ϕ are defined in Figure 1. Calculating the first three orientational moments of equation (4.98) yields the following conditions to be enforced

at $z = \pm 1$:

$$\frac{\mathrm{d}c}{\mathrm{d}z} = 0, \tag{4.99}$$

$$m_z = 0, \quad \frac{\mathrm{d}m_y}{\mathrm{d}z} = 0, \tag{4.100}$$

$$\frac{\mathrm{d}D_{zz}}{\mathrm{d}z} = 0, \quad \frac{\mathrm{d}D_{yy}}{\mathrm{d}z} = 0, \quad D_{yz} = 0. \tag{4.101}$$

While equations (4.99)–(4.101) are easily shown to imply that the no-flux conditions (4.25)–(4.27) on c, m_y,D_{yy}, D_{zz} are also satisfied, they are much more stringent conditions, with a significant impact on the distribution of particles near the wall.

First, in the absence of flow, we see that equations (4.33)–(4.35) now need to be solved subject to boundary conditions (4.99)–(4.101) at $z = \pm 1$. The uniform and isotropic solution with $c^{(0)} = 1$ and $m_z^{(0)} = D_{zz}^{(0)} = 0$ satisfies this system exactly. In other words, the condition of 4.98, by enforcing a zero concentration gradient and wall-normal polarization at the walls, is unable to capture the concentration/polarization boundary layer which is one of the key results predicted by the no-flux boundary condition and is a ubiquitous feature of experiments and particle models.

The impact of condition (4.98) on distributions under flow can be understood in the low Pe_f limit by modifying the derivation of §4.4.1. Since $m_z^{(0)} = 0$, the right-hand term in equation (4.66) now vanishes. Equation (4.66)–(4.67) are then rewritten as

$$Pe_s \frac{\mathrm{d}D_{yz}^{(1)}}{\mathrm{d}z} - 2\Lambda Pe_s^2 \frac{\mathrm{d}^2 m_y^{(1)}}{\mathrm{d}z^2} + m_y^{(1)} = 0, \tag{4.102}$$

$$\frac{Pe_s}{5} \frac{\mathrm{d}m_y^{(1)}}{\mathrm{d}z} - 2\Lambda Pe_s^2 \frac{\mathrm{d}^2 D_{yz}^{(1)}}{\mathrm{d}z^2} + 3D_{yz}^{(1)} = \frac{S(z)}{10}, \tag{4.103}$$

subject to the boundary conditions

$$\frac{\mathrm{d}m_y^{(1)}}{\mathrm{d}z} = 0, \quad D_{yz}^{(1)} = 0 \quad \text{at } z = \pm 1. \tag{4.104}$$

Taking a cross-sectional average of equation (4.102) subject to equation (4.104) shows that $\overline{m}_y^{(1)} = 0$. Therefore, the mean upstream velocity in the channel is exactly zero if the reflection boundary condition is enforced. The condition also imposes a zero streamwise nematic alignment ($D_{yz}^{(1)} = 0$) at the walls, which is not physical when a fluid flow satisfying the no-slip boundary condition is imposed. A closer look at equations (4.103)–(4.104) also reveals that the system is in fact ill-posed in the limit of $Pe_s \to 0$. For finite values of Pe_s, a numerical solution shows that the reflection boundary condition severely underpredicts the near-wall upstream polarization shown in figure (4.6). Finally, we note that the analysis presented in §4.4.2 in the strong-flow limit (and hence the scalings for the depletion boundary layer thickness and rationalization of the non-monoticity of the depletion index with Pe_f) describe the dynamics in the bulk of the channel and is not affected by the boundary condition imposed.

4.B Effect of steric exclusion

The analysis of this chapter entirely neglected the finite size of the active particles and in particular did not account for steric exclusion with the boundaries, which is expected to modify the distributions near the walls as observed experimentally [117]. As previously shown in the case of passive rods [144, 145, 146], excluded volume interactions can be incorporated by means of a more complex boundary condition. One

must first realize that steric exclusion prohibits those configurations near either of the two walls that lead to overlap of a section of a particle with the wall. The boundaries between such allowed and prohibited configurations define two hypersurfaces in the three-dimensional (z, θ, ϕ) space of particle configurations:

$$z = 1 - L^* \left|\cos\theta\right| \qquad \text{(top hypersurface)}, \tag{4.105}$$

$$z = -1 + L^* \left|\cos\theta\right| \qquad \text{(bottom hypersurface)}, \tag{4.106}$$

where $L^* = L/2H$ is the ratio of the particle length to the channel width. At any position z inside the channel, this restricts the allowable range of θ to an interval of the form $[\theta_1(z), \theta_2(z)]$, with

$$\theta_1(z) = \begin{cases} 0 & \text{for } 1 - |z| \geq L^*, \\ \cos^{-1}\left(\dfrac{1-|z|}{L^*}\right) & \text{for } 1 - |z| \leq L^*, \end{cases} \tag{4.107}$$

and

$$\theta_2(z) = \begin{cases} \pi & \text{for } 1 - |z| \geq L^*, \\ \cos^{-1}\left(\dfrac{-1+|z|}{L^*}\right) & \text{for } 1 - |z| \leq L^*, \end{cases} \tag{4.108}$$

and consequently, any integral with respect to $\mathbf{p}$ of a field variable $A(z, \mathbf{p})$ must be restricted to these configurations:

$$\int_\Omega A(z, \mathbf{p})\, \mathrm{d}\mathbf{p} \equiv \int_0^{2\pi} \int_{\theta_1(z)}^{\theta_2(z)} A(z, \mathbf{p}) \sin\theta \, \mathrm{d}\theta \, \mathrm{d}\phi. \tag{4.109}$$

To ensure that prohibited configurations are never realized, the boundary condition (4.7) must be replaced by a more general no-flux condition on the hypersurfaces

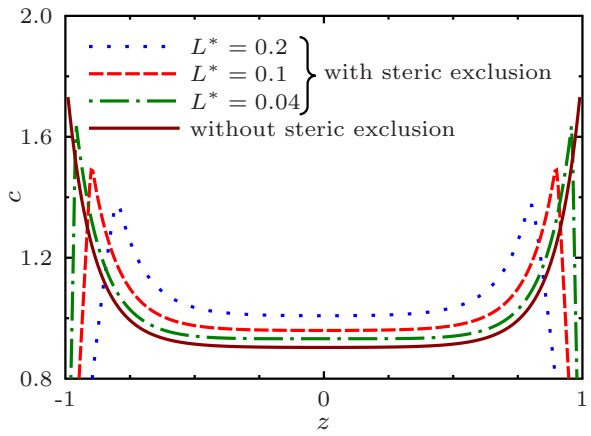

Figure 4.17: (Color online) Effect of steric exclusion on the steady concentration profile in the absence of flow and for $Pe_s = 0.25$. The plot compares numerical results for three different values of $L^* = L/2H$ to the case where steric exclusion is neglected ($L^* \to 0$).

defined in equations (4.105)–(4.106). Introduce the generalized flux vector $\mathbf{J}$ as

$$\mathbf{J}(z, \mathbf{p}, \Psi) = (\dot{\mathbf{x}} + \dot{\mathbf{p}})\,\Psi = J_z \hat{\mathbf{z}} + J_\theta \hat{\boldsymbol{\theta}} + J_\phi \hat{\boldsymbol{\phi}}, \tag{4.110}$$

with

$$J_z = Pe_s \cos\theta\,\Psi - 2\Lambda Pe_s^2 \frac{\partial \Psi}{\partial z}, \tag{4.111}$$

$$J_\theta = \frac{1}{2}\left(Pe_f S(z) \cos^2\theta \sin\phi\,\Psi - \frac{\partial \Psi}{\partial \theta} \right), \tag{4.112}$$

$$J_\phi = \frac{1}{2}\left(Pe_f S(z) \cos\theta \cos\phi\,\Psi - \frac{1}{\sin\theta}\frac{\partial \Psi}{\partial \phi} \right). \tag{4.113}$$

Denoting by $\hat{\mathbf{n}}(z, \theta)$ the normal unit vector on one of the two hypersurfaces, the generalized no-flux condition is simply expressed as

$$\hat{\mathbf{n}}(z, \theta) \cdot \mathbf{J}(z, \mathbf{p}, \Psi) = 0, \tag{4.114}$$

which, upon calculation of the normal $\hat{\mathbf{n}}$, leads to the two conditions:

$$J_z \mp L^* \sin\theta J_\theta = 0 \qquad \text{at } \; z = 1 - L^* \left|\cos\theta\right|, \tag{4.115}$$

$$J_z \pm L^* \sin\theta J_\theta = 0 \qquad \text{at } \; z = -1 + L^* \left|\cos\theta\right|. \tag{4.116}$$

In each case, the upper sign is used when $\theta \in [0, \pi/2]$ and the lower one when $\theta \in [\pi/2, \pi]$. Numerical solution of the conservation equation (4.6) subject to the boundary conditions (4.115)–(4.116) can be done using finite volumes as described in Appendix B. Typical results for the concentration profile $c(z)$ in the absence of flow are shown in figure 4.17 for different values of L^* and compared to the solution obtained previously using the boundary condition (4.7), which corresponds to the limit of $L^* \to 0$. When steric exclusion is accounted for, a depletion layer is observed close to the walls whose thickness is of the order of L^*. Steric exclusion leads to a decrease in concentration in the near wall region because it suppresses the orientations aligned towards the wall and hence the wall normal polarization. Under stronger confinement (higher L^*), this leads to a concentration peak at the edge of the depletion layer due to wall accumulation, and this peak increases in magnitude and shifts closer to the wall as L^* decreases. For very small values of L^*, the concentration profile approaches the profile obtained by neglecting steric effects, and steric exclusion can be safely neglected outside of the depletion layer itself whenever $L^* \lesssim 0.01$. This is indeed the appropriate regime in most microfluidic experiments with bacterial suspensions, which justifies the use of the simpler boundary condition (4.7) in the work presented here.

4.C Finite-volume numerical algorithm

In this Appendix, we describe the algorithm used for the numerical solution of equation (4.13) for the distribution function. The method is based on a finite-volume discretization of the Smoluchowski equation [158], which has the advantage of satisfying conservation locally to machine precision while also allowing for an easy implementation of no-flux boundary conditions such as (4.7) or (4.115)–(4.116). To avoid the cost of large matrix inversions, we solve the time-dependent Smoluchowski equation to steady state using an explicit scheme. In conservative form, the governing equation can be written as

$$\frac{\partial \Psi}{\partial t} + \nabla_J \cdot \mathbf{J} = 0, \tag{4.117}$$

where $\mathbf{J}$ is the generalized flux vector defined in equations (4.110)–(4.113), and ∇_J is the gradient operator in the three-dimensional (z, θ, ϕ) space of particle configurations:

$$\nabla_J \equiv \frac{\partial}{\partial z}\hat{\mathbf{z}} + \frac{\partial}{\partial \theta}\hat{\boldsymbol{\theta}} + \frac{1}{\sin\theta}\frac{\partial}{\partial \phi}\hat{\boldsymbol{\phi}}. \tag{4.118}$$

We note that $\Psi(z, \theta, \phi)$ is defined on a hypervolume obtained by extruding the unit sphere in the z dimension. This computational domain is discretized into finite volumes using a uniform grid with respect to (z, r, ϕ), where $r = \cos\theta$. The nodal points (z^i, r^j, ϕ^k) where Ψ is evaluated are located at the centers of each volume and

have coordinates

$$z^i = \frac{2i-1}{N_z} - 1 \qquad \text{for} \quad i = 1, ..., N_z, \tag{4.119}$$

$$r^j = \frac{2j-1}{N_r} - 1 \qquad \text{for} \quad j = 1, ..., N_r, \tag{4.120}$$

$$\phi^k = \frac{2\pi(k-1)}{N_\phi} \qquad \text{for} \quad k = 1, ..., N_\phi, \tag{4.121}$$

where N_z, N_r, and N_ϕ are the total numbers of points in each direction. We also define the grid spacing in each direction as

$$\Delta z = \frac{2}{N_z}, \quad \Delta r = \frac{2}{N_r}, \quad \Delta\phi = \frac{2\pi}{N_\phi}. \tag{4.122}$$

The advantage of this discretization (compared to a uniform grid with respect to θ) is that it divides the sphere of orientations into elements of equal area, which reduces restrictions on the time step arising from the rotational flux.

A typical finite volume centered around node (i, j, k) is illustrated in figure 4.18. It is delimited by eight grid points denoted A through H, with indices $(i_\pm, j_\pm, k_\pm)$ where we have introduced the notations $i_\pm = i \pm 0.5$, $j_\pm = j \pm 0.5$ and $k_\pm = k \pm 0.5$. The cell edges have lengths

$$AB = DC = EF = HG = \Delta\ell_\theta \equiv \cos^{-1}(r^{j-}) - \cos^{-1}(r^{j+}), \tag{4.123}$$

$$AD = EH = \Delta\ell_\phi^- \equiv \frac{2\pi \sin\theta^{j-}}{N_\phi}, \quad BC = FG = \Delta\ell_\phi^+ \equiv \frac{2\pi \sin\theta^{j+}}{N_\phi}, \tag{4.124}$$

$$AE = BF = DH = CG = \Delta z. \tag{4.125}$$

In figure 4.18, faces $ABCD$ and $EFGH$ have unit normal $\hat{\mathbf{z}}$ and surface area $\Delta r \Delta\phi$.

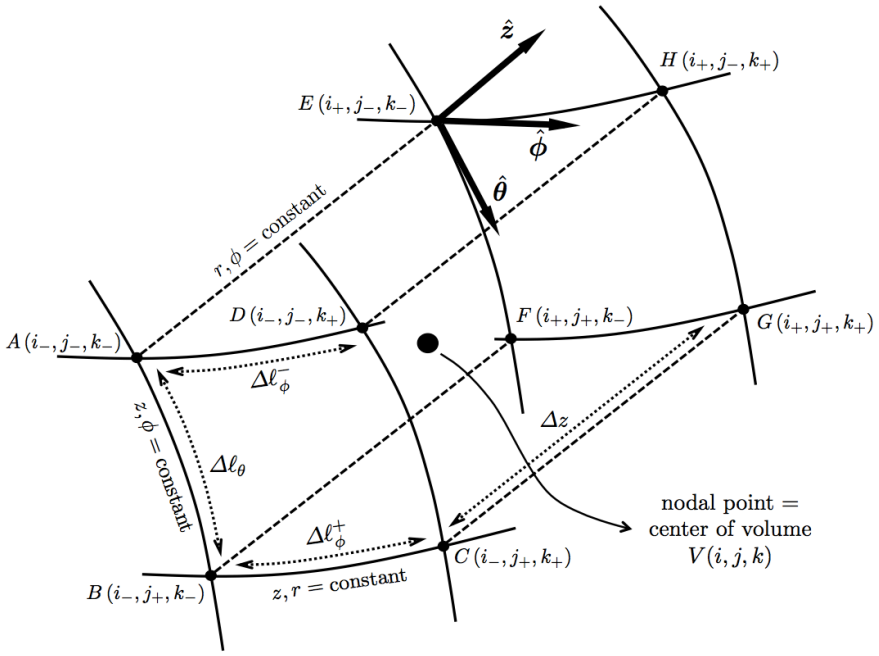

Figure 4.18: Typical finite volume in three-dimensional (z, θ, ϕ) space, centered around an arbitrary nodal point with indices (i, j, k). The uniform discretization with respect to (z, r, ϕ) ensures that all such computational cells have equal volume $\Delta V = \Delta z \Delta r \Delta\phi$.

Similarly, faces $ADHE$ and $BCGF$ have unit normal $\hat{\boldsymbol{\theta}}$ and areas $\Delta z \Delta\ell_\phi^-$ and $\Delta z \Delta\ell_\phi^+$, respectively, whereas faces $ABFE$ and $DCGH$ have unit normal $\hat{\boldsymbol{\phi}}$ and area $\Delta z \Delta\ell_\theta$. The volume of the computational cell is $\Delta V = \Delta z \Delta r \Delta\phi$.

In order to satisfy conservation of the distribution function exactly in each finite volume, we first integrate equation (4.117) over computational cell $V(i, j, k)$:

$$\iiint\limits_{V(i,j,k)} \left(\frac{\partial \Psi}{\partial t} + \nabla_J \cdot \mathbf{J} \right) \mathrm{d}z \, \mathrm{d}r \, \mathrm{d}\phi = 0. \tag{4.126}$$

After applying the divergence theorem to the second term, this can be recast as

$$\begin{aligned} 0 = \frac{\partial}{\partial t} \iiint\limits_{V(i,j,k)} \Psi \, \mathrm{d}z \, \mathrm{d}r \, \mathrm{d}\phi + \iint\limits_{ABCD} J_z \, \mathrm{d}r \, \mathrm{d}\phi - \iint\limits_{EFGH} J_z \, \mathrm{d}r \, \mathrm{d}\phi \\ + \iint\limits_{ADHE} J_\theta \, \mathrm{d}z \, \mathrm{d}\phi - \iint\limits_{BCGF} J_\theta \, \mathrm{d}z \, \mathrm{d}\phi \\ + \iint\limits_{ABFE} J_\phi \, \mathrm{d}z \, \mathrm{d}r - \iint\limits_{DCGH} J_\phi \, \mathrm{d}z \, \mathrm{d}r. \end{aligned} \tag{4.127}$$

Volume and surface integrals in equation (4.127) are approximated to second-order using a midpoint rule. After division by ΔV, this leads to the discretized equation:

$$\begin{aligned} 0 = \frac{\partial \Psi^{i,j,k}}{\partial t} + \frac{1}{\Delta z} \left[J_z(i_+, j, k) - J_z(i_-, j, k) \right] \\ + \frac{1}{\Delta r} \left[J_\theta(i, j_+, k) \sin\theta^{j_+} - J_\theta(i, j_-, k) \sin\theta^{j_-} \right] \\ + \frac{\Delta \ell_\theta}{\Delta r \Delta \phi} \left[J_\phi(i, j, k_+) - J_\phi(i, j, k_-) \right]. \end{aligned} \tag{4.128}$$

In order to integrate this equation, we must first obtain approximate expressions for the fluxes at the centers of the six volume faces. This is done using linear interpolation for terms involving Ψ, and centered finite differences for terms involving derivatives of Ψ. In the z and ϕ directions, this gives

$$J_z(i_+, j, k) \approx Pe_s \cos\theta^j \left(\frac{\Psi^{i+1,j,k} + \Psi^{i,j,k}}{2} \right) - 2\Lambda Pe_s^2 \left(\frac{\Psi^{i+1,j,k} - \Psi^{i,j,k}}{\Delta z} \right), \tag{4.129}$$

$$\begin{aligned} J_\phi(i, j, k_+) \approx \frac{1}{2} \Bigg[Pe_f S(z^i) \cos\theta^j \cos\phi^{k_+} \left(\frac{\Psi^{i,j,k+1} + \Psi^{i,j,k}}{2} \right) \\ - \frac{1}{\sin\theta^j} \left(\frac{\Psi^{i,j,k+1} - \Psi^{i,j,k}}{\Delta \phi} \right) \Bigg], \end{aligned} \tag{4.130}$$

with similar expressions for $J_z(i_-, j, k)$ and $J_\phi(i, j, k_-)$. The approximation of J_θ is slightly more involved due to the non-uniformity of the mesh with respect to θ.

Derivatives with respect to θ are calculated using symmetric central finite differences in terms of r after application of the chain rule, and linear interpolation is used with respect to the θ variable, leading to the approximation

$$J_\theta(i,j_+,k) \approx \frac{1}{2}\left\{Pe_f S(z^i)\cos\theta^{j_+}\cos\phi^k\left[\lambda^{j_+}\Psi^{i,j+1,k}+(1-\lambda^{j_+})\Psi^{i,j,k}\right]\right. \\ \left. +\sin\theta^{j_+}\left(\frac{\Psi^{i,j+1,k}-\Psi^{i,j-1,k}}{\Delta r}\right)\right\}, \tag{4.131}$$

with a similar expression for $J_\theta(i,j_-,k)$. The interpolation weight λ^{j_+} is given by

$$\lambda^{j_+} = \frac{\cos^{-1}(r^j+\frac{\Delta r}{2})-\cos^{-1}(r^j)}{\cos^{-1}(r_j+\Delta r)-\cos^{-1}(r^j)}. \tag{4.132}$$

When integrating equation (4.128) in time, care must be taken when dealing with cells adjacent to the poles of the unit sphere ($j=1$ and N_r), as these cells are missing one face. For instance, cells with $j=1$ are such that $A=D$ and $E=H$ in the diagram of figure 4.18, so that face $ADHE$ is missing and the corresponding flux should not be included in the discretized equation.

Boundary conditions also need to be specified to proceed with the time integration. Periodic boundary conditions are used in the ϕ direction, yielding:

$$J_\phi(1/2,j,k) = J_\phi(N_\phi-1/2,j,k) \quad \text{and} \quad J_\phi(N_\phi+1/2,j,k) = J_\phi(3/2,j,k). \tag{4.133}$$

Treatment of the boundaries in the θ and z directions differs depending on whether steric exclusion with the walls is included or not.

4.C.1 Without steric exclusion

When steric exclusion is not included and the simple boundary condition of equation (4.7) is used, θ varies over its full range $[0, \pi]$. However, no boundary condition is needed along θ as the boundary cells with $j = 1$ and N_r are missing one face as explained above, which eliminates the need to specify $J_\theta(i, 1/2, k)$ and $J_\phi(i, N_r + 1/2, k)$. Along the z direction, the boundary condition is simply the no-flux condition (4.7), which translates into

$$J_z(i, j, 1/2) = J_z(i, j, N_z + 1/2) = 0. \tag{4.134}$$

4.C.2 With steric exclusion

The situation is more complex when steric exclusion is accounted for, as the boundary conditions needs to be enforced on the hypersurfaces defined in equations (4.105)–(4.106). It is convenient in this case to choose N_z and N_r such that

$$\Delta z = L^* \Delta r \quad \text{or} \quad N_z = \frac{N_r}{L^*}. \tag{4.135}$$

Indeed this ensures that the hypersurfaces fall onto grid points and eliminates the need for further interpolation. However, if L^* is small, this implies that a significantly finer resolution is needed along z than along θ. As we discussed in Appendix A, the hypersurfaces limit the range of allowable values of θ to an interval of the form $[\theta_1(z), \theta_2(z)] \subset [0, \pi]$ for particles located near the walls. After discretization of the domain and choosing N_z and N_r to satisfy condition (4.135), we find that for any nodal point with coordinate z^i, there is a finite range $[\theta^{j_1(i)}, \theta^{j_2(i)}]$ of allowable values

of θ^j, with

$$j_1(i) = \begin{cases} \dfrac{N_r}{2} + 1 - i & \text{if } z \leq -1 + L^*, \\ \dfrac{N_r}{2} - N_z + i & \text{if } z \geq 1 - L^*, \\ 1 & \text{otherwise,} \end{cases} \tag{4.136}$$

$$j_2(i) = \begin{cases} \dfrac{N_r}{2} + i & \text{if } z \leq -1 + L^*, \\ \dfrac{N_r}{2} + N_z + 1 - i & \text{if } z \geq 1 - L^*, \\ N_r & \text{otherwise.} \end{cases} \tag{4.137}$$

Interior nodal points such that $j \in [j_1(i) + 1, j_2(i) - 1]$ are such that full cuboidal finite volumes in (z, r, ϕ) can be constructed around them, and therefore do not require any special boundary treatment. Boundary nodal points such that $j = j_1(i)$ or $j_2(i)$, however, are contained inside prisms whose hypotenuses coincide with the hypersurfaces. These finite volumes can be treated in the same way as interior control volumes by prescribing zero-flux contributions from surfaces lying outside of the domain, by multiplying the volume ΔV by 0.5, and by adjusting the surface area of faces $ABFE$ and $DCGH$ to a reduced triangular area given by

$$\Delta A = \frac{\Delta z \Delta l_\theta}{2} + \left[r^j \Delta l_\theta - 2 \sin\left(\frac{\Delta l_\theta}{2}\right) \cos\left(\frac{\theta^{j+} + \theta^{j-}}{2}\right) \right]. \tag{4.138}$$

4.D Active particle trajectories and shear trapping

In this Appendix, we rationalize the linear dependence of the depletion layer thickness δ_D upon Pe_s/Pe_f by deriving the trajectory of a deterministic swimmer

whose dynamics result from self-propulsion and shear rotation via Jeffery's equation. A similar derivation was previously presented by Zottl and Stark [135, 136]. In dimensional variables, the equations of motion of the swimmer are written

$$\dot{z}(t) = V_s \cos\theta(t), \tag{4.139}$$

$$\dot{\mathbf{p}}(t) = (\mathbf{I} - \mathbf{pp})\cdot(\zeta\mathbf{E} + \mathbf{W})\cdot\mathbf{p}. \tag{4.140}$$

Here, ζ is a shape parameter, with $\zeta \approx 1$ for a slender particle as we have assumed in the rest of the chapter. The two second-order tensors $\mathbf{E}$ and $\mathbf{W}$ are the rate-of-strain and vorticity tensors of the imposed flow, respectively:

$$\mathbf{E} = \frac{\dot{\gamma}_w}{2} z(t) \left(\hat{\mathbf{y}}\hat{\mathbf{z}} + \hat{\mathbf{z}}\hat{\mathbf{y}}\right), \qquad \mathbf{W} = \frac{\dot{\gamma}_w}{2} z(t) \left(\hat{\mathbf{y}}\hat{\mathbf{z}} - \hat{\mathbf{z}}\hat{\mathbf{y}}\right). \tag{4.141}$$

Parameterizing the orientation vector as $\mathbf{p} = (\sin\theta\cos\phi, \sin\theta\sin\phi, \cos\theta)$, we can use equation (4.140) to obtain expressions for the time rate of change of the polar and azimuthal angles of the swimmer as

$$\dot{\theta}(t) = \frac{\dot{\gamma}_w}{2} z(t) \sin\phi(t) \left[(\zeta+1)\cos^2\theta(t) - (\zeta-1)\sin^2\theta(t)\right], \tag{4.142}$$

$$\dot{\phi}(t) = \frac{\dot{\gamma}_w}{2} z(t) (\zeta+1) \frac{\cos\theta(t)\cos\phi(t)}{\sin\theta(t)}. \tag{4.143}$$

Equations (4.139), (4.142) and (4.143) form a closed system of coupled ordinary differential equations that can be solved for the swimmer dynamics.

Any swimmer that is not perfectly aligned with the walls ($\cos\theta \neq 0$) will tend to migrate towards one of the boundaries due to self-propulsion, while shear rotation tends to align it along the flow direction causing it to get trapped. Recalling the

definition of χ as the ratio of the time scale for shear rotation to the time it takes for a swimmer to cross the channel,

$$\chi = \frac{V_s}{2\dot{\gamma}_w H} = \frac{Pe_s}{Pe_f}, \tag{4.144}$$

we expect two different regimes. When $\chi \gg 1$, any swimmer released from the centerline with initial orientation (θ_0, ϕ_0) will reach one of the walls before becoming trapped. On the other hand, when $\chi \ll 1$, we expect there to exist a position $z_{trap}(\theta_0, \phi_0)$ inside the channel where the swimmer gets trapped due to shear alignment. This indeed corresponds to the regime discussed in §4.4.2, where depletion from the centerline and shear-trapping were predicted to occur for $Pe_s \ll 1$ and $Pe_f \gg 1$.

To derive a quantitative estimate for z_{trap}, we calculate the value of z at which θ first reaches $\pm\pi/2$. We first consider the case of a particle with initial position $z_0 = 0$ and orientation defined by $\theta_0 \in [0, \pi/2)$, $\phi_0 = 3\pi/2$. For this specific initial configuration, $\dot{\phi}(0) = 0$ which implies $\phi(t) = 3\pi/2$ for all times. The motion is two-dimensional in this case, and the dynamics is governed by the two coupled ordinary differential equations

$$\dot{z}(t) = V_s \cos\theta(t), \tag{4.145}$$

$$\dot{\theta}(t) = -\frac{\dot{\gamma_w}}{2} z(t) \left[(\zeta + 1)\cos^2\theta(t) - (\zeta - 1)\sin^2\theta(t) \right]. \tag{4.146}$$

An equation for the swimmer trajectory can then be obtained by taking the ratio of (4.145) and (4.146):

$$\frac{\mathrm{d}\theta}{\mathrm{d}z} = \frac{z}{H} \left[\frac{(\zeta + 1) - 2(\zeta - 1)\sin^2\theta(t)}{2\chi\cos\theta} \right]. \tag{4.147}$$

This can be integrated from $(z,\theta) = (0,\theta_0)$ to $(z_{trap}, \pi/2)$, yielding

$$\left(\frac{z_{trap}(\theta_0)}{H}\right)^2 = \chi\sqrt{\frac{1}{2\zeta(\zeta+1)}}\left(\tanh^{-1}\sqrt{\frac{2\zeta}{\zeta+1}} - \tanh^{-1}\sqrt{\frac{2\zeta}{\zeta+1}\sin\theta_0}\right). \quad (4.148)$$

For a typical swimmer of aspect ratio 10, we estimate $\zeta \approx 0.98$. Taking the initial configuration to be $\theta_0 = 0$, equation (4.148) simplifies to $z_{trap}/H \approx \sqrt{3\chi} \approx 1.73\sqrt{Pe_s/Pe_f}$. This estimate is consistent with the high-Pe_f scaling analysis of §4.4.2, as well as with the numerical results of §4.4.3 where we found $\delta_D \approx 2.404\sqrt{Pe_s/Pe_f}$.

The more general case of an arbitrary initial orientation (θ_0, ϕ_0) can also be solved analytically. Combining equations (4.142) and (4.143) to eliminate $z(t)$, we find after integration:

$$\cos\phi = \cos\phi_0\left|\frac{(\zeta+1)\operatorname{cosec}^2\theta - 2\zeta}{(\zeta+1)\operatorname{cosec}^2\theta_0 - 2\zeta}\right|^{\frac{1}{2}}. \quad (4.149)$$

Now, using equations (4.139) and (4.142), we get

$$\left(\frac{z_{trap}(\phi_0,\theta_0)}{H}\right)^2 = 2\chi\int_{\theta_0}^{\pi/2}\frac{\cos\theta}{\left(\zeta+1-2\,\zeta\sin^2\theta\right)\sqrt{1-\cos^2\phi}}\,\mathrm{d}\theta, \quad (4.150)$$

where $\sin\phi$ is known in terms of θ using (4.149). This expression confirms the scaling of z_{trap} with $\sqrt{\chi}$, and it can in fact be shown that z_{trap} in equation (4.150) has an upper bound given by the previous estimate (4.148).

Chapter 5

On the distribution and swim pressure of run-and-tumble particles in confinement

5.1 Introduction

The propensity of confined self-propelled particles to accumulate at boundaries is a trademark of active matter and has been reported in many experiments on bacterial suspensions [118, 130, 159] as well as simulations based on various models [33, 125, 134]. Several disparate mechanisms have been proposed in explanation, including wall hydrodynamic interactions [118] and scattering due to collisions with the walls [123], though recent the oretical efforts have shown that the mere interplay of self-propulsion, stochastic processes and confinement is sufficient to explain accumulation [133, 157, 23]. With few exceptions, however, these models have necessitated particle diffusion, which in reality is nearly negligible in bacterial suspensions where stochasticity in the

dynamics takes instead the form of run-and-tumble random walks [160].

An understanding of the distribution of active particles in confinement is especially critical for determining the mechanical force per unit area exerted by the suspension on the boundaries, or so-called 'swim pressure'. This novel concept, which has received much scrutiny recently, describes the force that must be applied on containing osmotic walls to keep self-propelled particles confined. Models based on the virial theorem [161, 162, 163] and on direct calculations of the wall mechanical pressure [164] in infinite or semi-infinite collections of spherical swimmers have all arrived at a simple ideal-gas law Π_i for the swim pressure in the limit of infinite dilution:

$$\Pi_i = n\zeta D_t = n\zeta \frac{V_0^2}{3\lambda}, \tag{5.1}$$

where n is the mean number density, ζ is the viscous drag coefficient of a particle and $D_t = V_0^2/3\lambda$ is the long-time translational diffusivity of an unconfined run-and-tumble swimmer expressed in terms of its speed V_0 and mean tumbling rate λ [160]. Equation (5.1) and its extension to finite concentrations have proven useful to explain motility-induced phase separation in suspensions of self-propelled colloids [161, 165], though its general validity as a thermodynamic equation of state for the pressure of active matter remains controversial [166, 167, 168] and appears to be limited to unconfined spherical particles [162, 164, 169].

In this work, we analyze the simple case of a dilute suspension of athermal run-and-tumble spherical swimmers confined between two parallel flat plates. We propose in §2 a kinetic model based on two probability density functions describing the spatial and orientational distribution of the particles inside the gap and at the walls, which are coupled via flux conditions and only account for the effects of swimming

and orientation decorrelation by tumbling. Further, our model implicitly captures hard-wall steric interactions without resorting to a soft potential to describe wall collisions as in previous theories [164, 169]. A semi-analytical solution method is outlined in §3, which provides the full probability density functions and allows for a direct calculation of the mechanical swim pressure exerted on the walls in terms of the polarization of the surface distributions. Results for the distributions and swim pressure are presented in §4, where they are shown to compare very favorably with Monte-Carlo simulations.

5.2 Problem definition and theoretical model

5.2.1 Problem formulation

As a minimal model for an active suspension in confinement, we consider a dilute collection of self-propelled spherical particles confined between two infinite parallel plates separated by a distance $2H$ (see figure 5.1). The swimmers are non-Brownian and simply perform a run-and-tumble random walk: straight runs of duration τ at constant velocity V_0 along the unit director $\mathbf{p}$ alternate with instantaneous tumbling events causing random and uncorrelated reorientations of $\mathbf{p}$. The time τ between tumbles is an exponentially distributed random variate with mean λ^{-1}, where the tumbling rate λ is assumed to be independent of position and orientation. To elucidate the interplay between run-and-tumble dynamics and confinement, we focus on the dilute limit and entirely neglect interparticle interactions. Particle-wall interactions are purely steric: as a swimmer meets one of the two surfaces, the normal component of its swimming motion is cancelled by a hard-core repulsive force causing it to stay

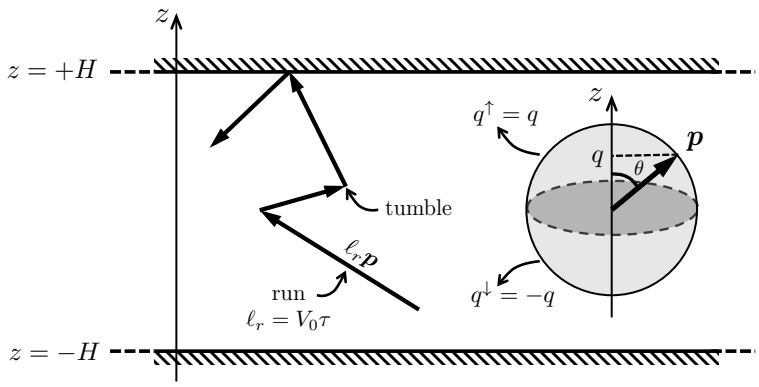

Figure 5.1: Problem definition: run-and-tumble particles are confined between two flat plates separated by $2H$. The distribution of particles is a function of z and $q = \mathbf{p} \cdot \hat{\boldsymbol{z}} = \cos\theta \in (-1, 1)$. Orientations pointing towards the top and bottom walls are parametrized by $q^{\uparrow} = q$ and $q^{\downarrow} = -q$, respectively, both defined in $(0, 1)$.

at and push against the wall until a subsequent tumbling event reorients it into the bulk. Tumbling events occurring at the walls can lead to reorientation into the wall or into the bulk, so that a particle at a surface may need to undergo more than one tumble before it is able to escape.

There are only two length scales in the problem: the mean run length $\ell_r = V_0\lambda^{-1}$ and the channel width $2H$. We define their ratio as the Péclet number $Pe = \ell_r/2H = V_0/2\lambda H$, where the two limits $Pe \to 0$ and $Pe \to \infty$ describe weak and strong confinement, respectively. Due to the symmetry of the problem, the distribution of particles in the channel only depends on two degrees of freedom: the wall-normal coordinate $z \in (-H, H)$ and the wall-normal component of the particle director $q = \mathbf{p} \cdot \hat{\mathbf{z}} = \cos\theta \in (-1, 1)$. It is convenient to distinguish particles pointing towards the top and bottom walls, and to this end we divide the unit sphere of orientations into two hemispheres and define two distinct orientation coordinates $q^{\uparrow} = q \in (0, 1)$ and $q^{\downarrow} = -q \in (0, 1)$ for particles pointing up or down, respectively, as depicted in

figure 5.1.

The distribution of particles in the channel is then fully described by a bulk probability density function $\psi(z,q)$ and by two surface probability density functions $\psi_s^{\uparrow}(q^{\uparrow})$ and $\psi_s^{\downarrow}(q^{\downarrow})$, which are only defined over half of the orientations since the surfaces cannot sustain a concentration of particles pointing towards the bulk. By symmetry, we expect

$$\psi(z,-q)=\psi(-z,q), \quad \psi(z,q^{\uparrow})=\psi(-z,q^{\downarrow}) \quad \text{and} \quad \psi_s^{\uparrow}(q^{\uparrow})=\psi_s^{\downarrow}(q^{\downarrow}) \tag{5.2}$$

for $q^{\uparrow}=q^{\downarrow}$. Next, we describe the coupled bulk/surface conservation equations satisfied by these distributions, together with the appropriate boundary conditions.

5.2.2 Bulk conservation equation

The steady bulk probability density function $\psi(z,q)$ satisfies the conservation equation

$$V_0\, q\, \frac{\partial}{\partial z}\psi\,(z,q) = -\lambda\,\psi\,(z,q) + \frac{1}{2}\int_{-1}^{1} \lambda\,\psi\,(z,q')\;\mathrm{d}q'. \tag{5.3}$$

The left-hand side describes transport along z due to self-propulsion. Run-and-tumble dynamics is captured by the right-hand side, where the first term accounts for depletion due to swimmers tumbling away from orientation q, and the second term for restoration due to swimmers tumbling from orientations q' into q. It is also useful to define the orientational moments of order j of the bulk probability density function on the full sphere and on the upper/lower hemispheres of orientations as

$$M_j(z)=\int_{-1}^{1} q^j\,\psi\,(z,q)\;\mathrm{d}q \quad \text{and} \quad M_j^{\uparrow\downarrow}(z)=\int_{0}^{1} (q^{\uparrow\downarrow})^j\,\psi(z,q^{\uparrow\downarrow})\,\mathrm{d}q^{\uparrow\downarrow}, \tag{5.4}$$

and we note that the zeroth, first and second moments correspond to the concentration, polarization, and nematic alignment fields:

$$c(z) = M_0(z), \qquad m(z) = M_1(z), \qquad S(z) = M_2(z), \tag{5.5}$$

$$c^{\uparrow\downarrow}(z) = M_0^{\uparrow\downarrow}(z), \qquad m^{\uparrow\downarrow}(z) = M_1^{\uparrow\downarrow}(z), \qquad S^{\uparrow\downarrow}(z) = M_2^{\uparrow\downarrow}(z). \tag{5.6}$$

By symmetry, it is straightforward to see that full moments of even order are even functions of z whereas those of odd order are odd functions. With these notations, the bulk conservation equation (5.3) simplifies to

$$\ell_r \, q \, \frac{\partial}{\partial z} \psi \left(z, q \right) = -\psi(z, q) + \tfrac{1}{2} c(z). \tag{5.7}$$

Taking the zeroth and first orientational moments of equation (5.7) and applying symmetry conditions immediately shows that the polarization is zero and the nematic alignment is uniform across the channel:

$$m(z) = 0 \quad \text{and} \quad S(z) = S_0 \quad \forall z \in (-H, H), \tag{5.8}$$

where S_0 is a constant independent of z.

5.2.3 Surface conservation equations

Similarly, conservation equations for the steady surface probability density functions at the walls can be written. We first define the surface concentration and

polarization as

$$c_s = \int_0^1 \psi_s^{\uparrow\downarrow}(q^{\uparrow\downarrow})\,\mathrm{d}q^{\uparrow\downarrow} \quad \text{and} \quad m_s = \int_0^1 q^{\uparrow\downarrow}\,\psi_s^{\uparrow\downarrow}(q^{\uparrow\downarrow})\,\mathrm{d}q^{\uparrow\downarrow}, \tag{5.9}$$

and note that the values of c_s and m_s are the same at both walls. With these notations, the conservation equation at the upper wall ($z = +H$) reads

$$V_0\, q^{\uparrow}\, \psi(H, q^{\uparrow}) = \lambda \left[\psi_s^{\uparrow}(q^{\uparrow}) - \tfrac{1}{2} c_s\right], \tag{5.10}$$

and a similar equation holds at $z = -H$. The right-hand side in equation (5.10) describes tumbling processes at the wall. The left-hand side, on the other hand, captures the flux of particles that enter the surface from the bulk by self-propulsion, and is therefore proportional to the bulk probability density function $\psi(H, q^{\uparrow})$ next to the wall. Evaluating the zeroth and first moments of equation (5.10) yields simple relations between c_s and m_s and the values of the bulk moments in the vicinity of the wall:

$$c_s = 2\ell_r m^{\uparrow}(H), \qquad m_s - \tfrac{1}{4} c_s = \ell_r S^{\uparrow}(H). \tag{5.11a, b}$$

5.2.4 Boundary condition and particle number conservation

Equation (5.10) can be interpreted as a boundary condition for orientations pointing into the wall. For orientations pointing away from the wall, the swimming flux away from the wall must be balanced by tumbling of particles from the surface towards the bulk. Simply stated, particles on the surface that tumble to an orientation pointing into the bulk are transported away by self-propulsion. This leads to the

additional condition

$$V_0\, q^{\downarrow}\, \psi(H, q^{\downarrow}) = \tfrac{1}{2}\lambda\, c_s \qquad \text{or} \qquad \ell_r\, q^{\downarrow}\, \psi(H, q^{\downarrow}) = \tfrac{1}{2} c_s. \tag{5.12}$$

As c_s is constant and finite, this condition suggests divergence and discontinuity of the bulk probability density function for orientations parallel to the wall ($q^{\downarrow} \to 0$), as will indeed be verified in our analytical solution and stochastic simulations. Taking the zeroth and first moments of equation (5.12) provides the two additional relations

$$c_s = 2\ell_r m^{\downarrow}(H), \qquad c_s = 4\ell_r S^{\downarrow}(H). \tag{5.13a, b}$$

Finally, the above system of equations for the bulk and surface distributions is supplemented by a constraint on the total number of particles in the channel:

$$2\, c_s + \int_{-H}^{H} c(z)\, \mathrm{d}z = N, \tag{5.14}$$

where N is the particle number in a vertical slice of unit horizontal cross-section.

5.3 Method of solution and swim pressure calculation

5.3.1 Integral equation for the moments

We now outline a solution method for the system described in §5.2. As a first step, we derive an integral equation relating the bulk orientational moments to the concentration field. The bulk concentration equation (5.7) can be viewed as a

linear inhomogeneous ordinary differential equation for $\psi(z, q)$ where q is a parameter. We solve it by the method of variation of constants, treating orientations $q^{\uparrow}$ and $q^{\downarrow}$ separately. After applying the boundary condition (5.12), we obtain a general expression for the bulk density function:

$$\psi(z, q^{\uparrow\downarrow}) = \frac{c_s}{2\ell_r\, q^{\uparrow\downarrow}} \exp\left[-\frac{(H \pm z)}{\ell_r\, q^{\uparrow\downarrow}}\right] \pm \int_{\mp H}^{z} \frac{c(z')}{2\ell_r\, q^{\uparrow\downarrow}} \exp\left[\mp\frac{(z - z')}{\ell_r\, q^{\uparrow\downarrow}}\right] \mathrm{d}z'. \tag{5.15}$$

Note that the bulk and surface concentrations $c(z)$ and c_s both appear on the right-hand side and are still unknown. However, equation (5.15) shows that their knowledge entirely specifies the bulk distribution $\psi(z, q)$. The bulk moments of order j on both hemispheres of orientations are immediately obtained by integration:

$$M_j^{\uparrow\downarrow}(z) = \frac{c_s}{2\ell_r}\mathcal{E}_{j+1}\left[\frac{H \pm z}{\ell_r}\right] \pm \int_{\mp H}^{z} \frac{c(z')}{2\ell_r}\, \mathcal{E}_{j+1}\left[\pm\frac{(z - z')}{\ell_r}\right] \mathrm{d}z', \tag{5.16}$$

where $\mathcal{E}_j$ is the exponential integral function defined as

$$\mathcal{E}_j(z) = \int_0^1 u^{j-2} \exp\left(-\frac{z}{u}\right) \mathrm{d}u. \tag{5.17}$$

Finally, the moment of order j on the full sphere of orientations can be shown to be

$$M_j(z) = \frac{c_s}{2\ell_r}\left(\mathcal{E}_{j+1}\left[\frac{H + z}{\ell_r}\right] + \mathcal{E}_{j+1}\left[\frac{H - z}{\ell_r}\right]\right) + \int_{-H}^{H} \frac{c(z')}{2\ell_r}\mathcal{E}_{j+1}\left[\left|\frac{z - z'}{\ell_r}\right|\right] \mathrm{d}z'. \tag{5.18}$$

5.3.2 Concentration field and solution procedure

Setting $j = 0$ in equation (5.18) immediately provides an integral equation for the yet unknown concentration profile:

$$c(z) = \frac{c_s}{2\ell_r}\left(\mathcal{E}_1\left[\frac{H+z}{\ell_r}\right] + \mathcal{E}_1\left[\frac{H-z}{\ell_r}\right]\right) + \int_{-H}^{H} \frac{c(z')}{2\ell_r}\mathcal{E}_1\left[\left|\frac{z-z'}{\ell_r}\right|\right] \mathrm{d}z'. \qquad (5.19)$$

Dividing through by c_s, we obtain an equation for $c(z)/c_s$ that can be solved numerically. For finite ℓ_r, we find that an approximate solution is easily obtained iteratively by casting equation (5.19) in the form $c_{k+1}(z)/c_s = f[c_k(z)/c_s]$, starting with an initial guess which we take to be $c_0(z) = 0$. In strong confinement ($Pe \gtrsim 10$), the solution converges in $O(20)$ iterations, though more iterations are required in wider channels.

To complete the solution for the concentration field, the value of the surface concentration c_s must be calculated. Having previously obtained $c(z)/c_s$, it is easily evaluated by recasting the constraint (5.14) as

$$c_s = N\left[2 + \int_{-H}^{H} \frac{c(z)}{c_s}\,\mathrm{d}z\right]^{-1}. \qquad (5.20)$$

Knowledge of $c(z)$ and c_s then directly provides all the remaining variables. The bulk probability density function is given by equation (5.15), while the bulk partial and full moments can be calculated using equations (5.16) and (5.18). Finally, the surface orientation distribution is provided by equation (5.10) and the surface polarization by equation (5.11*b*). Solutions obtained by this method are presented in §5.4, where excellent agreement with results from Monte-Carlo simulations will be shown.

5.3.3 Swim pressure calculation

The above formulation provides a direct way of estimating the swim pressure in the system, which is simply the force per unit area exerted by the particles at the walls as they push on the surface. Specifically, the normal component of the motion of each particle at the upper wall is resisted by a force $\zeta V_0 q^{\uparrow}$, where ζ is the viscous drag coefficient of one particle [161]. Knowing the surface probability density function $\psi_s^{\uparrow}$, an expression for the swim pressure is then easily found as

$$\Pi_s = \int_0^1 \zeta V_0 q^{\uparrow} \psi_s^{\uparrow}(q^{\uparrow}) \, \mathrm{d}q^{\uparrow} = \zeta V_0 m_s, \tag{5.21}$$

where m_s is the surface polarization. Combining equations (5.11b) and (5.13b) to solve for m_s yields a simple relation between the swim pressure and the second moment S_0 of the bulk distribution function:

$$\Pi_s = \zeta V_0 \ell_r \left[S^{\uparrow}(H) + S^{\downarrow}(H) \right] = \zeta \frac{V_0^2}{\lambda} S(H) = \zeta \frac{V_0^2}{\lambda} S_0. \tag{5.22}$$

A similar result was obtained by Solon *et al.* [164]. In bulk unconfined systems, previous models have led to the ideal-gas pressure Π_i of equation (5.1), which contains no information on particle orientations due to isotropy but follows the same scaling as equation (5.22). To compare both predictions, we define a dimensionless pressure as the ratio of equations (5.22) and (5.1):

$$\mathcal{P} = \frac{\Pi_s}{\Pi_i} = \frac{3 m_s}{n \ell_r} = \frac{3 S_0}{n}, \tag{5.23}$$

where $n = N/2H$ is the mean number density in our system. $\mathcal{P} - 1$ quantifies the departure from the ideal-gas swim pressure. In an infinitely wide channel ($Pe \to 0$), the bulk distribution at the centerline is expected to be isotropic, implying $S_0 = n/3$ and therefore $\mathcal{P} \to 1$. This will be confirmed in our numerical results in §4, where we also show that $\mathcal{P}$ deviates from 1 when $Pe > 0$ as a result of confinement.

5.4 Results and comparison to simulations

5.4.1 Simulation method

To validate our model, we also perform Markov-chain Monte-Carlo simulations of run-and-tumble swimmers between two hard walls. During a run of duration τ, the swimmer trajectory simply evolves as $\mathbf{x}(t + \Delta t) = \mathbf{x}(t) + V_0\mathbf{p}\,\Delta t$ where Δt is a short time step. Each run is then followed by a tumbling event, where the new orientation vector $\mathbf{p}$ is picked randomly on the unit sphere. The time τ between two consecutive tumbles is drawn from an exponential distribution with cumulative distribution function $F(\tau) = 1 - \exp[-\lambda\tau]$. When a swimmer meets a wall, it remains there and continues to tumble until it reorients towards the bulk and swims away. Time-averaged bulk and surface probability density functions were extracted from orientational and spatial histograms, and convergence was checked with respect to Δt and to the duration of the simulation.

5.4.2 Theoretical and numerical results

Solutions for the bulk concentration profile are depicted in figure 5.2, where both the full concentration $c(z)$ and the partial 'up' concentration $c^{\uparrow}(z)$ are plotted for

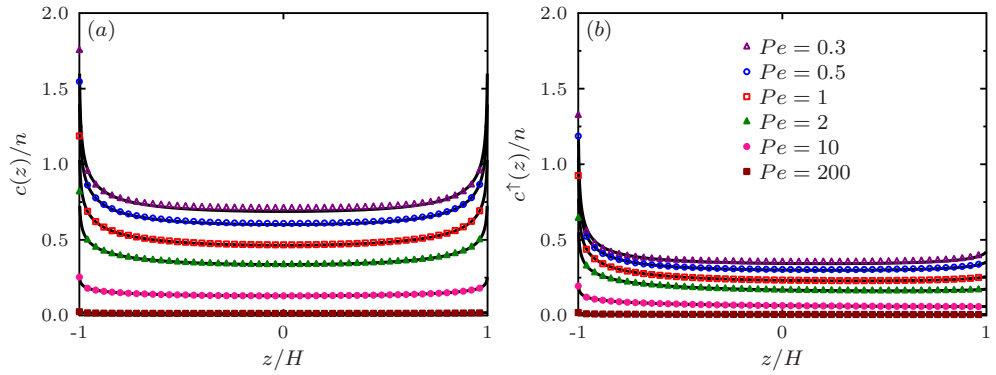

Figure 5.2: Concentration profiles across the channel for various values of $Pe = \ell_r/2H$: (a) full concentration $c(z)$, and (b) partial 'up' concentration $c^{\uparrow}(z)$. Solid lines show the semi-analytical solution of §5.3, and symbols are Monte-Carlo simulation results.

various values of the Péclet number, which measures the degree of confinement. The full concentration profiles in figure 5.2(a) show significant accumulation at the walls, with wall boundary layers whose thickness scales with ℓ_r. An interesting and unique feature of non-interacting and non-aligning spherical run-and-tumble particles is that accumulation occurs in the absence of polarization, and $m(z)$ is found to be strictly zero throughout the channel as already derived in equation (5.8). A non-zero polarization would indeed lead to a net flux of particles in the wall-normal direction, which cannot happen in a confined athermal system, unlike in Brownian suspensions where this flux can be balanced by diffusion [23]. The profiles also show the presence of a singularity in $c(z)$ at the walls, which is a direct consequence of the boundary condition (5.12) and is also obvious from the solution (5.19) where $\mathcal{E}_1(0)$ diverges. Concentration singularities were also predicted by Elgeti and Gompper [157], though their model did not capture orientation distributions. As confinement becomes significant and Pe increases, the bulk concentration decreases throughout the channel to reach nearly zero at $Pe = 200$, indicating that strongly confined particles spend most of their time at the boundaries. Excellent quantitative agreement is obtained between theory and

Monte-Carlo simulations.

Figure 5.2(b) also shows the partial 'up' concentration obtained by only counting particles pointing towards the top wall. The asymmetry of the profiles and the singularity at the bottom wall indicates that on average there are more particles pointing away from the wall than towards it inside the wall accumulation layers. However, in order to satisfy no net polarization in the bulk, this implies that those particles pointing towards the wall are more strongly polarized than those pointing away. This point is confirmed in figure 5.3(a–b), showing the orientation distributions in the bulk in the vicinity of the top wall for orientations pointing away from and towards the wall. Figure 5.3(a) confirms the divergence of the bulk probability density in the neighborhood of orientations parallel to the wall ($q^{\downarrow} \to 0$) as expected from boundary condition (5.12), which is also captured by the simulations. The presence of this discontinuity can be rationalized as follows: particles that leave the surface at an orientation $q^{\downarrow} \gtrsim 0$ swim nearly parallel to the surface and therefore remain there much longer than particles leaving in other orientations. The distribution of particles pointing towards the wall in figure 5.3(b) shows no such singularity, but exhibits a weak finite peak at a critical value of $q^{\uparrow}$ for an intermediate range of Péclet numbers between 5 and 50, whose physical origin remains unclear. The orientation distribution $\psi_s^{\uparrow}(q^{\uparrow})$ of particles on the top wall is shown in figure 5.3(c) and shows a preferential alignment normal to the wall rather than parallel to it. However, this distribution becomes nearly isotropic under very strong confinement ($Pe = 1000$), for reasons that we elucidate below.

Taking moments of $\psi_s^{\uparrow}(q^{\uparrow})$ provides the surface concentration c_s and surface polarization m_s, which are plotted versus Péclet number in figure 5.4(a–b). Both

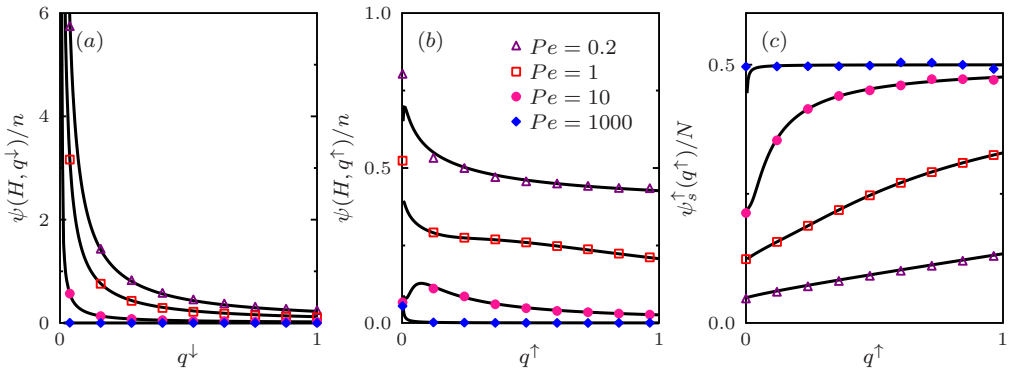

Figure 5.3: Bulk probability density at the top wall for (a) orientations pointing away from the wall and (b) orientations pointing towards it. (c) Surface probability density at the top wall as a function of $q^{\uparrow}$. Solid lines show the semi-analytical solution of §5.3, and symbols are Monte-Carlo simulation results.

quantities increase with increasing confinement, but asymptote as $Pe \to \infty$. The asymptote for c_s is $N/2$, meaning that in very narrow channels the particles spend all their time at the boundaries; indeed, the time $2H/V_0$ it takes them to cross the gap is infinitesimal compared to the mean run time λ^{-1}. This is also consistent with the decrease in the bulk concentration seen in figure 5.2(a). In this limit, particles tumbling away from one wall reach the other wall nearly instantaneously, leading to an isotropic surface orientation distribution in agreement with figure 5.3(c), hence the asymptote of $N/4$ for the wall polarization.

Lastly, the dependence of the dimensionless swim pressure $\mathcal{P}$ on the degree of confinement is illustrated in figure 5.4(c). In the limit of weak confinement ($H \gg \ell_r$ or $Pe \to 0$), the swim pressure is seen to tend to the ideal-gas law of equation (5.1) in both our model and simulations: $\mathcal{P} \to 1$ or $\Pi_s \to \Pi_i$. This corresponds to the limit of a single wall where the gap width $2H$ plays no role, and validates the results of previous studies in infinite or semi-infinite systems for which the expression for Π_i was first derived [161, 164]. Confinement, however, causes a decrease in the swim pressure,

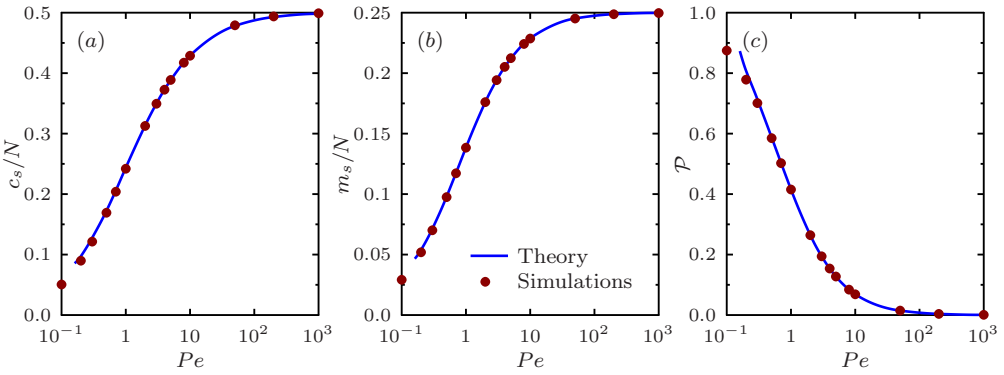

Figure 5.4: (a) Surface concentration c_s, (b) surface polarization m_s, and (c) dimensionless pressure $\mathcal{P}$ as functions of Péclet number $Pe = \ell_r/2H$. Solid lines show the semi-analytical solution of §5.3, and symbols are Monte-Carlo simulation results.

which in fact tends to zero for fixed n in very narrow gaps. The high-Pe asymptote for m_s describes the limiting behavior:

$$\mathcal{P} \to \frac{3}{4} Pe^{-1}, \quad \text{i.e.} \quad \Pi_s \to \frac{3}{4} Pe^{-1} \Pi_i = \frac{nH\zeta V_0}{2} = \frac{N\zeta V_0}{4} \tag{5.24}$$

as $Pe \to \infty$ (or $H \to 0$), which corresponds to $N/2$ particles pushing with an average force of $\zeta V_0/2$ against each wall. The decrease in pressure and the details of the asymptote agree with the previous two-dimensional results of Yang *et al.* [162], who also verified them in numerical simulations of self-propelled disks. They are also consistent with the study of Ray *et al.* [166], who analyzed the force on two nearby parallel plates in an active particle bath and proposed that the pressure inside the gap in a one-dimensional system with constant run length varies as $\Pi_i/(1 + Pe)$.

5.4.3 Summary and discussion

We have presented a simple continuum model for a dilute suspension of spherical run-and-tumble particles confined between two hard walls and interacting via purely

steric forces with the walls. The model improves upon our previous theory for confined Brownian suspensions [23] by allowing us to address the limit of zero temperature within a continuum framework and by incorporating a more realistic treatment of surface interactions and exchange processes between surfaces and the bulk. This description also provides a direct and simple way of calculating the mechanical swim pressure exerted on the walls and serves as a complementary approach to the work of Solon *et al.* [164], where a continuous description of the same problem using a soft potential for wall interactions was used to calculate the pressure. We have outlined an elegant approach to derive a semi-analytical solution for the probability density functions, and demonstrated excellent quantitative agreement between our model and results from discrete Monte-Carlo simulations.

Our theoretical predictions and simulation results have highlighted several striking features of confined suspensions of run-and-tumble particles, namely the presence of a singularity and discontinuity in the bulk probability density function for orientations nearly parallel to the walls in the near-wall region, and the existence of a concentration boundary layer of thickness of the order of ℓ_r that actually diverges at the walls. Our pressure calculations were shown to match the recently proposed ideal-gas equation of state of active matter in wide channels, thus further validating this ideal-gas law and confirming the prediction that the precise nature of particle-wall steric interactions has no impact on the wall mechanical pressure for spherical particles [164]. We demonstrated, however, that confinement leads to departures from this ideal behavior and specifically to a decrease in the swim pressure, which in fact vanishes in the limit of an infinitely narrow gap when the mean number density is held fixed. In this case, we found that swimmers spend all their time at the boundaries, which

provides the basis for previous models of strongly confined systems that only account for the surface distribution of swimmers [170].

While capturing the salient features of confined active suspensions, the problem under consideration remained minimal. Yet, the kinetic model presented here could be further modified to incorporate other effects and provide a more realistic description of biological or synthetic active systems. In particular, many active particles are rod-shaped and therefore also incur an aligning torque as they interact with boundaries. Recent theoretical work has shown that the wall pressure is modified in that case and becomes dependent upon the details of particle-wall interactions [169, 171]. In addition, experiments show that the surface-to-bulk tumbling of biological swimmers as well as certain types of synthetic swimmers is not uncorrelated but rather results in the preferential release of the particles near a specific angle [150, 172, 173]. Incorporating such details in our model is straightforward and would modify the distribution of particles near the walls with unexpected consequences for the mechanical pressure. Our basic model, validated here in the dilute limit, could also be modified to account for hydrodynamic couplings and to study the structure of the self-generated flows and collective dynamics of interacting active particles in confinement. In more complicated problems such as the ones described above, a complete solution for the bulk and surface probability density functions may not be tractable semi-analytically. Orientational moment equations with a suitable closure model [174, 23] likely would not perform well either because of the near-wall singularities in the bulk probability density function as well as complications arising from having to develop governing equations and closure approximations for the partial moments as opposed to the full ones. Extending the present model to non-planar boundaries, whether concave or convex, is not

straightforward either but would be of great interest for the theoretical description of active particle transport in complex geometries or of their interaction with and transport of passive payloads. This rich avenue is the focus of our future work.

Acknowledgement: Chapter 5, in part, is a reprint of the material as it appears in Journal of Fluid Mechanics: Rapids 2015. "On the distribution and swim pressure of run-and-tumble particles in confinement" by Ezhilan, Barath; Alonso, Roberto; Saintillan, David, Cambridge University Press, 2015. The dissertation author was the primary investigator and author of this paper.

Chapter 6

Transition to spontaneous directional flows in confined active suspensions

6.1 Introduction

Recent years have seen significant developments in the understanding of the emergence of collective motion in biologically active suspensions. There is widespread consensus that self-organization is such suspensions are driven by the stresses exerted by the active particles on the fluid as they propel themselves [175, 10, 4, 5, 12, 9, 33, 34, 19, 20, 176, 105]. Continuum kinetic theories, where a Smoluchowski equation for the probability distribution of the active particle positions and orientations is coupled to the Stokes equation for the flow arising from the active stresses, is an extremely powerful approach for understanding active fluids (as has been demonstrated in the preceding chapters). In this approach, the emergent behaviour in active systems is viewed as a

breakdown of stability of the various equilibrium states [19, 20, 39, 41, 85, 42, 21].

While collective self-organization in unconfined systems have been studied rigorously, analogous studies on confined active suspensions have been relatively scarce. Recent experiments have shown that confinement can stabilize the collective motion into controlled patterns such a robust double vortex in flattened drops [104, 177, 105] and stable unidirectional rotation in circular racetracks [178]. Such fascinating experiments motivate our interest in the theoretical investigation of the rich interplay between confinement and interactions in active suspensions.

While various phenemenological models for active liquid crystals have focussed on the effect of confinement on collective behavior, predicting fascinating features including spontaneous flow transitions [151, 152, 153, 154, 155], such predictions are yet to be confirmed from a hydrodynamics first-principles perspective. A few studies have attempted to use mean-field theories in confined active suspensions [142, 22, 1, 143, 179], but their treatment of the boundary conditions (for the active particle probability distribution function) have been very approximate. Moreover, these studies also included an external field (such as gravity or chemotaxis), hence making it difficult to understand the sole effect of confinement on the activity-driven emergent behavior.

Recent theoretical studies (including one of our own works discussed in chapter 4) have identified that the appropriate way of incorporating confinement within the mean-field framework for suspensions of Brownian swimmers is to prescribe a zero wall-normal translational active particle probability flux at both walls [125, 180, 23]. This condition essentially requires that the self-propulsive flux on the wall has to be balanced by a translational diffusive flux, which leads to polarity sorting. The striking

result, which is in agreement with experiments and Brownian Dynamics simulations, is that wall accumulation and wall-normal polarization in confined active suspensions happens even in the absence of external fields, hydrodynamic or alignment interactions and is simply a result of swimming, translational diffusion and confinement.

In the light of these recent theoretical insights, confinement can change the dynamics of active self-organization in a multitude of ways as outlined below.

- **Polarized and spatially inhomogenous base states**: The existence of polarized and spatially inhomogeneous equilibrium distributions in confined active suspensions has interesting implications for their stability when coupled to hydrodynamic interactions (as compared to unconfined systems where base states are uniform isotropic or uniform nematic).

- **Correlation length**: The stability of a uniform isotropic or nematic base states in unconfined systems reveal the zero wavenumber ($k = 0$) mode to be most unstable, and numerical simulations show (in agreement) that concentration and director fields are correlated over length scales comparable to that of the size of the simulation box. Confinement introduces another length scale into the picture and momentum screening by the walls on length scales of the order of the channel height could potentially control the correlation length of active self-organization.

- **No-slip on the fluid velocity**: In confined active suspensions, a no-slip condition has to be imposed on fluid velocity on the confining walls, which changes the structure of the self-generated flows and hence, the overall morphology of the self-organization.

We explore these effects in this chapter by investigating the dynamics in a suspension of hydrodynamically-interacting active Brownian pusher particles confined between two parallel plates. The kinetic model is presented in section 6.2. A linear stability analysis of a one dimensional perturbation in the wall normal direction to the base state in confined active suspensions is presented in section 6.3. The computational framework for a confined forced-Stokes flow solver is presented in section 6.4. With the aid of this solver, non-linear simulations are performed in section 6.5 to investigate the stability and non-linear dynamics in two dimensions before we finish with concluding remarks in section 6.6.

6.2 Kinetic Model

We consider a suspension of active Brownian pusher particles suspended in a viscous fluid. The active particles swim with velocity V_s, have constant translational and rotational diffusivities denoted by d_t and d_r, respectively and exert force dipoles on the fluid with negative stresslet strength σ_0. The suspension, with mean number density n, is confined between two parallel walls $z = \pm H$ with half-width of seperation H. Dimensional analysis of the governing equations identifies three relevant dimensionless groups:

$$Pe_s = \frac{V_s}{2d_r H}, \quad \alpha = \frac{\sigma_0 n}{\mu d_r}, \quad \Lambda = \frac{d_r d_t}{V_s^2}. \tag{6.1}$$

The swimming Peclet number Pe_s is the ratio of the persistence length to the channel height and is a measure of degree of confinement. The activity parameter α measures the strength of active stresses relative to dissipation by viscosity and rotational diffusion and is directly proportional to the mean number density n. The

swimmer specific parameter Λ compares the strength of diffusion to self-propulsion and is constant for a specific swimmer.

The configuration of an active particles can be specified in terms of the first three orientational moments of the active particle probability density $\Psi(\mathbf{x}, \mathbf{p}, t)$. After non-dimensionalization using the length scale $l_c = H$ and time scale $t_c = d_r^{-1}$, the conservation equations for concentration, polarization vector and the nematic order parameter tensor c, $\mathbf{m}$ and $\mathbf{D}$ read [29, 23]:

$$\frac{\partial c}{\partial t} = -\frac{\partial}{\partial x_l}\left[u_l c + 2Pe_s m_l - 4\Lambda Pe_s^2 \frac{\partial c}{\partial x_l}\right], \tag{6.2}$$

$$\frac{\partial m_i}{\partial t} = -\frac{\partial}{\partial x_l}\left[u_l m_i + 2Pe_s\left(D_{il} + c\frac{\delta_{il}}{3}\right) - 4\Lambda Pe_s^2 \frac{\partial m_i}{\partial x_l}\right] + \left(\frac{3}{5}E_{il} + W_{il}\right) m_l - 2m_i, \tag{6.3}$$

$$\frac{\partial D_{ij}}{\partial t} = -\frac{\partial}{\partial x_l}\left[u_l D_{ij} + 2Pe_s\left[\frac{1}{5}\left(m_i\delta_{jl} + m_j\delta_{il}\right) - \frac{2}{15}m_l\delta_{ij}\right] - 4\Lambda Pe_s^2\frac{\partial D_{ij}}{\partial x_l}\right] + \left[\frac{2}{5}cE_{ij} + \frac{3}{7}\left(E_{il}D_{lj} + D_{il}E_{lj}\right)\right] + \left[W_{il}D_{lj} - D_{il}W_{lj}\right] - 6D_{ij}, \tag{6.4}$$

where the flux terms (the terms with divergence) include contributions from advection by the disturbance flow, self-propulsion and translational diffusion and the source terms arise from rotational diffusion and from alignment and rotation by the rate-of-strain and vorticity tensors $\mathbf{E}$ and $\mathbf{W}$ of the disturbance velocity field $\mathbf{u}$:

$$E_{ij} = \frac{1}{2}\left(\frac{\partial u_i}{\partial x_j} + \frac{\partial u_j}{\partial x_i}\right), \tag{6.5}$$

$$W_{ij} = \frac{1}{2}\left(\frac{\partial u_i}{\partial x_j} - \frac{\partial u_j}{\partial x_i}\right). \tag{6.6}$$

These equations are subject to the corresponding no-flux boundary conditions

at the wall (at $z = \pm 1$) which are a balance of the self-propulsive and diffusive fluxes.

$$\begin{aligned} m_z - 2\Lambda Pe_s \frac{\partial c}{\partial z} &= 0, & (6.7)\\ D_{i3} + c\frac{\delta_{i3}}{3} - 2\Lambda Pe_s \frac{\partial m_i}{\partial z} &= 0, & (6.8)\\ \frac{1}{5}\left(m_i\delta_{j3} + m_j\delta_{i3}\right) - \frac{2}{15}m_z\delta_{ij} - 2\Lambda Pe_s \frac{\partial D_{ij}}{\partial z} &= 0. & (6.9) \end{aligned}$$

The fluid velocity satisfies the Stokes equations subject to the no-slip condition $u_i\left(z = \pm 1\right) = 0$. The Stokes equation reads:

$$\frac{\partial u_l}{\partial x_l} = 0, \quad -\frac{\partial p}{\partial x_i} + \frac{\partial u_i}{\partial x_l \partial x_l} + \alpha \frac{\partial D_{li}}{\partial x_l} = 0. \tag{6.10}$$

6.3 Linear stability analysis

Analytical expressions for the equilibrium concentration $c^0(z)$, wall-normal polarization $m_z^0(z)$ and nematicity $D_{zz}^0(z)$ profiles in the dilute limit were previously derived [23] in chapter 4 and omitted here for brevity. In this section, we investigate the stability of these equilibrium states in confined active suspensions to hydrodynamic coupling.

We specifically analyze the stability of a one-dimensional perturbation in the wall-normal direction to the quiescent state of the form $\Psi\left(z, \mathbf{p}, t\right) = \Psi^0\left(z, \theta\right) + \epsilon\Psi'(z, \mathbf{p})\exp(\sigma t)$. In 1D, the disturbance velocity can be analytically solved for as

$$u_y(z) = -\int_{-1}^{z}\left(\alpha D_{yz} - \frac{\alpha}{2}\int_{-1}^{1} D_{yz}\, dz\right)\, \mathrm{d}z. \tag{6.11}$$

In the linear limit, an one-dimensional perturbation in the wall-normal direction

only leads to changes in wall-parallel (or stream-wise) polarization m_y and shear nematic alignment D_{yz}. The growth rate of the instability can be solved for as an eigenvalue problem shown below.

$$\begin{aligned}\sigma {m_y}' &= -2Pe_s\frac{\mathrm{d}{D_{yz}}'}{\mathrm{d}z} + 4\Lambda Pe_s^2\frac{\mathrm{d}^2{m_y}'}{\mathrm{d}z^2} - 2{m_y}' + \\ &\quad \frac{4\alpha}{5}\left(\frac{1}{2}\int_{-1}^{1}{D_{yz}}'\,dz - {D_{yz}}'\right){m_z}^0, \qquad (6.12)\\ \sigma {D_{yz}}' &= -2\frac{Pe_s}{5}\frac{\mathrm{d}{m_y}'}{\mathrm{d}z} + 4\Lambda Pe_s^2\frac{\mathrm{d}^2{D_{yz}}'}{\mathrm{d}z^2} - 6{D_{yz}}' \\ &\quad +\alpha\left(\frac{1}{2}\int_{-1}^{1}{D_{yz}}'\,dz - {D_{yz}}'\right)\left(\frac{c^0}{5} + {D_{zz}}^0\right). \qquad (6.13)\end{aligned}$$

subject to the following boundary conditions at $z = \pm 1$.

$$\begin{aligned}{D_{yz}}' &= 2\Lambda Pe_s\frac{\mathrm{d}{m_y}'}{\mathrm{d}z}, \qquad (6.14)\\ \frac{1}{5}{m_y}' &= 2\Lambda Pe_s\frac{\mathrm{d}{D_{yz}}'}{\mathrm{d}z}. \qquad (6.15)\end{aligned}$$

The eigenvalue problem has 4 contributions: self-propulsion, translational and rotational diffusion and the crucial fourth term which accounts for the alignment of the polarized and inhomogeneous base state with the self-generated fluid velocity gradient. Solving this numerically reveals a symmetry-breaking phase-transition from a quiescent state to a steady spontaneous flowing state above a critical level of activity or concentration for pusher suspensions as shown in figure 6.1(a). The marginal stability curve shows that higher concentrations and weaker confinements are more unstable. This unique instability is driven by the interaction of the base state wall-normal polarization and concentration with the self-generated fluid velocity gradient. It has to be noted that there is no analogous instability or net pumping in unconfined systems.

The fastest growing mode leads to a symmetric velocity profile in the channel with net fluid pumping as shown in figure 6.1(b). Interestingly, the second fastest growing mode interestingly leads to an anti-symmetric velocity profile with no net fluid pumping. The non-linear one-dimensional simulations of the full probability density function $\Psi(z, \mathbf{p})$ also confirms this fact, where a purely anti-symmetric perturbation leads to an steady spontaneous flow state with an anti-symmetric velocity profile, while any other perturbation inevitably leads to steady spontaneous flow state with a symmetric velocity profile (because of its higher growth rate). We note that Marenduzzo *et al.* [155] had predicted similar results using phenomenological active liquid crystal models but reported that the symmetric and anti-symmetric modes has the same growth rate.

This spontaneous steady flow state can also be viewed as another, more stable base state in confined active systems. A perturbation to the no-flow base state leads to a self-generated disturbance flow in an arbitrary direction through the channel which results in upstream polarization and streamwise alignment reducing the accumulation and wall-parallel polarization. However, this streamwise alignment also reinforces the perturbation leading to fluid pumping and hence, forming the basis of the instability mechanism.

6.4 Confined forced-Stokes solver

Note: For simplicity of notation, ∇_x is replaced by ∇ in this section.

In this section, we develop a confined solver for Stokes equation (in 2 dimensions

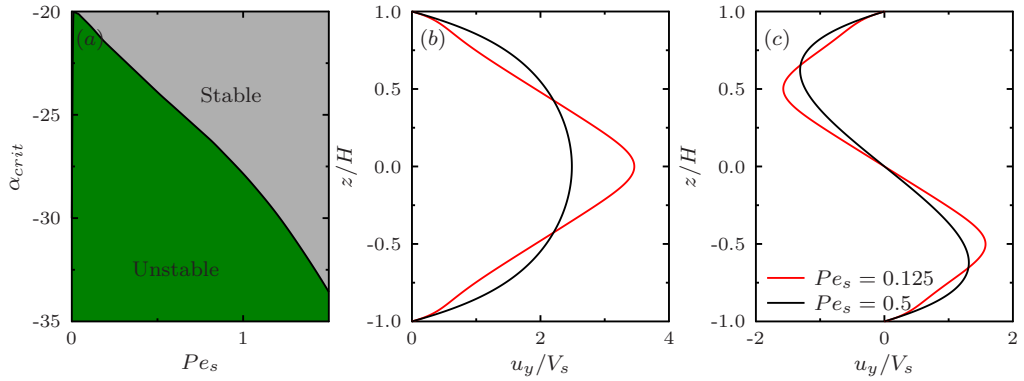

Figure 6.1: (color online).(a) Marginal stability curve in the (α, Pe_s) parameter space (b) fastest growing velocity mode (c) second fastest growing velocity mode.

y and z) which read:

$$-\nabla^2 \mathbf{u} + \nabla \mathbf{P} = \mathbf{F}_a, \quad \mathbf{u}(z = \pm H) = 0. \tag{6.16}$$

The stream-wise direction $\hat{\mathbf{y}}$ is considered to be periodic.

This confined Stokes equation is handled by taking advantage of their linearity and decomposing the solution into 3 parts:

- **Analytic solution** for the mean pumping velocity field ($u_p \hat{\mathbf{y}}$) arising from the stream-wise averaged force,
- **Hasimoto Fourier solution ($\mathbf{u}_h$)** for Stokes equation with net active particle forcing but with periodic boundary condition,
- **Boundary correction ($\mathbf{u}_c$)**: A semi-analytical solution to correct the boundary velocity from the Fourier solution.

Once the three components are computed as explained in the following subsec-

tions, the self-generated fluid velocity $\mathbf{u}$ is calculated as their superposition.

$$\mathbf{u}(\mathbf{x}) = u_p\hat{\mathbf{y}} + \mathbf{u}_h(\mathbf{x}) - \mathbf{u}_c(\mathbf{x}). \tag{6.17}$$

6.4.1 Analytical solution

We derive here the analytic solution for the mean pumping velocity field ($u_p\hat{\mathbf{y}}$) arising from the stream-wise averaged active force, $\bar{\mathbf{F}}(z)$, whose components are given by:

$$\bar{F}_y(z) = \alpha\frac{\partial}{\partial z}\bar{D}_{yz}, \tag{6.18}$$

$$\bar{F}_z(z) = \alpha\frac{\partial}{\partial z}\bar{D}_{zz}, \tag{6.19}$$

where

$$\bar{D}_{yz} = \int_0^{L_y} D_{yz}\,\mathrm{d}y, \tag{6.20}$$

$$\bar{D}_{zz} = \int_0^{L_y} D_{zz}\,\mathrm{d}y. \tag{6.21}$$

While $\bar{F}_z$ is balanced by the pressure, $\bar{F}_y$ drives the stream-wise velocity which can be solved as,

$$\bar{u}_y = \alpha\left(\frac{z+1}{2}\int_{-1}^{1}\bar{D}_{yz}\,\mathrm{d}z - \int_{-1}^{z}\bar{D}_{yz}\,\mathrm{d}z\right). \tag{6.22}$$

This basically corresponds to the solution for the $k_y = 0$ mode.

6.4.2 Hasimoto Fourier solution

We outline here the Fourier solution method derived by [77] to solve the Stokes equation with net active particle forcing ($\mathbf{F'}_a = \mathbf{F}_a - \bar{\mathbf{F}}$) but with periodic boundary condition. The periodic flow field $\mathbf{u}_h(\mathbf{x})$ defined in $y \in (0, L_y), z \in (-1, 1)$ satisfies:

$$-\nabla^2 \mathbf{u}_h + \nabla P = \mathbf{F'}_a, \tag{6.23}$$

$$\nabla \cdot \mathbf{u}_h = 0, \tag{6.24}$$

subject to periodic BC. We expand the velocities and pressure in a Fourier series as

$$\mathbf{u}_h(y,z) = \sum_{k_z}\sum_{k_y} \hat{\mathbf{u}}_p(k_y,k_z)\, e^{2\pi \mathrm{i}(k_y y + k_z z)}, \tag{6.25}$$

$$p(y,z) = \sum_{k_z}\sum_{k_y} \hat{p}(k_y,k_z)\, e^{2\pi \mathrm{i}(k_y y + k_z z)}. \tag{6.26}$$

Upon Fourier transformation of the Stokes equation, we have

$$4\pi^2 k^2 \hat{\mathbf{u}}_h + 2\pi \mathrm{i}\mathbf{k}\hat{p} = \hat{\mathbf{F}}_a, \tag{6.27}$$

$$2\pi \mathrm{i}\mathbf{k} \cdot \hat{\mathbf{u}}_h = 0, \tag{6.28}$$

from which we can solve for the Fourier coefficient of the periodic velocity $\hat{\mathbf{u}}_h$ as

$$\hat{\mathbf{u}}_h = \frac{1}{4\pi^2 k^2}\left(\mathbf{I} - \hat{\mathbf{k}}\hat{\mathbf{k}}\right) \cdot \hat{\mathbf{F}}_a. \tag{6.29}$$

6.4.3 Boundary correction

The periodic solution $\mathbf{u}_p(\mathbf{x})$ has non-zero values for velocities at the boundaries given by

$$\mathbf{u}(z=-1) = \mathbf{u}_1, \tag{6.30}$$

$$\mathbf{u}(z=1) = \mathbf{u}_2. \tag{6.31}$$

In order to satisfy the no-slip condition, this has to be corrected with the boundary correction velocity $\mathbf{u}_c$. We solve the Stokes equation without active stress forcing, subject to the boundary velocities of the periodic solution, to obtain $\mathbf{u}_c$.

$$-\nabla^2\mathbf{u}_c + \nabla P = 0, \tag{6.32}$$

$$\nabla \cdot \mathbf{u}_c = 0. \tag{6.33}$$

subject to

$$\mathbf{u}_c(z=-1) = \mathbf{u}_1, \tag{6.34}$$

$$\mathbf{u}_c(z=1) = \mathbf{u}_2. \tag{6.35}$$

We expand the flow and pressure field in a Fourier series in y with Fourier coefficients $\hat{\mathbf{u}}(k_y, z)$ and $\hat{P}(k_y, z)$.

$$\mathbf{u}_c(y,z) = \sum_{k_y} \hat{\mathbf{u}}_c(k_y,z)\, e^{2\pi \mathrm{i} k_y y}, \tag{6.36}$$

$$P(y,z) = \sum_{k_y} \hat{P}(k_y,z)\, e^{2\pi \mathrm{i} k_y y}. \tag{6.37}$$

Pressure solution

The fluid pressure satisfies the Laplace's equation and we can immediately solve the Fourier coefficient of the pressure as

$$\hat{P} = a\left(k_y\right)\cosh qz + b\left(k_y\right)\sinh qz, \tag{6.38}$$

where

$$q^2 = 4\pi^2 k_y^2, \tag{6.39}$$

and $a\left(k_y\right)$ and $b\left(k_y\right)$ are constants (which will be solved for later). Substituting eq. (6.38) into the Fourier transform of eq. (6.32) gives a non-homogeneous ODE with non-homogeneous (Dirichlet) boundary condition.

$$q^2\hat{\mathbf{u}}_c - \frac{\mathrm{d}^2\hat{\mathbf{u}}_c}{\mathrm{d}z^2} + \left(2\pi \mathrm{i} k_y \hat{P}\hat{\mathbf{y}} + \frac{\mathrm{d}\hat{P}}{\mathrm{d}z}\hat{\mathbf{z}}\right) = 0, \tag{6.40}$$

subject to

$$\hat{\mathbf{u}}_c\left(z=-1\right) = \hat{\mathbf{u}}_1\left(k_y\right), \tag{6.41}$$

$$\hat{\mathbf{u}}_c\left(z=1\right) = \hat{\mathbf{u}}_2\left(k_y\right). \tag{6.42}$$

We split this problem into a non-homogeneous ODE with homogeneous boundary condition to solve for $\hat{\mathbf{u}}_{c1}$ and a homogenous ODE with non-homogeneous (Dirichlet) boundary condition to solve for $\hat{\mathbf{u}}_{c2}$.

Solution for $\hat{\mathbf{u}}_{c1}$

$\hat{\mathbf{u}}_{c1}$ satisfies

$$q^2\hat{\mathbf{u}}_{c1} - \frac{\mathrm{d}^2\hat{\mathbf{u}}_{c1}}{\mathrm{d}z^2} = 0, \tag{6.43}$$

subject to

$$\hat{\mathbf{u}}_{c1}\left(z=-1\right) = \hat{\mathbf{u}}_1, \tag{6.44}$$

$$\hat{\mathbf{u}}_{c1}\left(z=1\right) = \hat{\mathbf{u}}_2. \tag{6.45}$$

Solving we get,

$$\hat{\mathbf{u}}_{c1} = \mathscr{C}(z)\left(\frac{\hat{\mathbf{u}}_1+\hat{\mathbf{u}}_2}{2}\right) + \mathscr{S}(z)\left(\frac{\hat{\mathbf{u}}_2-\hat{\mathbf{u}}_1}{2}\right), \tag{6.46}$$

where

$$\mathscr{C}(z) = \frac{\cosh qz}{\cosh q}, \tag{6.47}$$

$$\mathscr{S}(z) = \frac{\sinh qz}{\sinh q}. \tag{6.48}$$

Solution for $\hat{\mathbf{u}}_{c2}$

$\hat{\mathbf{u}}_{c2}$ satisfies

$$q^2\hat{\mathbf{u}}_{c2} - \frac{\mathrm{d}^2\hat{\mathbf{u}}_{c2}}{\mathrm{d}z^2} + \left(2\pi\mathrm{i}k_y\hat{P}\hat{\mathbf{y}} + \frac{\mathrm{d}\hat{P}}{\mathrm{d}z}\hat{\mathbf{z}}\right) = 0, \tag{6.49}$$

subject to

$$\hat{\mathbf{u}}_{c2}\left(z=-1\right) = 0, \tag{6.50}$$

$$\hat{\mathbf{u}}_{c2}\left(z=1\right) = 0. \tag{6.51}$$

Solving we get,

$$\hat{\mathbf{u}}_{c2} = \frac{\mathrm{i}}{2}\left(a\Gamma_1 + b\Gamma_2\right)\hat{\mathbf{y}} + \frac{1}{2}\left(a\Gamma_2 + b\Gamma_1\right)\hat{\mathbf{z}}, \tag{6.52}$$

where $\Gamma_1(z)$ and $\Gamma_2(z)$ are given by

$$\Gamma_1(z) = \sinh q\left[z\mathscr{S}(z) - H\mathscr{C}(z)\right], \tag{6.53}$$

$$\Gamma_2(z) = \cosh q\left[z\mathscr{C}(z) - H\mathscr{S}(z)\right]. \tag{6.54}$$

Solving for pressure co-efficients

By forcing $\hat{\mathbf{u}}_{c1} + \hat{\mathbf{u}}_{c2}$ to satisfy the continuity equation, we solve for a and b.

$$2\pi\mathrm{i}k_y\hat{v} + \frac{\mathrm{d}\hat{w}}{\mathrm{d}z} = 0. \tag{6.55}$$

Also note that,

$$\mathscr{C}'(z) = q\mathscr{S}(z)\tanh q, \tag{6.56}$$

$$\mathscr{S}'(z) = q\mathscr{C}(z)\coth q, \tag{6.57}$$

$$\Gamma_1'(z) = \sinh q\left[\left(1 - q\tanh q\right)\mathscr{S}(z) - \left(qz\coth q\right)\mathscr{C}(z)\right], \tag{6.58}$$

$$\Gamma_2'(z) = \cosh q\left[\left(1 - q\coth q\right)\mathscr{C}(z) - \left(qz\tanh q\right)\mathscr{S}(z)\right]. \tag{6.59}$$

The solution for a and b are given by

$$a = \frac{q\mathrm{i}\left(\hat{v}_1 + \hat{v}_2\right)\sinh q + q\left(\hat{w}_2 - \hat{w}_1\right)\cosh q}{q - \sinh q\cosh q}, \tag{6.60}$$

$$b = \frac{-q\mathrm{i}\left(\hat{v}_2 - \hat{v}_1\right)\cosh q - q\left(\hat{w}_2 + \hat{w}_1\right)\sinh q}{q + \sinh q\cosh q}. \tag{6.61}$$

The correction velocity is finally obtained as $\mathbf{u}_c = \mathbf{u}_{c1} + \mathbf{u}_{c2}$.

6.5 Numerical Simulations

6.5.1 Method

We complement the linear stability analysis of section 6.3 by performing fully non-linear simulations of the kinetic model presented in section 6.2. The numerical simulation is based on a finite-volume solution of the conservation equation for the order fields eq. (6.2)-(6.4), which allows for an easy implementation of the boundary conditions eq. (6.7)-(6.9), and a second-order Adam-Bashforth's time integration scheme. The Stokes equation is handled using the confined flow solver developed in section 6.4. The velocity grid points are staggered with respect to the finite-volume discretization of the order parameter fields and are defined such that the extremum points coincide with the two walls. We use 256×512 grid points in the $y \times z$ space. At time $t = 0$, the order parameter fields are initialized with a no-flow base state plus a two-dimensional perturbation. The simulations are run till a statistically steady state is reached.

6.5.2 Results and Discussion

The non-linear simulations confirm the predictions of the linear stability analysis presented in section 6.3 and show that the quiescent no-flow base state is destablized above critical activity levels shown in figure 6.1(a). Figure 6.2 shows the time evolution of the self-generated fluid velocity profiles in the channel. The transient dynamics is characterized by the formation of circular vortical patterns with characteristic lengths

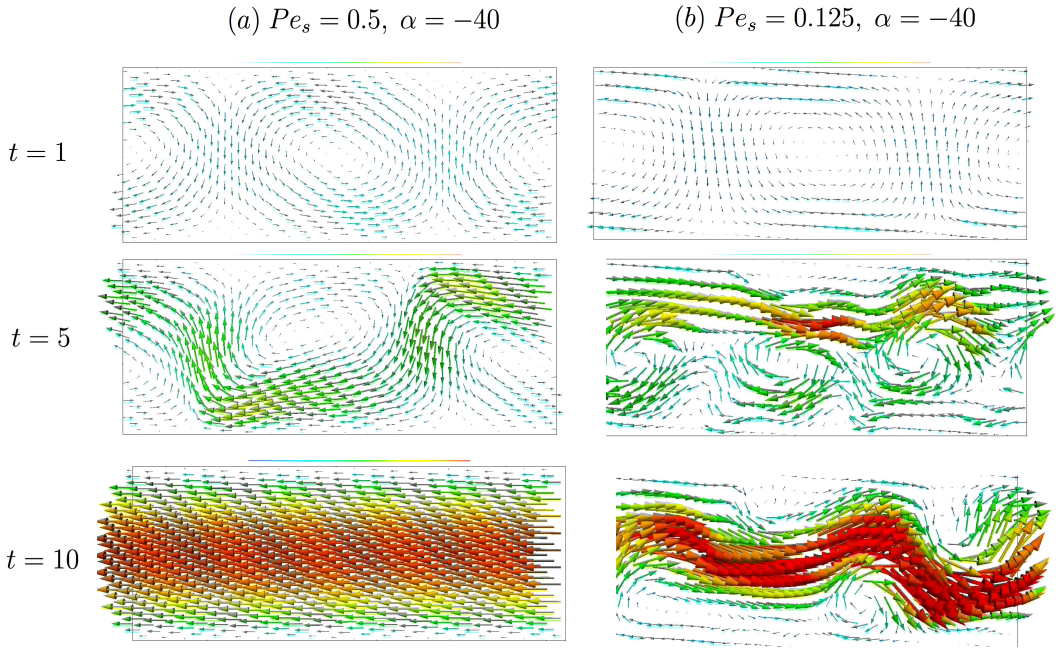

Figure 6.2: (color online) Time evolution of the self-generated fluid velocity profiles in the channel.

on the scale of the channel width. The dynamics at long times is a strong function of the degree of confinement. In strong confinement (at $Pe_s = 0.5$ and $\alpha = -40$ shown in 6.2 (a)), there is a transition to a steady spontaneously flowing state. The direction of fluid pumping is spontaneous and arbitrary. In weak confinement (at $Pe_s = 0.125$ and $\alpha = -40$ shown in 6.2 (b)), the spontaneous flow state is unstable and the resultant active turbulence state is characterized by chaotic vortical patterns, with net (time-averaged) fluid pumping in an arbitrary direction. The morphology of the emergent structures observed in our simulations are strikingly similar to that reported in recent microfluidic experiments of bacterial fluids in linear confinement and in race tracks [181].

Figure 6.3 (a) shows net rate of fluid pumped as a function of time. The net flow rate reaches a steady state for strongly confined suspensions ($Pe_s = 0.5$) but fluctuates with time for the case of weak confinement ($Pe_s = 0.125$) where active

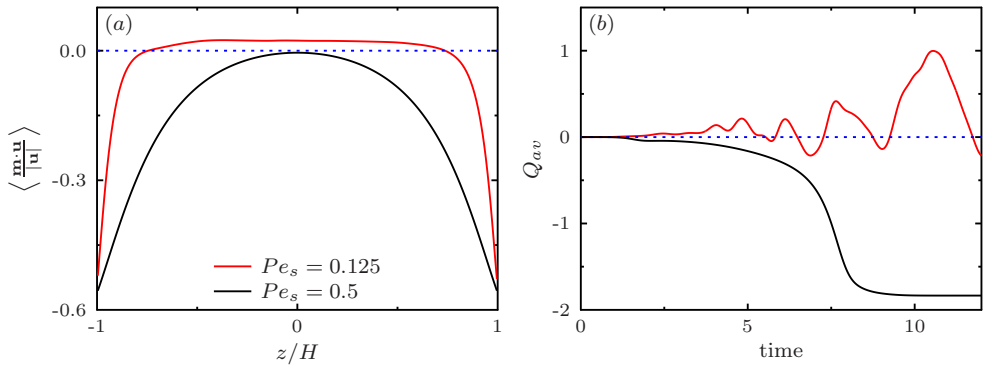

Figure 6.3: (color online) (a) average flow rate pumped Q_{av} as a function of time, (b) Correlation between velocity and polarization field across the channel (averaged over stream-wise coordinate and time) for different degrees of confinement Pe_s.

turbulence leads to fluctuations in the direction and magnitude of fluid pumping.

The relative alignment of the bacteria with self-generated flows has been vividly discussed in recent works [105, 182, 183, 181]. We explore this aspect in figure 6.3 (b) where the correlation between the polarization of the suspension **m** and the fluid velocity **u** (averaged over stream-wise coordinate and time) is plotted as a function of wall-normal coordinate z. The steady flowing state, observed in strongly confined active fluids, is characterized by particles swimming against the flow everywhere in the channel, in agreements with experiments [105, 181]. The underlying mechanism is similar to the mechanism for upstream swimming in externally imposed Poiseuille flows [23]. Confinement leads to polarization towards the wall in the base state, which coupled to shear alignment leads to upstream swimming. The active turbulence state, reported in weakly confined active fluids, is characterized by particles swimming against the flow in the near-wall region and particles swimming with the flow in the bulk.

6.6 Conclusions and Outlook

In this chapter, we have investigated the hydrodynamic stability of active suspensions in linear confinement using linear stability analysis and numerical simulations. Our analysis has shown that confinement can stabilize active self-organization and lead to steady spontaneous directed fluid pumping. Our first-principles kinetic theory approach has also provided us valuable insights on the mechanism that allows for the existence of such a steady flowing state in confined active suspensions. Our results are in striking qualitative agreement with recent experiments on confined bacterial suspensions [181], thus validating the use of such continuum kinetic theories for the study of confined active suspensions, even in the semi-dilute concentration regime.

The kinetic theory framework for confined active suspensions brings a wide range of exciting problems within the realm of analytical and computational tractability. Using direct extensions of our framework, we have recently studied active self-organization in circular disks and race tracks [184], reproducing and providing physical insight into the rich features observed in recent experiments [105, 178, 183, 181], such as spontaneous double vortex, unidirectional bands, traveling wave spirals and other chaotic states.

This opens up a really intriguing question. Can we optimize the confining topology to constructively control self-generated flows into desired patterns? This rich avenue is the focus of our future work.

Bibliography

[1] T. V. Kasyap and D. L. Koch, "Chemotaxis driven instability of a confined bacterial suspension," *Phys. Rev. Lett.*, vol. 108, p. 038101, 2012.

[2] T. Vicsek, "Universal patterns of collective motion from minimal models of flocking," in *Self-Adaptive and Self-Organizing Systems, 2008. SASO '08. Second IEEE International Conference on*, pp. 3–11, Oct 2008.

[3] T. Vicsek, A. Czirók, E. Ben-Jacob, I. Cohen, and O. Shochet, "Novel type of phase transition in a system of self-driven particles," *Phys. Rev. Lett.*, vol. 75, pp. 1226–1229, Aug 1995.

[4] C. Dombrowski, L. Cisneros, S. Chatkaew, R. E. Goldstein, and J. O. Kessler, "Self-concentration and large-scale coherence in bacterial dynamics," *Phys. Rev. Lett.*, vol. 93, p. 098103, Aug 2004.

[5] L. Cisneros, R. Cortez, C. Dombrowski, R. E. Goldstein, and J. O. Kessler, "Fluid dynamics of self-propelled micro-organisms, from individuals to concentrated populations," *Exp. Fluids*, vol. 43, pp. 737–753, 11 2007.

[6] A. Sokolov and I. S. Aranson, "Reduction of viscosity in suspensions of swimming bacteria," *Phys. Rev. Lett.*, vol. 103, p. 148101, 2009.

[7] N. Sambelashvili, A. Lau, and D. Cai, "Dynamics of bacterial flow: Emergence of spatiotemporal coherent structures," *Physics Letters A*, vol. 360, no. 45, pp. 507 – 511, 2007.

[8] L. Cisneros, J. O. Kessler, S. Ganguly, and R. E. Goldstein, "Dynamics of swimming bacteria: Transition to directional order at high concentration," *Phys. Rev. E*, vol. 83, p. 061907, 2011.

[9] K. C. Leptos, J. S. Guasto, J. P. Gollub, A. I. Pesci, and R. E. Goldstein, "Dynamics of enhanced tracer diffusion in suspensions of swimming eukaryotic microorganisms," *Phys. Rev. Lett.*, vol. 103, p. 198103, Nov 2009.

[10] X.-L. Wu and A. Libchaber, "Particle diffusion in a quasi-two-dimensional bacterial bath," *Phys. Rev. Lett.*, vol. 84, no. 13.

[11] N. H. Mendelson, A. Bourque, K. Wilkening, K. R. Anderson, and J. C. Watkins, "Organized Cell Swimming Motions in Bacillus subtilis Colonies: Patterns of Short-Lived Whirls and Jets," *J. Bacteriol.*, vol. 181, no. 2, pp. 600–609, 1999.

[12] A. Sokolov, I. S. Aranson, J. O. Kessler, and R. E. Goldstein, "Concentration dependence of the collective dynamics of swimming bacteria," *Phys. Rev. Lett.*, vol. 98, p. 158102, Apr 2007.

[13] E. Lauga, "An introduction to the hydrodynamics of locomotion on small scales," in *Les Houches 2012 Summer School Proceedings, Oxford University Press*, 2013.

[14] E. M. Purcell, "Life at low reynolds number," vol. 45, pp. 3–11, 1977.

[15] K. Drescher, R. E. Goldstein, N. Michel, M. Polin, and I. Tuval, "Direct measurement of the flow field around swimming microorganisms," *Phys. Rev. Lett.*, vol. 105, p. 168101, 2010.

[16] J. S. Guasto, K. A. Johnson, and J. P. Gollub, "Oscillatory flows induced by microorganisms swimming in two dimensions," *Phys. Rev. Lett.*, vol. 105, p. 168102, 2010.

[17] H. C. Berg and D. A. Brown, "Chemotaxis in *Escherichia coli* analysed by three-dimensional tracking," *Nature*, vol. 239, p. 500, 1972.

[18] M. Doi and S. F. Edwards, *The Theory of Polymer Dynamics*. Oxford University Press, 1986.

[19] D. Saintillan and M. J. Shelley, "Instabilities and pattern formation in active particle suspensions: Kinetic theory and continuum simulations," *Phys. Rev. Lett.*, vol. 100, p. 178103, Apr 2008.

[20] D. Saintillan and M. J. Shelley, "Instabilities, pattern formation, and mixing in active suspensions," *Phys. Fluids*, vol. 20, no. 12, p. 123304, 2008.

[21] B. Ezhilan, M. J. Shelley, and D. Saintillan, "Instabilities and nonlinear dynamics of concentrated active suspensions," *Phys. Fluids*, vol. 25, p. 070607, 2013.

[22] B. Ezhilan, A. A. Pahlavan, and D. Saintillan, "Chaotic dynamics and oxygen transport in thin films of aerotactic bacteria," *Phys. Fluids*, vol. 24, p. 091701, 2012.

[23] B. Ezhilan and D. Saintillan, "Transport of a dilute active suspension in pressure driven channel flow," *J. Fluid. Mech.*, p. submitted, 2015.

[24] B. Ezhilan, R. Alonso-Matilla, and D. Saintillan, "On the distribution and swim pressure of run-and-tumble particles in confinement," *J. Fluid Mech.*, vol. 781, p. R4, 2015.

[25] H. Kurtuldu, J. S. Guasto, K. A. Johnson, and J. P. Gollub, "Enhancement of biomixing by swimming algal cells in two-dimensional films," *Proc. Natl. Acad. Sci. USA*, vol. 108, p. 10391, 2011.

[26] T. Ishikawa, "Suspension biomechanics of swimming microbes," *J. R. Soc. Interface*, vol. 6, p. 815, 2009.

[27] S. Ramaswamy, "The mechanics and statistics of active matter," *Annu. Rev. Cond. Mat. Phys.*, vol. 1, p. 323, 2010.

[28] D. L. Koch and G. Subramanian, "Collective hydrodynamics of swimming microorganisms: Living fluids," *Annu. Rev. Fluid Mech.*, vol. 43, p. 637, 2011.

[29] D. Saintillan and M. J. Shelley, "Active suspensions and their nonlinear models," *C. R. Physique*, vol. 14, pp. 497–517, 2013.

[30] R. A. Simha and S. Ramaswamy, "Hydrodynamic fluctuations and instabilities in ordered suspensions of self-propelled particles," *Phys. Rev. Lett.*, vol. 89, p. 058101, 2002.

[31] I. S. Aranson, A. Sokolov, J. O. Kessler, and R. E. Goldstein, "Model for dynamical coherence in thin films of self-propelled microorganisms," *Phys. Rev. E*, vol. 75, p. 040901, 2007.

[32] C. W. Wolgemuth, "Collective swimming and the dynamics of bacterial turbulence," *Biophys. J.*, vol. 95, p. 1564, 2008.

[33] J. P. Hernández-Ortiz, C. G. Stoltz, and M. D. Graham, "Transport and collective dynamics in suspensions of confined swimming particles," *Phys. Rev. Lett.*, vol. 95, p. 204501, 2005.

[34] D. Saintillan and M. J. Shelley, "Orientational order and instabilities in suspensions of self-locomoting rods," *Phys. Rev. Lett.*, vol. 99, p. 058102, Jul 2007.

[35] T. Ishikawa and T. J. Pedley, "Coherent structures in monolayers of swimming particles," *Phys. Rev. Lett.*, vol. 100, p. 088103, 2008.

[36] T. Ishikawa, J. T. Locsei, and T. J. Pedley, "Development of coherent structures in concentrated suspensions of swimming model micro-organisms," *J. Fluid Mech.*, vol. 615, p. 401, 2008.

[37] P. T. Underhill, J. P. Hernández-Ortiz, and M. D. Graham, "Diffusion and spatial correlations in suspensions of swimming particles," *Phys. Rev. Lett.*, vol. 100, p. 248101, 2008.

[38] D. Saintillan and M. J. Shelley, "Emergence of coherent structures and large-scale flows in motile suspensions," *J. Royal Soc. Interface*, vol. 9, p. 571, 2012.

[39] G. Subramanian and D. L. Koch, "Critical bacterial concentration for the onset of collective swimming," *J. Fluid Mech.*, vol. 632, pp. 359–400, 2009.

[40] Y. Hatwalne, S. Ramaswamy, M. Rao, and R. Aditi Simha, "Rheology of active-particle suspensions," *Phys. Rev. Lett.*, vol. 92, p. 118101, 2004.

[41] C. Hohenegger and M. Shelley, "Stability of active suspensions," *Phys. Rev. E*, vol. 81, p. 046311, 2010.

[42] A. Alizadeh Pahlavan and D. Saintillan, "Instability regimes in flowing suspensions of swimming micro-organisms," *Phys. Fluids*, vol. 23, p. 011901, 2011.

[43] N. C. Darnton, L. Turner, S. Rojevsky, and H. C. Berg, "Dynamics of bacterial swarming," *Biophys. J.*, vol. 98, p. 2082, 2010.

[44] H. P. Zhang, A. Be'er, E. Florin, and H. L. Swinney, "Collective motions and density fluctuations in bacterial colonies," *Proc. Natl. Acad. Sci. USA*, vol. 107, p. 13626, 2010.

[45] X. Chen, X. Dong, A. Be'er, H. L. Swinney, and H. P. Zhang, "Scale-invariant correlations in dynamical bacterial clusters," *Phys. Rev. Lett.*, vol. 108, p. 148101, 2012.

[46] N. Sambelashvili, A. W. C. Lau, and D. Cai, "Dynamics of bacterial flow: Emergence of spatiotemporal coherent structures," *Phys. Lett. A*, vol. 360, p. 507, 2007.

[47] A. Baskaran and M. C. Marchetti, "Statistical mechanics and hydrodynamics of bacterial suspensions," *Proc. Natl. Acad. Sci. USA*, vol. 106, p. 15567, 2009.

[48] M. G. Forest, Q. Wang, and R. Zhou, "Kinetic theory and simulations of active polar liquid crystalline polymers," *Soft Matter*, vol. 9, p. 5207, 2013.

[49] G. B. Jeffery, "The motion of ellipsoidal particles immersed in a viscous fluid," *Proc. R. Soc. Lond. A*, vol. 102, pp. 161–179, 1922.

[50] F. P. Bretherton, "The motion of rigid particles in a shear flow at low Reynolds number," *J. Fluid Mech.*, vol. 14, pp. 284–304, 1962.

[51] T. Ishikawa and M. Hota, "Interaction of two swimming *Paramecia*," *J. Exp. Biol.*, vol. 209, p. 4452, 2006.

[52] M. Doi and S. F. Edwards, "Dynamics of rod-like macromolecules in concentrated solution," *J. Chem. Soc. Faraday Trans. II*, vol. 74, p. 560, 1978.

[53] P. G. de Gennes and J. Prost, *The Physics of Liquid Crystals*. Oxford: Clarendon Press, 1993.

[54] P. G. de Gennes, "Phenomenology of short-range-orger effects in the isotropic phase of nematic materials," *Phys. Lett. A*, vol. 30, p. 454, 1969.

[55] A. N. Beris and B. J. Edwards, *Thermodynamics of Flowing Systems*. Oxford: Oxford University Press, 1994.

[56] T. B. Liverpool and M. C. Marchetti, "Hydrodynamics and rheology of active polar filaments," in *Cell Motility*, Biological and Medical Physics, Biomedical Engineering, pp. 177–206, Springer New York, 2008.

[57] M. E. Cates, O. Heinrich, D. Marenduzzo, and K. Stratford, "Lattice-boltzmann simulations of liquid crystalline fluids: active gels and blue phases," *Soft Matter*, vol. 5, p. 3791, 2009.

[58] A. Baskaran and M. C. Marchetti, "Hydrodynamics of self-propelled hard rods," *Phys. Rev. E*, vol. 77, p. 011920, 2008.

[59] A. Baskaran and M. C. Marchetti, "Nonequilibrium statistical mechanics of self-propelled hard rods," *J. Stat. Mech. Theor. Exp.*, p. P04019, 2010.

[60] L. Onsager, "The effects of shapes on the interaction of colloidal particles," *Ann. N. Y. Acad. Sci.*, vol. 51, p. 527, 1949.

[61] W. Maier and A. Saupe, "Eine einfache molekulare theorie des nematischen kristallinflüssigen zustandes," *Z. Naturforsch.*, vol. 13A, p. 564, 1958.

[62] K. Drescher, J. Dunkel, L. H. Cisneros, S. Ganguly, and R. E. Goldstein, "Fluid dynamics and noise in bacterial cell-cell and cell-surface scattering," *Proc. Natl. Acad. Sci. USA*, vol. 108, pp. 10940–10945, 2011.

[63] M. Garcia, S. Berti, P. Peyla, and S. Rafaï, "Random walk of a swimmer in a low-Reynolds-number medium," *Phys. Rev. E*, vol. 83, p. 035301, 2011.

[64] H. Brenner, "A general theory of Taylor dispersion phenomena," *PhysicoChem. Hydrodyn.*, vol. 1, pp. 91–123, 1980.

[65] P. D. Cobb and J. E. Butler, "Simulations of concentrated suspensions of rigid fibers: Relationship between short-time diffusivities and the long-time rotational diffusion," *J. Chem. Phys.*, vol. 123, p. 054908, 2005.

[66] G. K. Batchelor, "The stress system in a suspension of force-free particles," *J. Fluid Mech.*, vol. 41, p. 545, 1970.

[67] G. K. Batchelor, "Transport properties of two-phase materials with random structure," *Annu. Rev. Fluid Mech.*, vol. 6, p. 227, 1974.

[68] D. Saintillan, "The dilute rheology of swimming suspensions: A simple kinetic model," *Exp. Mech.*, vol. 50, pp. 1275–1281, 2010.

[69] D. Saintillan, "Kinetic models for biologically active suspensions," in *Natural Locomotion in Fluids and on Surfaces* (S. Childress, A. Hosoi, W. W. Schultz, and J. Wang, eds.), vol. 155 of *The IMA Volumes in Mathematics and its Applications*, pp. 53–71, Springer New York, 2012.

[70] E. J. Hinch and L. G. Leal, "Effect of brownian motion on rheological properties of a suspension of non-spherical particles," *J. Fluid Mech.*, vol. 52, p. 683, 1972.

[71] E. J. Hinch and L. G. Leal, "Constitutive equations in suspension mechanics. Part 2. Approximate forms for a suspension of rigid particles affected by Brownian rotations," *J. Fluid Mech.*, vol. 76, pp. 187–208, 1976.

[72] E. Lushi and C. S. Peskin, "Modeling and simulation of active suspensions containing large numbers of interacting micro-swimmers," *Computers and Structures*, vol. 122, pp. 239–248, 2013.

[73] E. S. G. Shaqfeh and G. H. Fredrickson, "The hydrodynamic stress in a suspension of rods," *Phys. Fluids A*, vol. 2, p. 7.

[74] D. J. Jeffrey, J. F. Morris, and J. F. Brady, "The pressure moments for two spheres in a low-reynolds-number flow," *Phys. Fluids A*, vol. 5, p. 2317, 1993.

[75] P. R. Nott and J. F. Brady, "Pressure-driven flow of suspensions: Simulation and theory," *J. Fluid Mech.*, vol. 275, p. 157, 1994.

[76] P. R. Nott, E. Guazzelli, and O. Pouliquen, "The suspension balance model revisited," *Phys. Fluids*, vol. 23, p. 043304, 2011.

[77] H. Hasimoto, "On the periodic fundamental solutions of the stokes equations and their application to viscous flow past a cubis array of spheres," *J. Fluid Mech.*, vol. 5, p. 317, 1959.

[78] G. K. Batchelor, "Slender-body theory for particles of arbitrary cross-section in stokes flow," *J. Fluid Mech.*, vol. 44, p. 419, 1970.

[79] S. Park, P. M. Wolanin, E. A. Yuzbashyan, P. Silberzan, J. B. Stock, and R. H. Austin, "Motion to form a quorum," *Science*, vol. 301, no. 5630, p. 188, 2003.

[80] D. A. Brown and H. C. Berg, "'temporal stimulation of chemotaxis in *Escherichia coli*," *Proc. Natl. Acad. Sci. USA*, vol. 71, p. 1388, 1974.

[81] I. Tuval, L. Cisneros, C. Dombrowski, C. W. Wolgemuth, J. O. Kessler, and R. E. Goldstein, "Bacterial swimming and oxygen transport near contact lines," *Proc. Natl. Acad. Sci. U.S.A.*, vol. 102, no. 7, pp. 2277–2282, 2005.

[82] E. O. Budrene and H. C. Berg, "Complex patterns formed by motile cells of *Escherichia coli*," *Nature*, vol. 349, p. 630, 1991.

[83] M. J. Kim and K. S. Breuer, "Enhanced diffusion due to motile bacteria," *Phys. Fluids*, vol. 16, no. 9, pp. L78–L81, 2004.

[84] P. T. Underhill and M. D. Graham, "Correlations and fluctuations of stress and velocity in suspensions of swimming microorganisms," *Phys. Fluids*, vol. 23, p. 121902, 2011.

[85] G. Subramanian, D. L. Koch, and S. R. Fitzgibbon, "The stability of a homogeneous suspension of chemotactic bacteria," *Phys. Fluids*, vol. 23, p. 041901, 2011.

[86] W. Alt, "Biased random walk models for chemotaxis and related diffusion approximations," *J. Math. Biol.*, vol. 9, p. 147, 1980.

[87] R. N. Bearon and T. J. Pedley, "Modelling run-and-tumble chemotaxis in a shear flow," *Bull. Math. Biol.*, vol. 62, pp. 775–791, 2000.

[88] K. C. Chen, R. M. Ford, and P. T. Cummings, "Cell balance equation for chemotactic bacteria with a biphasic tumbling frequency," *J. Math. Biol.*, vol. 47, p. 518, 2003.

[89] C. E. Zobell, "Some factors which influence oxygen consumption by bacteria in lake water," *Biol. Bull.*, vol. 78, p. 388, 1940.

[90] E. Lushi, R. Goldstein, and M. Shelley, "Collective chemotactic dynamics in the presence of self-generated fluid flows," *Phys. Rev. E*, vol. 86, p. 040902, Oct 2012.

[91] A. Alizadeh Pahlavan and D. Saintillan, "Instability regimes in flowing suspensions of swimming micro-organisms," *Phys. Fluids*, vol. 23, p. 011901, 2011.

[92] T. Pedley, "Instability of uniform micro-organism suspensions revisited," *Journal of Fluid Mechanics*, vol. 647, pp. 335–359, 3 2010.

[93] L. Rothschild, "Non-random distribution of bull spermatozoa in a drop of sperm suspension," *Nature*, vol. 198, pp. 1221–1222, 1963.

[94] D. M. Woolley, "Motility of spermatozoa at surfaces," *Reproduction*, vol. 126, pp. 259–270, 2003.

[95] S. S. Suarez and A. A. Pacey, "Sperm navigation in the female reproductive tract," *Human Reproduction Update*, vol. 12, pp. 23–37, 2006.

[96] P. Denissenko, V. Kanstler, D. J. Smith, and J. Kirkman-Brown, "Human spermatozoa migration in micro channels reveals boundary-following navigation," *Proc. Natl. Acad. Sci. USA*, vol. 109, pp. 8007–8010, 2012.

[97] V. Kantsler, J. Dunkel, M. Blayney, and R. E. Goldstein, "Rheotaxis facilitates upstream navigation of mammalian sperm cells," *eLife*, vol. 3, p. 02403, 2014.

[98] R. Rusconi, S. Lecuyer, L. Guglielmini, and H. A. Stone, "Laminar flow around corners triggers the formation of biofilm streamers," *J. R. Soc. Interface*, vol. 7, pp. 1293–1299, 2010.

[99] S. Lecuyer, R. Rusconi, Y. Chen, A. Forsyth, H. Vlamakis, R. Kolter, and H. A. Stone, "Shear stress increases the residence time of adhesion of *Pseudomonas aeruginosa*," *Biophys. J.*, vol. 100, pp. 341–350, 2011.

[100] M. Y. Kim, K. Drescher, O. S. Park, B. Bassler, and H. A. Stone, "Filaments in curved streamlines: rapid formation of *Staphylococcus aureus* biofilm streamers," *N. J. Phys.*, vol. 16, p. 065024, 2014.

[101] L. Lu and W. A. Walker, "Pathologic and physiologic interactions of bacteria with the gastrointestinal epithelium," *Am. J. Clin. Nutr.*, vol. 73, pp. 1124–1130, 2001.

[102] J. P. Cellia, B. S. Turner, N. H. Afdhal, S. Keates, I. Ghiran, C. P. Kelly, R. H. Ewoldt, G. H. McKinley, P. So, S. Erramilli, and R. Bansil, "*Helicobacter pylori* moves through mucus by reducing mucin viscoelasticity," *Proc. Natl. Acad. Sci. USA*, vol. 106, pp. 14321–14326, 2009.

[103] I. H. Riedel, K. Kruse, and J. Howard, "A self-organized vortex array of hydrodynamically entrained sperm cells," *Science*, vol. 309, pp. 300–303, 2005.

[104] H. Wioland, F. G. Woodhouse, J. Dunkel, J. O. Kessler, and R. E. Goldstein, "Confinement stabilizes a bacterial suspension into a spiral vortex," *Phys. Rev. Lett.*, vol. 110, p. 268102, 2013.

[105] E. Lushi, H. Wioland, and R. E. Goldstein, "Fluid flows created by swimming bacteria drive self-organization in confined suspensions," *Proc. Natl. Acad. Sci. USA*, vol. 111, pp. 9733–9738, 2014.

[106] P. Galajda, J. Keymer, P. Chaikin, and R. Austin, "A wall of funnel concentrates swimming bacteria," *J. Bacteriol.*, vol. 189, pp. 8704–8707, 2007.

[107] S. E. Hulme, W. R. DiLuzio, S. S. Shevkoplyas, L. Turner, M. Mayer, H. C. Berg, and G. M. Whitesides, "Using ratchets and sorters to fractionate motile cells of *Escherichia coli* by length," *Lab on a Chip*, vol. 8, pp. 1888–1895, 2008.

[108] G. Lambert, D. Liao, and R. H. Austin, "Collective escape of chemotactic swimmers through microscopic ratchets," *Phys. Rev. Lett.*, vol. 104, p. 168102, 2010.

[109] A. Kaiser, H. H. Wensink, and H. Löwen, "How to capture active particles," *Phys. Rev. Lett.*, vol. 108, p. 268307, 2012.

[110] E. Altshuler, G. Miño, C. Pérez-Penichet, L. del Río, A. Lindner, A. Rousselet, and E. Clément, "Flow-controlled densification and anomalous dispersion of *E. coli* through a constriction," *Soft Matter*, vol. 9, pp. 1864–1870, 2013.

[111] A. Sokolov, M. M. Apodaca, B. A. Grzybowski, and I. S. Aranson, "Swimming bacteria power microscopic gears," *Proc. Natl. Acad. Sci. USA*, vol. 107, pp. 969–974, 2010.

[112] R. Di Leonardo, L. Angelani, D. Dell'Arciprete, G. Ruocco, V. Iebba, S. Schippa, M. P. Conte, F. Mecarini, F. De Angelis, and E. Di Fabrizio, "Bacterial ratchet motors," *Proc. Natl. Acad. Sci. USA*, vol. 107, pp. 9541–9545, 2010.

[113] N. Koumakis, A. Lepore, C. Maggi, and R. Di Leonardo, "Targeted delivery of colloids by swimming bacteria," *Nature Comm.*, vol. 4, p. 2588, 2013.

[114] A. Kaiser, A. Peshkov, A. Sokolov, B. ten Hagen, H. Löwen, and I. S. Aranson, "Transport powered by bacterial turbulence," *Phys. Rev. Lett.*, vol. 112, p. 158101, 2014.

[115] J. G. Gibbs, S. Kothari, D. Saintillan, and Y.-P. Zhao, "Geometrically designing the kinematic behavior of catalytic nanomotors," *Nano Lett.*, vol. 11, pp. 2543–2550, 2011.

[116] D. Takagi, A. Braunschweig, J. Zhang, and M. J. Shelley, "Dispersion of self-propelled rods undergoing fluctuation-driven flips," *Phys. Rev. Lett.*, vol. 110, p. 038301, 2013.

[117] D. Takagi, J. Palacci, A. Braunschweig, M. Shelley, and J. Zhang, "Hydrodynamic capture of microswimmers into sphere-bound orbits," *Soft Matter*, vol. 10, pp. 1784–1789, 2014.

[118] A. P. Berke, L. Turner, H. C. Berg, and E. Lauga, "Hydrodynamic attraction of swimming microorganisms by surfaces," *Phys. Rev. Lett.*, vol. 101, p. 038102, 2008.

[119] E. Lauga, W. R. DiLuzio, G. M. Whitesides, and H. A. Stone, "Swimming in circles: Motion of bacteria near solid boundaries," *Biophys. J.*, vol. 90, pp. 400–412, 2006.

[120] S. E. Spagnolie and E. Lauga, "Hydrodynamics of self-propulsion near boundaries: predictions and accuracy of far-field approximations," *J. Fluid Mech.*, vol. 700, pp. 105–147, 2012.

[121] L. J. Fauci and A. McDonald, "Sperm motility in the presence of boundaries," *Bull. Math. Biol.*, vol. 57, pp. 679–699, 1995.

[122] G. Li and J. X. Tang, "Accumulation of microswimmers near a surface mediated by collision and rotational Brownian motion," *Phys. Rev. Lett.*, vol. 103, p. 078101, 2009.

[123] G. Li, J. Bensson, L. Nisimova, D. Munger, P. Mahautmr, J. X. Tang, M. R. Maxey, and Y. V. Brun, "Accumulation of swimming bacteria near a solid surface," *Phys. Rev. E*, vol. 84, p. 041932, 2011.

[124] A. Costanzo, R. Di Leonardo, G. Ruocco, and L. Angelani, "Transport of self-propelling bacteria in micro-channel flow," *J. Phys.: Condens. Matter*, vol. 24, p. 065101, 2012.

[125] J. Elgeti and G. Gompper, "Wall accumulation of self-propelled spheres," *Europhys. Lett.*, vol. 101, p. 48003, 2013.

[126] J. Hill, O. Kalkanci, J. L. McMurry, and H. Koser, "Hydrodynamic surface interactions enable *Escherichia coli* to seek efficient routes to swim upstream," *Phys. Rev. Lett.*, vol. 98, p. 068101, 2007.

[127] T. Kaya and H. Koser, "Characterization of hydrodynamic surface interactions of *Escherichia coli* cell bodies in shear flow," *Phys. Rev. Lett.*, vol. 103, p. 138103, 2009.

[128] T. Kaya and H. Koser, "Direct upstream motility in *Escherichia coli*," *Biophys. J.*, vol. 102, pp. 1514–1523, 2012.

[129] R. Rusconi, J. S. Guasto, and R. Stocker, "Bacterial transport suppressed by fluid shear," *Nature Phys.*, vol. 10, pp. 212–217, 2014.

[130] J. Gachelin, G. Miño, H. Berthet, A. Lindner, A. Rousselet, and E. Clement, "Non-Newtonian viscosity of *Escherichia coli* suspensions," *Phys. Rev. Lett.*, vol. 110, p. 268103, 2013.

[131] B. M. Haines, A. Sokolov, I. S. Aranson, L. Beryland, and D. A. Karpeev, "Three-dimensional model for the effective viscosity of bacterial suspensions," *Phys. Rev. E*, vol. 80, p. 041922, 2009.

[132] J. P. Hernández-Ortiz, P. T. Underhill, and M. D. Graham, "Dynamics of confined suspensions of swimming particles," *J. Phys.: Condens. Matter*, vol. 21, p. 204107, 2009.

[133] C. F. Lee, "Active particles under confinement: aggregation at the wall and gradient formation inside a channel," *New J. Phys.*, vol. 15, p. 055007, 2013.

[134] G. Li and A. M. Ardekani, "Hydrodynamic interaction of microswimmers near a wall," *Phys. Rev. E*, vol. 90, p. 013010, 2014.

[135] A. Zöttl and H. Stark, "Nonlinear dynamics of a microswimmer in Poiseuille flow," *Phys. Rev. Lett.*, vol. 108, p. 218104, 2012.

[136] A. Zöttl and H. Stark, "Periodic and quasiperiodic motion of an elongated microswimmer in Poiseuille flow," *Eur. Phys. J. E*, vol. 36, p. 4, 2013.

[137] R. W. Nash, R. Adhikari, J. Tailleur, and M. E. Cates, "Run-and-tumble particles with hydrodynamics: Sedimentation, trapping, and upstream swimming," *Phys. Rev. Lett.*, vol. 104, p. 258101, 2010.

[138] S. Chilukuri, C. H. Collins, and P. T. Underhill, "Impact of external flow on the dynamics of swimming microorganisms near surfaces," *J. Phys.: Condens. Matter*, vol. 26, p. 115101, 2014.

[139] M. C. Marchetti, J. F. Joanny, S. Ramaswamy, T. B. Liverpool, J. Prost, M. Rao, and R. Aditi Simha, "Hydrodynamics of soft active matter," *Rev. Mod. Phys.*, vol. 85, pp. 1143–1189, 2013.

[140] D. Saintillan and M. J. Shelley, "Instabilities and pattern formation in active particle suspensions: Kinetic theory and continuum particle simulations," *Phys. Rev. Lett.*, vol. 100, p. 178103, 2008.

[141] D. Saintillan and M. J. Shelley, "Instabilities, pattern formation, and mixing in active suspensions," *Phys. Fluids*, vol. 20, p. 123304, 2008.

[142] R. N. Bearon, A. L. Hazel, and G. J. Thorn, "The spatial distribution of gyrotactic swimming micro-organisms in laminar flow fields," *J. Fluid Mech.*, vol. 680, pp. 602–635, 2011.

[143] T. V. Kasyap and D. Koch, "Instability of an inhomogeneous bacterial suspension subjected to a chemo-attractant gradient," *J. Fluid Mech.*, vol. 741, pp. 619–657, 2014.

[144] J. M. Nitsche and H. Brenner, "On the formulation of boundary conditions for rigid non spherical Brownian particles near solid walls: Applications to orientation-specific reactions with immobilized enzymes," *J. Colloid Interface Sci.*, vol. 138, pp. 21–41, 1990.

[145] R. L. Schiek and E. S. G. Shaqfeh, "A nonlocal theory for stress in bound, Brownian suspensions of slender, rigid fibres," *J. Fluid Mech.*, vol. 296, pp. 271–324, 1995.

[146] P. J. Krochak, J. A. Olson, and D. M. Martinez, "Near-wall estimates of the concentration and orientation distribution of a semi-dilute rigid fibre suspension in Poiseuille flow," *J. Fluid Mech.*, vol. 653, pp. 431–462, 2010.

[147] D. Saintillan, "Extensional rheology of active suspensions," *Phys. Rev. E*, vol. 81, p. 056307, 2010.

[148] H. Brenner, "Rheology of a dilute suspension of axisymmetric Brownian particles," *Intl. J. Multiphase Flow*, vol. 1, pp. 195–341, 1974.

[149] J. Gachelin, A. Rousselet, A. Lindner, and E. Clement, "Collective motion in an active suspension of *Escherichia coli* bacteria," *New J. Phys.*, vol. 16, p. 025003, 2014.

[150] V. Kantsler, J. Dunkel, M. Polin, and R. E. Goldstein, "Ciliary contact interactions dominate surface scattering of swimming eukaryotes," *Proc. Natl. Acad. Sci. USA*, vol. 110, pp. 1187–1192, 2013.

[151] R. Voituriez, J. F. Joanny, and J. Prost, "Spontaneous flow transition in active polar gels," *Europhys. Lett.*, vol. 70, pp. 404–410, 2005.

[152] S. A. Edwards and J. M. Yeomans, "Spontaneous flow states in active nematics: a unified picture," *Europhys. Lett.*, vol. 85, p. 18008, 2009.

[153] M. Ravnik and J. M. Yeomans, "Confined active nematic flow in cylindrical capillaries," *Phys. Rev. Lett.*, vol. 110, p. 026001, 2013.

[154] S. Fürthauer, M. Neef, S. W. Grill, K. Kruse, and F. Jülicher, "The Taylor-Couette motor: spontaneous flows of active polar fluids between two coaxial cylinders," *New J. Phys.*, vol. 14, p. 023001, 2012.

[155] D. Marenduzzo, E. Orlandini, and J. Yeomans, "Hydrodynamics and rheology of active liquid crystals: A numerical investigation," *Phys. Rev. Lett.*, vol. 98, p. 118102, 2007.

[156] D. Marenduzzo, E. Orlandini, M. Cates, and J. Yeomans, "Steady-state hydrodynamic instabilities of active liquid crystals: Hybrid lattice Boltzmann simulations," *Phys. Rev. E*, vol. 76, p. 031921, 2007.

[157] J. Elgeti and G. Gompper, "Run-and-tumble dynamics of self-propelled particles in confinement," *Europhys. Lett.*, vol. 109, p. 58003, 2015.

[158] J. H. Ferziger and M. Perić, *Computational Methods for Fluid Dynamics*. Springer, 2002.

[159] N. Figueroa-Morales, G. Miño, A. Rivera, R. Caballero, E. Clément, E. Altshuler, and A. Lindner, "Living on the edge: transfer and traffic of E. coli in a confined flow," *Soft Matter*, vol. 11, pp. 6284–6293, 2015.

[160] H. C. Berg, *Random Walks in Biology*. Princeton University Press, 1993.

[161] S. C. Takatori, W. Yan, and J. F. Brady, "Swim pressure: Stress generation in active matter," *Phys. Rev. Lett.*, vol. 113, p. 028103, 2014.

[162] X. Yang, M. L. Manning, and M. C. Marchetti, "Aggregation and segregation of confined active particles," *Soft Matter*, vol. 10, pp. 6477–6484, 2014.

[163] R. G. Winkler, A. Wysocki, and G. Gompper, "Virial pressure in systems of active Brownian particles," *Soft Matter*, vol. 11, pp. 6680–6691, 2015.

[164] A. P. Solon, J. Stenhammar, R. Wittkowski, M. Kardar, Y. Kafri, M. E. Cates, and J. Tailleur, "Pressure and phase equilibria in interacting active Brownian spheres," *Phys. Rev. Lett.*, vol. 114, p. 198301, 2015.

[165] S. C. Takatori and J. F. Brady, "Towards a thermodynamics of active matter," *Phys. Rev. E*, vol. 91, p. 032117, 2015.

[166] D. Ray, C. Reichhardt, and C. J. O. Reichhardt, "Casimir effect in active matter systems," *Phys. Rev. E*, vol. 90, p. 013019, Jul 2014.

[167] S. A. Mallory, C. Valeriani, and A. Cacciuto, "Curvature-induced activation of a passive tracer in an active bath," *Phys. Rev. E*, vol. 90, p. 032309, Sep 2014.

[168] F. Ginot, I. Theurfauff, D. Levis, C. Ybert, L. Bocquet, L. Berthier, and C. Cottin-Bizonne, "Nonequilibrium equation of state in suspensions of active colloids," *Phys. Rev. X*, vol. 5, p. 011004, 2015.

[169] A. P. Solon, Y. Fily, A. Baskaran, M. E. Cates, Y. Kafri, M. Kardar, and J. Tailleur, "Pressure is not a state function for generic active fluids," *Nature Phys.*, vol. 11, pp. 673–678, 2015.

[170] Y. Fily, A. Baskaran, and M. F. Hagan, "Dynamics of self-propelled particles under strong confinement," *Soft Matter*, vol. 10, pp. 5609–5617, 2014.

[171] A. Wysocki, J. Elgeti, and G. Gompper, "Giant adsorption of microswimmers: Duality of shape asymmetry and wall curvature," *Phys. Rev. E*, vol. 91, p. 050302, 2015.

[172] M. Molaie, M. Barry, R. Stocker, and J. Sheng, "Failed escape: Solid surfaces prevent tumbling of *Escherichia coli*," *Phys. Rev. Lett.*, vol. 113, p. 068103, 2014.

[173] G. Volpe, I. Buttinoni, D. Vogt, H.-J. Kümmerer, and C. Bechinger, "Microswimmers in patterned environments," *Soft Matter*, vol. 7, pp. 8810–8815, 2011.

[174] D. Saintillan and M. J. Shelley, "Active suspensions and their nonlinear models," *C. R. Physique*, vol. 14, pp. 497–517, 2013.

[175] T. J. Pedley and J. O. Kessler, "Hydrodynamic phenomena in suspensions of swimming microorganisms," *Annu. Rev. Fluid Mech.*, vol. 24, no. 1, pp. 313–358, 1992.

[176] P. T. Underhill, J. P. Hernandez-Ortiz, and M. D. Graham, "Diffusion and spatial correlations in suspensions of swimming particles," *Phys. Rev. Lett.*, vol. 100, p. 248101, Jun 2008.

[177] F. G. Woodhouse and R. E. Goldstein, "Spontaneous circulation of confined active suspensions," *Phys. Rev. Lett.*, vol. 109, p. 168105, 2012.

[178] A. Creppy, F. Plouraboue, O. Praud, X. Druart, S. Cazin, and P. Degond, "Symmetry-breaking phase-transitions in highly concentrated semen," p. submitted, 2015.

[179] T. V. Kasyap, D. Koch, and M. Wu, "Bacterial collective motion near the contact line of an evaporating sessile drop," *Phys. Fluids*, vol. 26, p. 111703, 2014.

[180] E. Yariv and O. Schnitzer, "Ratcheting of brownian swimmers in periodically corrugated channels: A reduced fokker-planck approach," *Phys. Rev. E*, vol. 90, p. 032115, Sep 2014.

[181] H. Wioland, "Self-organization of confined active matter," 2014.

[182] A. C. H. Tsang and E. Kanso, "Circularly confined microswimmers exhibit multiple global patterns," *Phys. Rev. E*, vol. 91, p. 043008, 2015.

[183] H. Wioland, F. G. Woodhouse, J. Dunkel, and R. E. Goldstein, "Ferromagnetic and antiferromagnetic order in bacterial vortex lattices," *Nature Phys.*, p. to appear, 2015.

[184] M. Theillard, B. Ezhilan, and D. Saintillan, "Geometric control of active self-organization," 2016.